Electrokinetic Phenomena and Singularity-Driven Flows in Nematic Liquid Crystals

A THESIS
SUBMITTED TO THE FACULTY OF THE GRADUATE SCHOOL
OF THE UNIVERSITY OF MINNESOTA
BY

Christopher Conklin

IN PARTIAL FULFILLMENT OF THE REQUIREMENTS
FOR THE DEGREE OF
DOCTOR OF PHILOSOPHY

Adviser: Jorge Viñals

November, 2017

Acknowledgements

I am indebted to the support I have received from my adviser, Jorge Viñals. Jorge has the rare quality of providing constructive feedback while remaining positive and forward-looking. He has provided significant guidance while still allowing me to make creative choices of my own.

This work would not have been possible without the experimental support from Oleg D. Lavrentovich, Chenhui Peng, Sathyanarayana Paladugu, and others in the Lavrentovich lab. The dialogue between theory and experiments has been incredibly productive in understanding the fundamentals of this system. I have also benefited from numerous discussions with Carme Calderer, Dmitry Golovaty, Noel Walkington, Oriol T. Valls, and many others.

I would not have reached this point were it not for the numerous scientific mentors along the way, and I am particularly grateful to have learned the foundations from Bill Prem, Mike Maas, and Vince Thomas in Eden Prairie. I had incredible mentors at St. Olaf College, including Amy Kolan, whose lessons on PDEs I still use today, and Jim Cederberg, who gave me my first experience in physics research. At the University of Minnesota, I am grateful to have worked with Jim Kakalios, who taught me about communicating challenging concepts, and Ron Polling, who taught me about leadership. I would also like to thank the staff at the School of Physics and Astronomy, whose attention to detail allowed me to focus on my research. This work was also supported by the National Science Foundation under contract DMS 1435372, and the Minnesota Supercomputing Institute.

My parents, Pete and Sue, have done so much for me in this process, starting with instilling curiosity in me from an early age, and creating a culture of striving for excellence. Their mentoring and support throughout my entire education is what has

allowed me to believe no task was too daunting to achieve. I am also grateful to my sister Kayla, who shares and enhances my enthusiasm for setting big goals.

Finally, I could not have made it through this process without the support and encouragement from my wife Julie. From working through problem sets to developing presentations, Julie has been an incredible scientific mind with whom I can work through ideas. She has also helped foster an environment in which I can thrive, and has done an incredible amount of work the past few months to allow me to focus on writing. I look forward to returning the favor in a couple years, and I am so glad that we are collaborators for life.

Dedication

To Dr. Harold F. Hardman, M.D. Ph.D, whose photo has been on my desk since day one of graduate school.

Abstract

Electrokinetic phenomena, including electrophoresis and electroosmosis, provide a significant tool for engineering the transport of fluids and particles at microscopic scales. This thesis describes additional mechanisms for generating electrokinetic flow by using a nematic liquid crystal electrolyte. Under an applied electric field the anisotropic properties of the liquid crystal lead to separation of ionic impurities present in the fluid, which couple with the applied field to produce electrostatic forces that drive fluid and particle motion. This force is quadratic in the electric field, implying that systematic flow occurs even in the presence of an oscillating field. This thesis presents numerical and analytical investigations of this electrokinetic mechanism. We show that the charge density and fluid velocity of a system depends strongly on the topology of the liquid crystal orientation, and we present results for several distinct configurations, including periodic distortions, isolated disclinations, and particle suspensions. We also show that liquid crystal electrokinetic systems can be designed to mimic the behaviors of active nematics – collections of particles which can self-propel along a particular direction.

Contents

List of Tables

List of Figures

Chapter 1

Introduction

1.1 Motivation

The use of electric fields to transport fluids (electroosmosis) and particles (electrophoresis), generally referred to as electrokinetics, is an important tool for particle, second phase, or fluid transport in a wide variety of engineering, soft matter, and biological systems. For instance, electrokinetics have been used to create "lab-on-chip" micropumps, nanofluidic diodes, microfluidic field-effect transistors, and e-ink devices such as the Amazon Kindle [7–10].

Many electrokinetic applications use direct current (DC) fields, which allow for direct manipulation of charged colloidal particles, with particle velocity proportional to the applied field [9]. However, these systems suffer from reduction of electric field strength due to charge accumulation near electrodes [11]. Instead, nonlinear electrokinetics, in which velocities are proportional to the square of the electric field, allow for the use of alternating current (AC) fields with frequencies much faster than the rate of charge accumulation at electrodes. Two examples of nonlinear electrokinetics are depicted in Fig. 1.1. The applied field polarizes solid boundaries, causing ionic impurities within the solvent to form charge double-layers near the polarized boundaries. These charged regions couple again with the applied field to drive flow [8]. The charge density is linear in the electric field, and fluid velocity is proportional to the electrostatic force $\rho \boldsymbol{E}$. Thus the velocity is proportional to the square of the electric field, and thus persists even in an oscillating field. Systematic flow can be generated by using asymetric electrodes

or nonuniform suspended particles [1, 2, 8]. Limitations in nonlinear electrokinetics with isotropic fluids arise when one wishes to create systematic flow with symmetrical electrodes or symmetrical particles. Furthermore, the design of complex flow patterns, such as those used for mixing two species, requires the fabrication of a fluid cell with obstructions, pressure gradients, or a complex scheme of electrodes [12].

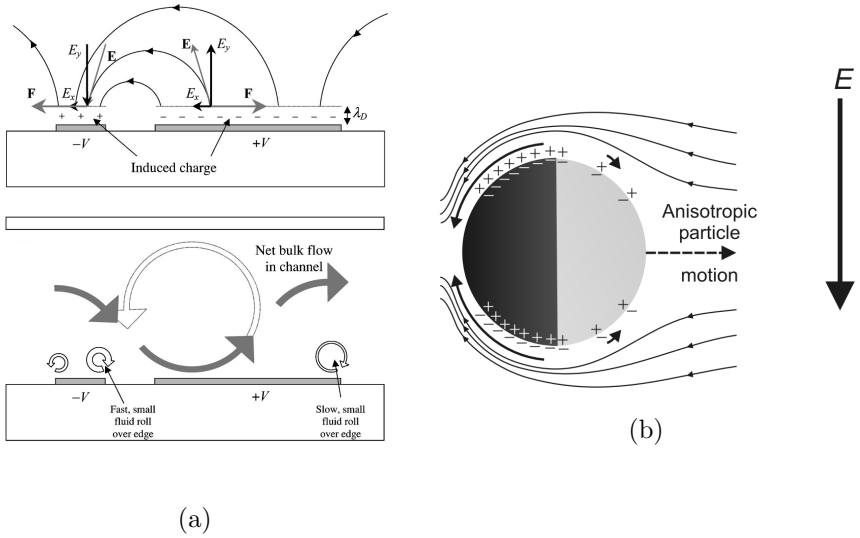

(a) (b)

Figure 1.1: Two examples of nonlinear electrokinetic flow in isotropic fluids. (a) Two electrodes are placed in such a way as to create a nonuniform electric field. Charges accumulate near the electrodes due to the presence of the applied field. The charges then couple with the field again to generate an electrostatic force on the fluid that is to the right on the right electrode, and to the left on the left electrode. The asymmetry of the electrodes leads to systematic flow in the channel. This figure is reproduced from Ref. [1]. (b) A nonuniform "Janus Particle" comprised of a dielectric and a metallic hemisphere is placed in a uniform electric field. The applied field polarizes the particle, leading to a layer of charged ions in the fluid collecting near the particle surface. The ions couple with the electric field again to drive fluid flow toward the center of the figure. The asymmetry of the particle permittivity leads to systematic particle motion. This figure is reproduced from Ref. [2].

In this thesis we present theoretical results regarding a new technique for fluid-flow engineering driven by electric fields: liquid crystal electrokinetics (LCEK). Liquid crystal molecules are anisotropic with at least one primary axis and can be visualized as long, thin rods. In their nematic state, liquid crystals form a fluid with a (potentially)

nonuniform orientational order. This orientational order is determined by boundary conditions and depends strongly on the topology of the system. In LCEK, the nematic liquid crystal replaces the isotropic solvent in traditional electrokinetics, and the assymentry of the nematic solvent provides an additional mechanism for ionic charge separation, leading to nonlinear electrokinetic flow. By manipulating the orientational order of the nematic, LCEK can produce flow behaviors not possible with isotropic nonlinear electrokinetics, such as the systematic transport of spherically symmetrical particles [5], systematic fluid pumping, and micromixing using symmetrical electrodes [3,13]. In particular, the structure of the LCEK flow depends strongly on the topology of the nematic orientation.

1.2 Notational Conventions

Throughout this thesis, variables are occasionally presented in both dimensional and dimensionless forms. Wherever confusion may arise, we use an asterisk to denote dimensional variables, while dimensionless variables have no asterisk (e.g. L^* has units of length, while $L = L^*/\ell^*$ is dimensionless). For physical parameters which always appear as dimensional in the thesis, such as field frequency ω, mobilities $\mu_\parallel, \mu_\perp$, permittivity of free space ϵ_0, we do not use an asterisk. We use L^* to denote system size, and ℓ^* for a characteristic length of the configuration under study (in some cases $\ell^* = L^*$, while in others ℓ^* is the radius of a suspended particle or the separation between topological defects). We use ρ to denote charge density and ϱ to denote mass density. Finally, in all equations, unless otherwise noted, summation is implied over repeated indices (e.g. $u_i v_i = u_x v_x + u_y v_y + u_z v_z$).

1.3 Structure

This thesis investigates the physical mechanisms behind LCEK through analytical and numerical results. Chapter 2 discusses the LCEK model, the nature of topological defects in nematics, and the numerical method used to investigate LCEK systems. We compare two methods for describing order in nematics, and discuss the mechanisms responsible for electrokineitc flow using a simple example.

Chapter 3 investigates prototypical configurations to ascertain the relationship between topological defects and fluid flow by considering the LCEK behavior of thin films with imposed orientational patterns containing singularities. This numerical work is in coordination with a series of benchmark experiments performed to further establish this relationship between topology and fluid flow. We find a direct relationship between the topological charge of the orientational singularities and the angular structure of the charge density and fluid velocity. Additionally we find that while the orientational patterns are singular, the charge density and velocity fields are both bounded at the orientational singularities.

Chapter 4 generalizes the results of Chapter 3 for arbitrary director pattern. We find a Green's function for the LCEK-induced charge density at small mobility and dielectric anisotropy, and we use these results to determine the charge and velocity behavior for various multipole moments of the director field.

Chapter 5 extends the results for patterned cells to systems of particles suspended in a nematic matrix. We show that the boundary conditions around the suspended particles necessitate the nucleation of topological defects, and that defect nucleation breaks symmetry and drives systematic particle motion. Additionally, we consider the effects of backflows on fluid velocity and nematic orientation. In conjunction with experiments, we show that the velocity of suspended particles can be manipulated and even reversed by adjusting the relative anisotropy of nematic dielectric permittivity. We also find that electrokineitc flows produce an attractive or repulsive force between two suspended particles depending on the relative orientation of the nematic molecule and the particle surface.

Chapter 6 compares LCEK to another system of recent interest, active nematics, in which collections of self-propelling particles (such as bacteria) drive fluid flow through their collective motion [14]. We present an electrokinetic system analog in which the numerically-obtained velocity field agrees with experimental studies of active nematics with the same nematic orientation. We determine a set of conditions in which the driving force in electrokinetic systems matches the driving force in active systems, and we discuss how the behavior of ionic concentrations compare to the behavior of bacterial concentrations.

Finally, in Chapter 7 we summarize our findings.

Chapter 2

Background, model equations, and connection to experiments

Liquid crystals are materials with large molecular anisotropy which leads to the appearance of phases which are intermerdiate between a solid and a liquid as a function of temperature or concentration. In the so-called nematic phase, rotational invariance is broken, while translational invariance remains. In this chapter we discuss how this symmetry breaking may be used as a mechanism to produce electrokinetic phenomena. We begin by discussing the nematic order parameter, its topology, and the energy associated with elastic distortions. Next we discuss two different descriptions of the nematic order, and present the corresponding derivations of the governing equations for LCEK. We illustrate the mechanisms responsible for electrokinetic fluid flow by using a simple example configuration, and make contact with experiments expressely designed to verify the model introduced. We end the chapter with a description of the numerical method that we use to solve the governing equations for more complex configurations.

2.1 Order Parameter

The simplest ordered liquid crystal phase is the uniaxial nematic. In the nematic state, a non polar molecular axis is oriented on average parallel to a common direction $\hat{\boldsymbol{n}}$, called the director. The director $\hat{\boldsymbol{n}}$ is defined as a unit vector, and the states $\hat{\boldsymbol{n}}$ and $-\hat{\boldsymbol{n}}$ are indistinguishable.

Let $\hat{\boldsymbol{a}}$ be the axis of a liquid crystal molecule. In a coordinate system where $\hat{\boldsymbol{z}} = \hat{\boldsymbol{n}}$ with polar angle θ and azimuthal angle ϕ, define $p(\theta, \phi)d\Omega$ as the probability of finding $\hat{\boldsymbol{a}}$ within a solid angle $d\Omega$. We expect cylindrical symmetry about $\hat{\boldsymbol{n}}$, so p is independent of ϕ, and invariance under $\hat{\boldsymbol{n}} \to -\hat{\boldsymbol{n}}$ implies $p(\theta) = p(\pi - \theta)$. Suppose we write p as a multipole expansion,

$$p(\theta) = \sum_{n=0}^{\infty} C_n P_n(\cos\theta), \tag{2.1}$$

where P_n is the n^{th} Legendre polynomial and,

$$C_n = \frac{2n+1}{2} \int_0^{\pi} p(\theta) P_n(\cos\theta) \sin\theta \; d\theta. \tag{2.2}$$

We find $C_0 = 1/(4\pi)$ due to normalization requirements for p and $C_1 = 0$ since $p(\theta) = p(\pi - \theta)$. Thus the first nontrivial term in Eq. (2.1) is the quadrupole term. We describe the degree to which molecules are aligned with $\hat{\boldsymbol{n}}$ by the the *scalar order parameter* S, which is proportional to the quadrupole moment of p,

$$S = \int p(\theta) P_2(\cos\theta) d\Omega, \tag{2.3}$$

$$P_2(\cos\theta) = \frac{1}{2}(3\cos^2\theta - 1).$$

Note that S is a function of temperature, $S = 1$ in the completely aligned state, and $S = 0$ in the disordered (isotropic) state.

While S describes the degree of orientational order and $\hat{\boldsymbol{n}}$ describes the direction of orientational order, a complete description of nematic order, invariant under $\hat{\boldsymbol{n}} \to -\hat{\boldsymbol{n}}$, is given by the symmetric, traceless tensor order parameter $\boldsymbol{Q}$. For the uniaxial nematic, $Q_{ij} = S(T)(n_i n_j - \delta_{ij}/d)$, where d is the dimensionality of space. Following Landau theory, one can write a mean field theory of liquid crystals with the free energy for nematic-isotropic transitions a functional of scalar combinations of $\boldsymbol{Q}$,

$$F^*(T) = \int [A(T) Q_{ij} Q_{ji} + B(T) Q_{ij} Q_{jk} Q_{ki} + C(T) Q_{ij} Q_{jk} Q_{kl} Q_{li}] d^d x^*, \tag{2.4}$$

or, using the definition of $\boldsymbol{Q}$, as a functional of S,

$$F^*(T) = \int [A(T)S^2 + B(T)S^3 + C(T)S^4] d^d x^*, \tag{2.5}$$

where $A(T), B(T), C(T)$ are phenomenological functions of temperature. It is generally assumed B and C are constant in T, while $A(T) = A_0(T - T_c)$, where T_c is the transition temperature. In two dimensions, the fact that $\boldsymbol{Q}$ is symmetric and traceless implies $\mathrm{Tr}(\boldsymbol{Q}^3) = 0$, so the cubic terms in Eqs. 2.4 and 2.5 vanish. Thus the nematic-isotropic transition is first order for $d = 3$ and second order for $d = 2$.

2.1.1 Elasticity

If the molecular orientation is not uniform, one defines $\boldsymbol{Q}(\boldsymbol{r}^*)$, $S(\boldsymbol{r}^*)$, and $\hat{\boldsymbol{n}}(\boldsymbol{r}^*)$ as their local average over a ball of radius R^* centered at r^*, with $a^* \ll R^* \ll L^*$, where $a^* \sim 10\text{Å}$ is the length of a liquid crystal molecule and $L^* \sim 1$ μm is the typical distortion scale [15]. We expect an elastic term f^*_{el} in the free energy density which is a functional of gradients of $\boldsymbol{Q}$. Since nematic systems are invariant under uniform rotations of $\boldsymbol{Q}$, f^*_{el} cannot contain terms proportional to $\nabla^* \boldsymbol{Q}$. Thus to second order in $\nabla^* \boldsymbol{Q}$, $f^*_{eq} = \tilde{K}_{ijklmn} \partial^*_i Q_{jk} \partial^*_l Q_{mn}$, where $\tilde{K}_{ijklmn}$ is a tensor that may be a function of $\boldsymbol{Q}$. This description involves many phenomenological constants and requires that short scale phenomena and energies beyond experimental resolution are correctly described [15, 16]. Typical analytical studies of nematics using $\boldsymbol{Q}$ assume a single elasticity parameter, $K_{ijklmn} = (K/2)\delta_{il}\delta_{jm}\delta_{kn}$. The complete free energy density including elastic distortions is known as the *Landau-de Gennes free energy density*, written as,

$$f^*_{LdG} = \frac{\tilde{K}}{2}(\partial^*_i Q_{kj})^2 + a(T) Q_{ij} Q_{ji} + b(T) Q_{ij} Q_{jk} Q_{ki} + c(T) Q_{ij} Q_{jk} Q_{kl} Q_{li}. \tag{2.6}$$

While the complete description of the phenomenological constants in the $\boldsymbol{Q}$-tensor elastic free energy is beyond the scope of current experiments, for weak distortions, $a^* \ll L^*$, the magnitude of the anisotropy of the optical properties of the liquid crystal are observed to depend only on $\hat{\boldsymbol{n}}$, implying S is independent of $\boldsymbol{r}^*$ [15]. Thus we may consider f^*_{el} to be an expansion in gradients of $\hat{\boldsymbol{n}}$. Thus to second order in $\nabla^* \hat{\boldsymbol{n}}$, $f^*_{el} = K_{ijkl} \partial^*_i n_j \partial^*_k n_l$, where K_{ijkl} again may be a function of $\hat{\boldsymbol{n}}$. Given $|\hat{\boldsymbol{n}}|^2 = 1$ and

considering that f_{el}^* must be invariant under $\boldsymbol{r}^* \to -\boldsymbol{r}^*$ and $\hat{\boldsymbol{n}} \to -\hat{\boldsymbol{n}}$, one finds that f_{el}^* reduces to three bulk terms [17],

$$f_{OF}^* = \frac{K_1}{2}(\nabla^* \cdot \hat{\boldsymbol{n}})^2 + \frac{K_2}{2}(\hat{\boldsymbol{n}} \cdot (\nabla^* \times \hat{\boldsymbol{n}}))^2 + \frac{K_3}{2}(\hat{\boldsymbol{n}} \times (\nabla^* \times \hat{\boldsymbol{n}}))^2, \tag{2.7}$$

where K_1, K_2, K_3 are the splay, twist, and bend elastic constants, respectively. Equation (2.7) is often referred to as the *Oseen-Frank elastic free energy density* [15]. The elastic constants in Eq. (2.7) can be accurately determined experimentally with typical values around $10\,pN$. Under the assumption $K_1 = K_2 = K_3 = K$, Eq. (2.7) matches the elastic term in Eq. (2.6), with S uniform and $K = 2S^2\tilde{K}$. Furthermore, in this one-constant approximation, the total elastic energy is

$$F_{OF} = \int \frac{K}{2}(\nabla \hat{\boldsymbol{n}})^2 d^d x. \tag{2.8}$$

Using calculus of variations, the director field in elastic equilibrium satisfies Laplace's equation, $\nabla^{*2} n_i = 0$, with the normalization condition, $|\hat{\boldsymbol{n}}|^2 = 1$. While the one-elastic constant approximation is generally not true experimentally, it is often used in analysis due to the simplification of the equations governing director orientation.

2.2 Topological Defects

Topological defects in nematics are singularities in $\hat{\boldsymbol{n}}$. Mathematically, the director $\hat{\boldsymbol{n}}$ is a mapping from the domain of the system Ω to the order parameter space $\mathcal{R}$, and the topology of singularities in $\hat{\boldsymbol{n}}$ depends on the topology of $\mathcal{R}$. Since $\hat{\boldsymbol{n}}$ is a unit vector and the system is invariant under $\hat{\boldsymbol{n}} \to -\hat{\boldsymbol{n}}$, the order parameter space in two dimensions is a circle with opposite ends identified, $S^1/\mathbb{Z}_2$, while in three dimensions $\mathcal{R}$ is the unit sphere with opposite ends identified, $S^2/\mathbb{Z}_2$.

In d dimensions, a k-dimensional contour encloses a $(d-k-1)$-dimensional singularity. For instance, a one-dimensional contour encloses a point defect in two dimensions and a line defect in three dimensions, while a two-dimensional contour encloses a point defect in three dimensions. The stability of a $(d-k-1)$-dimensional singularity is determined by the topology of k-dimensional contours on $\mathcal{R}$.

Two directed k-dimensional contours γ_1, γ_2 on $\mathcal{R}$ are said to be *homotopic* if γ_1 can

be continuously deformed into γ_2. The set of all contours that are mutually homotopic forms a *homotopy class*. Let G_M be the set of directed contours passing through an aribitrary base point $M \in \mathcal{R}$. Define the operation $\otimes$ such that $\gamma_1 \otimes \gamma_2$ is the contour that traverses γ_1 followed by γ_2. Then the set of all contours passing through M with the operation as defined above form a group; for any $\gamma_1, \gamma_2 \in G_M$, $\gamma_1 \otimes \gamma_2 \in G_M$, the operation $\otimes$ is associative, the identity element is the point M, and the inverse of $\gamma_1 \in G_M$ traverses the same path as γ_1 in the opposite direction. Furthermore, we can define the group $\pi_k(\mathcal{R})$ as the set of homotopy classes in $\mathcal{R}$ with the operation $A \otimes B = \gamma_A \otimes \gamma_B$, where $\gamma_A, \gamma_B \in G_M$ are representatives of the homotopy classes A, B. The group $\pi_k(\mathcal{R})$ is known as the k^{th} *homotopy group*. If d is the dimensionality of Ω, stable $(d-k-1)$-dimensional defects exist in Ω if $\pi_k(\mathcal{R})$ is nontrivial [18].

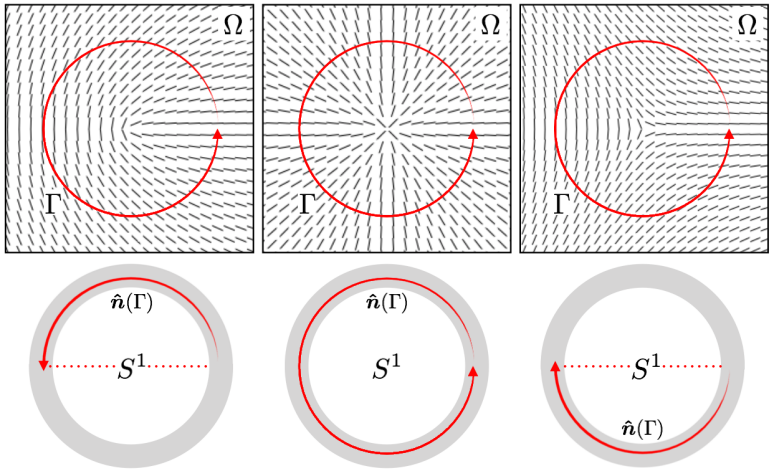

(a) $m = 1/2$ (b) $m = 1$ (c) $m = -1/2$

Figure 2.1: Three sample topological defects in two dimensions, with the director depicted as thin lines. The director $\hat{\boldsymbol{n}}$ maps a directed closed contour Γ enclosing the defect onto the order parameter space $S^1/\mathbb{Z}_2$, the unit circle with opposite ends identified. The topological charge m is the number of times $\gamma = \hat{\boldsymbol{n}}(\Gamma)$ wraps around S^1, with $m < 0$ if the direction of $\hat{\boldsymbol{n}}(\Gamma)$ is opposite Γ. (a) Along the countour Γ, the director $\hat{\boldsymbol{n}}$ completes a half revolution around S^1, giving it a topological charge $m = 1/2$. (b) The director traces a full revolution along Γ; thus the defect charge is $m = 1$. (c) The mapping $\hat{\boldsymbol{n}}(\Gamma)$ completes a half revolution around S^1 but in the opposite direction of Γ. Therefore the topological charge is $m = -1/2$.

In two dimensions point defects are stable, and the homotopy classes of $\pi_1(\mathcal{R})$ are

characterized by the topological charge m; the number of times an arbitrary closed contour $\gamma = \hat{\boldsymbol{n}}(\Gamma)$ wraps around S^1. Specifically, if $\hat{\boldsymbol{n}}(\boldsymbol{r}) = (\cos[\theta(\boldsymbol{r})], \sin[\theta(\boldsymbol{r})])$,

$$m = \frac{1}{2\pi} \oint_\Gamma \nabla\theta \cdot d\boldsymbol{l}. \tag{2.9}$$

Since $\hat{\boldsymbol{n}} = -\hat{\boldsymbol{n}}$, half-integral values of m are allowed.

Fig. 2.1 shows three sample topological defects in two dimensions. Let the directed contour Γ be a circle of radius R centered at the origin, directed in the counter-clockwise direction. We see that in Fig. 2.1a $\hat{\boldsymbol{n}}$ completes half a revolution as we trace along Γ, in Fig. 2.1b $\hat{\boldsymbol{n}}$ completes a full revolution, and in Fig. 2.1c completes half a revolution but in the opposite (clockwise) direction of Γ. Therefore the topological charges in Fig. 2.1 are $m = 1/2, 1, -1/2$, respectively.

More quantitatively, in polar coordinates with the origin at the defect center, the nematic configurations depicted in Fig. 2.1 are defined by $\theta(r, \phi) = m\phi$, where $m = 1/2, 1, -1/2$ respectively. Using Eq. (2.9), the topological charge of each configuration is therefore,

$$\frac{1}{2\pi} \oint_\Gamma \nabla\theta \cdot d\boldsymbol{l} = \frac{1}{2\pi} \int_0^{2\pi} \frac{1}{R} \frac{\partial\theta}{\partial\phi} R d\phi = \frac{1}{2\pi} \int_0^{2\pi} m d\phi = m. \tag{2.10}$$

Because the topological charges of these three configurations are different, they belong to different homotopy classes, and one configuration cannot be continuously transformed into another.

Using the group operation defined above, one can see that the inverse of a topological defect of charge m is a defect of charge $-m$. Figure 2.2a shows a pair of $(1/2, -1/2)$ defects. If Γ is a contour enclosing both defects, the mapping $\gamma = \hat{\boldsymbol{n}}(\Gamma)$ completes zero net revolutions around the unit circle S^1. Thus the contour $\hat{\boldsymbol{n}}(\Gamma)$ can be continuously deformed to a point, and the director field $\hat{\boldsymbol{n}}(\boldsymbol{r})$ can be continuously deformed into a uniform field, Figs. 2.2b-2.2c. Furthermore, the total topological charge of a system of N defects is simply the sum of the topological charges of the individual defects. In mathematical terms, the first homotopy group for the unit circle with opposite ends identified, $\pi_1(S^1/\mathbb{Z}_2)$, is isomorphic to the group $\frac{1}{2}\mathbb{Z}$ – the set of half-integers under addition.

In three dimensions, both line defects (called disclinations) and point defects are

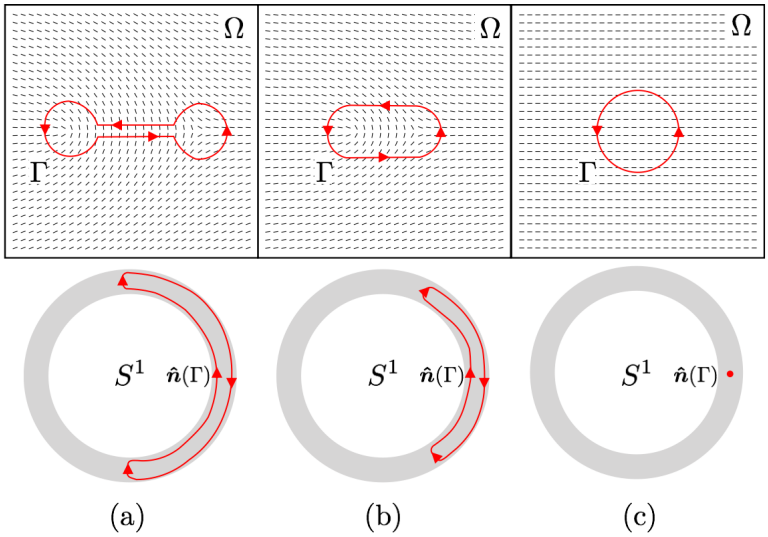

Figure 2.2: (a) Two topological point defects in two dimensions. The left defect has charge $m = 1/2$, while the right defect has charge $m = -1/2$. On a contour Γ enclosing both defects, the director $\hat{\boldsymbol{n}}$ traverses half the unit circle in one direction, then half the unit circle in the opposite direction. Thus the net number of revolutions of $\hat{\boldsymbol{n}}(\Gamma)$ about the unit circle S^1 is zero. This implies the director field $\hat{\boldsymbol{n}}(\boldsymbol{r})$ may be continuously deformed into a uniform alignment, as shown in (b)-(c).

stable. Similar to two dimensions, if a disclination passes through a directed closed one-dimensional contour Γ, the topological charge is the number of times $\hat{\boldsymbol{n}}(\Gamma)$ wraps around the unit sphere. Unlike two dimensions, integer-strength disclinations do not exist in three dimensions, as they can be continuously deformed into the uniform state. Figure 2.3 shows an example $(+1)$ disclination line in the $\hat{\boldsymbol{z}}$ direction. By rotating $\hat{\boldsymbol{n}}$ about $\hat{\boldsymbol{\phi}}$, the azimuthal direction, the director field is continuously deformed until it reaches a uniform state. On the unit sphere, we see the mapping $\hat{\boldsymbol{n}}(\Gamma)$ is deformed from a great circle around the equator to a point at the top of the sphere.

While integer-strength disclinations do not exist in three dimensions, we may recall that opposite ends of the unit sphere are equivalent for the order parameter space of $\hat{\boldsymbol{n}}$. Since contours whose ends remain on opposite ends of the sphere cannot be continuously deformed into a point, half-integer disclinations are topologically distinct from uniform director fields. Unlike in two dimensions, however, we find that $(+1/2)$-strength disclinations and $(-1/2)$-strength disclinations may be continuously deformed

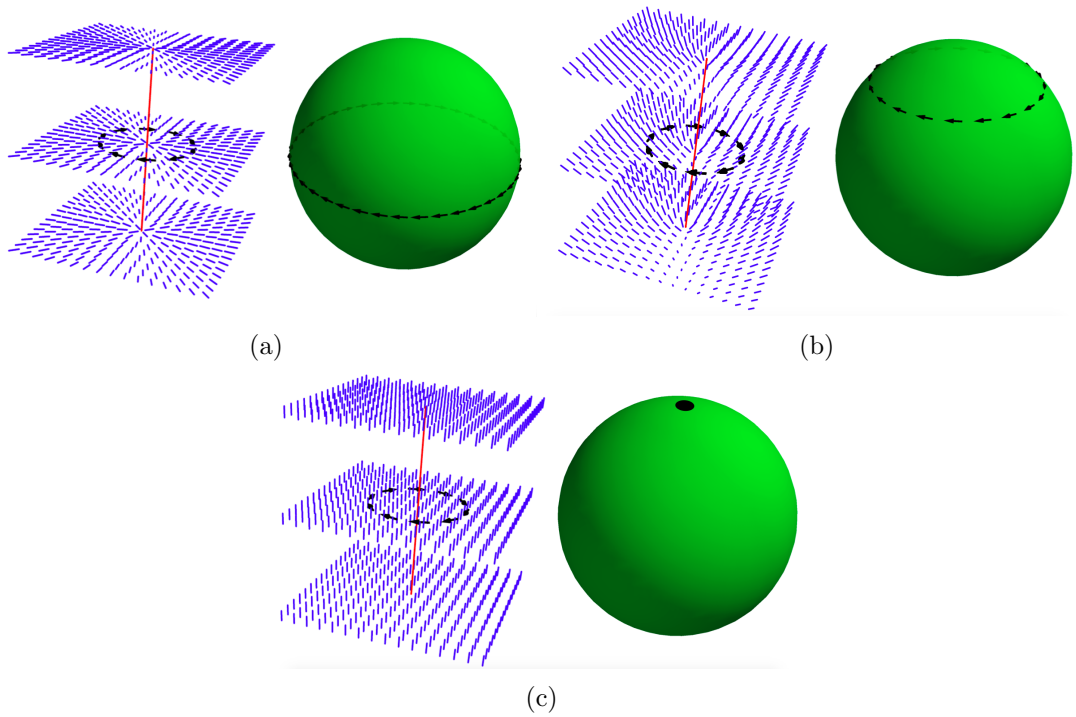

Figure 2.3: The director $\hat{\boldsymbol{n}}$ maps a directed, closed contour onto the unit sphere. (a) The contour encloses a disclination of topological charge (+1) as shown by the mapping completing one revolution around the unit sphere. (b)-(c) as $\hat{\boldsymbol{n}}$ is rotated about the azimuthal direction $\hat{\boldsymbol{\phi}}$, the mapping of the contour shrinks to a point. Thus a (+1) disclination line is topologically equivalent to a uniform director field. Thus (+1) disclination lines are not topologically stable.

into one another, making them topologically equivalent. Figure 2.4 depicts a director field with a (+1/2)-strength disclination line in the $\hat{\boldsymbol{z}}$ direction undergoing a continuous rotation about $\hat{\boldsymbol{y}}$, eventually becoming a (−1/2)-strength disclination. Therefore in three dimensions there are only two homotopy classes in the first homotopy group: one corresponding to no singularity, and one corresponding to a contour traversing half the unit sphere. Thus $\pi_1(S^2/\mathbb{Z}_2) = \mathbb{Z}_2$.

In three dimensions, the second homotopy group $\pi_2(S^2/\mathbb{Z}_2)$ classifies the topological characteristics of point defects, known as *hedgehogs*. Instead of a contour encircling a disclination line, we consider a surface σ_1 on Ω surrounding a point defect. $\hat{\boldsymbol{n}}$ maps σ_1 into the surface Σ_1 on $S^2/\mathbb{Z}_2$. The set of homotopy classes formed by surfaces along with an operation combining surfaces forms the second homotopy group $\pi_2(S^2/\mathbb{Z}_2)$.

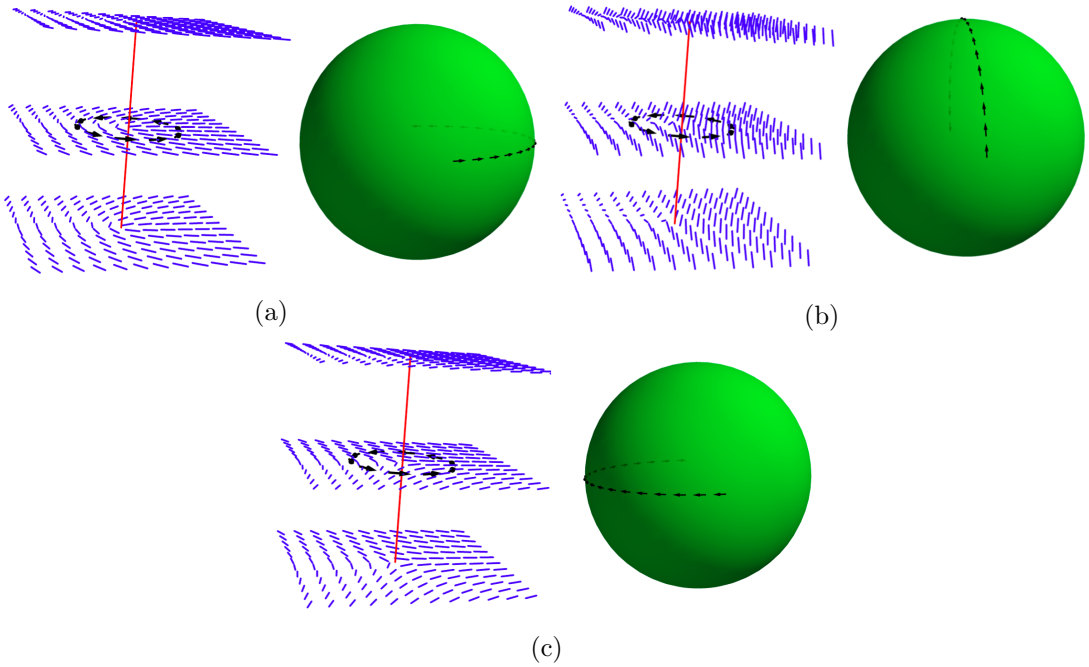

Figure 2.4: In three dimensions, half-integer disclinations of different charge can be continuously deformed into each other. (a) Along a contour enclosing a $(+1/2)$ disclination, the director $\hat{\boldsymbol{n}}$ traces a path halfway around the unit sphere. (b) $\hat{\boldsymbol{n}}$ is rotated about $\hat{\boldsymbol{y}}$. (c) After rotating about $\hat{\boldsymbol{y}}$ by π, the director field is now disclination of charge $(-1/2)$, with $\hat{\boldsymbol{n}}$ tracing a path halfway around the unit sphere in the opposite direction. Any two half-integer strength disclinations can by continuously deformed into each other by similar methods.

One finds $\pi_2(S^2/\mathbb{Z}_2) = \mathbb{Z}$, i.e. point defects can have integer topological charge, which can be computed by integrating over the surface σ_1 [19],

$$m = \frac{1}{4\pi} \int_{\sigma_1} \hat{\boldsymbol{n}} \left(\frac{\partial \hat{\boldsymbol{n}}}{\partial u_1} \times \frac{\partial \hat{\boldsymbol{n}}}{\partial u_2} \right) du_1 d_u 2, \tag{2.11}$$

where u_1 and u_2 are coordinates on the surface σ_1. Note that Eq. (2.11) is odd in $\hat{\boldsymbol{n}}$, thus there is some ambiguity in the sign of a point defect, as m changes sign with $\hat{\boldsymbol{n}} \to -\hat{\boldsymbol{n}}$. Thus for two point defects with charges m_1, m_2, it is unclear whether together they have a topological charge of magnitude $|m_1 + m_2|$ or $|m_1 - m_2|$. This ambiguity is resolved by choosing a base point M on the unit sphere S^2, and requiring that the mapping of all surfaces used to compute topological charges pass through M [20]. This

restriction constrains the sign of $\hat{\boldsymbol{n}}$ in Eq. (2.11), resolving the ambiguity of the sign of m_1, m_2, and the topological charge of the two hedgehogs together is just their sum $m_1 + m_2$.

The topological charge of closed disclination loops can also be characterized by the second homotopy group by considering the homotopy class of the image of a surface enclosing the disclination loop. It has been shown that stable discllination loops have the same topological charge as point defects [21]; thus point defects can can expand into (1/2)-strength disclination loops, and (1/2)-strength loops can shrink into a point defect.

One may consider more complicated topological structures, such as systems with point defects and disclination lines, knotted disclination loops, hopfions, and more [20, 22]. These cases are beyond the scope of this thesis. We will restrict our studies to the three defect types described above: point defects in two dimensions, line defects in three dimensions, and point defects in three dimensions.

2.3 Electrokinetic transport model

The anisotropy, elasticity, and topology of nematics distinguish nematic hydrodynamics from the hydrodymatics of isotropic fluids. A number of hydrodynamics models for liquid crystals have been proposed using either the director $\hat{\boldsymbol{n}}$ [23–25] or $\boldsymbol{Q}$-tensor [26–28] as order parameter, describing how orientational distortions produce elastic stresses, coupling the order parameter to the velocity and pressure fields.

Our research is motivated by ongoing experiments that help narrow the wide range of physical phenomena that are present and values of parameters to explore. In them, a thin cell is filled with a nematic fluid with typical lateral dimension $L^* \sim 10\ mm$, much larger than the cell thickness $h^* \sim 50 - 100\ \mu$m (Fig. 2.5). The fluid is subjected to an applied AC electric potential. In addition to liquid crystalline molecules, ions are always present in the fluid which originate synthetic impurities, or being produced at electrodes, through dissociation of neutral molecules, absorption from surroundings such as glue, alignment layers, etc. [29]. Thus in LCEK the nematic response strongly depends on the presence and evolution of ionic impurities under an applied electric potential. In addition to conventional distortions in a nematic fluid due to specified conditions at the

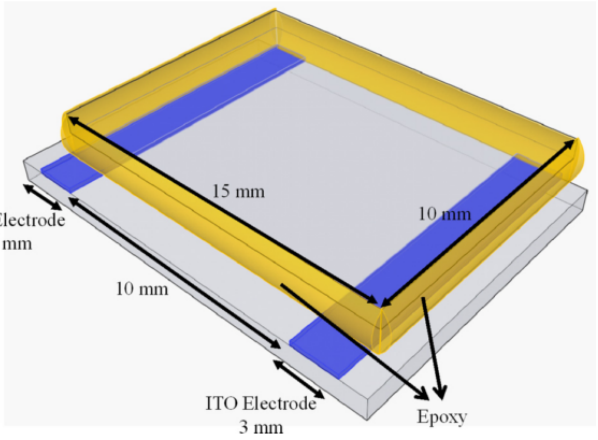

Figure 2.5: Typical experimental cell used for LCEK experiments. A chamber with lateral dimension ~ 10 mm and thickness $\sim 50 - 100$ μm is filled with a nematic fluid. Two indium-tin-oxide (ITO) electrodes separated by a distance ~ 10 mm apply an AC electric potential, generating LCEK flows

boundaries, we investigate two configurations of special interest: Nonuniform boundary conditions induced by photopatterning of the top and bottom cell boundaries, Sec. 2.4, or those induced by suspended dielectric particles, Chapter 5.

In this section we introduce two hydrodynamic models to account for LCEK behavior. We first present a model generalizing the Leslie-Ericksen hydrodynamic model [23], in which the orientational order is described by the director $\hat{\boldsymbol{n}}$. Next we present an alternative derivation of the governing equations using the $\boldsymbol{Q}$-tensor and the principle of energy dissipation [30]. We then discuss the merits of each of the models.

2.3.1 Leslie-Ericksen Electrokinetics

Consider $k = 1, \ldots, N$ ionic species of charge ez_k, where e is the elementary (positive) charge and z_k an integer, immersed in a liquid crystalline fluid (neutrally charged). We assume that the masses of the ionic species are small compared to the masses of the liquid crystal molecules. The liquid crystal is in its nematic phase (exhibiting long range orientational order, but no positional order), characterized by the local nematic director $\hat{\boldsymbol{n}}(\boldsymbol{r})$. We write continuity for the k species as $\partial_{t^*} c_k^* + \nabla^* \cdot \boldsymbol{J^*}_k = 0$, where c_k^* is the concentration of species k and $\boldsymbol{J^*}_k$ its number density flux. Using standard irreversible

thermodynamics for electrolyte solutions [31], we decompose the flux $\boldsymbol{J^*}_k$ into a reactive component including advection of a local element of volume at the barycentric velocity $\boldsymbol{v^*}$ (which includes the liquid crystal), and a dissipative contribution arising from species diffusion and drift induced by the electrostatic field $\boldsymbol{E^*} = -\nabla^*\Phi^*$,

$$\boldsymbol{J^*}_k = c_k^*\boldsymbol{v}^* - \boldsymbol{D}\cdot\nabla^* c_k^* - c_k^* z_k \boldsymbol{\mu}\cdot\nabla^*\Phi^*.$$

The quantities $\boldsymbol{D}$ and $\boldsymbol{\mu}$ are the diffusivity and ionic mobility tensors respectively, which will be assumed to be anisotropic and depend on the local orientation of the liquid crystalline molecule. They are also assumed to obey Einstein's relation $\boldsymbol{D} = \frac{k_B T}{e}\boldsymbol{\mu}$. Given the ratios of masses between the ionic species and the liquid crystalline matrix, we will approximate $\boldsymbol{v^*}$ in what follows by the velocity of the liquid crystal alone. By mass continuity the equation governing the evolution of the concentration of species k,

$$\frac{\partial c_k^*}{\partial t^*} + \nabla^*\cdot(\boldsymbol{v}^* c_k^*) = \nabla^*\cdot(\boldsymbol{D}\cdot\nabla^* c_k^* + c_k^* z_k\boldsymbol{\mu}\cdot\nabla^*\Phi^*) \tag{2.12}$$

The mobility tensor $\boldsymbol{\mu}$ is assumed to be anisotropic and to depend on the local orientation of the nematic [32]. In Cartesian components, $\mu_{ij} = \mu_\perp\delta_{ij} + \Delta\mu\ n_i n_j$ where δ_{ij} is the Kroenecker delta, and we define $\Delta\mu = \mu_\parallel - \mu_\perp$, where $\mu_\parallel$ and $\mu_\perp$ are the ionic mobilities parallel and perpendicular to $\hat{\boldsymbol{n}}$, respectively. They have been experimentally determined for the liquid crystaline system of interest [3]; the calculations below correspond to a nematic fluid which has $\mu_\parallel/\mu_\perp \approx 1.4$. If c_0 is the equilibrium concentration of carriers in the system, we further define the electrical conductivity tensor $\sigma_{ij} = ec_0\mu_{ij}$. As there is no information on the number and nature of the dissolved carriers in the experiments, but only about their overall concentration, we consider in this thesis only two species of charge $z_1 = 1$ and $z_2 = -1$, and the system as a whole is assumed electrically neutral.

In the time scales of interest, the system is assumed to be in electrostatic equilibrium, so that the total electrostatic potential in the medium Φ^* satisfies

$$-\epsilon_0\nabla^*\cdot(\boldsymbol{\epsilon}\cdot\nabla^*\Phi^*) = \sum_{k=1}^{N} e z_k c_k^* \tag{2.13}$$

Although the liquid crystal molecules are not charged, they are polarizable [15]. The nematic is assumed to be a linear dielectric medium, with dielectric tensor $\epsilon_{ij} = \epsilon_\perp \delta_{ij} + \Delta\epsilon\, n_i n_j$, with $\Delta\epsilon = \epsilon_\parallel - \epsilon_\perp$, where $\epsilon_\parallel$ and $\epsilon_\perp$ are the dielectric constants parallel and perpendicular to $\hat{\mathbf{n}}$, respectively. The fluid is assumed under a uniform and oscillatory electrostatic field along the x^* direction, $\boldsymbol{E^*} = E_0^* \cos(\omega t^*)\hat{\boldsymbol{x}}$.

In terms of momentum conservation, we assume that the total mass density and velocity $\boldsymbol{v^*}$ of an element of volume can be well approximated by those of the liquid crystal. The liquid crystal is incompressible, $\nabla^* \cdot \boldsymbol{v}^* = 0$, and flow is overdamped. The incompressibility assumption is justified since a typical electrokinetic velocity is negligibly small compared to the speed of sound in nematics [33], corresponding to a Mach number $\sim 10^{-8}$. Typical velocities considered are $v^* \sim 10\mu m/s$ or less, and the characteristic length scales of the flow is on the order of the film thickness (of order μm). With liquid crystal densities $\varrho^* \sim 10^3 kg/m^3$ and viscosities $\eta \sim 0.1 kg/(ms)$ [15, 19] one estimates the Reynolds number $Re = \varrho^* v^* \ell^*/\eta$ to be $Re \sim 10^{-5} - 10^{-4}$; hence inertia can be neglected. Momentum balance then reduces to the balance between the incompressible viscous stresses and the body force exerted by the ionic species in a field,

$$0 = \nabla^* \cdot \boldsymbol{T^*} - \sum_{k=1}^{N} e z_k c_k^* \nabla^* \Phi^* \tag{2.14}$$

In Cartersian components, the stress tensor is $T_{ij}^* = -p^* \delta_{ij} + T_{ij}^{*e} + \tilde{T}_{ij}^*$, where p^* is the hydrostatic pressure and $\boldsymbol{T^e}$ is the elastic stress,

$$T_{ij}^{*e} = -\frac{\partial f^*}{\partial(\partial_j^* n_k)} \frac{\partial n_k}{\partial x_i^*} \tag{2.15}$$

where f^* is the Oseen-Frank elastic free energy density [15]. The viscous stress $\boldsymbol{\tilde{T}^*}$ is [15],

$$\tilde{T}_{ij}^* = \alpha_1^* n_i n_j n_k n_l A_{kl}^* + \alpha_2^* N_i^* n_j + \alpha_3^* n_i N_j^* + \alpha_4^* A_{ij}^* + \alpha_5^* n_j A_{ik}^* n_k + \alpha_6^* n_i A_{jk}^* n_k \tag{2.16}$$

with $N_i^* = \dot{n}_i^* - \Omega_{ij}^* n_j$, and $A_{ij}^* = \frac{1}{2}\left(\frac{\partial v_j^*}{\partial x_i^*} + \frac{\partial v_i^*}{\partial x_j^*}\right)$ and $\Omega_{ij}^* = \frac{1}{2}\left(\frac{\partial v_i^*}{\partial x_j^*} - \frac{\partial v_j^*}{\partial x_i^*}\right)$ the symmetric and antisymmetric parts of the velocity gradient tensor. The coefficients α_i are the Leslie viscosities [34], and $\dot{n}_i^* = \partial n_i/\partial t^* + (\boldsymbol{v}^* \cdot \nabla^*) n_i$.

Finally, we consider angular momentum conservation, which defines the dynamics of the director $\hat{\boldsymbol{n}}$. For a nematic in an electric field, the balance of torques yields: [15]

$$\hat{\boldsymbol{n}} \times \boldsymbol{h}^{0*} - \hat{\boldsymbol{n}} \times \boldsymbol{h}'^{*} + \epsilon_0 \Delta\epsilon (\hat{\boldsymbol{n}} \cdot \boldsymbol{E}^*)(\hat{\boldsymbol{n}} \times \boldsymbol{E}^*) = 0, \tag{2.17}$$

where

$$h_i^{0*} = -\frac{\partial f^*}{\partial n_i} + \frac{\partial}{\partial x_j^*} \frac{\partial f^*}{\partial(\partial_j^* n_i)}, \tag{2.18}$$

and

$$h_i'^{*} = \gamma_1^* N_i^* + \gamma_2^* A_{ij}^* n_j, \tag{2.19}$$

where $\gamma_1^* = \alpha_3^* - \alpha_2^*$ and $\gamma_2^* = \alpha_3^* + \alpha_2^*$ are rotational viscosities. The first term in Eq. (2.17) corresponds to the elastic torque on the director field, the second term corresponds to viscous torque, and the third term is the torque due to the anisotropy of nematic polarization.

Equations (2.12) through (2.17) are the complete set of governing equations together with the incompressibility condition. A more complete derivation of this transport model has been described in Ref. [35].

2.3.2 *Q*-Tensor Electrokinetics

There are a variety of variational principles governing transport in nonequilibrium systems [36]. In classical mechanics, for instance, irreversible dynamics of a system can be described by means of a Rayleigh dissipation function $\mathcal{R} = \frac{1}{2}\xi_{ij}\dot{q}_i\dot{q}_j$ quadratic in generalized velocities $\dot{q} = (\dot{q}_1, ..., \dot{q}_M)$. The basic idea is to balance frictional and conservative forces in Lagrange's dynamical equations

$$\frac{d}{dt}\frac{\partial \mathcal{L}}{\partial \dot{q}_m} - \frac{\partial \mathcal{L}}{\partial q_m} + \frac{\partial \mathcal{R}}{\partial \dot{q}_m} = 0, \tag{2.20}$$

where $q = (q_1, ..., q_M)$ are generalized coordinates conjugated with the velocities $\dot{q}$ and $\mathcal{L} = \frac{1}{2}a_{ij}(q)\dot{q}_i\dot{q}_j - \mathcal{U}(q)$ is the Lagrangian of the system, defined as the difference between the kinetic energy $\frac{1}{2}a_{ij}(q)\dot{q}_i\dot{q}_j$ and the potential energy $\mathcal{U}(q)$. In what follows, we assume that the matrices (ξ_{ij}) and (a_{ij}) are symmetric.

Equations (2.20) can be recast into a variational problem as their solutions provide

critical points of the functional

$$\int_\Omega d^3r \left\{ \dot{\mathcal{E}} + \mathcal{R} \right\}$$

with respect to a special class of variations $\delta\dot{q}$ of the generalized velocities $\dot{q}$. Here $\Omega \subset \mathbb{R}^3$ is the region occupied by the system, $\mathcal{E} = \mathcal{L} + 2\mathcal{U}$ is the total energy and the superimposed dot (as well as $\frac{d}{dt}$) denotes the total or material time derivative. Unlike Hamilton's principle of stationary action, the current approach "freezes" both the configuration q and the generalized forces $X_m = \frac{d}{dt}\frac{\partial \mathcal{L}}{\partial \dot{q}_m} - \frac{\partial \mathcal{L}}{\partial q_m}$, $m = 1, \ldots, M$ acting on the system at a given time. The state of the system is then varied by imposing arbitrary instantaneous variations $\delta\dot{q}$ of the velocities $\dot{q}$. Note that variations δq, $\delta\dot{q}$, and $\delta\ddot{q}$ are mutually independent except for the condition that the generalized forces $X_m,\ m = 1, \ldots, M$ should remain unaltered [37]. Then, by using the product rule and relabeling, we indeed have

$$\begin{aligned}
\frac{\delta}{\delta\dot{q}_m}\int_\Omega d^3r \left\{ \dot{\mathcal{E}} + \mathcal{R} \right\} &= \frac{\delta}{\delta\dot{q}_m}\int_\Omega d^3r \left\{ a_{ij}\ddot{q}_j\dot{q}_i + \frac{1}{2}\frac{\partial a_{ij}}{\partial q_k}\dot{q}_k\dot{q}_j\dot{q}_i + \frac{\partial \mathcal{U}}{\partial q_i}\dot{q}_i + \mathcal{R} \right\} \\
&= \frac{\delta}{\delta\dot{q}_m}\int_\Omega d^3r \left\{ \left[\frac{d}{dt}\left(a_{ij}\dot{q}_j\right) - \frac{1}{2}\frac{\partial a_{kj}}{\partial q_i}\dot{q}_k\dot{q}_j + \frac{\partial \mathcal{U}}{\partial q_i} \right]\dot{q}_i + \mathcal{R} \right\} = \frac{\delta}{\delta\dot{q}_m}\int_\Omega d^3r \left\{ X_i\dot{q}_i + \mathcal{R} \right\} \\
&= X_m + \frac{\partial \mathcal{R}}{\partial \dot{q}_m} = \frac{d}{dt}\frac{\partial \mathcal{L}}{\partial \dot{q}_m} - \frac{\partial \mathcal{L}}{\partial q_m} + \frac{\partial \mathcal{R}}{\partial \dot{q}_m}, \quad (2.21)
\end{aligned}$$

for every $m = 1, \ldots, M$. Hence, the Euler-Lagrange equations

$$\frac{\delta}{\delta\dot{q}}\int_\Omega d^3r \left\{ \dot{\mathcal{E}} + \mathcal{R} \right\} = 0 \quad (2.22)$$

are identical to the generalized equations of motion (2.20) and thus govern dynamics of a dissipative mechanical system. Since the conservative forces are assumed to be fixed here and $\mathcal{R}$ is a positive-definite function, Eqs. (2.22) yield a minimum of energy dissipation [38,39]. It is worth noting that for overdamped systems—where $\ddot{q} = 0$—this principle of minimum energy dissipation is equivalent to Onsager's variational approach [40].

Again consider a nematic liquid crystal that contains $k = 1 \ldots N$ species of ions with charge ez_k at concentrations c_k^*. We assume that all ionic concentrations are

small so that the resulting electrolyte solution is dilute. In LCEK experiments [5], the concentration of ions is on the order of 10^{19} m^{-3}, which correspond to typical distances between isolated ions to be rather large, ~ 0.5 micrometer in absence of the electric field. Then one can write the energy density of the ionic subsystem as a sum of the entropic and Coulombic contributions

$$\mathcal{E}^*_{ion} = k_B T \sum_{k=1}^{N} c_k^* \ln c_k^* + \sum_{k=1}^{N} e c_k^* z_k \Phi^*, \tag{2.23}$$

where k_B and T stand for the Boltzmann constant and the absolute temperature, respectively, Φ^* denotes the electric potential, and e the elementary charge. Under the action of the field, the ions move with the effective velocities $\boldsymbol{u}^{k*}$ which satisfy the continuity equations $\partial_{t^*} c_k^* + \nabla^* \cdot (c_k^* \boldsymbol{u}^{k*}) = 0$.

In order to take into account the interaction between the electric field $\boldsymbol{E}^* = -\nabla^* \Phi^*$ and the liquid crystal, we have to supplement the Landau-de Gennes free energy, Eq. (2.6), with

$$\mathcal{E}^*{}_E = -\frac{1}{2} \boldsymbol{D^*} \cdot \boldsymbol{E^*}, \tag{2.24}$$

where $\boldsymbol{D^*}$ denotes the electric displacement vector $D_i^* = \epsilon_0 \epsilon_{ij} E_j^*$, where in this case the dielectric tensor $\boldsymbol{\epsilon}$ is defined as,

$$\epsilon_{ij} = \frac{1}{3}(\epsilon_\parallel + 2\epsilon_\perp)\delta_{ij} + \Delta\epsilon Q_{ij} \tag{2.25}$$

Neglecting inertia of molecular rotations ($\ddot{Q}_{ij} = 0$), one can write the total energy per unit volume of the system in the form

$$\mathcal{E}^* = \frac{1}{2} \varrho^* v_i^* v_i^* + F_{LdG}^* + \mathcal{E}_E + \mathcal{E}_{ion} \tag{2.26}$$

with ϱ^* being the nematic mass density and $\boldsymbol{v}^*$ the macroscopic velocity of its flow which we assume to be incompressible, $\nabla^* \cdot \boldsymbol{v}^* = 0$.

We require the dissipation function to be frame-indifferent, positive-definite and quadratic in the generalized velocities. Then, choosing $\boldsymbol{v}^*$ and $\dot{\boldsymbol{Q}}^*$ to be the generalized velocities, the dissipation function of a nematic liquid crystal $\mathcal{R}_{nem}$ has to be quadratic in $\boldsymbol{v}^*$ and $\dot{\boldsymbol{Q}}^*$. This restriction, however, does not specify the dependence of the dissipation

function on $\boldsymbol{Q}$ which, in general allows for a large number of nematic viscosity coefficients [38]. Following Ref. [41], we reduce the number of these coefficients by restricting $\mathcal{R}_{nem}$ to the terms that are at most quadratic in the scalar order parameter S. Then

$$2\mathcal{R}_{nem} = \zeta_1^* \mathring{Q}_{ij}^* \mathring{Q}_{ji}^* + 2\zeta_2^* A_{ij}^* \mathring{Q}_{ji}^* + 2\zeta_3^* A_{ij}^* \mathring{Q}_{jk}^* Q_{ki} + 2\zeta_4^* A_{ij}^* A_{jk}^* Q_{ki} + \zeta_5^* A_{ij}^* A_{jk}^* Q_{kl} Q_{li} + \zeta_6^* \left(A_{ij}^* Q_{ji}\right)^2 + \zeta_7^* A_{ij}^* A_{ji}^* Q_{kl} Q_{lk} + \zeta_8^* A_{ij}^* A_{ji}^*, \quad (2.27)$$

where $A_{ij}^* = \frac{1}{2}(\partial_j^* v_i^* + \partial_i^* v_j^*)$ represents the symmetric part of the velocity gradient and $\mathring{Q}_{ij}^* = \dot{Q}_{ij}^* - \Omega_{ik}^* Q_{kj} - \Omega_{jk}^* Q_{ki}$, with $\Omega_{ij}^* = \frac{1}{2}(\partial_j^* v_i^* - \partial_i^* v_j^*)$, gives the rate of the $\boldsymbol{Q}$-tensor change relative to a flow vorticity [38]. Inserting the uniaxial representation of the tensorial order parameter $\boldsymbol{Q}$ in Eq. (2.27) and taking into account that $N_i^* = \dot{n}_i^* - \Omega_{ij}^* n_j$ and assuming $\dot{S}^* = 0$, the dissipation function takes the form

$$2\mathcal{R}_{nem}^{(\boldsymbol{n})} = (\alpha_3^* - \alpha_2^*) N_i^{*2} + 2(\alpha_5^* - \alpha_6^*) N_i^* A_{ij}^* n_j + (\alpha_5^* + \alpha_6^*)(A_{ij}^* n_j)^2 + \alpha_4^* (A_{ij}^*)^2 + \alpha_1^* (n_i A_{ij}^* n_j)^2, \quad (2.28)$$

when written in terms of the director $\hat{\boldsymbol{n}}$. Now one can relate the viscosities ζ_i^* to the Leslie viscosities α_j^* in the viscous stress tensor derived with $\hat{\boldsymbol{n}}$, Eq. (2.16) [42]:

$$\begin{aligned} \alpha_3^* - \alpha_2^* &= 2S^2 \zeta_1^*, & \alpha_6^* - \alpha_5^* &= 2S\zeta_2^* + \frac{1}{3} S^2 \zeta_3^*, \\ \alpha_1^* &= S^2 \zeta_6^*, & \alpha_5^* + \alpha_6^* &= S\zeta_4^* + \frac{1}{2} S^2 \zeta_5^*, \\ \alpha_4^* &= \zeta_8^* - \frac{1}{3} S\zeta_4^* + \frac{1}{3} S^2 \left(\frac{1}{3}\zeta_5^* + 2\zeta_7^*\right). \end{aligned} \quad (2.29)$$

It follows from Eq. (2.29) that the viscosities ζ_3^*, ζ_5^*, and ζ_7^* are higher-order corrections to the Leslie viscosities in terms of the scalar order parameter S. Thus, one can set $\zeta_3^* = \zeta_5^* = \zeta_7^* = 0$ and arrive at a simpler form of the dissipation function

$$2\mathcal{R}_{nem} = \zeta_1^* \mathring{Q}_{ij}^* \mathring{Q}_{ji}^* + 2\zeta_2^* A_{ij}^* \mathring{Q}_{ji}^* + 2\zeta_4^* A_{ij}^* A_{jk}^* Q_{ki} + \zeta_6^* \left(A_{ij}^* Q_{ji}\right)^2 + \zeta_8^* A_{ij}^* A_{ji}^*, \quad (2.30)$$

which involves only five nematic viscosities.

For the nematic electrolyte, we also need to incorporate dissipation due to the diffusive motion of the ions. Taking into account that the mobilities of ions along and perpendicular to the director $\hat{\boldsymbol{n}}$ are different and treating the ionic velocities $\boldsymbol{u}^{k*}$ with

$1 \leq k \leq N$ as the generalized velocities, the contribution of ions to dissipation is given by [43]

$$2\mathcal{R}_{ion} = k_B T \sum_{k=1}^{N} c_k^* (D_{ij})^{-1} (u_i^{k*} - v_i^*)(u_j^{k*} - v_j^*). \tag{2.31}$$

Here the diffusion matrix $D_{ij} = (D_\parallel + 2D_\perp)\delta_{ij}/3 + (D_\parallel - D_\perp)Q_{ij}$ accounts for the anisotropy of the liquid crystal electrolyte. The expression (2.31) is a direct analog of the dissipation functional for ordinary colloidal solutions [40].

Thus, the total energy dissipation rate in the nematic electrolyte is equal to the sum $\mathcal{R} = \mathcal{R}_{nem} + \mathcal{R}_{ion}$ with $\mathcal{R}_{nem}$ as specified in Eq. (2.30).

Once the energy $\mathcal{E}^*$, the dissipation $\mathcal{R}$, and the generalized velocities of the system are specified, we are in a position to derive equations describing electro-osmotic flows in nematics. The equations are implicitly given by

$$\begin{aligned}
\frac{\delta}{\delta \boldsymbol{v}^*} \int_\Omega d^3r \left\{ \dot{\mathcal{E}}^* + \mathcal{R} - p'(\partial_i^* v_i^*) - \Lambda Q_{ii} \right\} = 0, \\
\frac{\delta}{\delta \dot{Q}} \int_\Omega d^3r \left\{ \dot{\mathcal{E}}^* + \mathcal{R} - p'(\partial_i^* v_i^*) - \Lambda Q_{ii} \right\} = 0, \\
\frac{\delta}{\delta \boldsymbol{u}^{k*}} \int_\Omega d^3r \left\{ \dot{\mathcal{E}}^* + \mathcal{R} - p'(\partial_i^* v_i^*) - \Lambda Q_{ii} \right\} = 0,
\end{aligned} \tag{2.32}$$

where the two Lagrange multipliers, p' and Λ, are associated with the flow incompressibility and the tracelessness of the tensor order parameter, respectively. We impose Dirichlet conditions on $\partial\Omega$,

$$\boldsymbol{v}^* = 0, \quad \dot{Q}^* = 0, \quad \boldsymbol{u}^{k*} = 0 \quad \text{on } \partial\Omega. \tag{2.33}$$

Neglecting inertia, the resulting system of equations governing LCEK are,

$$\begin{cases} \frac{\partial c_k^*}{\partial t^*} + \nabla^* \cdot \left[c_k^* \boldsymbol{v}^* - \frac{c_k^*}{k_B T} \boldsymbol{D} (\nabla^* \mu^k) \right] = 0, \\ \frac{\partial f_{LdG}^*}{\partial \boldsymbol{Q}} - \nabla^* \cdot \left[\frac{\partial f_{LdG}}{\partial (\nabla^* \boldsymbol{Q})} \right] - \Lambda \mathbb{I} - \frac{1}{2} \epsilon_0 \Delta \epsilon \boldsymbol{E}^* \boldsymbol{E}^* + \zeta_1^* \mathring{\boldsymbol{Q}}^* + \zeta_2 \boldsymbol{A}^* = 0, \\ \nabla \cdot \left[-\boldsymbol{T}^{\mathrm{el}*} + p^* \mathbb{I} - T^{V*} - \epsilon_0 \boldsymbol{E}^* (\boldsymbol{\epsilon} \cdot \boldsymbol{E}^*) \right] = 0, \\ \nabla^* \cdot \left[\frac{1}{3} \left(\epsilon_{\parallel} + 2\epsilon_{\perp} \right) \boldsymbol{E}^* + \Delta \epsilon \boldsymbol{Q} \cdot \boldsymbol{E}^* \right] = \frac{e}{\epsilon_0} \sum_{k=1}^{N} c_k z_k, \\ \mu^k = k_B T (\ln c_k^* + 1) + e z_k \Phi^*, \\ \nabla^* \cdot \boldsymbol{v}^* = 0, \\ \mathrm{Tr}\ \boldsymbol{Q} = 0, \end{cases} \tag{2.34}$$

where $\mathbb{I}$ is the identity tensor, $T_{ik}^{\mathrm{el}*} = -\dfrac{\partial f_{LdG}^*}{\partial(\partial_k^* Q_{mn})}(\partial_i^* Q_{mn})$ is the elastic stress tensor, and $\boldsymbol{T}^{V*}$ is the viscous stress tensor:

$$\begin{aligned} T_{ij}^{V*} = \zeta_1^* \left(\mathring{Q}_{jk}^* Q_{ki} - \mathring{Q}_{ik}^* Q_{kj} \right) + \zeta_2^* \mathring{Q}_{ij}^* + (\zeta_4^* + \zeta_2^*) A_{jk}^* Q_{ki} + \\ + (\zeta_4^* - \zeta_2^*) A_{ik}^* Q_{kj} + \zeta_6^* \left(A_{kl}^* Q_{lk} \right) Q_{ij} + \zeta_8^* A_{ij}^*. \end{aligned} \tag{2.35}$$

2.3.3 Discussion of the two models

The primary difference between the Leslie-Ericksen electrokinetic model, Eqs. (2.12)-(2.17), and the $\boldsymbol{Q}$-tensor model, Eq. (2.34), is that the Leslie-Ericksen model assumes the scalar order parameter S is fixed. Inserting $Q_{ij} = S(n_i n_j + \delta_{ij}/3)$ into Eq. (2.34), one finds the Leslie-Ericksen electrokinetics match the $\boldsymbol{Q}$-tensor electrokinetics with fixed S, apart from a body force term $D_j^* \partial_j^* E_i^*$, and with the substitutions,

$$\begin{aligned} \epsilon_{\parallel} &\to \frac{1}{3}(\epsilon_{\parallel}(1-S) + \epsilon_{\perp}(2+S)), \\ \epsilon_{\perp} &\to \frac{1}{3}(\epsilon_{\parallel}(1+2S) + 2\epsilon_{\perp}(1-S)), \\ D_{\parallel} &\to \frac{1}{3}(D_{\parallel}(1-S) + D_{\perp}(2+S)), \\ D_{\perp} &\to \frac{1}{3}(D_{\parallel}(1+2S) + 2D_{\perp}(1-S)). \end{aligned} \tag{2.36}$$

The body force term $f_i^{p*} = D_j^* \partial_j^* E_i^*$ is the force on the nematic per unit volume

due to dielectric polarization. We now show that for systems of interest, this term is negligible. Using the definition of the displacement field,

$$f_i^{p*} = \epsilon_0 \epsilon_\perp E_j^* \frac{\partial E_i^*}{\partial x_j^*} + \epsilon_0 \Delta\epsilon n_j n_k E_k^* \frac{\partial E_i^*}{\partial x_j^*}. \tag{2.37}$$

Using the vector calculus identity,

$$\frac{1}{2}\nabla(\boldsymbol{A}\cdot\boldsymbol{A}) = \nabla\times(\nabla\times\boldsymbol{A}) + (\boldsymbol{A}\cdot\nabla)\boldsymbol{A},$$

and the fact that $\nabla\times\boldsymbol{E} = 0$, Eq. (2.37) becomes,

$$f_i^{p*} = \frac{\partial}{\partial x_i^*}\left(\frac{1}{2}\epsilon_0\epsilon_\perp E^{*2}\right) + \epsilon_0\Delta\epsilon n_j n_k E_k^* \frac{\partial E_i^*}{\partial x_j^*}. \tag{2.38}$$

The first term on the right hand side of Eq. (2.38) contributes only to a change in pressure, and does not change the flow velocity. The second term on the right hand side of Eq. (2.38) can, however, generate flows.

We can estimate the size of this term relative to the force density due to the ionic charges, $\rho\boldsymbol{E}^*$, where $\rho^* = \sum_{k=1}^{N} e z_k c_k^*$ is the charge density. Suppose the system is subject to an applied field $\boldsymbol{E}_0\cos(\omega t)$ which is spatially uniform. Then by Poisson's equation, spatial variations in $\boldsymbol{E}^*$ will scale with the charge density, i.e. $\nabla^*\boldsymbol{E}^* \sim \rho/(\bar{\epsilon}\epsilon_0)$, with $\bar{\epsilon} = (\epsilon_\parallel + \epsilon_\perp)/2$. Thus we anticipate $|\boldsymbol{f}^{p*}/(\rho^*\boldsymbol{E})| \sim \Delta\epsilon/\bar{\epsilon}$. For typical experiments considered here $\Delta\epsilon/\bar{\epsilon} \sim 0 - 0.5$, and for most other experimental studies of interest, $\Delta\epsilon/\bar{\epsilon} \ll 10^{-3}$ [3, 5, 44]. Therefore, the force due to dielectric polarization is negligible relative to $\rho^*\boldsymbol{E}^*$ for the parameters of interest.

While both models describe the same electrokinetic phenomena in the limit of small anisotropy and small variations of S, the primary analysis in this thesis is based on the Leslie-Ericksen electrokinetic model. This choice is based on that fact that its elastic constants K_1, K_2, K_3, and associated viscosities can be accurately determined experimentally. Although the Leslie-Ericksen elastic constants can be mapped onto the Landau-de Gennes elastic constants for small distortions, there remain open questions about the mapping, and about the boundedness of the resulting free energy when not within the single constant approximation [45]. Due to these uncertainties, finite element formulations of the Leslie-Ericksen model such as the one employed here are one of the

methods of choice to investigate topological defects in nematics [46, 47].

Nevertheless, the choice of the Leslie-Ericksen model presents a numerical challenge of resolving singularities in the director field (in the tensor description, the singular defect core is replaced by a small defect region, on the order of 10 nm in thermotropic liquid crystals where Q remains finite. [48, 49]). In Chapter 3 we show that the charge distributions and velocities fields associated with a single disclination are not themselves singular; hence the difficulties associated with short scale singularities do not explicitly arise. In Chapter 5 we introduce a regularization technique in our numerical method in order to solve for equilibrium director distortions containing singularities.

2.4 LCEK Mechanisms: Periodic Anchoring

In order to illustrate the mechanisms of electrokinetic flow, and validate our model and numerical analysis, we begin by investigating a two-dimensional domain with a fixed periodically anchored director, $\hat{\boldsymbol{n}}(y^*) = (\cos(q^* y^*), \sin(q^* y^*))$. This is a simple case that can be solved analytically to obtain the scalings of the change density and flow velocity in terms of the physical parameters. It has been recently investigated in experiments custom-made to validate this LCEK model [3]. The experiments enforce periodic anchoring through a photo-patterning method described below.

Lithographic surface patterning offers the opportunity of tailoring flow fields in nematics for specific applications, for example, to engineer flows in microfluidic channels, to effect immersed particle motion or species separation, or to create stirring flows at the microscale. An example experimental setup is shown in Fig. 2.6. A nematic fluid is confined within a thin cell. A photo-sensitive material is coated onto the two glass plates bounding the cell, which are then exposed to light that has been polarized through a mask with nanoslits etched in the desired orientational pattern $\hat{\boldsymbol{n}}_0(\boldsymbol{r}^*)$ [3]. This exposure aligns the primary axes of photo-sensitive molecules with the desired pattern [50]. The two glass plates are then used to form a cell whose thickness h^* is much smaller than the lateral dimension of the system ℓ^*.

Define a coordinate system (x^*, y^*, z^*) such that the glass plates are located at $z^* = \pm h^*/2$. The anchoring energy of a the nematic orientation $\hat{\boldsymbol{n}}(\boldsymbol{r}^*)$ on the surface of

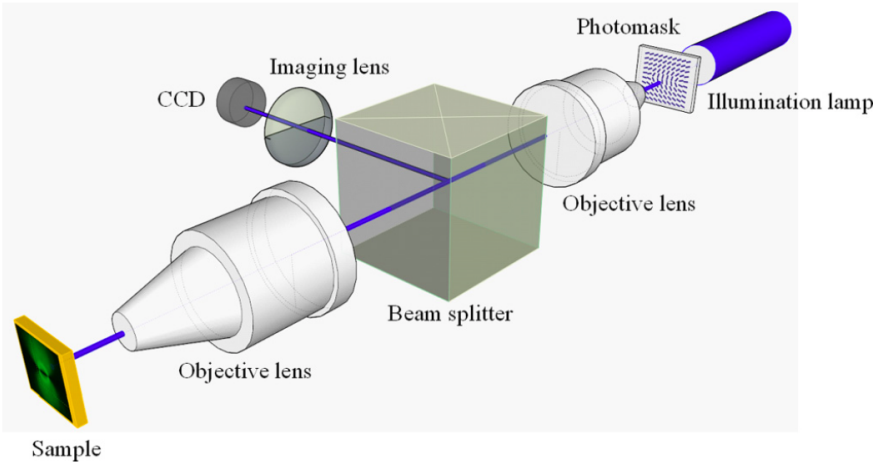

Figure 2.6: Experimental photoalignment configuration described in Ref. [3]. A photomask with the desired pattern polarizes a light source, which then causes a photosensitive substrate on the bounding glass plate of the cell to align with the desired pattern. The director is then aligned with the substrate.

the glass plates is given by [51],

$$F_s^* = \iint \frac{w^*}{2}\left(1 - \left[\hat{\boldsymbol{n}}\left(x^*, y^*, \pm\frac{h^*}{2}\right)\cdot\hat{\boldsymbol{n}}_0(x^*, y^*)\right]^2\right)dx^*dy^*, \tag{2.39}$$

where w^* is a coupling constant. The ratio of elastic and anchoring effects at the cell boundaries can be estimated as $w^*\ell^*/K$, where K is an average elastic constant. For typical experimental values, w^* is much larger than $K/\ell^* \sim 10^{-5}\ J/m^2$ [52], so we may assume $\hat{\boldsymbol{n}}\left(x, y, \pm\frac{h}{2}\right) = \hat{\boldsymbol{n}}_0(x, y)$. Furthermore, with $h^* \ll \ell^*$ and assuming elastic torques are much larger than viscous torques, we may assume the system is approximately two-dimensional, with the director fixed by the imposed pattern – in this case $\hat{\boldsymbol{n}}(y^*) = (\cos(q^*y^*), \sin(q^*y^*))$. We will discuss more complex applications of this photo-patterning technique in Chapters 3 and 4.

In addition to the photo-patterning experiments described here, electroosmosis of nematic fluids due to periodic distortions have also been investigated both experimentally [53, 54] and analytically [55–57], as small spontaneous periodic director distortions subject to an AC field lead to electrohydrodynamic convection [15]. The numerous investigations of this specific pattern make it a good benchmark system for validating our

model, which unlike Refs. [55–57], considers the dynamics of individual ionic species.

Since the director field is a function of y^* only, we assume concentrations, velocities, and induced electric fields do not depend on x^*. Furthermore, by symmetry $v_y^* = 0$. For two ionic species we define $\Delta c^* = c_1^* - c_2^*$ and $C^* = c_1^* + c_2^*$ and write Eq. (2.12) as

$$\frac{\partial C^*}{\partial t^*} = \frac{\partial}{\partial y^*}\left(D_{yy}\frac{\partial C^*}{\partial y*} + \Delta c^* \mu_{yi}\frac{\partial \Phi^*}{\partial x_i^*}\right) \tag{2.40}$$

$$\frac{\partial \Delta c^*}{\partial t^*} = \frac{\partial}{\partial y^*}\left(D_{yy}\frac{\partial \Delta c^*}{\partial y^*} + C^* \mu_{yi}\frac{\partial \Phi^*}{\partial x_i^*}\right) \tag{2.41}$$

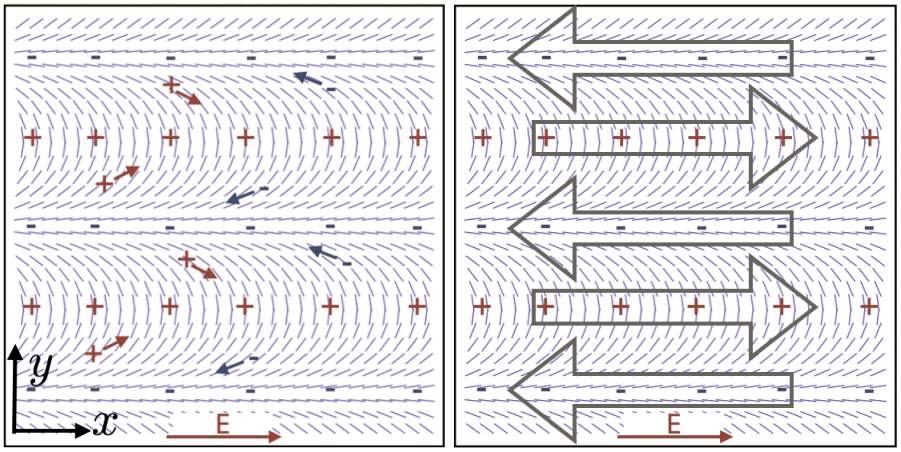

(a) (b)

Figure 2.7: (a) Ionic mobility anisotropy leads positive and negative ions to collect in different regions of the cell under an applied electric field. (b) Regions with high concentration of positive ions will flow in the direction of the electric field, while regions of high negative concentration will flow opposite to the electric field.

Under the applied field, anisotropic mobility leads to charge separation through the drift term in the right-hand side of Eq. (2.41), and is schematically illustrated in Figure 2.7a (the director is shown as thin lines in the figure). With an electric field in the $+\hat{\boldsymbol{x}}$ direction, positive ions move to the right. Since the mobility is higher parallel to $\hat{\boldsymbol{n}}$, positive ions drift in this pattern toward regions where $\hat{\boldsymbol{n}}$ is parallel to the y axis. Negative ions on the other hand drift to the left toward regions where $\hat{\boldsymbol{n}}$ is parallel to the x axis.

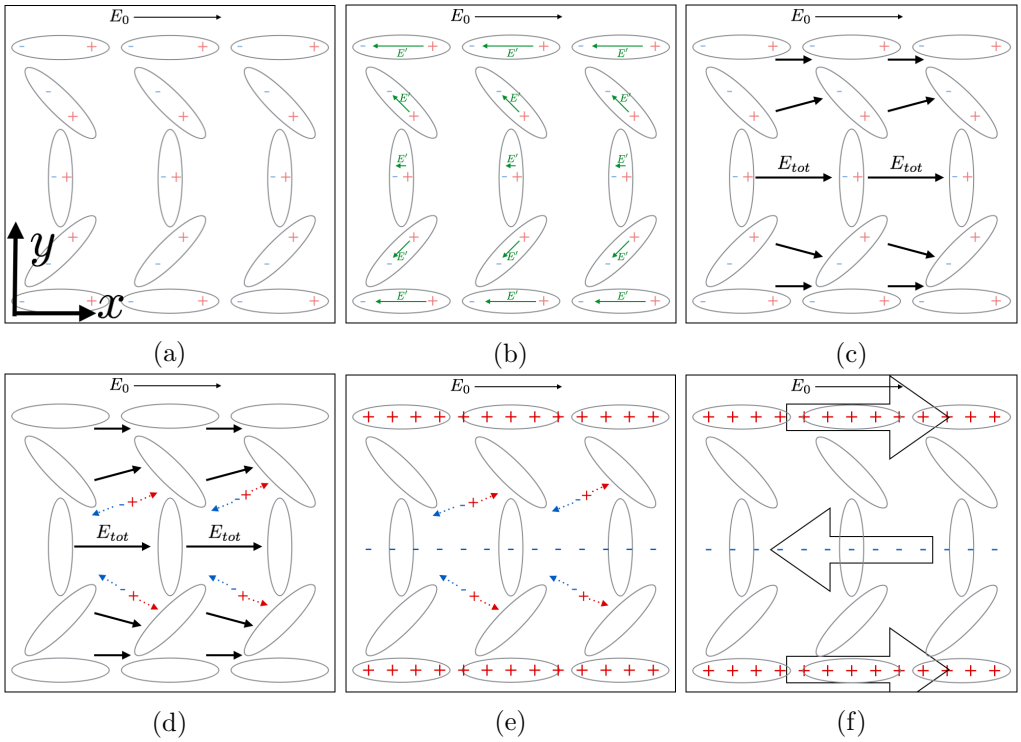

Figure 2.8: (a) Dielectric anisotropy leads to polarization which varies as a function of director orientation. (b)-(c) Nematic polarization generates nonuniform electric fields in response to the applied field, creating an overall nonuniform electric field. (d)-(e) The nonuniform electric field causes positive and negative ions to collect in different regions of the fluid. Note the sign of the charges in a given region is opposite that of Fig. 2.7a. (f) Regions of positive and negative charge density drive nematic flow in opposite directions.

Charge separation due to dielectric permittivity anisotropy also occurs via the drift term in the right-hand side of Eq. (2.41) and its coupling with Poisson's equation, Eq. (2.13); Figure 2.8 illustrates this mechanism. If the dielectric permittivity is higher parallel to the director ($\Delta\epsilon > 0$), polarization will reduce the electric field more strongly when it is parallel to the director than perpendicular. Thus an applied field in the $+\hat{\boldsymbol{x}}$ direction will generate a total electric field with sources where $\hat{\boldsymbol{n}}$ is parallel to the y axis and sinks where $\hat{\boldsymbol{n}}$ is parallel to x axis, as shown in Fig. 2.8c. Therefore the concentration of positive ions will be high in regions where $\hat{\boldsymbol{n}}$ is parallel to $\hat{\boldsymbol{x}}$, while the concentration of negative ions will be higher in regions where $\hat{\boldsymbol{n}}$ is parallel to $\hat{\boldsymbol{y}}$, as

shown in Fig. 2.8e.

After charge separation has taken place, fluid elements experience an electrostatic body force through the last term on the right-hand-side of Eq. (2.14) as indicated schematically in Figs. 2.7b and 2.8f. Note that the net charge density in a given region due to dielectric anisotropy has a sign opposite to that of charge separation due to mobility anisotropy, thus implying the two mechanisms can counteract each other. Importantly, when the electric field polarity is inverted, charge separation is also reversed, but the body force direction is unchanged. This is because the charge density is induced by the electric field, $\rho^* \sim E^*$, and therefore the body force depends on two powers of E^*, $\rho E^* \sim E^{*2}$. Therefore this system will exhibit systematic flow even under an AC field.

For both mechanisms, the charge separation induced by the applied field saturates by species diffusion and the additional transverse field $-\partial\Phi^*/\partial y^*$ induced by charge separation itself. Both effects lead to different characteristic times for saturation, which can be deduced by examining Eq. (2.41) and Poisson's equation. If saturation is due to the induced transverse field, the characteristic time scale is $\tau_\rho = \bar{\epsilon}\epsilon_0/(c_0 e\bar{\mu})$. On the other hand, the mass diffusion time is $\tau_D = (\bar{D}q^{*2})^{-1}$, with q^* set by the director patterning scale. For typical liquid crystal parameters, $\bar{\epsilon} \sim 10$, $\bar{\mu} \sim 10^{-9}\ m^2/(Vs)$, $c_0 \sim 10^{19}\ m^{-3}$, $2\pi/q^* \sim 100\mu m$, and at room temperature, we find $\tau_\rho \sim 0.1\ s$ and $\tau_D \sim 10\ s$, hence diffusive saturation of charge separation is negligible for pattern scales on the order of 100 μm or smaller. Furthermore, both characteristic times need to be compared to the frequency of the applied field ω. From Eq. (2.41) when $\omega \gg 1/\tau_\rho$, Δc will be out of phase with the imposed field by $\pi/2$. In the limit $\omega \to 0$, on the other hand, the imposed field and Δc will be in phase. Therefore, since the body force on the liquid crystal medium, Eq. (2.14), involves the product of the charge and the applied field, we expect systematic transport to occur only for sufficiently low frequencies, $\epsilon_0\bar{\epsilon}\omega/c_0 e\bar{\mu} < 1$.

Charge separation can also induce variations in the total concentration C^* by the last term on the right-hand side of Eq. (2.40). We estimate the size of this term relative to $\partial C^*/\partial t^*$ by first using Poisson's equation to estimate the size of Δc^*: $\Delta c^* \sim \epsilon_0\bar{\epsilon}q^* E_0/e$.

Then if we assume the scale of C is $C^* \sim c_0$, we estimate

$$\frac{\left|\frac{\partial}{\partial y^*}\left(\Delta c^* \mu_{yi}[\partial \Phi^*/\partial x_i^*]\right)\right|}{|\partial C^*/\partial t^*|} \sim \frac{(q^* E_0)^2 \bar{\epsilon}\epsilon_0 \bar{\mu}}{\omega e c_0}. \tag{2.42}$$

This ratio is very small, $\sim 10^{-3}$, and thus variations in C^* are negigible so that $C^* \approx c_0$, independent of time. Under these conditions, and by defining the charge density $\rho^* = e\Delta c^*$, Eq. (2.41) becomes simply

$$\frac{\partial \rho^*}{\partial t^*} = \frac{\partial}{\partial y}\left(\sigma_{yj}\frac{\partial \Phi^*}{\partial x_j^*}\right), \tag{2.43}$$

where we recall and $\sigma_{ij} = \sigma_\perp \delta_{ij} + (\sigma_\parallel - \sigma_\perp) n_i n_j = c_0 e \mu_{ij}$. Equations (2.13) and (2.43) can be solved to yield

$$\rho^*(y^*, t^*) = \left(-\frac{\Delta\sigma}{\bar{\sigma}} + \frac{\Delta\epsilon}{\bar{\epsilon}}\right)\epsilon_0 \bar{\epsilon} E_0 \frac{\partial}{\partial y^*}\left[\frac{\bar{\sigma}\cos(\omega t^* - \delta(y^*))\sin(2q^* y^*)}{2\sqrt{[\sigma_{yy}(y^*)]^2 + [\omega\epsilon_0\epsilon_{yy}(y^*)]^2}}\right], \tag{2.44}$$

$$\tan\delta(y^*) = \frac{\omega\epsilon_0\epsilon_{yy}(y^*)}{\sigma_{yy}(y^*)},$$

where $\Delta\sigma = \sigma_\parallel - \sigma_\perp$ and $\bar{\sigma} = (\sigma_\parallel + \sigma_\perp)/2$.

Note that the induced charge density vanishes linearly with anisotropies $\Delta\sigma$ and $\Delta\epsilon$, is linear in the applied field, and oscillates with frequency ω at a phase shift $\delta(y^*)$ from the applied field. As anticipated, charge separation due to mobility and dielectric anisotropy are of opposite signs in a given region.

By assuming no variation along x^*, Eq. (2.14) reduces to $\frac{\partial}{\partial y^*}\tilde{T}_{xy}^* + \rho^* E_x^* = 0$, which can be integrated explcitly,

$$\tilde{T}_{xy}^* = \left(\frac{\Delta\sigma}{\bar{\sigma}} - \frac{\Delta\epsilon}{\bar{\epsilon}}\right)\frac{\epsilon_0\bar{\epsilon}\bar{\sigma}E_0^2\cos(\omega t^*)\cos(\omega t^* - \delta(y^*))\sin(2q^* y^*)}{2\sqrt{[\sigma_{yy}(y^*)]^2 + [\omega\epsilon_0\epsilon_{yy}(y^*)]^2}} \tag{2.45}$$

At high frequencies, $\omega \gg \sigma_{yy}/(\epsilon_0\epsilon_{yy})$, $\delta = \pi/2$, and the stress oscillates around zero with a small average. At low frequencies, $\delta \approx \pi$, and the resulting stress has a non zero average, hence leading to systematic flow.

By using $\nabla^* \cdot \boldsymbol{v}^* = 0$, the assumption of variation in y^* only, and fact that $\hat{\boldsymbol{n}}$ is fixed,

one finds

$$\frac{\partial v_x^*}{\partial y^*} = \left(\frac{\Delta\sigma}{\bar{\sigma}} - \frac{\Delta\epsilon}{\bar{\epsilon}}\right) \frac{\epsilon_0\bar{\epsilon}\bar{\sigma}E_0^2 \sin(2q^*y^*)\cos(\omega t^*)\cos(\omega t^* - \delta(y^*))}{2\sqrt{[\sigma_{yy}(y^*)]^2 + [\omega\epsilon_0\epsilon_{yy}(y^*)]^2}} \times \frac{1}{\left[\frac{\alpha_1^*}{2}\sin^2(2q^*y^*) + (\alpha_2^* + \alpha_3^*)\cos(2q^*y^*) + \alpha_3^* + \alpha_4^* + \alpha_5^*\right]} \tag{2.46}$$

This equation can be integrated exactly. Like the charge density, the velocity is proportional to the difference in relative mobility and dielectric anisotropy. The velocity magnitude is proportional to the square of the electric field, and the phase shift $\delta(y^*)$ indicates that as the driving frequency increases, the systematic part of the velocity approaches zero.

We mention that the analytic expression for the flow field suggests a method for experimentally determining the so-called Miezowicz viscosities of the liquid crystal – three viscosities η_a, η_b, η_c associated with three fundamental geometries in a simple shear flow: (a) $\hat{\boldsymbol{n}} \perp \boldsymbol{v}^*$ and $\hat{\boldsymbol{n}} \perp \nabla^*\boldsymbol{v}^*$; (b) $\hat{\boldsymbol{n}} \parallel \boldsymbol{v}^*$ and $\hat{\boldsymbol{n}} \perp \nabla^*\boldsymbol{v}^*$; and (c) $\hat{\boldsymbol{n}} \perp \boldsymbol{v}^*$ and $\hat{\boldsymbol{n}} \parallel \nabla^*\boldsymbol{v}^*$ [15]. For the periodic pattern at $y = 0$, the velocity is parallel to the director and hence

$$\frac{1}{2}(\alpha_3^* + \alpha_4^* + \alpha_6^*)\left[\partial_y^{*2} v_x^*\right]_{y^*=0} = \left(-\frac{\Delta\sigma}{\bar{\sigma}} + \frac{\Delta\epsilon}{\bar{\epsilon}}\right) \frac{\bar{\epsilon}\epsilon_0\bar{\sigma}E_0^2\cos(\omega t^*)\cos(\omega t^* - \delta_\perp)}{\sqrt{\sigma_\perp^2 + (\omega\epsilon_\perp\epsilon_0)^2}}, \tag{2.47}$$

$$tan\delta_\perp = \frac{\omega\epsilon_0\epsilon_\perp}{\sigma_\perp},$$

whereas at $y^* = \pi/(2q^*)$, we find,

$$\frac{1}{2}(-\alpha_2^* + \alpha_4^* + \alpha_5^*)\left[\partial_y^{*2} v_x^*\right]_{y^*=\frac{\pi}{2q^*}} = \left(-\frac{\Delta\sigma}{\bar{\sigma}} + \frac{\Delta\epsilon}{\bar{\epsilon}}\right) \frac{\bar{\epsilon}\epsilon_0\bar{\sigma}E_0^2\cos(\omega t^*)\cos(\omega t^* - \delta_\parallel)}{\sqrt{\sigma_\parallel^2 + (\omega\epsilon_\parallel\epsilon_0)^2}}, \tag{2.48}$$

$$\tan\delta_\parallel = \frac{\omega\epsilon_0\epsilon_\parallel}{\sigma_\parallel}.$$

The Leslie viscosity combinations in the left hand sides of Eqs. (2.47) and (2.48) precisely correspond to the Miezowicz viscosities, $\eta_\parallel = \eta^b = \frac{1}{2}(\alpha_3^* + \alpha_4^* + \alpha_6^*)$ and $\eta_\perp = \eta^c = \frac{1}{2}(-\alpha_2^* + \alpha_4^* + \alpha_5^*)$ [15]. Therefore one can use the experimentally determined flow fields near $y^* = 0$ and $y^* = \pi/(2q^*)$ to obtain $\eta_\parallel$ and $\eta_\perp$.

2.5 Nondimensionalization of Equations

In order to further investigate the relative sizes of LCEK effects, we use the results of Sec. 2.4 to recast Eqs. (2.12)-(2.17) in dimensionless form. Specifically we note that for periodic anchoring, the total ionic concentration is approximately uniform, c_0, while Eq.(2.44) demonstrates the charge density scales as $\left(\frac{\Delta\mu}{\bar{\mu}} - \frac{\Delta\epsilon}{\bar{\epsilon}}\right)\bar{\epsilon}\epsilon_0 E_0 q^*$, where $\bar{\mu} = \frac{1}{2}(\mu_\parallel + \mu_\perp)$ is the average mobility[1] . Equation (2.46) suggests the velocity scales as approximately $\left(\frac{\Delta\mu}{\bar{\mu}} - \frac{\Delta\epsilon}{\bar{\epsilon}}\right)\bar{\epsilon}\epsilon_0 E_0^2/(\eta q^*)$, where η is the average viscosity.

We use these results to determine appropriate scalings for nondimensionalization. We scale time by applied field frequency ω and total concentration $C^* = c_1^* + c_2^*$ by c_0. Lengths are scaled by characteristic length ℓ^*; for systems with a single disclination, ℓ^* is the system size L^*, for sets of disclination, ℓ^* is the separation length between disclinations, and for colloidal systems, ℓ^* is the radius of the suspended particles. Electric potential is scaled by $E_0\ell^*$, the Leslie viscosities α_i^* are scaled by their average, η, and the free energy density f^* is scaled by K/ℓ^{*2}. We use the results of Sec. 2.4 discussed above to determine charge and velocity scales, but we do not include the mobility and permittivity anisotropies in our scaling so that they appear explicitly in the governing equations. Thus we scale charge density $\rho^* = c_1^* - c_2^*$ by $\epsilon_0\bar{\epsilon}\ell^{*-1}E_0$ and velocity by $\epsilon_0\bar{\epsilon}\ell^*\eta^{-1}E_0^2$. We also scale the pressure by $\epsilon_0\bar{\epsilon}E_0^2$. We can then write Eqs. (2.12) through (2.17) in dimensionless form:

$$\Omega\frac{\partial C}{\partial t} + W\frac{\partial C v_i}{\partial x_i} = \gamma\frac{\partial}{\partial x_i}\left[\frac{D_{ij}}{\bar{D}}\frac{\partial C}{\partial x_j}\right] + Y^2\frac{\partial}{\partial x_i}\left[\rho\frac{\mu_{ij}}{\bar{\mu}}\frac{\partial\Phi}{\partial x_j}\right] \tag{2.49}$$

$$\Omega\frac{\partial \rho}{\partial t} + W\frac{\partial \rho v_i}{\partial x_i} = \gamma\frac{\partial}{\partial x_i}\left[\frac{D_{ij}}{\bar{D}}\frac{\partial \rho}{\partial x_j}\right] + \frac{\partial}{\partial x_i}\left[C\frac{\mu_{ij}}{\bar{\mu}}\frac{\partial\Phi}{\partial x_j}\right] \tag{2.50}$$

$$\frac{\partial}{\partial x_i}\left[\frac{\epsilon_{ij}}{\bar{\epsilon}}\frac{\partial\Phi}{\partial x_j}\right] = -\rho, \tag{2.51}$$

$$0 = \nabla\cdot\boldsymbol{T} - \rho\nabla\Phi, \quad \boldsymbol{T} = -p\mathbb{I} + \frac{1}{\mathrm{Er}}\boldsymbol{T}^e + \tilde{\boldsymbol{T}}, \tag{2.52}$$

[1] Note that $\Delta\mu/\bar{\mu} = \Delta\sigma/\bar{\sigma}$. We choose to refer to mobilities rather than conductivities going forward

$$\hat{\boldsymbol{n}} \times \boldsymbol{h}^0 - \mathrm{Er}\left(\hat{\boldsymbol{n}} \times \boldsymbol{h'} - \frac{\Delta\epsilon}{\bar{\epsilon}}(\hat{\boldsymbol{n}} \cdot \boldsymbol{E})(\hat{\boldsymbol{n}} \times \boldsymbol{E})\right) = 0, \tag{2.53}$$

where $\Omega = \omega\tau_\rho$ is the size of the driving frequency relative to the characteristic time for charge separation (as in Sec. 2.4, $\tau_\rho = \epsilon_0\bar{\epsilon}/(ec_0\bar{\mu})$), $W = \tau_\rho\epsilon_0\bar{\epsilon}E_0^2/\eta$ is the charging time relative to advection time, $\gamma = \tau_\rho\bar{D}/\ell^{*2}$ is the ratio of diffusion and charge separation, $Y = \epsilon_0\bar{\epsilon}E_0/(\ell^* ec_0)$ is the charge density relative to the total ionic concentration, and $\mathrm{Er} = \epsilon_0\bar{\epsilon}E_0^2\ell^{*2}/K$ is the Ericksen number – the ratio of viscous to elastic torques. Note that γ can be also be written as $\gamma = \lambda_D^{*2}/\ell^{*2}$, where $\lambda_D^* = \sqrt{\epsilon_0\bar{\epsilon}k_BT/(e^2c_0)}$ is the Debye length. We also note that in the scaled variables $N_i = (\Omega/W)\partial_t n_i + v_j\partial_j n_i - \Omega_{ij}n_j$. Eqs. (2.49)-(2.53) represent the full set of governing equations in dimensionless form, and will be used throughout the thesis.

2.6 Numerical Method

Equations (2.49) through (2.53), together with the incompressibility condition, completely describe our system. We solve them numerically in two dimensions with the finite element commercial package COMSOL; the code developed is available for download [58].

An advantage to the finite element method is the ability to create nonuniform meshes, allowing for higher resolution in regions where gradients are large. The domain of our system is composed of triangular and quadrilateral elements, with the numerical solution to the dependent variables of the system defined by its values at element nodes. If $u(\boldsymbol{x})$ is a solution for one of the dependent variables of the system, the numerical approximation of $u(\boldsymbol{x})$ is $\tilde{u}(\boldsymbol{x}) = \sum_\alpha u_\alpha N_\alpha(\boldsymbol{x})$, where the sum is taken over the nodes α and $N_\alpha(\boldsymbol{x})$ are a set of basis functions, polynomials defined locally within each element such that $N_\alpha(\boldsymbol{x}_\beta) = \delta_{\alpha\beta}$. In our numerical study, the pressure is represented with linear basis functions, with a node at each element vertex. All other variables are represented by quadratic basis functions, with nodes at vertices and at midpoints between vertices.

All numerical solutions were obtained in a square domain S_0 with side length L. For periodic anchoring, we choose $L = 1$; for anchored disclinations, $L = 15$; and for studies with suspended particles, $L = 48$. We define a coordinate system (x, y), the origin of which is at the center of S_0. We specify the electrostatic potential at the boundaries

$\Phi(x = L/2, y) = 0$ and $\Phi(x = -L/2, y) = -L\cos(t)$, and use the Neumann boundary conditions $\epsilon_{yi}\partial_i\Phi = 0$ at $y = \pm L/2$. Thus the applied AC field is uniform and parallel to the x axis.

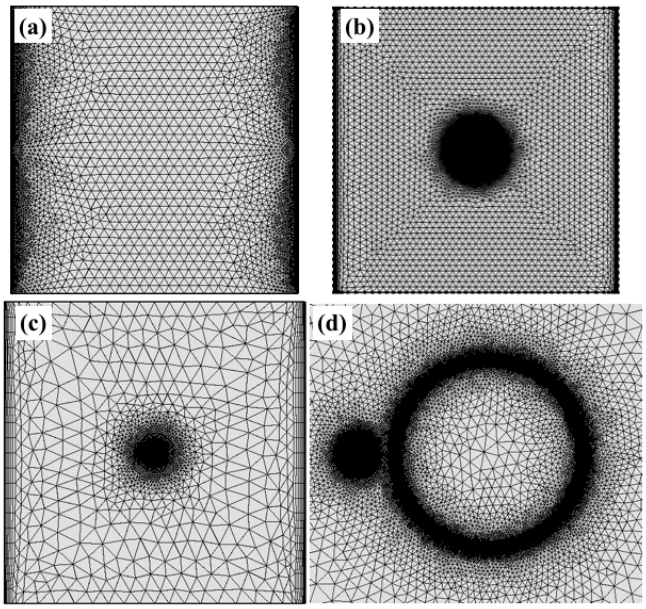

Figure 2.9: (a) Mesh used in the numerical solution in which $\hat{\boldsymbol{n}}$ is periodic. The mesh uses thin quadrilateral boundary-layer elements on the lateral walls and triangular elements throughout the remaining domain. (b) Mesh used for the solution involving anchored disclinations. The central region and lateral walls are much more refined than the outer regions. (c) Mesh used for studies with suspended particles, which is more refined in the center of the cell. (d) Magnification of mesh used for particle studies, showing the finer elements near the particle boundary and the companion defect.

For periodic anchoring, periodic boundary conditions were used on the domain walls normal to the direction of the applied electric field ($y = \pm 1/2$). On $x = \pm 1/2$, no-slip boundary conditions were used for the velocity, and no flux boundary conditions for each of the ionic concentrations. Figure 2.9a shows the mesh used for this case of periodic anchoring. Although COMSOL does have an option for periodic boundary conditions, to insure the mesh was periodic in the y direction we created a mesh for half of the domain ($y > 0$) and then reflected the mesh about the line $y = 0$. The mesh consists of 9876 triangular elements of maximum linear size 3.5×10^{-2} and minimum size 1.0×10^{-3}. The mesh is finer near $x = \pm 1/2$ to resolve the boundary layer that forms there.

For anchored disclinations, we use no-slip boundary conditions for the velocity and zero flux boundary conditions for ion currents on all boundaries. The numerical implementation involves two meshes with different resolutions. Within the square S_0 we create a circle C_0 with radius $R = 0.1L$ in which the mesh is finer. Figure 2.9b shows the mesh used for disclinations. C_0 contains 109,196 triangular elements, with maximum linear size 1.3×10^{-2}, and minimum size 4.8×10^{-5}. The remainder of S_0 contains 12,800 triangular elements with linear size between 1.2×10^{-3} and 1.0, and 240 thin quadrilateral boundary layer elements near the domain boundaries at $x = \pm L/2$.

For studies involving suspended particles, we again use no-slip boundary conditions for velocity and zero flux boundary conditions for ion currents on all boundaries. We impose $\hat{\boldsymbol{n}} = \hat{\boldsymbol{x}}$ on the boundary of S_0, and $\hat{\boldsymbol{n}}$ normal to the surface of the suspended particle. Within S_0 we create a circle C_0 with radius $r_0 = 3$; at the center of C_0 is a disk-shaped particle C_1 with radius $r_1 = 1$. A circle C_2 of radius $r_2 = 0.17$ is located at $(-1/\sqrt{2}, 0)$ to resolve the defect that appears due to topological considerations. C_2 consists of 11,808 triangluar elements with linear size between 6×10^{-4} and 5×10^{-3}; C_1 has 23,434 triangular elements with linear size between 0.015 and 4.44, C_0 has 43,816 triangular elements with linear size between 11.24×10^{-4} and 0.3, and S_0 has 1990 elements with linear size between 0.015 and 4.44. Additionally, C_0 contains 11,520 quadrilateral elements at the boundary with C_1, and S_0 has 320 quadrilateral elements on the domain boundaries at $x = \pm L/2$. Figures 2.9c and 2.9d show the mesh used for single-particle studies.

To determine the behavior of the system, Eqs. (2.49) through (2.53) are written in weak form, in which an integral equation must be satisfied for arbitrary weight functions. The time dependent solution is found using the IDA algorithm; an implicit solver which utilizes the Backward Differentiation Formula (BDF) methods for iterating in time along with Newton's method for solving the nonlinear equations at each time step [59]. For systems with an imposed director field (Chapters 3 and 4), Eq. (2.53) is not solved, rather $\hat{\boldsymbol{n}}$ is taken as fixed. For systems which start with the director in elastic equilibrium (Chapter 5), first the stationary solution to Eq. (2.53) is found, with all other variables held constant. This solution is then used as an initial condition for $\hat{\boldsymbol{n}}$, and the entire set of equations is simultaneously solved.

A particular challenge of modeling topological defects is that the elastic stress $\boldsymbol{T}^e$,

Parameter	Value	Comment
c_0	10^{-19} m^{-3}	Total ion concentration
$\bar{\mu}$	1.45×10^{-9} m^2/(Vs)	Average ion mobility
$\bar{D}$	$k_B T\bar{\mu}/e = 3.69 \times 10^{-11}$ m^2/s	Average ion diffusivity
α_1	-29 mPa s	Leslie-Ericksen viscosity
α_2	-173 mPa s	Leslie-Ericksen viscosity
α_3	-30 mPa s	Leslie-Ericksen viscosity
α_4	118 mPa s	Leslie-Ericksen viscosity
α_5	137 mPa s	Leslie-Ericksen viscosity
α_6	-66 mPa s	Leslie-Ericksen viscosity

Table 2.1: Physical constants used in numerical calculations. e is the electron charge, k_B is Boltzmann's constant, and $T = 295K$, room temperature.

Eq. (2.15), is singular at defect cores. However by utilizing several properties of the elastic stress, we show that in elastic equilibrium, the leading divergence in the elastic stress only contributes to a change in pressure, allowing us to numerically solve Eq. (2.52) without this singular contribution. First, using Eq. (2.15), we find

$$-\partial_j T^e_{ij} = \partial_j(\pi_{kj}\partial_i n_k) = \partial_i n_k \partial_j \pi_{kj} + \pi_{kj}\partial_j(\partial_i n_k) \tag{2.54}$$

where $\pi_{ij} = \partial f/\partial(\partial_j n_i)$. Then with Eq. (2.18) we find

$$-\partial_j T^e_{ij} = \partial_i n_k \left(h^0_k + \frac{\partial f}{\partial n_k}\right) + \pi_{kj}\partial_j(\partial_i n_k) = h^0_k \partial_i n_k + \frac{\partial f}{\partial n_k}\partial_i n_k + \pi_{kj}\partial_j(\partial_i n_k) \tag{2.55}$$

Additionally, elastic equilibrium implies $\hat{\boldsymbol{n}} \times \boldsymbol{h}^0 = 0$, or alternatively $\boldsymbol{h}^0 = \lambda(\boldsymbol{r})\hat{\boldsymbol{n}}$, where $\lambda(\boldsymbol{r})$ is a Lagrange multiplier enforcing the normalization of $\hat{\boldsymbol{n}}$. Therefore note that $h^0_k \partial_i n_k = \lambda(\boldsymbol{r}) n_k \partial_i n_k = \frac{1}{2}\lambda(\boldsymbol{r})\partial_i(n_k^2) = 0$, since $n_k^2 = 1$. Using this and the definition of π_{ij}, we can write

$$\begin{aligned} -\partial_j T^e_{ij} &= \frac{\partial f}{\partial n_k}\partial_i n_k + \pi_{kj}\partial_j(\partial_i n_k) \\ &= \frac{\partial f}{\partial n_k}\partial_i n_k + \frac{\partial f}{\partial(\partial_j n_k)}\partial_j(\partial_i n_k) \end{aligned}$$

Parameter	Value	Comment
ω	10π rad/s	Applied field frequency
E_0	40 mV/μm	Applied field amplitude
$\bar{\epsilon}$	6	Average dielectric permittivity
$\Delta\mu/\bar{\mu}$	0.34	Relative mobility anisotropy
$\Delta\epsilon/\bar{\epsilon}$	0	Relative dielectric anisotropy
ℓ^*	160 μm	Wavelength of pattern

Table 2.2: Physical constants used in numerical calculations for imposed periodic director orientation. The relative mobility and dielectric anisotropies are as listed except as noted in Fig. 2.12.

And then noting $\partial_j(\partial_i n_k) = \partial_i(\partial_j n_k)$ and using the chain rule, we find

$$-\partial_j T^e_{ij} = \frac{\partial f}{\partial n_k}\partial_i n_k + \frac{\partial f}{\partial(\partial_j n_k)}\partial_i(\partial_j n_k) = \partial_i f. \tag{2.56}$$

Thus following a procedure similar to Stark [51], we numerically solve for $\tilde{p} = p + f/\mathrm{Er}$ rather than p and write Eq. (2.14) as

$$0 = -\frac{\partial \tilde{p}}{\partial x_i} + \frac{\partial}{\partial x_j}\tilde{T}_{ij} - \sum_{k=1}^{N} e z_k c_k \nabla\Phi. \tag{2.57}$$

Thus while the free energy near a nematic singularity diverges at director singularities, this divergence in f will be cancelled exactly by a divergence in the pressure p, so that the difference $\tilde{p}$ is finite. The velocity field given by Eq. (2.52) is not affected by this redefinition of the pressure (since the fluid is incompressible).

In order to study electrokinetic phenomena in realistic ranges of physical parameters, we have chosen a parameter set that corresponds to experimental studies of Refs. [3, 5, 44]. While we have shown good agreement between the numerical and experimental results, our comparison with experiments is limited by a number of factors: First, our numerical model is solved on a square domain of size ~ 1 mm^2 or smaller, while the experiments are done in a chamber of size ~ 100 mm^2, with the pattern imposed only on a similarly sized patterned region. Second, our equations are solved in two dimensions, and while there is no evidence of the third dimension affecting the overall experimental behavior, one would expect a Poiseuille-type flow across the cell

thickness that is unaccounted for in our calculations. Finally, while the Leslie viscosities in Table 2.1 are used for all numerical studies in this thesis, we compare our results with a wide variety of experimental conditions, many of which involve different liquid crystals or binary mixtures for which the Leslie viscosities have not been measured. In particular, the Leslie viscosities in Table 2.1 were determined by averaging the viscosities of MLC7026-000 and E7 liquid crystals at a ratio of 89.1:10.9, matching the experimental composition of Ref. [5].

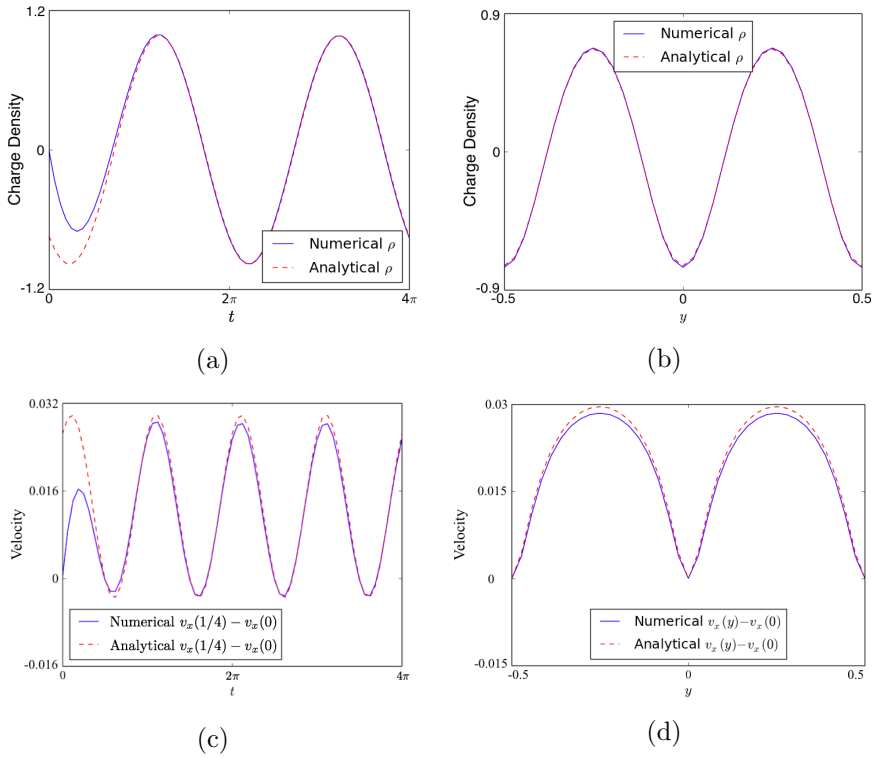

Figure 2.10: Analytic and numerical solutions in dimensionless units for charge density and velocity for periodic director patterning. (a) Charge density as a function of time at $y = 0$. (b) Charge density as a function of y at $t = 2\pi$. (c) Velocity difference between $y = 1/4$ and $y = 0$ as a function of time. (d) Velocity as a function of y relative to velocity at $y = 0$, at $t = 2\pi$.

We have used Eqs. (2.44) and (2.46) to validate our numerical code for the periodic director pattern discussed in Sec. 2.4 in a region of parameters for which the

approximate equations discussed hold, a region which is consistent with the experimental parameters described in Table 2.1 and Table 2.2. Figure 2.10 shows good agreement between the numerical solutions and Eqs.(2.44) and (2.46).

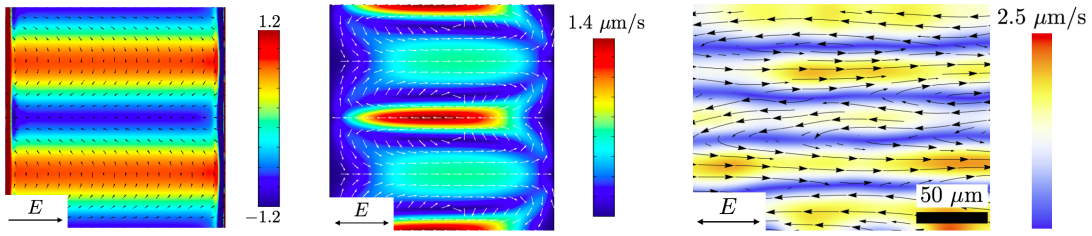

(a) (b) (c)

Figure 2.11: Numerical and experimental results for a periodically anchored director. (a) Numerical charge density in dimensionless units at $t = 2\pi$. (b) Velocity field averaged over a period of the electric field. (c) Experimental velocity for a periodic director pattern obtained by Particle Image Velocimetry by time averaging over the locations of tracer particles [3].

To further validate our model, we compare our numerical results with the experiments of of Peng, et al. [3]. While our numerical calculations for the periodic pattern use periodic boundary conditions along y and no slip boundary conditions on $x = \pm 1/2$, the experiments involve a small patterned sub-region within a larger cell with uniform top and bottom boundaries. Therefore open boundary conditions would be a closer representation of the experiments. As seen in Fig. 2.11a, the boundary layers near the ends of the computational domain are much smaller than the domain, and we have verified that the results presented are independent of system size. Nevertheless, Fig. 2.11 shows good agreement between our numerical results for the parameters listed in Table 2.1 and the experiments of Peng, et. al. [3] (Fig. 2.11c).

One particular consequence of Eqs. (2.45) and (2.46) is that flow can be reversed or completely stopped by simply changing the signs of the anisotropies in dielectric permittivity or ionic mobility. Flow reversals have been observed in isotropic electrolytes, but the mechanism is not yet understood [60]. In the nematic case, reversals arise from competing charge separation fluxes as described in Figs. 2.7 and 2.8. Flow reversals are illustrated by the numerical solution of the full set of governing equations as shown in Fig. 2.12 where we consider the cases of $\Delta\epsilon/\bar{\epsilon} - \Delta\sigma/\bar{\sigma} < 0$, $\Delta\epsilon/\bar{\epsilon} - \Delta\sigma/\bar{\sigma} = 0$, and

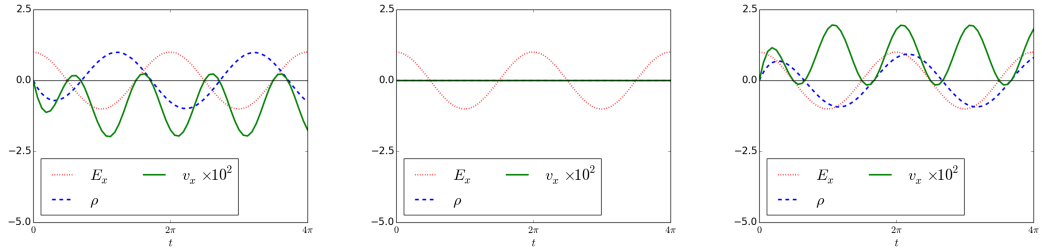

(a) $\Delta\epsilon/\bar{\epsilon} = 0,\ \Delta\sigma/\bar{\sigma} = 0.34$ (b) $\Delta\epsilon/\bar{\epsilon} = 0.34,\ \Delta\sigma/\bar{\sigma} = 0.34$ (c) $\Delta\epsilon/\bar{\epsilon} = 0.34,\ \Delta\sigma/\bar{\sigma} = 0$

Figure 2.12: Numerical solution showing the applied electric field, induced charge density, and x component of the velocity in dimensionless units as a function of time at $(0, 0)$ for periodic anchoring. The velocity direction changes when the quantity $\Delta\epsilon/\bar{\epsilon} - \Delta\sigma/\bar{\sigma}$ changes sign.

$\Delta\epsilon/\bar{\epsilon} - \Delta\sigma/\bar{\sigma} > 0$, with all other parameters constant.

In summary, we find that charge separation occurs due to two potentially competing mechanisms: mobility anisotropy produces a transverse component to ionic motion, while dielectric anisotropy leads to a spatially nonuniform electric field. The nematic fluid is then driven by a body force $\rho\boldsymbol{E}$, and since $\rho \to -\rho$ if $\boldsymbol{E} \to -\boldsymbol{E}$, the force on the fluid is invariant under $\boldsymbol{E} \to -\boldsymbol{E}$, and therefore the flow remains unchanged. We also see that our two-dimensional numerical model agrees well with both the approximate analytic solution and the experimental results.

Chapter 3

LCEK Flows in Thin Films Patterned with Isolated Disclinations

3.1 Introduction

Having validated our model and numerical code for the simple case of periodic patterning in the previous chapter, we now look to study more complex two-dimensional patterns, which can be created by the lithographic technique discussed. We focus on patterns comprising isolated disclinations of arbitrary topological charge, which can be used as building blocks for complex designer flow fields. An example of such a complex flow field is shown in Fig. 3.1, where an array of photo-patterned $(-1/2)$ and $(+1)$ disclinations produces an array of vortices. Additionally, investigation of fixed disclinations allows us to determine the effect of topology on electrokinetic flow patterns, which is useful in studying more complex electrokinetic systems, such as nematic colloids.

We begin with a numerical investigation of LCEK flow generated by a disclinations of charges $m = +1/2, +1, -1/2$. Next we obtain a perturbative solution for the charge density, along with a more general solution for the special case of the $(+1)$ disclination. We then discuss the effect of topological charge on the LCEK velocity field, approximating the viscous stress as Newtonian. Finally, we consider the electrokinetic flows of

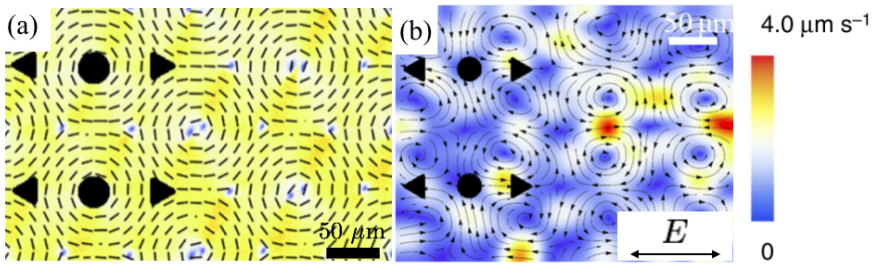

Figure 3.1: (a) Experimentally obtained director field consisting of an array of disclinations of topological charge $(-1/2)$ (triangle) and $(+1)$ (circle), created via the photopatterning method discussed in Chapter 2. (b) LCEK velocity field for the same disclination array subject to an AC field in the horizontal direction. The prescribed pattern generates an array of vortices with alternating vorticity.

sets of disclinations and compare numerical and experimental results in such a case.

3.2 Electrokinetics of a Single Disclination

Consider a two-dimensional configuration with a fixed nematic director orientation $\hat{\boldsymbol{n}}(\boldsymbol{r}) = (\cos\theta(\boldsymbol{r}), \sin\theta(\boldsymbol{r}))$, where $\theta(\boldsymbol{r})$ is the angle between the director and the x axis, and lengths are scaled by system size, $\ell^* = L^* = 1.2$ mm in our reference experiments. We begin with investigating the LCEK of a single defect of charge m, given by $\theta(\boldsymbol{r}) = m\phi$, where ϕ is the polar angle.

We have numerically solved Eq. (2.49) through (2.52) for this fixed director configuration on a square domain of side length $L = 1$. The parameters used are listed in Tables 2.1 and 3.1. Figure 3.2 shows the charge densities and velocity fields obtained for the cases $m = 1/2, 1$, and $-1/2$. Electrical neutrality is preserved for the $m = 1/2$ disclination through a boundary layer of positive charge on the outer walls of the cell (not shown in Fig. 3.2a). The remaining distributions are electrically neutral due to the angular dependence of the charge density. We see the angular behavior of both the charge density and velocity depend on the topological charge of the defect pattern.

3.2.1 Perturbative calculation of charge density

Although we assume that the director orientation is fixed, the governing equations, Eqs. (2.49)-(2.52) are still quite complex. In order to develop an analytical understanding

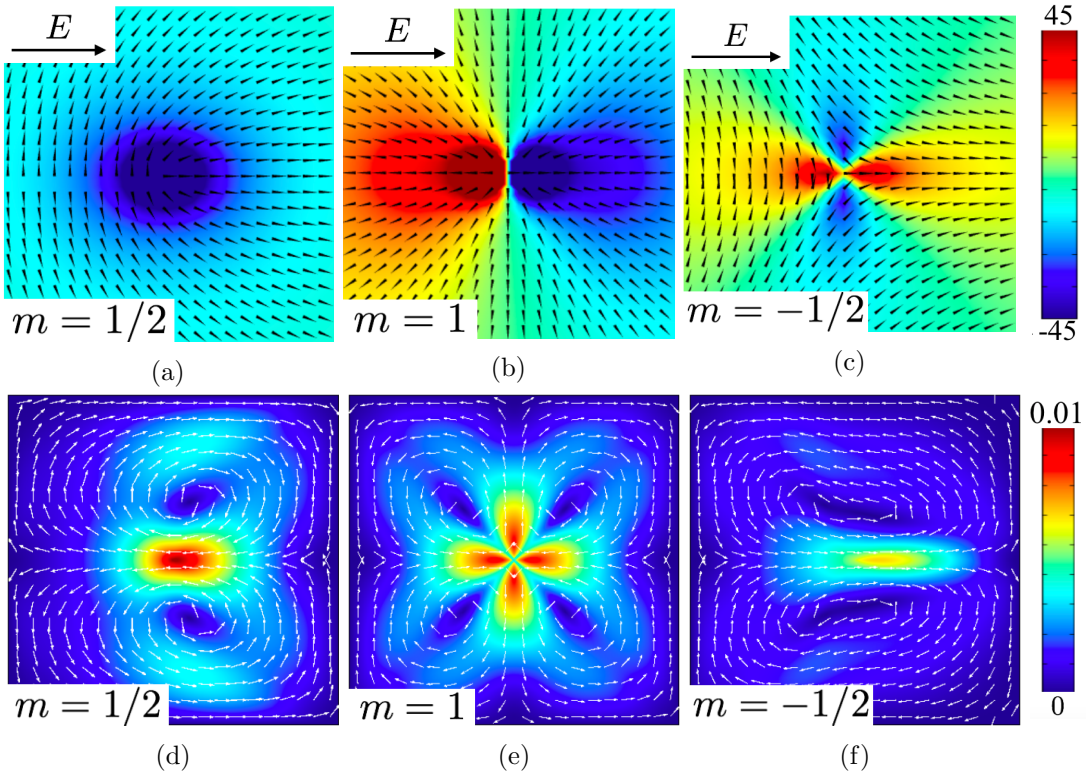

Figure 3.2: Numerical results at $t = 2\pi$ for single anchored disclinations with electric field applied in the horizontal direction. (a)-(c) Plots of charge density within a square of dimensionless side length $\frac{2}{15}$, centered at the disclination. (d)-(f) Velocity across the entire cell for various disclinations. Color indicates velocity magnitude.

of the charge density and velocity fields, we expand the dimensionless variables $\rho, C, \mathbf{v}$ and Φ in powers of $\Delta\mu/\bar{\mu}$ and $\Delta\epsilon/\bar{\epsilon}$, both assumed small and of the same order.

At zero-th order in Δ, the equations correspond to a purely isotropic medium with $c_{1,0} = c_{2,0} = 1/2$ ($\rho_0 = 0$, $C_0 = 1$), and $\boldsymbol{v}_0 = 0$. Zero charge density also implies from Eq. (2.13) that $\nabla^2\Phi_0 = 0$ which we take equal to the imposed field $\Phi_0 = -x\cos(t)$.

At first order and using Eq. (2.51), Eqs. (2.49) and (2.50) become,

$$\Omega\frac{\partial C_1}{\partial t} = \gamma\nabla^2 C_1 - Y^2\cos(t)\frac{\partial \rho_1}{\partial x} \tag{3.1}$$

$$\Omega\frac{\partial \rho_1}{\partial t} = \gamma\nabla^2\rho_1 - \rho_1 - \left(\frac{\Delta\mu}{\bar{\mu}} - \frac{\Delta\epsilon}{\bar{\epsilon}}\right)\frac{\cos[(2m-1)\phi]\cos(t)}{r} - \cos(t)\frac{\partial C_1}{\partial x}. \tag{3.2}$$

Parameter	Value	Comment
ω	10π rad/s	Applied field frequency
E_0	40 mV/μm	Applied field amplitude
$\bar{\epsilon}$	6	Average dielectric permittivity
$\Delta\mu/\bar{\mu}$	0.34	Relative mobility anisotropy
$\Delta\epsilon/\bar{\epsilon}$	0	Relative dielectric anisotropy

Table 3.1: Physical constants used in numerical calculations for nematics with imposed director orientation. The remaining parameters are listed in Table 2.1.

Recall that $\Omega = \omega\tau_\rho$ is the scale of the applied field frequency relative to the charging time $\tau_\rho = \bar{\epsilon}\epsilon_0/(ec_0\bar{\mu})$, $Y = \bar{\epsilon}\epsilon_0 E_0/(\ell^* ec_0)$ as the scale of charge separation relative to the total ionic concentration, and $\gamma = \lambda_D^{*2}/\ell^{*2}$, where λ_D^* is the Debye length. For typical values as given in Chapter 2, $\lambda_D^* \sim 10^{-6}m$, whereas cell sizes are on the order of $\ell^* \sim 10^{-4} - 10^{-2}m$, so $\gamma \sim 10^{-8} - 10^{-4}$. Thus the term proportional to γ in Eqs. (3.1) and (3.2) is a singular perturbation, negligible away from the disclination core, but important within a distance on the order of the Debye length from the core, $r \lesssim \sqrt{\gamma}$.

There is a driving term in the right hand side of Eq. (3.2) which explicitly shows $(\frac{\Delta\mu}{\bar{\mu}} - \frac{\Delta\epsilon}{\bar{\epsilon}})$ as a coefficient multiplying the order one angular factor. Note that the angular dependence of this term matches the angular dependence of the numerical charge density fields in Fig. 3.2.

To obtain a solution for the charge density at this order, we first write ρ_1 and C_1 as a Fourier series,

$$\rho_1(\boldsymbol{r}, t) = \sum_n a_n(\boldsymbol{r})e^{int},\ C = \sum_n b_n(\boldsymbol{r})e^{int} \tag{3.3}$$

Inserting Eq. (3.3) into Eqs. (3.1) and (3.2) yields

$$\Omega i n b_n = \gamma\nabla^2 b_n - \frac{Y^2}{2}\frac{\partial}{\partial x}(a_{n-1} + a_{n+1}) \tag{3.4}$$

$$\begin{aligned}\Omega i n a_n = \gamma\nabla^2 a_n - a_n - \frac{1}{2}\frac{\partial}{\partial x}(b_{n-1} + b_{n+1}) \\ - \left(\frac{\Delta\mu}{\bar{\mu}} - \frac{\Delta\epsilon}{\bar{\epsilon}}\right)\frac{m\cos[(2m-1)\phi]}{2r}(\delta_{n,1} + \delta_{n,-1})\end{aligned} \tag{3.5}$$

where $\delta_{m,n}$ is Kronecker delta.

We further simplify the problem and assume a system in which $Y^2/(4\gamma\sqrt{1+\Omega^2}) \ll 1$,[1] and we will now show that this assumption implies that spatial variations in $C = c_1 + c_2$ contribute negligibly to the charge density ρ_1. To begin we Fourier transform Eqs. (3.4) and (3.5) in space,

$$\hat{b}_n(\boldsymbol{q}) = -\frac{Y^2 i q_x}{2(\gamma q^2 + in\Omega)}[\hat{a}_{n-1}(\boldsymbol{q}) + \hat{a}_{n+1}(\boldsymbol{q})] \tag{3.6}$$

$$\begin{aligned}(\Omega n i + \gamma q^2 + 1)\hat{a}_n(\boldsymbol{q}) = &-\left(\frac{q_x Y}{2}\right)^2 \left[\frac{\hat{a}_{n-2}(\boldsymbol{q}) + \hat{a}_n(\boldsymbol{q})}{\gamma q^2 + i(n-1)\Omega} + \frac{\hat{a}_n(\boldsymbol{q}) + \hat{a}_{n+2}(\boldsymbol{q})}{\gamma q^2 + i(n+1)\Omega}\right] \\ &- F(\boldsymbol{q})(\delta_{n,1} + \delta_{n,-1})\end{aligned} \tag{3.7}$$

where

$$F(\boldsymbol{q}) = \iint e^{-i\boldsymbol{q}\cdot\boldsymbol{x}} d^2x \left(\frac{\Delta\mu}{\bar{\mu}} - \frac{\Delta\epsilon}{\bar{\epsilon}}\right) \frac{m\cos[(2m-1)\phi]}{2r} \tag{3.8}$$

Note that

$$\left|\left(\frac{q_x Y}{2}\right)^2 \frac{1}{[\gamma q^2 + i(n \pm 1)\Omega][\gamma q^2 + 1 + \Omega n i]}\right| \leq \frac{Y^2}{4\gamma\sqrt{1+\Omega^2}} \ll 1 \tag{3.9}$$

Which implies

$$\left|\left(\frac{q_x Y}{2}\right)^2 \frac{\hat{a}_n}{\gamma q^2 + i(n \pm 1)\Omega}\right| \ll |(\Omega n i + \gamma q^2 + 1)\hat{a}_n|$$

so we may approximate Eq. (3.7) as

$$\begin{aligned}(\Omega n i + \gamma q^2 + 1)\hat{a}_n(\boldsymbol{q}) = &-\left(\frac{q_x Y}{2}\right)^2 \left[\frac{\hat{a}_{n-2}(\boldsymbol{q})}{\gamma q^2 + i(n-1)\Omega} + \frac{\hat{a}_{n+2}(\boldsymbol{q})}{\gamma q^2 + i(n+1)\Omega}\right] \\ &- F(\boldsymbol{q})(\delta_{n,1} + \delta_{n,-1})\end{aligned} \tag{3.10}$$

We assume ρ is continuous and differentiable in time and space. Therefore $|a_n| \to 0$

[1] For typical values given in Tables 2.1 and 3.1, $Y^2/(4\gamma\sqrt{1+\Omega^2}) \approx 0.4$. While this quantity is not vanishingly small, we will show in this section that this assumption leads to an analytical expression that agrees well with our numerical results.

as $|n| \to \infty$. We use this assumption to show $|\hat{a}_3| \ll |\hat{a}_1|$. First suppose $|\hat{a}_{n-2}| \sim |\hat{a}_n|$ for $n \geq 3$. Inequality (3.9) along with Eq. (3.10) then implies $|\hat{a}_n| \ll |\hat{a}_{n+2}|$. Thus if $|\hat{a}_1| \sim |\hat{a}_3|$, then by induction $|\hat{a}_n|$ does not approach zero as $n \to \infty$, which contradicts our assumption that ρ is continuous and differentiable. Therefore $|\hat{a}_3| \ll |\hat{a}_1|$.

Equation (3.10) for $n = 1$ is

$$(\gamma q^2 + 1 + \Omega i)\hat{a}_1(\boldsymbol{q}) = -\left(\frac{q_x Y}{2}\right)^2 \frac{\hat{a}_{-1}(\boldsymbol{q})}{\gamma q^2} - \left(\frac{q_x Y}{2}\right)^2 \frac{\hat{a}_3(\boldsymbol{q})}{\gamma q^2 + 2\Omega i} - F(\boldsymbol{q}) \tag{3.11}$$

Inequality (3.9) and the fact that $|\hat{a}_3| \ll |\hat{a}_1|$ imply the second term on the right-hand-side of Eq. (3.11) is negligible relative to the left-hand-side. Additionally,

$$\frac{\left|\left(\frac{q_x Y}{2}\right)^2 \frac{\hat{a}_{-1}}{\gamma q^2}\right|}{|(\gamma q^2 + 1 + \Omega i)\hat{a}_1|} = \left(\frac{q_x Y}{2}\right)^2 \frac{1}{\gamma q^2 \sqrt{(\gamma q^2 + 1)^2 + \Omega^2}} \leq \frac{Y^2}{4\gamma\sqrt{1 + \Omega^2}} \ll 1$$

Thus the first term in Eq. (3.11) is negligible, and we may approximate Eq. (3.11) as

$$(\gamma q^2 + 1 + \Omega i)\hat{a}_1(\boldsymbol{q}) = -F(\boldsymbol{q}) \tag{3.12}$$

or in real space,

$$\gamma \nabla^2 a_1(r, \phi) - (1 + \Omega i) a_1(r, \phi) = \left(\frac{\Delta\mu}{\bar{\mu}} - \frac{\Delta\epsilon}{\bar{\epsilon}}\right) \frac{m \cos[(2m-1)\phi]}{2r} \tag{3.13}$$

Define $\xi = r/\sqrt{\gamma/(1 + i\Omega)}$; then the solution to Eq. (3.13) is

$$a_1(\xi, \phi) = \left(\frac{\Delta\mu}{\bar{\mu}} - \frac{\Delta\epsilon}{\bar{\epsilon}}\right) \frac{m \cos[(2m-1)\phi]}{2\sqrt{\gamma(1 + \Omega i)}} f_m(\xi) \tag{3.14}$$

We note that the angular dependence of charge density is a function of the topological charge m, varying as $\cos[(2m-1)\phi]$, and the radial dependence $f_m(\xi)$ solves,

$$f_m''(\xi) + \frac{1}{\xi} f_m'(\xi) - \left(\frac{(2m-1)^2}{\xi^2} + 1\right) f_m(\xi) = \frac{1}{\xi} \tag{3.15}$$

Note the radial dependence of the charge density is in general dependent on m. The homogeneous solutions to this differential equation are modified Bessel functions, $I_{|2m-1|}(\xi), K_{|2m-1|}(\xi)$.

The particular solutions can be found through variation of parameters, but may also be written in a simpler form for certain vales of m, which we discuss below.

For $m = 1/2$, the solution to Eq. (3.15) bounded for all ξ is

$$f_{\frac{1}{2}}(\xi) = \frac{\pi}{2}\left(L_0(\xi) - I_0(\xi)\right) \tag{3.16}$$

where $L_0(\xi)$ is the modified Struve function of order zero [61]. For $\xi \ll 1$, $I_0(\xi) \to 1$ and $L_0(\xi) \to \frac{2}{\pi}\xi$, so

$$f_{\frac{1}{2}}(\xi \to 0) \to \xi - \frac{\pi}{2}. \tag{3.17}$$

The charge density is finite as $r \to 0$, but it can be large, scaling as $\gamma^{-1/2}$. For $\xi \gg 1$, given the asymptotic relation [61],

$$L_\alpha(\xi) = I_{-\alpha}(\xi) - \frac{\left(\frac{\xi}{2}\right)^{\alpha-1}}{\Gamma\left(\alpha + \frac{1}{2}\right)\sqrt{\pi}} + \mathcal{O}(\xi^{\alpha-3}) \tag{3.18}$$

one has

$$f_{\frac{1}{2}}(\xi \to \infty) \to -\frac{1}{\xi}. \tag{3.19}$$

For $m = 1$, the solution to Eq. (3.15) bounded for all ξ is

$$f_1(\xi) = K_1(\xi) - \frac{1}{\xi}. \tag{3.20}$$

Note $f_1(\xi) \to 0$ as $r \to 0$ and $f_1(\xi)$ matches Eq. (3.19) for $\xi \gg 1$.

For $m \neq 1/2, 1$, the solution to Eq. (3.15) can be obtained by variation of parameters,

$$f_m(\xi) = I_{|2m-1|}(\xi)\int^{\xi} K_{|2m-1|}(\xi')d\xi' - K_{|2m-1|}(\xi)\int^{\xi} I_{|2m-1|}(\xi')d\xi' \tag{3.21}$$

The asymptotic behavior of $f_m(\xi)$ at long distances can be found by recalling the asymptotic expansions for $I_k(\xi), K_k(\xi)$ for large ξ:

$$I_k(\xi) = \frac{e^\xi}{\sqrt{2\pi\xi}}\left(1 + \mathcal{O}\left(\frac{1}{\xi}\right)\right), \tag{3.22}$$

$$K_k(\xi) = \sqrt{\frac{\pi}{2\xi}} e^{-\xi} \left(1 + \mathcal{O}\left(\frac{1}{\xi}\right)\right). \tag{3.23}$$

For $\xi \gg 1$, using integration by parts,

$$\int^{\xi} I_k(\xi')d\xi' = \frac{e^{\xi}}{\sqrt{2\pi\xi}} + \int^{\xi} \mathcal{O}(\xi'^{-3/2} e^{\xi'})d\xi', \tag{3.24}$$

$$\int^{\xi} K_k(\xi')d\xi' = -\sqrt{\frac{\pi}{2\xi}} e^{-\xi} + \int^{\xi} \mathcal{O}(\xi'^{-3/2} e^{-\xi'})d\xi'. \tag{3.25}$$

Therefore for $\xi \gg 1$, we find

$$f_m(\xi) \to -\frac{1}{\xi}. \tag{3.26}$$

For $\xi \ll 1$, note for integral $k > 1$,

$$I_k(\xi) = \frac{1}{k!}\left(\frac{\xi}{2}\right)^k (1 + \mathcal{O}(\xi^2)) \tag{3.27}$$

$$K_k(\xi) = \frac{(k-1)!}{2}\left(\frac{2}{\xi}\right)^k (1 + \mathcal{O}(\xi^2)) \tag{3.28}$$

Using these expansions in (3.21) we find, to leading order in ξ for $\xi \ll 1$,

$$f_m(\xi) \sim \frac{\xi}{|2m-1|([2m-1]^2 - 1)} \tag{3.29}$$

So a_1 linearly approaches zero as $\xi \to 0$.

Using Eq. (3.3), we may write the charge density in its complete form

$$\rho(\xi, \phi, t) = \left(\frac{\Delta\mu}{\bar{\mu}} - \frac{\Delta\epsilon}{\bar{\epsilon}}\right) \frac{m\cos[(2m-1)\phi]}{2\sqrt{\gamma}(1+\Omega^2)^{\frac{1}{4}}} [e^{i(t-\delta/2)} f_m(\xi) + e^{-i(t-\delta/2)} f_m^*(\xi)] \tag{3.30}$$

where $\tan\delta = \Omega$. Note that while the form of $f_m(\xi)$ depends on m; for all values of m the charge density is linear in ξ near the defect core (approaching zero for $m \neq 1/2$), and decays as ξ^{-1} far from the core. In particular, for $\xi \gg 1$ Eq. (3.30) can be approximated as

$$\rho(r, \phi, t) = -\left(\frac{\Delta\mu}{\bar{\mu}} - \frac{\Delta\epsilon}{\bar{\epsilon}}\right) \frac{m\cos(t-\delta)}{\sqrt{1+\Omega^2}} \frac{\cos[(2m-1)\phi]}{r} \tag{3.31}$$

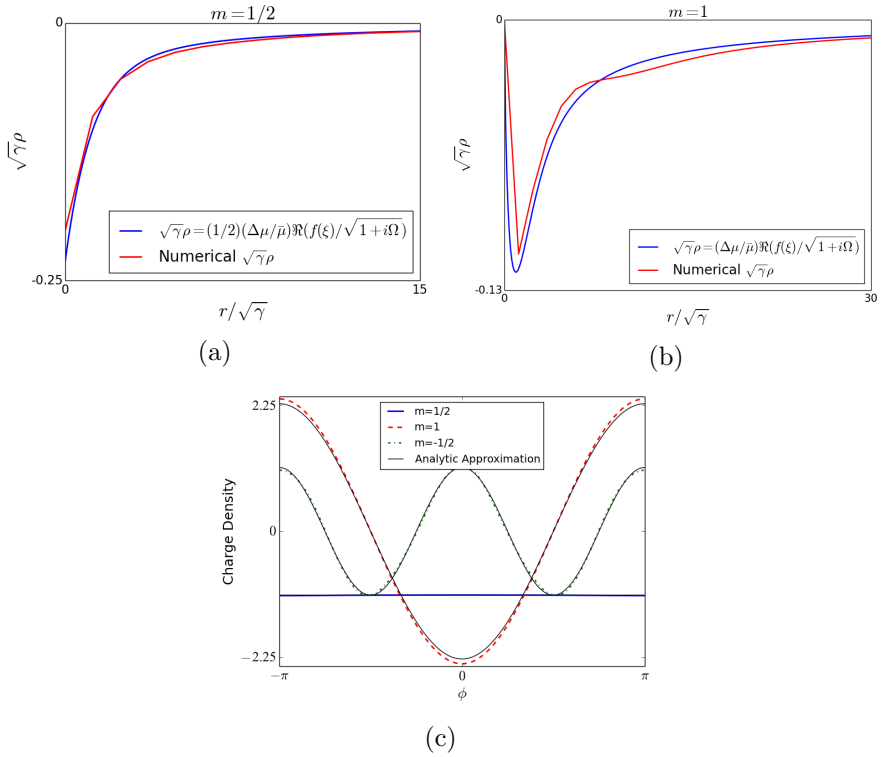

Figure 3.3: Numerical and analytical charge density results at $t = 2\pi$ for single anchored disclinations. (a)-(b) Numerical and analytical results along $\phi = 0$ for $m = 1/2$ and $m = 1$. (c) Numerical and analytical results plotted as a function of angle at a distance $r = 0.1$ from the disclination core.

Figure 3.3 compares Eq. (3.30) and the numerical charge density results for several topological charges. Despite the fact that the numerical solutions are obtained with $\Delta\mu/\bar{\mu}$ and $Y^2/(\gamma\sqrt{1+\Omega^2})$ not vanishingly small, Eq. (3.30) accurately describes the numerical results across a variety of length scales. In particular, our analysis above shows that despite the singularity in the director field, the charge density itself is not singular at the defect core. Importantly, our numerical method remains quite accurate in the determination of the -finite- charge density at the defect core, despite variations on the order of the Debye length.

3.2.2 Alternative expansion for (+1) disclination

Equation (3.30) is valid only for small mobility and permittivity anisotropies. Here we consider an alternative solution for the charge density generated by a (+1) disclination which does not require the assumption that the anisotropies be small. Instead, assume the time scale for charge separation is much smaller than either the characteristic advection time or the period of the applied field, $\Omega \ll 1$, and assume $Y^2/\gamma \ll 1$, implying a uniform total concentration, $C = 1$. For this case, we scale charge density with $\epsilon_0\epsilon_\perp E_0/\ell^*$ rather than $\epsilon_0\bar{\epsilon}E_0/\ell^*$, and we define $\gamma = \epsilon_0\epsilon_\perp D_\perp/(ec_0\mu_\perp\ell^{*2})$. Then with the above assumptions, and since $\boldsymbol{\mu}$ and $\boldsymbol{D}$ are related by Einstein's relation, Eq. (2.50) becomes,

$$0 \approx \frac{\partial}{\partial x_i}\left[\mu_{ij}\frac{\partial}{\partial x_j}(\gamma\rho + \Phi)\right] \tag{3.32}$$

Define $\psi = \gamma\rho + \Phi$. Then since we have a (+1) disclination, in polar coordinates Eq. (3.32) becomes,

$$\frac{\mu'}{r}\frac{\partial}{\partial r}\left(r\frac{\partial\psi}{\partial r}\right) + \frac{1}{r^2}\frac{\partial^2\psi}{\partial\phi^2} = 0. \tag{3.33}$$

where $\mu' = \mu_\parallel/\mu_\perp$. The general solution to Eq. (3.33) is,

$$\psi(r,\phi,t) = \alpha_0(t)\log r + \beta_0(t)\phi + \sum_{n=0}^{\infty}\left(A_n(t)r^{n/\sqrt{\mu'}} + B_n(t)r^{-n/\sqrt{\mu'}}\right)\left[C_n(t)\cos(n\phi) + D_n(t)\sin(n\phi)\right] \tag{3.34}$$

Assume our system is a disc of radius 1 with $\Phi(1,\phi,t) = -\cos\phi\cos t$ and $\rho(1,\phi,t) = 0$. Then Eq. (3.34) becomes

$$\psi(r,\phi,t) = -r^{1/\sqrt{\mu'}}\cos\phi\cos t \tag{3.35}$$

Using Poisson's equation, Eq. (3.35), and the definition $\psi = \gamma\rho + \Phi$, we find the charge density solves,

$$\frac{\gamma\epsilon'}{r}\frac{\partial}{\partial r}\left(r\frac{\partial\rho}{\partial r}\right) + \frac{\gamma}{r^2}\frac{\partial^2\rho}{\partial\phi^2} - \rho = \left(1 - \frac{\epsilon'}{\mu'}\right)r^{\frac{1}{\sqrt{\mu'}}-1}\cos\phi\cos t, \tag{3.36}$$

where $\epsilon' = \epsilon_{\parallel}/\epsilon_{\perp}$. Define $\xi = r/\sqrt{\epsilon'\gamma}$, then $\rho(\xi,\phi,t) = (1-\epsilon'/\mu')(\gamma\epsilon')^{\frac{1}{2\sqrt{\mu'}}-1} f(\xi)\cos\phi\cos t$ solves Eq. (3.36), with $f(\xi)$ solving,

$$f''(\xi) + \frac{1}{\xi}f'(\xi) - \left(\frac{\epsilon'^{-1}}{\xi^2} + 1\right) f(\xi) = \xi^{\frac{1}{\sqrt{\mu'}}-2}. \tag{3.37}$$

For arbitrary ϵ', μ', the homogeneous solutions to Eq. (3.37) are Modified Bessel functions $I_{\frac{1}{\sqrt{\epsilon'}}}(\xi), K_{\frac{1}{\sqrt{\epsilon'}}}(\xi)$. The particular solution to Eq. (3.37) can be found by variation of parameters,

$$f(\xi) = I_{\frac{1}{\sqrt{\epsilon'}}}(\xi)\int^{\xi} K_{\frac{1}{\sqrt{\epsilon'}}}(\xi_1)\xi_1^{\frac{1}{\sqrt{\mu'}}-1} d\xi_1 - K_{\frac{1}{\sqrt{\epsilon'}}}(\xi)\int^{\xi} I_{\frac{1}{\sqrt{\epsilon'}}}(\xi_1)\xi_1^{\frac{1}{\sqrt{\mu'}}-1} d\xi_1. \tag{3.38}$$

In the limit of small anisotropy, $\epsilon', \mu' \to 1$, Eq. (3.38) can be written as $f(\xi) = K_1(\xi) - 1/\xi$, matching the for $m = 1$ solution from Sec. 3.2.1. Unlike in Sec. 3.2.1, we find that in general the radial dependency of the charge density is a function of the system anisotropy. Specifically, away from defect cores, $\xi \gg 1$, using the asymptotic expansions given by Eqs. (3.22) and (3.23), we find,

$$\int^{\xi} K_{\frac{1}{\sqrt{\epsilon'}}}(\xi_1)\xi_1^{\frac{1}{\sqrt{\mu'}}-1} d\xi_1 \approx -\sqrt{\frac{\pi}{2}}\Gamma^i\left(\frac{1}{\sqrt{\mu'}} - \frac{1}{2}, \xi\right), \tag{3.39}$$

$$\int^{\xi} I_{\frac{1}{\sqrt{\epsilon'}}}(\xi_1)\xi_1^{\frac{1}{\sqrt{\mu'}}-1} d\xi_1 = -\frac{\xi^{\frac{1}{\sqrt{\mu'}}-\frac{1}{2}}}{\sqrt{2\pi}} E_{\frac{3}{2}-\frac{1}{\sqrt{\mu'}}}(-\xi), \tag{3.40}$$

where $\Gamma^i(s,x)$ is the incomplete Gamma function,

$$\Gamma^i(s,x) = \int_x^{\infty} t^{s-1}e^{-t}dt,$$

and $E_n(x)$ is the generalized Exponential Integral function,

$$E_n(x) = \int_1^{\infty} \frac{e^{-xt}}{t^n}dt.$$

The asymptotic expansions for $\Gamma^i(s,x)$ and $E_n(x)$ are [62],

$$\Gamma^i(s,x) \sim x^{s-1}e^{-x}\left(1+\mathcal{O}\left(\frac{1}{x}\right)\right), \tag{3.41}$$

$$E_n(x) \sim \frac{e^{-x}}{x}\left(1+\mathcal{O}\left(\frac{1}{x}\right)\right). \tag{3.42}$$

Therefore, far from the disclination core, Eq. (3.38) is $f(\xi \gg 1) \approx -\xi^{\frac{1}{\sqrt{\mu'}}-2}$, and the charge density is,

$$\rho(r,\phi,t) \approx \left(\frac{\epsilon'}{\mu'}-1\right) r^{\frac{1}{\sqrt{\mu'}}-2}\cos\phi\cos t = \frac{\mu_\perp}{\mu_\parallel}\left(\frac{\Delta\epsilon}{\epsilon_\perp}-\frac{\Delta\mu}{\mu_\perp}\right) r^{\sqrt{\frac{\mu_\perp}{\mu_\parallel}}-2}\cos\phi\cos t. \tag{3.43}$$

Thus at $r \gg \sqrt{\gamma\epsilon'}$, the radial dependency of the (+1) defect charge density decays as a power law which depends on the mobility anisotropy. In Sec. 3.2.1, we found that the charge decays as $1/r$, which is the small anisotropy limit of Eq. (3.43).

3.2.3 Analysis of velocity fields

In order to understand the flow structure shown in Fig. 3.2, as well as the large distance behavior of the velocity under a body force that decays as a power law of distance away from the defect we solve the simpler problem of a Newtonian fluid,

$$-\nabla p + \nabla^2 \boldsymbol{v} - \rho\nabla\Phi = 0; \quad \nabla\cdot\boldsymbol{v} = 0, \tag{3.44}$$

in a disk of radius 1, with $\boldsymbol{v} = 0$ at $r = 1$, and $\boldsymbol{v}$ finite for $r < 1$. We consider only the part of the body force that does not time-average to zero, which far from the defect core is,

$$-\rho\nabla\Phi = -\left(\frac{\Delta\mu}{\bar{\mu}}-\frac{\Delta\epsilon}{\bar{\epsilon}}\right)\frac{m\cos^2(t)}{(1+\Omega^2)}\frac{\cos[(2m-1)\phi]}{r} \tag{3.45}$$

Taking the curl of Eq. (3.44) and defining the stream function $\nabla\times(\psi_m\hat{\boldsymbol{z}}) = -\boldsymbol{v}$ one obtains

$$\nabla^4\psi_m(r,\phi,t) = \left(\frac{\Delta\mu}{\bar{\mu}}-\frac{\Delta\epsilon}{\bar{\epsilon}}\right)\frac{m\cos^2(t)}{(1+\Omega^2)r^2}[m\sin(2m\phi)+(m-1)\sin(2(m-1)\phi)] \tag{3.46}$$

Note that, as in the periodic case in Sec. 2.4, the velocity is linear in the anisotropy difference, and in the high frequency limit, $\Omega \gg 1$, the systematic flow in the cell will disappear. Additionally, the angular dependence of the flow is set by the right hand side of Eq. (3.46). In particular, the angular flow structure will be a superposition of $2m$ and $2(m-1)$ harmonics.

For $m = 1$ and $m = 1/2$, the solutions to (3.46) satisfying the stated boundary conditions are

$$\psi_1(r,\phi,t) = \left(\frac{\Delta\mu}{\bar{\mu}} - \frac{\Delta\epsilon}{\bar{\epsilon}}\right)\frac{\cos^2(t) r^2 \sin(2\phi)}{16(1+\Omega^2)}\left[\frac{1}{2}\left(1-r^2\right) + \log(r)\right] \tag{3.47}$$

$$\psi_{\frac{1}{2}}(r,\phi,t) = \left(\frac{\Delta\mu}{\bar{\mu}} - \frac{\Delta\epsilon}{\bar{\epsilon}}\right)\frac{\cos^2(t) r}{12(1+\Omega^2)}(r-1)^2 \sin\phi \tag{3.48}$$

Note that the angular dependence for the $m = 1$ is $\psi_1 \sim \sin(2\phi)$ (four vortices), since the $m-1$ term in Eq. (3.46) is zero, and the angular dependence for $m = 1/2$ is $\psi_{\frac{1}{2}} \sim \sin\phi$ (two vortices) since $\sin(2m\phi) = -\sin(2(m-1)\phi)$ for $m = 1/2$.

To find solutions for $m \neq 1/2, 1$, first note that the function

$$\begin{aligned} P_\alpha(r,\phi,t) = \left(\frac{\Delta\mu}{\bar{\mu}} - \frac{\Delta\epsilon}{\bar{\epsilon}}\right)&\frac{\cos^2(t) r^2 \sin(\alpha\phi)}{(1+\Omega^2)(\alpha+2)\alpha(\alpha-2)} \\ &\times \left(\frac{(\alpha-2)}{2} r^\alpha - \frac{\alpha}{2} r^{\alpha-2} + 1\right), \quad \alpha > 2, \end{aligned} \tag{3.49}$$

solves the equation

$$\nabla^4 P_\alpha(r,\phi,t) = \left(\frac{\Delta\mu}{\bar{\mu}} - \frac{\Delta\epsilon}{\bar{\epsilon}}\right)\frac{\cos^2(t)\alpha}{(1+\Omega^2) r^2}\sin(\alpha\phi) \tag{3.50}$$

with $\partial P_\alpha/\partial r$ and $(1/r)(\partial P_\alpha/\partial\phi)$ finite for $r < 1$, and

$$\left.\frac{\partial P_\alpha}{\partial r}\right|_{r=1} = \left.\frac{1}{r}\frac{\partial P_\alpha}{\partial\phi}\right|_{r=1} = 0 \tag{3.51}$$

Using this solution we find the stream functions for $m = -1/2, -1, 3/2$, and 2,

$$\psi_{-\frac{1}{2}}(r,\phi,t) = -\frac{1}{2}[\psi_{\frac{1}{2}}(r,\phi,t) + P_3(r,\phi,t)] \tag{3.52}$$

$$\psi_{-1}(r,\phi,t) = -\psi_1(r,\phi,t) - P_4(r,\phi,t) \tag{3.53}$$

$$\psi_{\frac{3}{2}}(r,\phi,t) = \frac{3}{2}[\psi_{\frac{1}{2}}(r,\phi,t) + P_3(r,\phi,t)] \tag{3.54}$$

$$\psi_2(r,\phi,t) = 2[\psi_1(r,\phi,t) + P_4(r,\phi,t)] \tag{3.55}$$

and the stream functions for all other values of m,

$$\psi_m(r,\phi,t) = m[P_{2m}(r,\phi,t) + P_{2(m-1)}(r,\phi,t)] \tag{3.56}$$

Thus we see that the angular structure of the flow is indeed a superposition of $\sin 2m\phi$ and $\sin 2(m-1)\phi$ terms, with the relative strength of each term determined by the specific topological charge m. Despite the simplification of assuming a Newtonian fluid, the angular depencence of Eqs. (3.47) ($m = 1$) and (3.48) ($m = 1/2$) and (3.52) ($m = -1/2$) agrees with the flow fields shown in Fig. 3.2.

In addition, our results for a Newtonian fluid suggest that given the slow decay of the charge density created by a single disclination, the fluid velocity would diverge at large distances in an infinite domain. The bounded nature of our numerical results follow from the no-slip boundary conditions.

3.3 Sets of Disclinations

Having analyzed the electrokinetic behavior induced by a single disclination, we consider next configurations comprising a set of disclinations with total topological change zero, which may be used to engineer more complex flow structures. We use the same scaling of dimensionless variables as in Sec. 3.2, except we use the defect separation as the characteristic length ℓ^* (to match the experiments of Ref. [3], we set $\ell^* = 80\ \mu m$).

We begin by deriving the charge density for an arbitrary imposed pattern $\theta(\boldsymbol{r})$, and we will use this result for the specific case where $\theta(\boldsymbol{r})$ is a set of disclinations. Following the same procedure as described at the beginning of Sec. 3.2, we find the equation for

charge density to first order in $\Delta\mu/\bar{\mu}$ and $\Delta\epsilon/\bar{\epsilon}$ with prescribed director angle $\theta(\boldsymbol{r})$ is,

$$\Omega\frac{\partial\rho}{\partial t} = \gamma\nabla^2\rho - \rho - \left(\frac{\Delta\mu}{\bar{\mu}} - \frac{\Delta\epsilon}{\bar{\epsilon}}\right)\frac{\cos(t)}{2}\left(\frac{\partial}{\partial x}\cos(2\theta(\boldsymbol{r})) + \frac{\partial}{\partial y}\sin(2\theta(\boldsymbol{r}))\right). \tag{3.57}$$

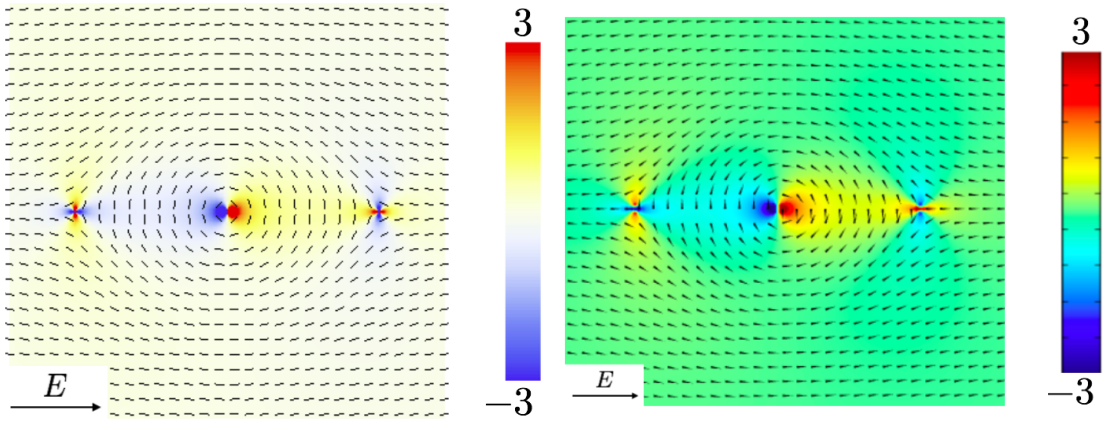

(a) (b)

Figure 3.4: (a) Analytic charge density according to Eq. (3.59) for a superposition of a (-1/2,1,-1/2) disclination triplet pattern expressed in dimensionless units at $t = 2\pi$. (b) Numerical charge density in dimensionless units at $t = 2\pi$ for the same parameters.

Far from disclination cores, the solution to Eq. (3.57) is,

$$\rho(\boldsymbol{r},t) = -\left(\frac{\Delta\mu}{\bar{\mu}} - \frac{\Delta\epsilon}{\bar{\epsilon}}\right)\frac{\cos(t-\delta)}{2\sqrt{1+\Omega^2}}\left(\frac{\partial}{\partial x}\cos(2\theta(\boldsymbol{r})) + \frac{\partial}{\partial y}\sin(2\theta(\boldsymbol{r}))\right). \tag{3.58}$$

In the low frequency limit, $\Omega \to 0$, Eq. (3.58) agrees with the analytic solution reported by Ref. [3]. While Eq. (3.58) is valid for arbitrary $\theta(\boldsymbol{r})$ far from singularities, it does not provide much insight into the effect of specific disclination combinations on the charge density.

We consider next a set of n disclinations. In general, the director field created by a set of isolated dislocations is not the sum of the individual contributions except in the one elastic constant approximation to the Oseen-Frank elastic energy, $K_1 = K_2 = K_3$. However, the one constant approximation allows us to investigate a variety of disclination patterns and compare the solutions with the single disclination solutions above. Consider a set of n disclinations, so the director field has the form $\theta(\boldsymbol{r}) =$

$\sum_{i=1}^{n} m_i\phi_i$, where m_i is the topological charge of disclination i located at (x_i, y_i), and $\tan\phi_i = (y-y_i)/(x-x_i)$. With this definition for $\theta(\boldsymbol{r})$, Eq. (3.58) becomes,

$$\rho(\boldsymbol{r},t) = -\left(\frac{\Delta\mu}{\bar{\mu}} - \frac{\Delta\epsilon}{\bar{\epsilon}}\right)\frac{\cos(t-\delta)}{\sqrt{1+\Omega^2}}\sum_{i=1}^{n}\frac{m_i\cos(2\theta(\boldsymbol{r})-\phi_i)}{r_i}, \qquad \tan\delta = \Omega, \tag{3.59}$$

where $r_i = \sqrt{(x-x_i)^2+(y-y_i)^2}$ is the distance from disclination i. Note that this solution reduces to Eq. (3.31) when $n = 1$. The solution is not quite a superposition of single-disclination charge densities, as the term $\cos(2\theta(\boldsymbol{r})-\phi_i)$ contributes cross-terms to the sum in Eq. (3.59).

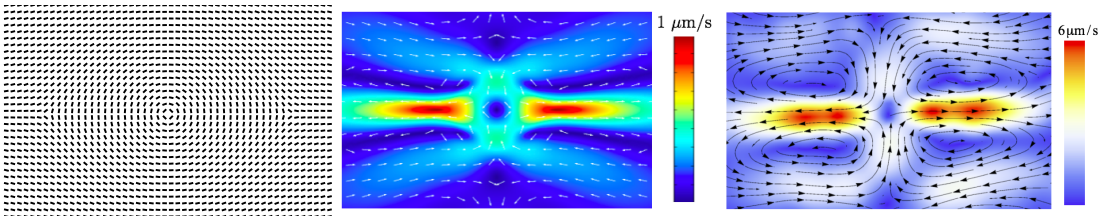

(a) (b) (c)

Figure 3.5: (a) Pattern with three disclinations; two with charge -1/2 and one with charge +1. (b) Time averaged velocity under AC field applied horizontally (c) Time averaged experimental velocity for the same configuration.

Figure 3.4 compares Eq. (3.59) to a numerical charge density solution obtained for a configuration with three disclinations of topological charge (-1/2, 1, -1/2), studied experimentally by Peng, et al. [3], showing good qualitative agreement between the analytical and numerical solutions. The numerical solution shown in Fig. 3.5b uses the same parameters as the single disclination studies, but with lengths scaled by the defect separation $\ell^* = 80\ \mu m$. We use no-slip boundary conditions on the velocity in the far field, while in the experiments, the director pattern is only imposed in a small subdomain of the experimental cell. Figure 3.5c shows the experimental flow field, which is close both in structure and magnitude to that in Fig. 3.5b which has been obtained numerically. The flow is a "pusher" flow, as the velocity along the axis of the defect set points outward.

In summary, the transport model of Chapter 2 both qualitatively and quantitatively

accounts for the main transport features in a nematic film with an imposed set of disclinations and subjected to an oscillatory, uniform, electrostatic field. For small mobility and dielectric anisotropies, the topological charge plays a crucial role in the angular structure of the charge density, but not in the radial structure away from defect cores. The angular structure of the electrokinetic flow is also determined by the topological charge of the disclination. One can extend the results for single disclinations to sets of disclinations, which can be used to design specific flow patterns. Both the spatial structure of the flows and the velocity amplitudes obtained for sets of isolated disclinations are in good agreement with the experiments.

Chapter 4

General Features of LCEK Charge Densities and Velocities Due to Fixed Director Patterns

4.1 Introduction

The LCEK results for a periodically modulated director pattern of Chapter 2, and results concerning isolated disclinations in Chapter 3, suggest some general characteristics of the charge density and velocity fields that are generated in a liquid crystalline fluid with a fixed director pattern subject to an AC field. In this chapter we discuss general features of charge density separation end electrokinetically generated flows by an *arbitrary* fixed director field $\hat{\boldsymbol{n}}$. We begin with a discussion of the charge density at first order in a perturbation expansion in mobility and dielectric anisotropies, including the derivation of a Green's function for arbitrary $\hat{\boldsymbol{n}}$. The velocity fields are more complicated to obtain, but we discuss a few methods for finding approximate solutions and predicting the far-field behavior of the flow.

4.1.1 Equation Scaling

In this chapter and throughout the remainder of the thesis, we make a small adjustment in nondimensionalization of variables. The scaling method is the same as Chapters 2 and

3, but with $\mu_\perp$, $\epsilon_\perp$ as the characteristic mobility and dielectric anisotropy rather than $\bar{\mu}$, $\bar{\epsilon}$. Thus charge density is now scaled by $\epsilon_0\epsilon_\perp\ell^{*-1}E_0$ and velocity by $\epsilon_0\epsilon_\perp\ell^*\eta^{-1}E_0^2$. With this adjustment Eqs. (2.49) through Eq. (2.53) become,

$$\Omega\frac{\partial C}{\partial t}+W\frac{\partial Cv_i}{\partial x_i}=\gamma\frac{\partial}{\partial x_i}\left[\frac{D_{ij}}{D_\perp}\frac{\partial C}{\partial x_j}\right]+Y^2\frac{\partial}{\partial x_i}\left[\rho\frac{\mu_{ij}}{\mu_\perp}\frac{\partial\Phi}{\partial x_j}\right] \tag{4.1}$$

$$\Omega\frac{\partial \rho}{\partial t}+W\frac{\partial \rho v_i}{\partial x_i}=\gamma\frac{\partial}{\partial x_i}\left[\frac{D_{ij}}{D_\perp}\frac{\partial \rho}{\partial x_j}\right]+\frac{\partial}{\partial x_i}\left[C\frac{\mu_{ij}}{\mu_\perp}\frac{\partial\Phi}{\partial x_j}\right] \tag{4.2}$$

$$\frac{\partial}{\partial x_i}\left[\frac{\epsilon_{ij}}{\epsilon_\perp}\frac{\partial\Phi}{\partial x_j}\right]=-\rho, \tag{4.3}$$

$$0=\nabla\cdot\boldsymbol{T}-\rho\nabla\Phi,\quad \boldsymbol{T}=-p\mathbb{I}+\frac{1}{\mathrm{Er}}\boldsymbol{T}^e+\tilde{\boldsymbol{T}}, \tag{4.4}$$

$$\hat{\boldsymbol{n}}\times\boldsymbol{h}^0-\mathrm{Er}\left(\hat{\boldsymbol{n}}\times\boldsymbol{h'}-\frac{\Delta\epsilon}{\epsilon_\perp}(\hat{\boldsymbol{n}}\cdot\boldsymbol{E})(\hat{\boldsymbol{n}}\times\boldsymbol{E})\right)=0, \tag{4.5}$$

Where $\Omega=\omega\tau_\rho$ is the ratio of the driving frequency to the characteristic time for charge separation, $\tau_\rho=\epsilon_0\epsilon_\perp/(ec_0\bar{\mu})$, $W=\tau_\rho\epsilon_0\epsilon_\perp E_0^2/\eta$ is the charging time relative to the advection time, $Y=\epsilon_0\epsilon_\perp E_0/(\ell^*ec_0)$ is the charge density relative to the total ionic concentration, $\mathrm{Er}=\epsilon_0\epsilon_\perp E_0^2\ell^{*2}/K$ is the Ericksen number, and $\gamma=\lambda_D^{*2}/\ell^{*2}$, where $\lambda_D^*=\sqrt{\epsilon_0\bar{\epsilon}k_BT/(e^2c_0)}$ is the Debye length.

This change of scaling does not change the governing equations. We choose this scaling for the remainder of the thesis because it allows for a more direct comparison with other studies [30, 44], and because this choice allows charge and velocity results from complex patterns to be written in a simpler form.

4.2 Charge Density

Suppose a nematic with arbitrary fixed pattern $\hat{\boldsymbol{n}}(\boldsymbol{r})$ is subjected to an applied field $\boldsymbol{E}=\hat{\boldsymbol{E}}_{\boldsymbol{0}}\cos t$, where $\hat{\boldsymbol{E}}_{\boldsymbol{0}}$ is an arbitrary unit vector. Following the same argument as in Chapter 3, to first order in Δ and assuming $Y^2/(\gamma\sqrt{1+\Omega^2})\ll 1$, the total concentration is uniform, $C=1$, the electric field $\boldsymbol{E}$ is simply the applied field, and the charge density

is,

$$\Omega\frac{\partial\rho}{\partial t} = \gamma\nabla^2\rho - \rho + (\tilde{\epsilon} - \tilde{\mu})\,\frac{\partial}{\partial x_i}(n_i n_j E_j), \tag{4.6}$$

where $\tilde{\epsilon} = \Delta\epsilon/\epsilon_\perp$ and $\tilde{\mu} = \Delta\mu/\mu_\perp$. If $\gamma \ll 1$ (i.e. the Debye length λ_D^* is much smaller than the characteristic system length ℓ^*), then the first term on the right hand side of Eq. (4.6) is a singular perturbation, significant only near defect cores. Far from defect cores, therefore, the charge density is,

$$\rho(\boldsymbol{r}, t) = \frac{(\tilde{\epsilon} - \tilde{\mu})\cos(t - \delta)}{\sqrt{1 + \Omega^2}}\frac{\partial}{\partial x_i}(n_i n_j \hat{E}_{0j}), \tag{4.7}$$

while near defect cores diffusion cannot be neglected. Note that in two dimensions one may alternatively write $\hat{\boldsymbol{n}} = (cos[\theta(\boldsymbol{r})], \sin[\theta(\boldsymbol{r})])$, in which case Eq. (4.7) is equivalent to Eq. (3.58), apart from the difference in scaling discussed above.

Since Eqn. (4.6) is linear and inhomogeneous, it can alternatively be solved using a Green's function $G(\boldsymbol{r}, t; \boldsymbol{r}', t')$ satisfying

$$\Omega\frac{\partial G}{\partial t} - \gamma\nabla^2 G + G = \delta(\boldsymbol{r} - \boldsymbol{r}')\delta(t - t')$$

Taking a Fourier transform with respect to $\boldsymbol{r}$ and t, one obtains,

$$i\omega\Omega G(\boldsymbol{q}, \omega; \boldsymbol{r}', t') + \gamma q^2 G(\boldsymbol{q}, \omega; \boldsymbol{r}', t') + G(\boldsymbol{q}, \omega; \boldsymbol{r}', t') = e^{-i\boldsymbol{q}\cdot\boldsymbol{r}'}e^{-i\omega t'},$$

thus,

$$G(\boldsymbol{q}, \omega; \boldsymbol{r}', t') = \frac{-ie^{-i\boldsymbol{q}\cdot\boldsymbol{r}'}e^{-i\omega t'}}{\Omega\omega - i(\gamma q^2 + 1)},$$

which implies,

$$G(\boldsymbol{q}, t; \boldsymbol{r}', t') = e^{-i\boldsymbol{q}\cdot\boldsymbol{r}'}\int_{-\infty}^{\infty}\frac{-ie^{i\omega(t-t')}}{\Omega\omega - i(\gamma q^2 + 1)}\frac{d\omega}{2\pi}. \tag{4.8}$$

The integrand in Eq. (4.8) has one pole at $i(\gamma q^2 + 1)/\Omega$. If $t > t'$, one can close the integral in the positive imaginary half of the complex plane, finding,

$$G(\boldsymbol{q}, t; \boldsymbol{r}', t') = \frac{1}{\Omega}e^{-i\boldsymbol{q}\cdot\boldsymbol{r}'}e^{-(\gamma q^2+1)(t-t')/\Omega}H(t - t'),$$

where $H(t - t')$ is the Heaviside step function. The Green's function in real space is

given by

$$G(\boldsymbol{r},t;\boldsymbol{r}',t') = \frac{1}{\Omega}e^{-(t-t')/\Omega}H(t-t')\iint \frac{e^{i\boldsymbol{q}\cdot(\boldsymbol{r}-\boldsymbol{r}')}e^{-\gamma q^2(t-t')/\Omega}d^2q}{4\pi^2}, \tag{4.9}$$

so

$$\begin{aligned} G(\boldsymbol{r},t;\boldsymbol{r}',t') = \frac{1}{\Omega}e^{-(t-t')/\Omega}H(t-t')\int_{-\infty}^{\infty}\frac{e^{iq_x(x-x')}e^{-\gamma q_x^2(t-t')/\Omega}dq_x}{2\pi} \\ \times\int_{-\infty}^{\infty}\frac{e^{iq_y(y-y')}e^{-\gamma q_y^2(t-t')/\Omega}dq_y}{2\pi}. \end{aligned} \tag{4.10}$$

We have two Fourier transforms of Gaussians, so using this result we get the Green function in real space:

$$G(\boldsymbol{r},t;\boldsymbol{r}',t') = \frac{1}{4\pi\gamma}\frac{H(t-t')e^{-(t-t')/\Omega}e^{-\Omega|\boldsymbol{r}-\boldsymbol{r}'|^2/(4\gamma(t-t'))}}{(t-t')}$$

Then the charge density to first order in the anisotropies for an arbitrary director pattern is,

$$\begin{aligned} \rho(\boldsymbol{r},t) = \frac{(\tilde{\epsilon}-\tilde{\mu})}{4\pi\gamma}\iint d^2r'\int_{-\infty}^{t}\frac{e^{-(t-t')/\Omega}e^{-\Omega|\boldsymbol{r}-\boldsymbol{r}'|^2/(4\gamma(t-t'))}}{(t-t')}\cos(t') \\ \times\frac{\partial}{\partial x_i'}(n_i(\boldsymbol{r}')n_j(\boldsymbol{r}')\hat{E}_{0j})dt' \end{aligned} \tag{4.11}$$

Assume $\gamma/\Omega \ll 1$, so the integrand is sharply peaked at $\boldsymbol{r} = \boldsymbol{r}'$. Then by Laplace's method, the leading order behavior of the spatial integral is,

$$\begin{aligned} \frac{1}{4\pi\gamma}\iint d^2r'\frac{e^{-\Omega|\boldsymbol{r}-\boldsymbol{r}'|^2/(4\gamma(t-t'))}}{(t-t')}\frac{\partial}{\partial x_i'}(n_i(\boldsymbol{r}')n_j(\boldsymbol{r}')\hat{E}_{0j}) \\ \approx \frac{1}{\Omega}\frac{\partial}{\partial x_i}(n_in_j\hat{E}_{0j}) \end{aligned} \tag{4.12}$$

Then the time integral is,

$$\int_{-\infty}^{t}e^{-(t-t')/\Omega}\frac{\cos t'}{\Omega}dt' = \frac{\cos(t-\delta)}{\sqrt{1+\Omega^2}}, \tag{4.13}$$

where $\tan\delta = \Omega$. Thus in this limit, far from defect cores, the Green's function produces

the far-field charge solution, Eq. (4.7).

4.3 Nematic Velocity

While the far-field solution for the charge density can be determined for arbitrary $\hat{\boldsymbol{n}}$, the velocity field is in general much more complicated, since the viscous stress $\tilde{\boldsymbol{T}}$ is a function of $\hat{\boldsymbol{n}}$. However, as shown in Chapter 3, one can determine many of the qualitative features of the velocity $\boldsymbol{v}$ by approximating the nematic viscosity as Newtonian and solving the Navier-Stokes equations,

$$-\nabla p + \nabla^2 \boldsymbol{v} + \rho \boldsymbol{E} = 0, \;\; \nabla \cdot \boldsymbol{v} = 0, \tag{4.14}$$

with ρ determined in Sec. (4.2). Equation (4.14) can be solved using a number of techniques, such as by finding stream function solutions or by using the two-dimensional analogue of the Oseen tensor [63].

We can use the general far-field features of the solution to the director field to predict the far-field radial behavior of the velocity. Consider N disclinations in a domain with size much larger than the separation between disclinations. Using complex variables $z = x + iy$, the solution for disclination j at position (x_j, y_j) with topological charge m_j is $\theta_j(\boldsymbol{r}) = \mathrm{Im}(m_j \log(z - z_j))$, where $z_j = x_j + iy_j$, again in the one elastic constant approximation. This is equivalent to the definition $\theta_j(\boldsymbol{r}) = m\phi_j$ from Chapter 3. Note that

$$\log(z - z_j) = \log z + \log\left(1 - \frac{z_j}{z}\right) = \log z + \sum_{n=1}^{\infty} \frac{1}{n}\left(\frac{z_j}{z}\right)^n. \tag{4.15}$$

Thus for N disclinations, $\theta(\boldsymbol{r}) = \mathrm{Im}[u(z)]$, where

$$u(z) = \left(\sum_{i=1}^{N} m_i\right) \log z + \sum_{n=1}^{\infty} \left[\frac{1}{nz^n}\left(\sum_{j=1}^{N} m_j z_j^n\right)\right] \tag{4.16}$$

Equation (4.16) is a 2D multipole expansion of u; we will use this to determine the behavior of the electrokinetic charge density ρ and velocity v far from the system of defects. Note that Eq. (4.7) implies $\rho \sim \nabla\theta$, and Eq. (4.14) implies $\nabla^2 v \sim \rho E$; thus the behavior of $\theta(\boldsymbol{r})$ at $r = |z| \gg 1$ will determine the behavior of ρ and v.

If the system has a nonzero total topological charge, then the leading order behavior of θ at large r is $\theta \sim (\sum_i m_i)\phi$, which implies $\rho \sim 1/r$ and $v \sim r$. This corresponds with the velocity behavior for single disclinations described in Chapter 3. For systems with zero total topological charge but nonzero dipole moment, $\theta \sim r^{-1}$, $\rho \sim r^{-2}$, $v \sim \log r$. For systems with zero total charge and zero dipole moment, $\theta \sim r^{-2}, \rho \sim r^{-3}, v \sim r^{-1}$.

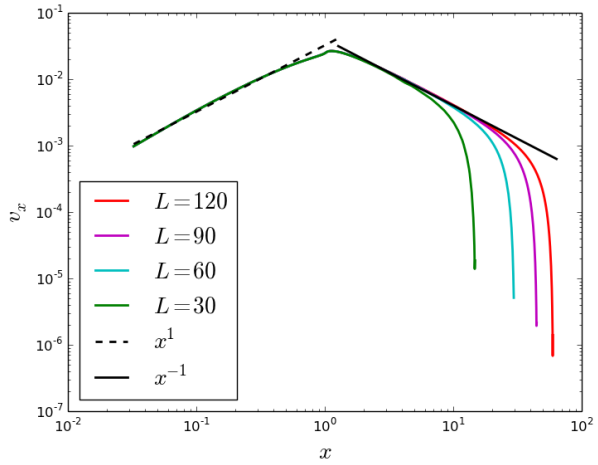

Figure 4.1: Log-log plot of the numerical velocity in the x direction as a function of position along $y = 0$ for the $(-1/2, +1, -1/2)$ disclination triplet, plotted for several numerical system sizes. The lines x^1 and x^{-1} are also plotted for reference. For $x \ll 1$, we expect the velocity to grow linearly in x, as is the case for single isolated disclinations. For $x \gg 1$, we expect $v \sim x^{-1}$ since the triplet pattern is quadrupolar. Near the boundary of the numerical domain the velocity changes rapidly to satisfy the no-slip boundary conditions.

The $(-1/2, 1, -1/2)$ disclination triplet is an example of a pattern with zero total charge and zero dipole moment. Figure 4.1 plots the numerical x-velocity along $y = 0$ for this pattern, for a variety of system sizes L. We see that near the disclination set the velocity is linear in x, which we expect for a single disclination. Far from the disclination set, $x \gg 1$, the velocity decays as x^{-1}, until it changes rapidly to satisfy no-slip boundary conditions. One would expect that for an infinite domain the velocity decay would remain as x^{-1}, and we see a better agreement between the numerical far-field velocity and the x^{-1} prediction as we increase L. In fact, a consequence of the multipole analysis above is that in infinite two dimensional domains, only director

patterns with zero total topological charge and zero dipole moment will have a bounded velocity as $r \to \infty$.

It is important to note that this analysis only considers the far-field charge density behavior, and does not account for far-field perturbations due to viscous forces near defect cores. Unlike the far-field charge density, which is explicitly determined by the driving term in Eq. (4.6), the far-field velocity solution cannot be fully determined without solving for the velocity field near defect cores. Thus the behavior of the velocity and charge density near singularities in $\hat{\boldsymbol{n}}$ can add homogeneous terms to the far-field velocity solution, as will be seen in Chapter 5. Still, the conclusions above that in two dimensions, director fields with nonzero topological charge or nonzero dipole moment diverge on an infinite domain, is valid, since the electrostatic body force $\rho\boldsymbol{E}$ will lead to unbounded inhomogeneous terms in $\boldsymbol{v}$.

In conclusion, we find that to first order in Δ and assuming little variation in C, the charge density can be determined analytically. The velocity field is more difficult to determine, yet one can show that in two dimensions the imposed director pattern must have zero topological charge and zero dipole moment to have a bounded velocity field on an infinite domain.

Chapter 5

LCEK of interacting particles

5.1 Introduction

Microscale manipulation of colloidal particles and fluids by electric fields is a broad area of active scientific research ranging from fundamental studies of non-equilibrium phenomena [60,64–66] to the development of practical devices for informational displays, portable diagnostics, sensing, delivery, and cell sorting [67–69]. When particles are suspended in a nematic matrix rather than an isotropic fluid, electrokinetic phenomena acquire qualitatively new characteristics, since space charge is generated in the medium because of director distortions which occur due to topological constraints, rather than at the interface between solid particles and the electrolyte.

In this chapter, we investigate the mechanisms for electrokinetic flow in systems of particles suspended in a nematic matrix. The presence of a colloidal particle leads to distortions in the director field $\hat{\boldsymbol{n}}$ due to the finite strength of surface anchoring. Define $\boldsymbol{\nu}(\boldsymbol{r})$ as the unit vector normal to the boundary $\partial\Omega$ of domain Ω. We will typically consider two types of anchoring: homeotropic, in which the $\hat{\boldsymbol{n}}(\boldsymbol{r})$ aligns perpendicular to $\boldsymbol{\nu}(\boldsymbol{r})$ at the surface, and planar anchoring, in which $\hat{\boldsymbol{n}}(\boldsymbol{r})$ aligns parallel to $\boldsymbol{\nu}(\boldsymbol{r})$ at the surface. In the general case, a phenomenological expression for the anchoring energy, in dimensionless units, is written as [51],

$$F_s = \int_{\partial\Omega} \left(\frac{w^* \ell^*}{K} \right) \frac{1}{2} (1 - (\hat{\boldsymbol{n}} \cdot \boldsymbol{\nu})^2) dS, \tag{5.1}$$

where lengths are scaled by $\ell^* = a^*$, the radius of the particle, and w^* is a coupling constant with units of energy per area, with $w^* > 0$ corresponding to homeotropic anchoring, and $w^* < 0$ corresponding to planar anchoring. For typical experimental values of the systems we examine in this thesis, $|w^*|$ is much larger than $K/\ell^* \sim 10^{-5}\ J/m^2$ [52], thus we can assume strong anchoring and replace the anchoring energy with boundary conditions $\hat{\boldsymbol{n}}(\boldsymbol{r}) = \boldsymbol{\nu}(\boldsymbol{r})$ for $\boldsymbol{r} \in \partial\Omega$ when $w^* > 0$ (homeotropic anchoring) and $\hat{\boldsymbol{n}}(\boldsymbol{r}) \cdot \boldsymbol{\nu}(\boldsymbol{r}) = 0$ for $\boldsymbol{r} \in \partial\Omega$ when $w^* < 0$ (planar anchoring). The topological characteristics of the anchoring on the surface of the particle and on the outer domain walls can lead to the nucleation of defects whose topological charge can impact electrokinetic flow, as seen in Chapter 3. We begin this chapter by discussing the nature of the director distortions in colloidal suspensions and the types of distortions which are topologically allowed. Next we describe the mechanisms for mobility of a single particle with a companion "hedgehog" point defect defect; a state in which the asymmetry of director distortions, rather than particle asymmetry, leads to systematic flow. We compare our numerical studies to experimental results about particle motion and interaction. We also examine how particles may be manipulated by changing the nematic dielectric anisotropy. Finally, we briefly discuss numerical results for electrokinetic flows of two-particle systems.

5.2 Particle suspension topology

5.2.1 Homeotropic anchoring

Consider a particle (with no holes) suspended in a nematic liquid crystal. Assume homeotropic anchoring of the director on the particle surface, i.e. $\hat{\boldsymbol{n}}(\boldsymbol{r}) = \boldsymbol{\nu}(\boldsymbol{r})$, while on the outer boundaries of the domain $\hat{\boldsymbol{n}}$ is uniform. Recall from Chapter 2 that the order parameter space for $\hat{\boldsymbol{n}}$ in two dimensions is $S^1/\mathbb{Z}_2$, the unit circle with opposite ends identified, and the topological charge within a domain is the number of revolutions $\hat{\boldsymbol{n}}(\boldsymbol{r})$ makes about the unit circle as it traces a contour enclosing the domain (Fig. 2.1). In a two-dimensions, $\hat{\boldsymbol{n}}$ completes one revolution around the unit circle as we trace a path around the surface of the particle. Therefore the particle has a topological charge of (+1). Since the director is uniform on outer domain boundaries, the total topological charge of the system is zero. Therefore there must be N point defects whose topological

charges sum to (-1); the simplest possibilities are a single (-1) defect, Fig. 5.1, or two defects each with charge $(-1/2)$, Fig. 5.2. We will discuss the relative stability of each of these configurations below.

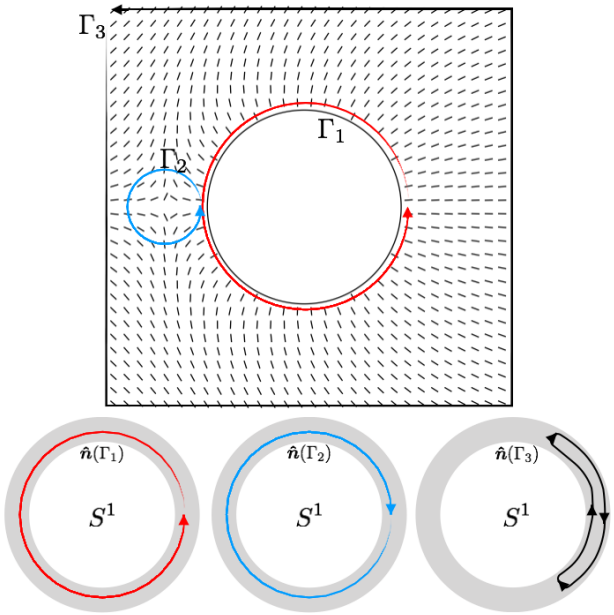

Figure 5.1: Topology of a two-dimensional particle with homeotropic anchoring and a companion defect. The director angle along a clockwise-oriented contour Γ_1 enclosing the particle surface traces a full revolution around the unit circle S^1 in the clockwise direction. Thus the particle has charge $(+1)$. Along Γ_2, which encloses the defect, the director completes a full revolution in the opposite direction as Γ_2, thus giving the defect a charge of (-1). Therefore, the total topological charge of the system is zero, which can be seen by considering a contour Γ_3 enclosing bot the particle and the defect. The mapping of Γ_3 onto the unit circle can be continuously deformed to a point, implying zero net topological charge enclosed.

In three dimensions, the suspended particle has a topological charge of magnitude $(+1)$ (recall from Chapter 2 there is some ambiguity to the sign of point defects in three dimensions; we choose to define the homotopy group $\pi(S^2/\mathbb{Z})$ such that the charge of the suspended particle is always positive). As with the two-dimensional system, the total charge of the remaining defects (hedgehogs and disclination loops) must sum to (-1). The simplest solutions satisfying this condition are a single companion point defect or disclination ring, Fig. 5.3.

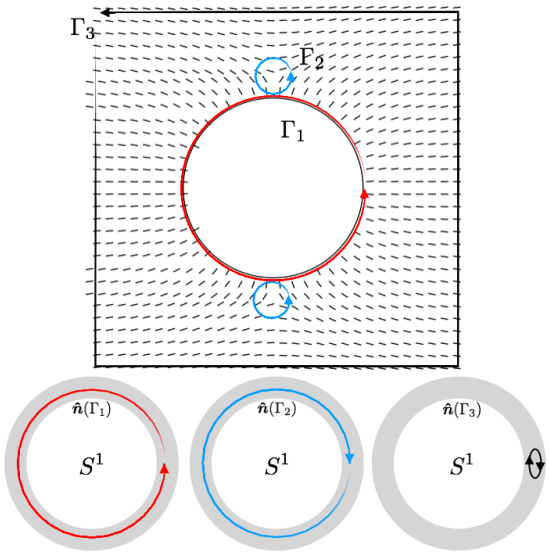

Figure 5.2: Topology of a two-dimensional particle with homeotropic anchoring and two companion defects. The director traces a full revolution around the unit circle along a contour Γ_1 enclosing the particle. Therefore the particle has a topological charge of $(+1)$. Along a contour Γ_2 enclosing either defect, the director completes half a rotation about the unit circle in the opposite direction as Γ_2, thus each defect has topological charge $(-1/2)$. The total topological charge of the system is the sum of the individual charges; therefore the topological charge is zero, as can be seen by the mapping of the contour Γ_3 onto the unit circle. The contour $\hat{\boldsymbol{n}}(\Gamma_3)$ can be continuously deformed to a point, implying the total charge enclosed is zero.

5.2.2 Planar anchoring

Consider the same system as above except with $\hat{\boldsymbol{n}}$ parallel to the particle surface, $\hat{\boldsymbol{n}}(\boldsymbol{r}) \cdot \boldsymbol{\nu}(\boldsymbol{r}) = 0$. In two dimensions, the topological charge of the particle is again $(+1)$; therefore there must be defects with topological charge totaling (-1), as above.

Unlike in two dimensions, planar anchoring in three dimensions leads to solutions topologically distinct from homeotropic anchoring solutions. An example solution for a sphere with tangential anchoring is shown in Fig. 5.4a. While planar anchoring in two dimensions (and homeotropic anchoring in three dimensions) fully specifies the director orientation at the particle surface, the planar anchoring condition $\hat{\boldsymbol{n}}(\boldsymbol{r}) \cdot \boldsymbol{\nu}(\boldsymbol{r}) = 0$ in three dimensions leaves one degree of freedom unconstrained, i.e. there are an infinite number of planar configurations which satisfy tangential anchoring, and the director

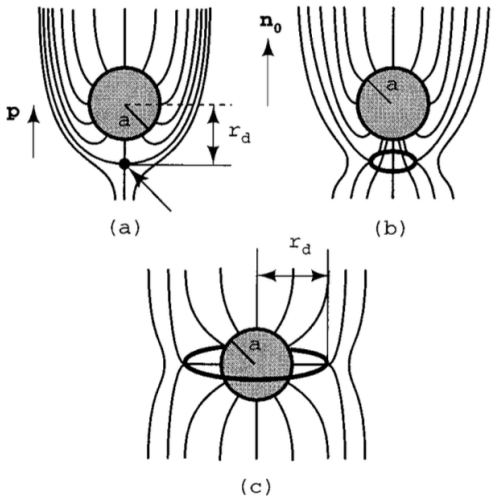

Figure 5.3: Three examples of director configurations around a sphere of radius a satisfying homeotropic anchoring at the surface of the sphere and uniform anchoring far from the sphere in the direction $\hat{\boldsymbol{n}}_0$ (director depicted as black streamlines in the figure). Homeotropic anchoring gives the suspended particle a topological charge of (+1). Uniform boundary conditions require zero total topological charge in the system, requiring the existence of director singularities in the bulk with topological charge totaling (-1). This condition may be satisfied by the inclusion of (a) a point defect or (b) a (1/2)-strength disclination loop. The configuration in which the disclination loop surrounds the equator of the particle, (c), is known as the "Saturn Ring" configuration. This figure is reproduced from Ref. [4].

orientation is specified by minimizing elastic distortions on the particle surface as well as in the bulk.

Unlike for two dimensional problems on a planar surface, the topology of the particle surface will impact the formation of surface defects. By the Poincaré-Brouwer theorem, the sum of the topological charges of defects on a surface must equal its Euler characteristic [70]. The Euler characteristic of a sphere is two, so there must be point defects on the particle surface, commonly known boojums, whose charges sum to (+2), Fig. 5.4b.

Despite the presence of defects on the surface two-dimensional surface, the three-dimensional topological charge of the particle is zero, as the director does not trace a path along the entire particle surface that covers the unit sphere, as shown in Fig. 5.5. When tracing a surface from one boojum to the other, the mapping begins at the

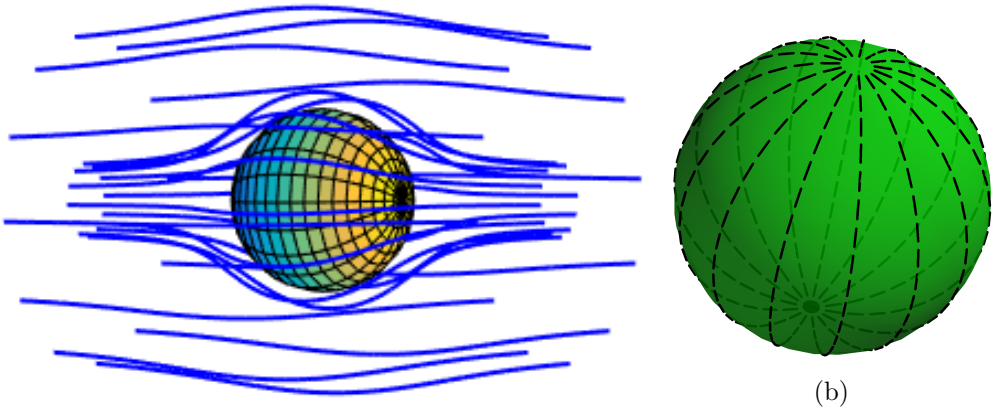

(a) (b)

Figure 5.4: (a) Director field for sphere with tangential anchoring, depicted as blue streamlines. (b) Director field on the surface of the sphere. The sum of the topological charges on the surface of the sphere must equal its Euler characteristic. This is satisfied here by two (+1) boojum defects at opposite poles.

equator of the unit sphere and moves upward (Fig. 5.5a), then moves back downward, ending again at the equator, (Fig. 5.5b). Thus the net covering of the unit sphere is zero, the topological charge of the particle is zero, and hence no defects are required within the bulk domain when the far-field director is uniform.

5.3 Elastic equilibrium

Since topology allows different types of configurations, we address here their relative stability with respect to the elastic energy of the nematic. Consider a radially symmetric particle, with either homeotropic or planar anchoring, suspended in a nematic domain of infinite size, with $\hat{\boldsymbol{n}}(r \to \infty) \to \hat{\boldsymbol{n}}_0$, where $\hat{\boldsymbol{n}}_0$ is uniform. In equilibrium $\hat{\boldsymbol{n}}$ minimizes the Oseen-Frank free energy, or the Landau-de Gennes free energy when using the order parameter $Q_{ij} = S(n_i n_j - \delta_{ij}/d)$, where d is the dimensionality of space. These equations are highly nonlinear, and while an analytic solution has been recently found for the so-called "Saturn ring" configuration [71], other director configurations cannot be found analytically. Instead, for the purposes of this qualitative discussion, we consider the one-constant approximation, $K_1 = K_2 = K_3 = K$, under which the Euler-Lagrange

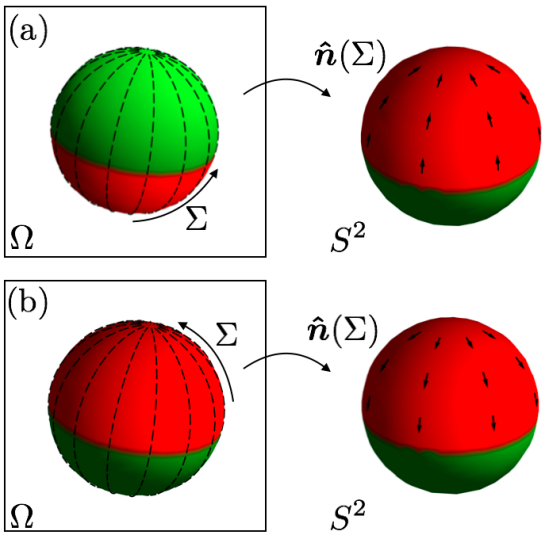

Figure 5.5: The mapping of the director orientation along the surface of a particle with tangential anchoring onto the order parameter space $S^2/\mathbb{Z}_2$ is shown in two steps. (a) Consider a surface Σ covering the lower half of the sphere. At the boojum at the base of the sphere, the director is mapped to the equator of the unit sphere. Tracing Σ up the sphere, the mapping also moves upward, reaching the top of S^2 as Σ reaches the equator of the particle. (b) Suppose Σ covers the upper half of the particle. At the equator of the particle, the director is uniformly upward, corresponding to the top of the unit sphere. The mapping moves downward as one traces along Σ upward, reaching the equator as Σ reaches the second boojum. Thus the mapping of the top half of the particle traverses S^2 in the opposite direction as the mapping of the bottom half of the particle. Thus the topological charge of the sphere is zero.

equations for the Oseen-Frank energy reduce to,

$$\nabla^2 \hat{\boldsymbol{n}} = 0, \quad |\hat{\boldsymbol{n}}|^2 = 1. \tag{5.2}$$

Below we discuss the possible director solutions in three and two dimensions.

5.3.1 Three Dimensions

Consider a spherical particle of radius 1, and define a coordinate system where $\hat{\boldsymbol{n}}_0 = \hat{\boldsymbol{z}}$. With these conditions and homeotropic anchoring, two director solutions have been experimentally found: the "hyperbolic hedgehog" configuration, consisting of a point defect on the z-axis near the particle [72], depicted in Fig. 5.6a, and the "Saturn ring"

configuration, consisting of a (1/2)-strength disclination ring around the equator of the particle in the xy plane [73], depicted in Fig. 5.3c. We explore the key characteristics of the director fields for these two configurations.

Even with the one-constant approxmation, Eq. (5.2) is still nonlinear in three dimensions due to the normalization condition, so we make a further approximation to investigate the behavior of $\hat{\boldsymbol{n}}(r \gg 1)$. Far from the particle, we approximate the director field as $\hat{\boldsymbol{n}} \approx (n_x, n_y, 1)$ with $n_x, n_y \ll 1$ and $\nabla^2 n_\alpha = 0,\ \alpha = x, y$. Since n_α solves Laplace's equation, regardless of anchoring we may write n_α as a multipole expansion [74],

$$n_\alpha(\boldsymbol{r}) = \frac{q_\alpha}{r} + 3\frac{p_{\alpha j}x_j}{r^3} + 5\frac{Q_{\alpha jk}x_j x_k}{r^5} + \cdots \quad \alpha = x, y;\ j, k = x, y, z \tag{5.3}$$

Throughout the remainder of this section, greek subscripts run over x, y, and i, j, k run over x, y, z. The leading order behavior of n_α can be determined by examining the symmetry of the two experimentally obtained solutions.

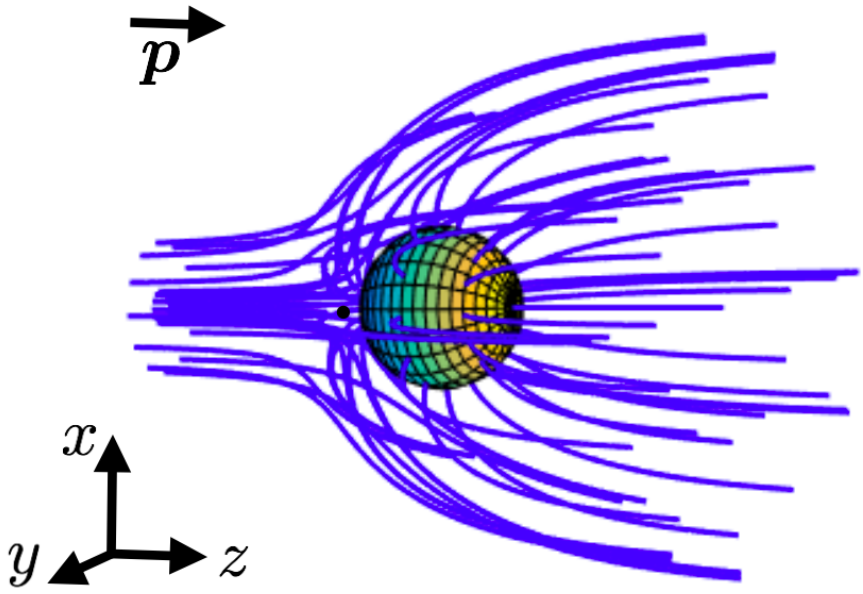

Figure 5.6: Director field of a generated by a sphere with homeotropic anchoring and corresponding "hedgehog" (located on the left). The structural dipole $\boldsymbol{p}$ is shown by an arrow, parallel to $\hat{\boldsymbol{z}}$.

The hyperbolic hedgehog is axisymmetric about $\hat{\boldsymbol{z}}$. Therefore we expect $\hat{\boldsymbol{n}} \cdot \hat{\boldsymbol{\phi}} = 0$, where $\hat{\boldsymbol{\phi}}$ is a unit vector in the azimuthal direction. Using Eq. (5.3), $\hat{\boldsymbol{n}} \cdot \hat{\boldsymbol{\phi}} = 0$ implies $q_\alpha = 0$, $p_{xx} = p_{yy}$ and all other values of $p_{\alpha j}$ zero. Thus the leading order behavior of the hedgehog-sphere pair is dipolar for $r \gg 1$,

$$n_\alpha(r \gg 1) \approx \frac{3 p_{xx} x_\alpha}{r^3} + \mathcal{O}(r^{-3}) \tag{5.4}$$

Note that $p_{xx} > 0$ when the hedgehog defect is below the sphere, while $p_{xx} < 0$ when the defect is above the sphere. We therefore define a vector $\boldsymbol{p}$ corresponding to the elastic dipole moment, directed from the hedgehog toward the sphere (see Fig. 5.6), and write Eq. (5.4) as,

$$n_\alpha(r \gg 1) \approx \frac{3(\boldsymbol{p} \cdot \hat{\boldsymbol{z}}) x_\alpha}{r^3} + \mathcal{O}(r^{-3}) \tag{5.5}$$

For the case of a Saturn ring, the director field is both axisymmetric and also symmetric for reflections in the xy plane at $z = 0$. Using $\hat{\boldsymbol{n}} = -\hat{\boldsymbol{n}}$, reflection symmetry across $z = 0$ implies $(n_x(x, y, -z), n_y(x, y, -z), n_z(x, y, -z)) = (-n_x(x, y, z), -n_y(x, y, z), n_z(x, y, z))$, which implies $p_{xx} = p_{yy} = 0$ (the remaining elements of $p_{\alpha j}$ along with q_α are again zero due to axisymmetry). Therefore the Saturn ring produces a quadrupolar director field at $r \gg 1$.

Experimental studies of particles with tangential anchoring show a director field with two boojums along the z axis at opposite ends of the particle [75], depicted in Fig. 5.4a. Like the Saturn ring, this configuration is axisymmetric and is symmetric about the plane $z = 0$; therefore the leading order behavior of $\hat{\boldsymbol{n}}$ far from the particle is quadrupolar.

Experimental studies of particles of size $\sim 1\ \mu m$ or greater with homeotropic anchoring find the particle-hedegehog configuration as the equilibrium state except when the thickness of the confining cell is on the order of the particle diameter [76]. Therefore, we will not focus on the Saturn ring configuration, and instead consider only particle-hedgehog pairs when the anchoring is homeotropic.

In order to perform further analysis of particle-hedgehog pairs, we wish to find a solution to the director at $r \lesssim 1$. However, an analytic solution to Eq. (5.2) is not known in three dimensions, due to the presence of the normalization condition. Instead

we seek an ansatz that will satisfy the boundary conditions at the particle surface and the far-field behavior of Eq. (5.3). For the hyperbolic hedgehog, such an approximate solution can be found by considering the electric field $\boldsymbol{\mathcal{E}}$ of a conducting sphere of radius $R = 1$ with charge q placed in a uniform electric field $\boldsymbol{\mathcal{E}}_0 = \hat{\boldsymbol{z}}$. The electric field corresponding to this system is [72],

$$\boldsymbol{\mathcal{E}} = \hat{\boldsymbol{z}} + q\frac{\boldsymbol{r}}{r^3} - \frac{1}{r^5}(r^2\hat{\boldsymbol{z}} - 3z\boldsymbol{r}) \tag{5.6}$$

Then $\hat{\boldsymbol{n}} = \boldsymbol{\mathcal{E}}/|\boldsymbol{\mathcal{E}}|$. This function satisfies the boundary conditions at $r = 1$ and the far-field behavior of Eq. (5.3). It has a point defect at $-z_0\hat{\boldsymbol{z}}$, where $z_0^3 - qz_0 + 2 = 0$. Neither q nor z_0 are defined. One proceeds variationally by minimizing the elastic with respect to thse parameters. In the one constant approximation the elastic energy,

$$E_{el} = \int \frac{1}{2}(\nabla\hat{\boldsymbol{n}})^2 d^3x, \tag{5.7}$$

it is minimized when $q \approx 3.078$, corresponding to $z_0 = 1.17$. We will use this solution in Sec. 5.4 to investigate the effect of dimensionality on LCEK flows.

5.3.2 Two Dimensions

Since the LCEK experiments of interest are performed in thin-film cells [44], we expect the system to be quasi two-dimensional. Therefore we investigate the conditions for elastic equilibrium in two dimensions, and compare the results to those in three dimensions.

In two dimensions, our particle is a disc of radius 1 centered at the origin of a coordinate system, with far field director orientation in the x direction, $\hat{\boldsymbol{n}}_0 = \hat{\boldsymbol{x}}$. While Eq. (5.2) is nonlinear in three dimensions, in two dimensions one can define the director angle $\theta(\boldsymbol{r})$ where $\hat{\boldsymbol{n}} = (\cos(\theta), \sin(\theta))$, and the elastic free energy, Eq. (5.7) becomes,

$$E_{el} = \int \frac{1}{2}(\nabla\theta)^2 d^2x, \tag{5.8}$$

which is minimized when $\nabla^2\theta = 0$. Thus $\theta(\boldsymbol{r})$ is a harmonic function. We solve for $\theta(\boldsymbol{r})$ by considering analogies to the electrostatics of point charges in two dimensions. The solution for an isolated disclination of charge m at $\boldsymbol{r}_0$ is $\theta(\boldsymbol{r}) = m\phi_0$, with $\tan\phi_0 = \frac{y-y_0}{x-x_0}$.

Note that $\theta(\boldsymbol{r}) = \mathrm{Im}(m\log(z - z_0))$ where $z = x + iy$, $z_0 = x_0 + iy_0$, and $i^2 = -1$. Thus the harmonic conjugate to $\theta(\boldsymbol{r}) = m\phi_i$ is $\Phi(\boldsymbol{r}) = \mathrm{Re}(m\log(z - z_0)) = m\ln(|\boldsymbol{r} - \boldsymbol{r}_0|)$, which is the 2D electrostatic potential of a point charge of size m. In fact, since $u(z) = \Phi(x, y) + i\theta(x, y)$ is analytic, the Cauchy-Riemann equations state $\partial_x\Phi = \partial_y\theta$, $\partial_y\Phi = -\partial_x\theta$. Thus $(\nabla\Phi)^2 = (\nabla\theta)^2$, so the free energy of a two dimensional nematic in elastic equilibrium is equivalent to the energy of the related electrostatic analog. In particular, a 2D system of disclinations in elastic equilibrium is equivalent to a system of 2D electric point charges at the same locations in electrostatic equilibrium. Additionally, since the the energy densities of both systems are the same, the force between two defects is the same as the force between two point charges,

$$\boldsymbol{F} = \frac{m_1 m_2(\boldsymbol{r}_1 - \boldsymbol{r}_2)}{|\boldsymbol{r}_1 - \boldsymbol{r}_2|^2} \tag{5.9}$$

Assume homeotropic anchoring on the disc, $\theta(1, \phi) = \phi$ and note that $\hat{\boldsymbol{n}}_0 = \hat{\boldsymbol{x}}$ implies $\theta(r \to \infty) \to 0$. This system can be solved by the method of image charges, in analogy to electrostatic systems. The solution is,

$$\theta(\boldsymbol{r}) = \mathrm{Im}\left(\log\left(\frac{z^2}{(z + x_0)(z + 1/x_0)}\right)\right), \tag{5.10}$$

which corresponds to a director field with with one (-1) defect at $(-x_0, 0)$ and two image defects within the particle, one of charge (+2) at the origin and one of charge (-1) at $(-1/x_0, 0)$. To see that the boundary conditions are satisfied, note that for $r \gg 1$,

$$\theta(\boldsymbol{r} \gg 1) \to \mathrm{Im}\left(\log\left(\frac{z^2}{z^2}\right)\right) = 0, \tag{5.11}$$

and for $r = 1$,

$$\begin{aligned}
\theta(r=1) &= \mathrm{Im}\left(\log\left(\frac{e^{2i\phi}}{(e^{i\phi}+x_0)(e^{i\phi}+x_0^{-1})}\right)\right) \\
&= \mathrm{Im}\left(-\log\left((1+x_0e^{-i\phi})(1+x_0^{-1}e^{-i\phi})\right)\right) \\
&= \mathrm{Im}\left(\log(x_0e^{i\phi}) - \log[(1+x_0e^{-i\phi})(1+x_0e^{i\phi})]\right) \\
&= \mathrm{Im}\left(\log x_0 + i\phi - \log(1+2x_0\cos\phi+x_0^2)\right) \\
&= \phi.
\end{aligned}$$

Note that $\theta(\boldsymbol{r})$ is harmonic everywhere in the domain excluding the defect.

The equilibrium position of the defect x_0 will be where the force on the defect from the image charges is zero,

$$-\frac{2}{x_0} + \frac{1}{x_0 - x_0^{-1}} = 0 \implies x_0 = \sqrt{2}. \tag{5.12}$$

As with the particle-hedgehog three-dimensional solution, the leading order behavior of Eq. 5.10 for $r \gg 1$ is dipolar, and we may define the elastic dipole $\boldsymbol{p}$ pointing from the defect to the center of the particle.

While the two- and three-dimensional particle-defect solutions are dipolar, Eq. (5.10) is not simply a two-dimensional slice of the three-dimensional solution. This is because the far-field behaviors of the two solutions, while both dipolar, have different radial dependencies. The leading order behavior of Eq. (5.10) at $r \gg 1$ decays as r^{-1}, while at $r \gg 1$ the three-dimensional particle-hedgehog solution decays as r^{-2}, as shown in Eq. (5.5).

A second solution satisfying homeotropic anchoring and $\hat{\boldsymbol{n}}_0 = \hat{\boldsymbol{x}}$ has two $(-1/2)$ defects at $(0, \pm y_0)$, one $(+2)$ image defect at the origin, and two $(-1/2)$ image defects at $(0, \pm 1/y_0)$, depicted in Fig. 5.2.

The director field is then,

$$\theta(\boldsymbol{r}) = \mathrm{Im}\left(\log\left(\frac{z^2}{\sqrt{(z-iy_0)(z-i/y_0)(z+iy_0)(z+i/y_0)}}\right)\right) \tag{5.13}$$

This configuration is quadrupolar rather than dipolar. Through the same force

balance argument, one finds $y_0 = \sqrt[4]{7/3}$ [77].

Since both the dipolar and quadrupolar solutions are topologically allowed, we must consider energetic arguments to determine the relative stability of the two solutions. However, since the director fields are singular, the elastic energy diverges. For instance, the director field of a point defect of charge m is $\theta = m\phi$, and the corresponding free energy density (the integrand in Eq. (5.8)) is $(1/2)(\nabla\theta)^2 = m^2/(2r^2)$, which diverges at the point defect. To avoid these singularities, we introduce a defect core of radius $\delta \ll 1$ and a core energy of approximately $E_{core}^{(m)} = m^2\pi$ [78]. Thus for the above example the energy of a point defect of radius m in a disc of radius R is $E_m = m^2 \log(R/\delta) + 2\pi m$.

For the dipole system the energy is [78],

$$E_{dip} = \pi \log 4 - \pi \log \delta + E_{core}^{(1)} = \pi(\log 4 - \log \delta + 1) \tag{5.14}$$

while the energy of the quadrupole system is [77],

$$\begin{aligned} E_{quad} &= \frac{\pi}{8}\left[3\log\left(\frac{7}{3}\right) + 4\log\left(\frac{7}{8\delta}\right)\right] + 2E_{core}^{\left(\frac{1}{2}\right)} \\ &= \frac{\pi}{8}\left[3\log\left(\frac{7}{3}\right) + 4\log\left(\frac{7}{8\delta}\right)\right] + \frac{\pi}{2}. \end{aligned} \tag{5.15}$$

The difference in energy is

$$E_{quad} - E_{dip} = \frac{\pi}{2}\left(\log\delta - 1 - \log 16 - \log\left[\frac{8}{7}\left(\frac{3}{7}\right)^{\frac{3}{4}}\right]\right) \tag{5.16}$$

If the core size small, $\delta \ll 1$, this difference is negative. Thus the quadrupolar structure is energetically preferred in two dimensions.

We have confirmed this energetic preference through numerical investigation in two dimensions. While thus far we have used the director $\hat{\boldsymbol{n}}$ to model nematic orientation, numerical studies involving $\hat{\boldsymbol{n}}$ only allow for integer-strength defects, since half integer defects would have a discontinuity at the branch cut where $\hat{\boldsymbol{n}} \to -\hat{\boldsymbol{n}}$. However, the $\boldsymbol{Q}$ tensor description does not have this discontinuity at half-integer defects, since for uniaxial nematics $Q_{ij} = n_i n_j - \delta_{ij}/2$. Thus for this investigation of the energetic preference between the two configurations, we solve the Euler-Lagrange equations for

the $\boldsymbol{Q}$-tensor in two dimensions:

$$-\nabla^2 Q_{ij} + \left(\frac{A\ell^{*2}}{\tilde{K}}\right) Q_{ij} + \left(\frac{C\ell^{*2}}{\tilde{K}}\right) Q_{ij}Q_{kl}Q_{kl} = 0. \tag{5.17}$$

Where $\tilde{K}$ is the elastic constant, ℓ^* is the particle radius, and A and C are phenomenological constants, as discussed in Chapter 2. Equation (5.17) was solved numerically using a damped Newton's method algorithm [59]. Figure 5.7a plots the stable equilibrium solution, with two (-1/2) defects at opposite ends of the particle. We find that for a variety of core sizes set by $\sqrt{A/K} < \ell^*$, the algorithm iterates away from an initial guess near the single defect solution, with the (-1) defect splitting into two $(-1/2)$ defects, thus confirming the stability of the quadrupolar structure relative to the dipolar structure.

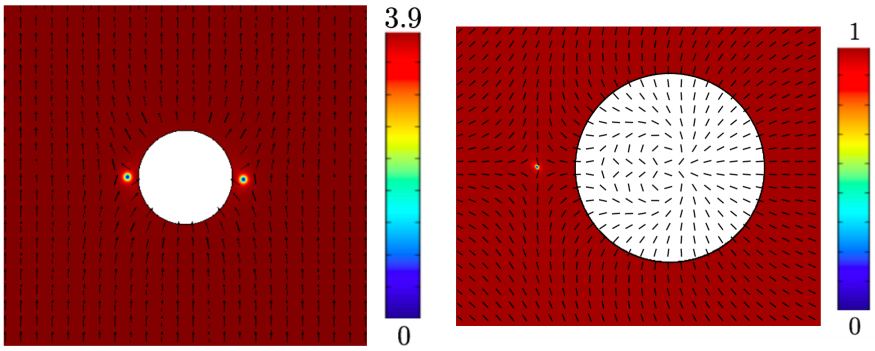

(a) (b)

Figure 5.7: (a) Numerical solution to Eq. (5.17) for one particle with homeotropic anchoring suspended in a square domain with uniform alignment on the outer walls. The director $\hat{\boldsymbol{n}}$ is plotted as black arrows, while the quantity $Q_{11}^2 + Q_{12}^2$ is plotted in color. We see the solution has two (-1/2) defects on either side of the suspended particle. (b) Comparison of the analytical and numerical solutions for $\hat{\boldsymbol{n}}$ corresponding to a particle-defect pair. Plotted in color is the dot product of the numerical solution minimizing Oseen-Frank energy with regularization term with core size $\delta = 0.01$, and the analytical solution $\hat{\boldsymbol{n}} = (\cos\theta, \sin\theta)$, where $\theta(\boldsymbol{r})$ is given by Eq. (5.10). The analytic director field is also plotted as thin lines for comparison. The two solutions align everywhere except within the defect core, where the magnitude of the numerical solution approaches zero while the magnitude of the analytic director remains uniform.

We see that the dimensionality of space plays a significant role in the relative energetic stability of the dipolar and quadrupolar director configurations. Furthermore, since the quadrupolar structure is energetically preferred in two dimensions and contains half-integer defects, investigating the two-dimensional electrokinetics of the minimum energy configuration requires the use of the $\boldsymbol{Q}$-tensor order parameter. However, as discussed in Chapter 2, it is more challenging to relate $\boldsymbol{Q}$-tensor numerical studies to experimental results, since it requires experimental knowledge of the structure of defect cores. Furthermore, two-dimensional studies using the quadrupolar solution may not provide much insight into thin-film experiments, since the director field is dipolar in most experiments, and because electrophoretic systems with quadrupolar symmetry do not produce net particle motion [5]. Therefore, we choose to numerically investigate thin film LCEK using the polar vector field $\hat{\boldsymbol{n}}$ (i.e. $\hat{\boldsymbol{n}}(\boldsymbol{r}) \neq -\hat{\boldsymbol{n}}(\boldsymbol{r})$), allowing us to more directly compare viscosities and elastic constants to experiments, and giving us the director structure most similar to experiments. While the solution for the polar vector field $\hat{\boldsymbol{n}}$ and the three-dimensional solution are both dipolar, it is important to note that the dipole term decays as r^{-1} in two dimensions, and as r^{-2} in three dimensions. We will discuss the consequences of this difference in far-field director behavior in Sec. 5.4.2.

Regularization near director singularities

As discussed above, the director field and the elastic energy density diverge at topological defects. This issue presents particular challenges in numerical modeling, as numerical methods are not well equipped to handle singular solutions and diverging energies. In order to compute director configurations and their dynamics on domains that include defects, we relax the normalization constraint, $|\hat{\boldsymbol{n}}|^2 = 1$, and instead introduce a free energy term term $f^*_{reg} = K/(4\delta^{*2})(\boldsymbol{n}^2-1)^2$ which penalizes deviations in the magnitude of $\boldsymbol{n}$. Here K is the average of the Frank elastic constants and δ^* is related to the size of the defect core. The total free energy f is the sum of f_{reg} and the Osseen-Frank elastic energy, f_{OF}. In the one-constant approximation, the molecular field $\boldsymbol{h}^0$ is then,

$$h^0_i = \frac{\partial}{\partial x_j}\frac{\partial f}{\partial(\partial_j n_i)} - \frac{\partial f}{\partial n_i} = \nabla^2 n_i - \frac{1}{\delta^2}(\boldsymbol{n}^2-1)n_i, \tag{5.18}$$

where $\delta = \delta^*/\ell^*$.

Recall the balance of torques, Eq. (4.5), is,

$$\boldsymbol{n} \times \boldsymbol{h}^0 - \mathrm{Er}\left(\boldsymbol{n} \times \boldsymbol{h'} - \frac{\Delta\epsilon}{\epsilon_\perp}(\boldsymbol{n}\cdot\boldsymbol{E})(\boldsymbol{n}\times\boldsymbol{E})\right) = 0, \tag{5.19}$$

where $h' = \gamma_1 N_i + \gamma_2 A_{ij} n_j$ and $N_i = (\Omega/W)\partial_t n_i + v_j \partial_j n_i - \Omega_{ij} n_j$. The inclusion of the regularization term does not change this equation, as $\boldsymbol{n}\times\boldsymbol{n} = 0$. In the set of governing equations, we do not make use of the director normalization condition, rather we allow the equation for the balance of torques to include changes in the magnitude of $\boldsymbol{n}$,

$$\boldsymbol{n}\cdot\boldsymbol{h^0} - \mathrm{Er}\left(\boldsymbol{n}\cdot\boldsymbol{h'} - \frac{\Delta\epsilon}{\epsilon_\perp}(\boldsymbol{n}\cdot\boldsymbol{E})^2\right) = 0. \tag{5.20}$$

Equations (5.19) and (5.20) can be written more compactly as $\boldsymbol{h^0} - \mathrm{Er}(\boldsymbol{h'} + \tilde{\epsilon}(\boldsymbol{n}\cdot\boldsymbol{E})\boldsymbol{E}) = 0$, where $\tilde{\epsilon} = \Delta\epsilon/\epsilon_\perp$. Note that the addition of f_{reg} does not change Eq. (5.19), since the new term in $\boldsymbol{h^0}$ is parallel to $\boldsymbol{n}$. Additionally, Eq. (5.20) reduces to the original normalization condition,$|\boldsymbol{n}|^2 = 1$, for $r \gg \delta$. Thus we expect this regularized director to produce the same results as the normalized director away from defect cores.

Figure 5.7b plots the dot product of the analytic and regularized ($\delta = 0.01$) numerical director solutions, with the analytic solution also plotted as thin lines for comparison. We see that despite the regularization condition and the fact that the numerical solution is on a finite cell and Eq. (5.10) assumes an infinite domain, the numerical solution agrees with the analytical solution everywhere except near the defect core, where the numerical magnitude approaches zero while the analytical magnitude remains constant.

For a disc with tangential anchoring, the solutions to $\theta(\boldsymbol{r})$ are the same as the homeotropic case but rotated everywhere by $\pi/2$. Since $\hat{\boldsymbol{n}} = -\hat{\boldsymbol{n}}$, there is no equivalent to a boojum on the surface of a disc. However, if we remove this condition, making $\hat{\boldsymbol{n}}$ a polar vector, then one-dimensional boojum-like singularities can exist on the surface of a disc, at places where $\hat{\boldsymbol{n}} \to -\hat{\boldsymbol{n}}$.

To create a two-dimensional analog to a particle with boojum surface defects, we solve for the polar field $\hat{\boldsymbol{n}}$ with particle boundary conditions $\theta(1,\phi) = (\phi \mod \pi) - \pi/2$, which are discontinuous at $x = \pm 1$, and $\theta(r \to \infty, \phi) \to 0$. The solution for these boundary conditions involves a $(+2)$ image defect at the origin and two (-1) defects at $x = \pm 1$, as shown in Fig. 5.8. Note that by rotating the solution about $y = 0$, one

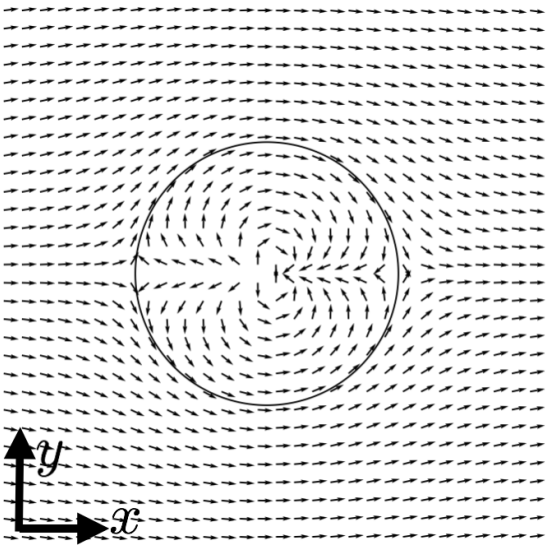

Figure 5.8: Analytic solution for polar director field in a two-dimensional analog to a sphere with tangential anchoring. We create a one-dimensional analog to a boojum with the boundary condition $\theta(1, \phi) = (\phi \mod \pi) - \pi/2$, which is discontinuous at $x = \pm 1$. The solution consists of a $(+2)$ image defect at the origin and (-1) defects at $x = \pm 1$, as shown in the figure. This configuration is used to model particles with tangential anchoring in thin films.

produces a director field on the surface which matches that of a spherical particle with tangential anchoring. Thus we use this configuration to model two dimensional flows around particles with tangential anchoring.

5.4 LCEK of a single particle-defect pair

5.4.1 Mechanism for Particle Mobility

Having described the equilibrium configurations of a particle suspended in a nematic fluid, we next consider the electrokinetic behavior of such suspensions. We begin by investigating the two-dimensional electrokinetics of a disc-shaped particle with homeotropic anchoring at its surface, a companion (-1) point defect, and uniform anchoring at cell boundaries. We consider an applied AC field that is either parallel or perpendicular to the elastic dipole $\boldsymbol{p}$ of the particle-defect pair.

In experiments, suspended particles are free to move, and the electrophoretic particle velocity is a key feature of nematic colloids [44]. To simplify the problem both analytically and numerically, however, the particle remains fixed in our study, with no-slip boundary conditions for velocity at the particle surface. The corresponding motion if the particle were free can be determined by finding the force on the fixed particle, which is obtained by integrating the normal component of the stress over the surface of the particle,

$$F_i = \oint T_{ij}\nu_j dS, \tag{5.21}$$

where $T_{ij} = -p\delta_{ij} + \mathrm{Er}^{-1}T^e_{ij} + \tilde{T}_{ij}$ is the stress tensor and $\boldsymbol{\nu}$ is the unit normal to the particle surface. We scale lengths by particle radius, $\ell^* = a^* = 4.8\mu m$; the remaining scalings are the same as in Chapter 4. We solve the governing equations, Eqs. (4.1)-(4.5), on a domain of dimensionless size $L = 48$. We assign the particle a dielectric constant of $\epsilon_p = 0.3\bar{\epsilon}$. The remaining parameters are listed in Table 5.1.

The electrokinetic behavior of this system is more complex than the patterned thin-film studies of Chapters 2-4 involving patterned director patterns for a number of reasons. First, the suspended particle is a physical barrier which distorts the fluid flow induced in the nematic. The particle itself is also polarizable, which implies that in the

Parameter	Value	Comment
ω	5π rad/s	Applied field frequency
E_0	19.75 mV/μm	Applied field amplitude
$\epsilon_\perp$	6	Perpendicular dielectric permittivity
$\Delta\mu/\mu_\perp$	0.4	Relative mobility anisotropy
$\Delta\epsilon/\epsilon_\perp$	0	Relative dielectric anisotropy

Table 5.1: Physical constants used in numerical calculations in Sec. 5.4.1, with all others listed in Table 2.1

presence of an applied field, the polarization of the particle can lead to charge accumulation at the particle surface through induced-charge electrokinetic (ICEK) mechanisms [2]. Our system is much more complex than induced-charge electrokinetics studies of colloids in isotropic fluids since, as we have seen, topological constrains on the director field lead to charge separation in the nematic through mobility and dielectric anisotropies. This is in addition to any charge separation due to polarization of solid surfaces (which is a weak effect in the cases considered).

This section investigates the effect of each of these added complexities on electrokinetic flow. To further simplify our study, we will initially use the one-constant approximation for elasticity, $K_1 = K_3 = K$ (recall in two dimensions there is no twist, K_2). We will discuss the consequences of $K_1 \neq K_3$ in Sec. 5.4.4. We also first assume elastic torques dominate over viscous torques (Er $\ll 1$), and will consider the effects of backflow (Er ~ 1) in Sec. 5.4.5. Under these assumptions, the director field $\boldsymbol{n}$ decouples from the remaining variables, and satisfies,

$$-\nabla^2 n_i + \frac{1}{\delta}(|\boldsymbol{n}|^2 - 1)n_i = 0. \tag{5.22}$$

The decoupling of $\boldsymbol{n}$ allows us to simplify the numerical problem by solving the governing equations in two steps: first, we solve Eq. (5.22) to find the director field corresponding to elastic equilibrium. Next we solve Eqs. (4.1)-(4.4) with the elastic equilibrium solution for $\boldsymbol{n}$ just obtained as given.

Furthermore, as shown in Chapter 2, elastic equilibrium implies the divergence of the elastic stress can be written as $\partial_j T^e_{ij} = -\partial_i f$. Thus we define $\tilde{p} = p + f/\mathrm{Er}$ and

numerically solve [51],

$$-\nabla\tilde{p} + \nabla\cdot\tilde{\boldsymbol{T}} + \rho\boldsymbol{E} = 0. \tag{5.23}$$

We consider systems in which the imposed AC field is parallel to the elastic dipole $\boldsymbol{p}$, and ones in which the field is perpendicular to $\boldsymbol{p}$. In Figs. 5.9 and 5.10, we plot the instantaneous charge density and time-averaged velocity for systems with the electric field parallel and perpendicular to $\boldsymbol{p}$, respectively. The velocity average is computed over a period of the applied field, after allowing for transient effects to die down. We compute the force on the particle, Eq. (5.21), and find that the force points opposite $\boldsymbol{p}$ for the parallel field case and along $\boldsymbol{p}$ in the transverse field case. The force is always parallel to $\boldsymbol{p}$, even when the imposed field is perpendicular to $\boldsymbol{p}$. Thus if the particles were free to move, they would move parallel to $\boldsymbol{p}$ regardless of the field direction.

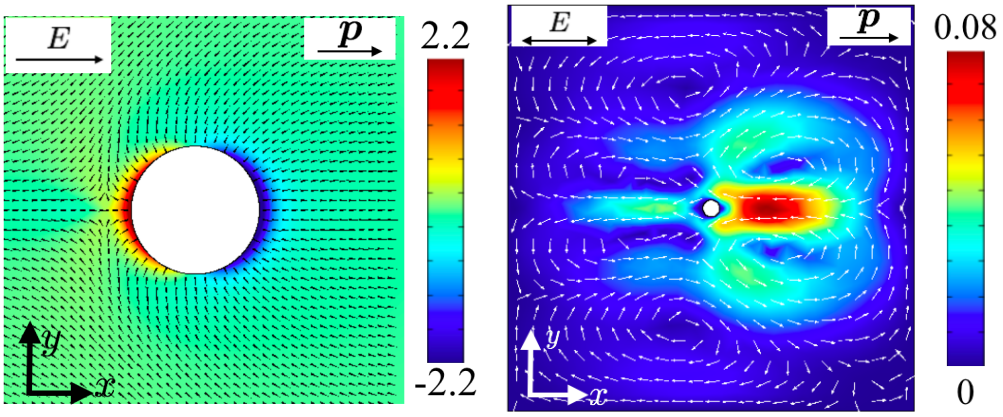

Figure 5.9: Numerical charge density at $t = 2\pi$ (a) and time-averaged velocity (b) of electrokinetic flow around a two-dimensional particle with electric field parallel to elastic dipole. The electrokinetic force on the particle, computed using Eq. (5.21), is found to point opposite the elastic dipole $\boldsymbol{p}$.

As a reference, and in order to further investigate the role of the director configuration on the charge and velocity distributions of Figs. 5.9 and 5.10, we have computed the corresponding electrokinetic flows for a fixed pair of isolated disclinations – one with charge $(+1)$ representing the particle, and another of charge (-1) representing the companion defect. The two defects are separated by a distance of $\sqrt{2}$, equal to the distance between the (-1) defect and the center of the particle at equilibrium in two-dimensions.

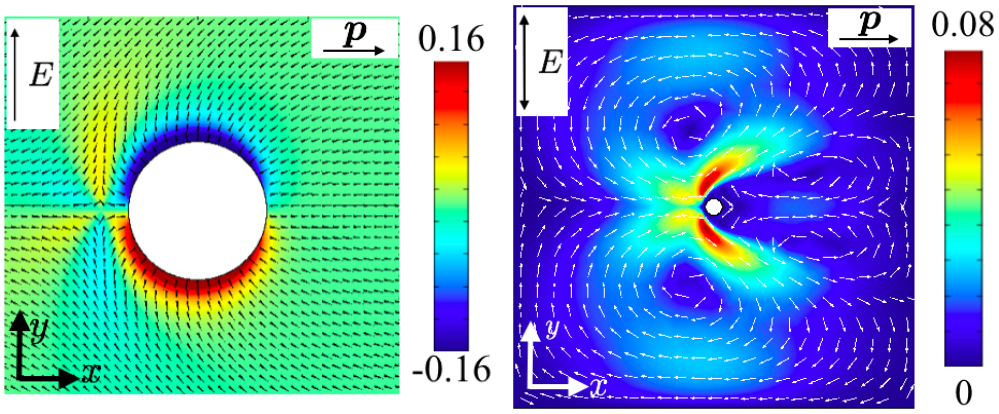

Figure 5.10: Numerical charge density at $t = 2\pi$ (a) and time-averaged velocity (b) of electrokinetic flow around a two-dimensional particle with electric field perpendicular to elastic dipole. The electrokinetic force on the particle, computed using Eq. (5.21), is found to point along the elastic dipole $\boldsymbol{p}$.

This system is topologically equivalent to the particle-defect system, yet since it has no suspended particle, the effects of particle polarization and no-slip boundary conditions at the particle surface will not be present. Therefore, by comparing the two studies, we can determine how the mechanisms for electrokinetic flow in colloidal systems compares with the mechanisms for systems of disclinations alone. We begin by comparing the two systems with the applied field parallel to the elastic dipole $\boldsymbol{p}$, and then we investigate the results with transverse fields.

Electric Field Parallel to Elastic Dipole

The numerical charge density for a $(-1, +1)$ disclination pair with applied field parallel to $\boldsymbol{p}$ is plotted in Fig. 5.11 alongside the corresponding charge density for the particle-defect pair. In Fig. 5.11a, the magnitude of the charge density near the $(+1)$ disclination is approximately the same as near the (-1) disclination. This is contrasted by the charge density near the suspended particle, Fig. 5.11b, where the charge density near the particle is much larger than near the (-1) defect. We anticipate this difference is due to the polarization of the suspended particle. Isotropic electrokinetics predicts charge screening within a Debye length λ_D^* from the particle [11]. For the values considered,

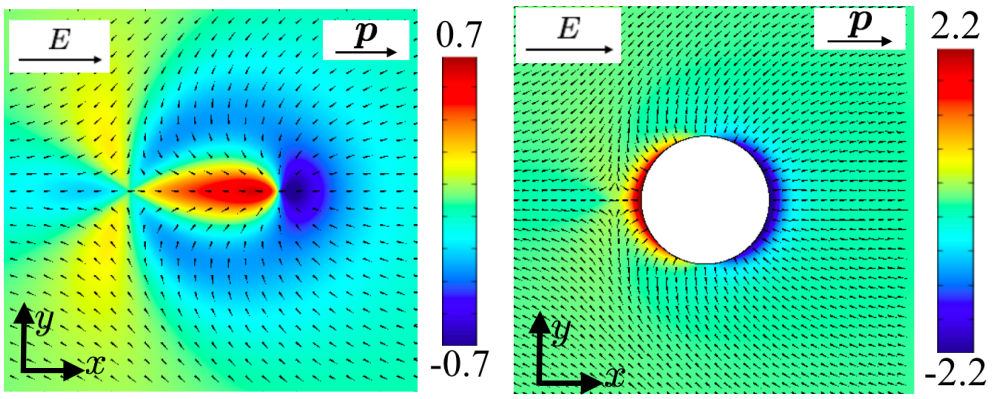

(a) (b)

Figure 5.11: Numerical charge density at $t = 2\pi$ for a $(-1, +1)$ disclination set, (a), and a particle-defect pair, (b).

$\lambda_D^* = 1.4\ \mu m = 0.29\ell^*$, so relative to the particle size the screening length is not small. Furthermore, near both a single $(+1)$ disclination and a polarized particle in an isotropic fluid, the charge density is dipolar, with the same dipole orientation. Therefore, near the particle surface both the LCEK and ICEK effects will contribute to accumulation of positive charge on the left side of the particle, and negative charge on the right, leading to the larger charge density shown in Fig. 5.11b.

Despite the difference in scale, we notice some similarities in the structure of the charge density. In particular, there are six charge lobes near the (-1) defect in both plots, with the sign of each lobe in Fig. 5.11b matching its corresponding lobe in Fig. 5.11a. Furthermore, since we expect the thickness of the charge layer induced by the particle polarization to be λ_D^*, charge separation at $r \gg 1$ will be due to LCEK effects only.

We can further quantify the far-field charge density at $r \gg 1$ using the techniques developed in Chapter 4. Recall that to first order in Δ, and assuming uniform total concentration, the equation for charge density due to LCEK is,

$$\Omega \frac{\partial \rho_\parallel}{\partial t} = \gamma \nabla^2 \rho_\parallel - \rho_\parallel + (\tilde{\epsilon} - \tilde{\mu}) \cos(t) \partial_i (n_i n_x), \tag{5.24}$$

where $\tilde{\epsilon} = \Delta\epsilon/\epsilon_\perp$, $\tilde{\mu} = \Delta\mu/\mu_\perp$, $\gamma = (\lambda_D^*/\ell^*)^2$, and $\Omega = \omega\tau_\rho$. If $\hat{\boldsymbol{n}} = (\cos[\theta(\boldsymbol{r})], \sin[\theta(\boldsymbol{r})])$, the equilibrium director angle $\theta(\boldsymbol{r})$ for a particle-defect pair is given in Eq. (5.10), while

for the $(-1,+1)$ set, the director angle is,

$$\theta^{(d)}(\boldsymbol{r}) = \mathrm{Im}\left(\log\left(\frac{z}{z+\sqrt{2}}\right)\right). \tag{5.25}$$

With the assumption of $\theta(\boldsymbol{r})$ fixed, Eq. (5.24) is a linear, inhomogeneous partial differential equation, whose solution can be found by use of a Green's function, as derived in Chapter 4. However, the particular form of $\theta(\boldsymbol{r})$ for a particle defect pair, Eq. (5.10), or even a $(-1,+1)$ set, Eq. (5.25), is very complicated, and thus the inhomogeneous term in Eq. (5.24) has a very complex dependency on position. Furthermore Eq. (5.24) does not account for the accumulation of charge due to particle polarization. Thus an analytic solution to the charge density at $r \sim 1$ is not known.

Instead of finding a complete solution, we note that diffusion is negligible far from disclination cores as discussed in Chapter 4, and the charge density may be written as,

$$\rho_{\parallel}(\boldsymbol{r},t) = (\tilde{\epsilon}-\tilde{\mu})\,\frac{\cos(t-\delta)}{2\sqrt{1+\Omega^2}}\left(\frac{\partial}{\partial x}\cos(2\theta(\boldsymbol{r})) + \frac{\partial}{\partial y}\sin(2\theta(\boldsymbol{r}))\right), \qquad \tan\delta = \Omega, \tag{5.26}$$

For the $(-1,+1)$ defect pair, the charge density is,

$$\rho_{\parallel}^{(d)}(\boldsymbol{r},t) = (\tilde{\epsilon}-\tilde{\mu})\,\frac{\cos(t-\delta)}{\sqrt{1+\Omega^2}}\left[\frac{2\cos(\phi-2\phi_{-1})}{r} - \frac{\cos(2\phi-3\phi_{-1})}{r_{-1}}\right], \tag{5.27}$$

where $r=\sqrt{x^2+y^2}$, $\tan(\phi)=y/x$, $r_{-1}=\sqrt{(x+\sqrt{2})^2+y^2}$, and $\tan\phi_{-1}=y/(x+\sqrt{2})$. Note that the behavior of the far-field charge density is independent of the behavior at $r \sim 1$. This is because the Laplacian term in Eq. (5.24) is negligible at $r \gg 1$, and therefore the far-field solution contains no homogeneous terms that need to be "matched" to an inner solution.

For the particle-defect pair, we combine Eqs. (5.10) and (5.24) to find the charge

density,

$$\rho_{\parallel}^{(p)}(\boldsymbol{r},t) = (\tilde{\epsilon}-\tilde{\mu})\,\frac{\cos(t-\delta)}{\sqrt{1+\Omega^2}}\left[\frac{2\cos(3\phi-2\phi_{-1}-2\tilde{\phi}_{-1})}{r}\right.$$
$$-\frac{\cos(4\phi-3\phi_{-1}-2\tilde{\phi}_{-1})}{r_{-1}}$$
$$\left.-\frac{\cos(4\phi-2\phi_{-1}-3\tilde{\phi}_{-1})}{\tilde{r}_{-1}}\right], \tag{5.28}$$

where in addition to r, ϕ, r_{-1}, and ϕ_{-1} defined above, $\tilde{r}_{-1} = \sqrt{(x+1/\sqrt{2})^2+y^2}$ and $\tan\tilde{\phi}_{-1} = y/(x+1/\sqrt{2})$.

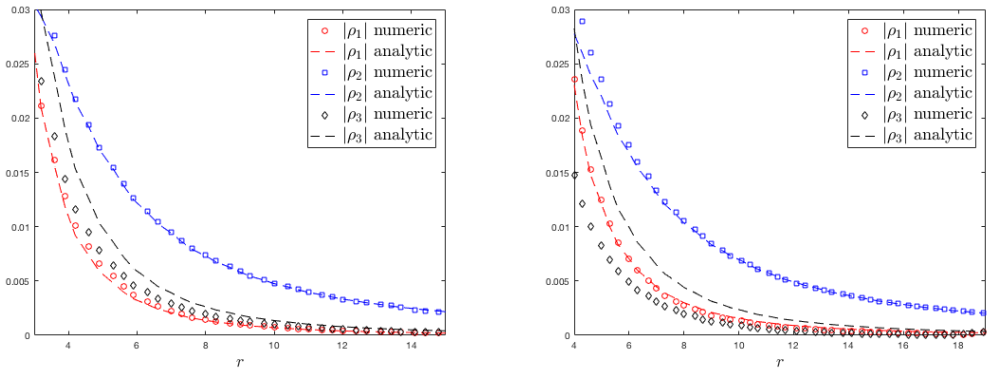

(a) $(-1,+1)$ Disclination Set (b) Particle-Defect Pair

Figure 5.12: Magnitude of the first three Fourier components of charge density for a (-1,+1) disclination set, (a), and a particle-defect pair, (b), at $t = 4\pi$. Numerically obtained values are plotted as points, while the analytic solutions at $r \gg \gamma^{-1/2}$, Eqs. (5.27) and (5.28) are plotted as dashed lines. The numerical solution approaches the analytic approximations as r increases, and at large r, we see that $|\rho_2|$ is much larger than the others, as expected.

Note that at $r \gg 1$, the leading order behavior of Eq. (5.27) is,

$$\rho_{\parallel}^{(d)}(r\gg 1,\phi,t) \approx (\tilde{\epsilon}-\tilde{\mu})\,\frac{\cos(t-\delta)}{\sqrt{1+\Omega^2}}\,\frac{\sqrt{2}\cos(2\phi)}{r^2}, \tag{5.29}$$

while the leading order behavior of Eq. (5.28) is,

$$\rho_{\parallel}^{(p)}(r \gg 1, \phi, t) \approx (\tilde{\epsilon} - \tilde{\mu}) \frac{\cos(t-\delta)}{\sqrt{1+\Omega^2}} \frac{3\cos(2\phi)}{\sqrt{2}r^2}. \tag{5.30}$$

Thus at large distances the charge behavior of both systems is the same, with $\rho_{\parallel}^{(p)} = (3/2)\rho_{\parallel}^{(d)}$.

In order to compare the analytical and numerical charge densities, we may write $\rho_{\parallel}$ as a Fourier series, $\rho_{\parallel}(r, \phi, t) = \sum_n \rho_n(r, t)e^{in\phi}$. Figure 5.12a plots the numerical magnitudes $|\rho_1|, |\rho_2|, |\rho_3|$, at $t = 2\pi$ as a function of r for the $(-1, +1)$ set, along with the corresponding analytical values from Eq. (5.27). Similarly, Fig. 5.12b plots the first three Fourier components for the particle-defect pair, both numerically-obtained and from Eq. (5.28). In both plots we see that as r increases, the numerical solution approaches the analytical solution, and the component $|\rho_2|$ decays more slowly than the other components, dominating the charge behavior at large distances.

The angular structure of the charge density at $r \gg 1$ is qualitatively different than near defects or particle boundaries. As discussed in Chapter 3, the angular structure of a single $(+1)$ defect has two lobes, ($|\rho_1|$ large), while a single (-1) defect has six charge lobes ($|\rho_3|$ large). Figures. 5.9a and 5.11a show two charge lobes near the particle and $(+1)$ defect, respectively, and both show six charge lobes near the (-1) defect. Thus the charge behavior near defects and particle boundaries matches the structure of single disclinations, while at $r \gg 1$ the director field is dipolar, and the second angular harmonic dominates.

To summarize, the charge density near a particle-defect pair is complicated, involving director distortions, charge diffusion diffusion, and particle polarization effects. At distances much larger than a Debye length from the particle surface or the defect core, the charge density is determined by LCEK only, and can be written in an analytic form which agrees well with the numerical solution. At very large distances, the charge density matches that of a $(-1, +1)$ disclination set, differing only by a factor of $(3/2)$.

Velocity Field

While the charge density fields of the particle-defect pair and the $(-1, +1)$ disclination are similar, the velocity fields, plotted in Fig. 5.13, are qualitatively very different, even

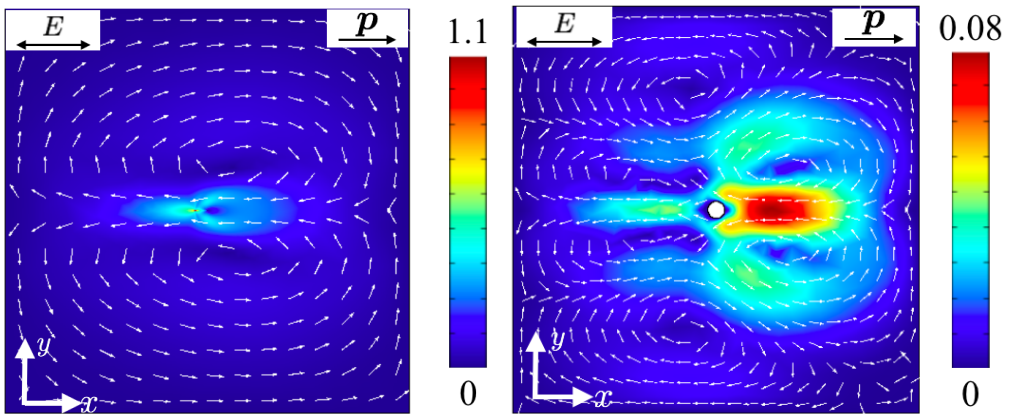

Figure 5.13: Numerical velocity fields for a (-1,+1) disclination set, (a), and a particle-defect pair, (b), averaged over a period of the applied field. While the director fields in both systems are topologically equivalent, the presence of the particle boundary leads to a qualitatively different flow, with two vortices in (a) and six vortices in (b)

at $r \gg 1$. Near the disclination set and the particle-defect pair the flow direction is the same (to the left, toward the (-1) defect), but six vortices are seen in Fig. 5.13b, while only two appear in Fig. 5.13a. Thus the presence of the particle has a more significant effect on the far-field velocity than the far-field charge density.

We can explore the origins of these differences by approximating the hydrodynamics of a the nematic with those of a Newtonian fluid with body force $\rho\boldsymbol{E}$,

$$-\nabla p + \nabla^2 \boldsymbol{v} + \rho \boldsymbol{E} = 0 \tag{5.31}$$

To find the velocity for the $(-1,+1)$ disclination system , we solve Eq. (5.31) on a disc of radius $R \gg 1$, with no-slip boundary conditions at $r = R$. To find the velocity for the particle-defect system, we solve Eq. (5.31) on an annulus with unit inner radius and outer radius $R \gg 1$, with no-slip boundary conditions at $r = 1$ and $r = R$.

In order to better investigate the difference in angular structure between the two systems, we write the body force in Eq. (5.31) as a Fourier series; specifically, we write $\rho\boldsymbol{E} = \sum_n \boldsymbol{f}_n(r,\phi,t)$, where,

$$\boldsymbol{f}_n = f_n^{(r)}(r,t)e^{in\phi}\hat{\boldsymbol{r}} + f_n^{(\phi)}(r,t)e^{in\phi}\hat{\boldsymbol{\phi}} \tag{5.32}$$

Then using linearity, we write the solutions for pressure and velocity as $\boldsymbol{v}(r,\phi,t) = \sum_n \boldsymbol{v}_n(r,\phi,t)$, $p(r,\phi,t) = \sum_n p_n(r,\phi,t)$, where,

$$\boldsymbol{v}_n = v_n^{(r)}(r,t)e^{in\phi}\hat{\boldsymbol{r}} + v_n^{(\phi)}(r,t)e^{in\phi}\hat{\boldsymbol{\phi}}, \tag{5.33}$$

$$p_n = p_n(r,t)e^{in\phi}, \tag{5.34}$$

and $\boldsymbol{v}_n$, p_n solve,

$$-\nabla p_n + \nabla^2 \boldsymbol{v}_n + \boldsymbol{f}_n = 0, \;\; \nabla \cdot \boldsymbol{v}_n = 0 \tag{5.35}$$

We may furthermore define the stream function ψ_n such that $\nabla \times (-\psi_n \hat{\boldsymbol{z}}) = \boldsymbol{v}_n$. Taking the curl of Eq. (5.35), one finds ψ_n solves,

$$\nabla^4 \psi_n + \nabla \times \boldsymbol{f}_n = 0 \tag{5.36}$$

No slip boundary conditions at $r = R$ imply $\psi(R,\phi) = 0$, $\partial_r \psi(R,\phi) = 0$. The particle-defect system has additional no-slip conditions at the particle surface, $\psi(1,\phi) = 0$, $\partial_r \psi(1,\phi) = 0$.

Having formulated the equations for pressure and stream function at each harmonic n, one could use the method of matched asymptotic expansions to investigate the differences in flow field between the paricle-defect and $(-1,+1)$ disclination systems. For either system, using Eqs. (5.29) and (5.30), the electrostatic body force at $r \gg 1$ is,

$$\rho_{\parallel} \boldsymbol{E}_{\parallel} \approx (\tilde{\epsilon} - \tilde{\mu}) \frac{\cos^2 t}{1+\Omega^2} \frac{\alpha}{2r^2} [\hat{\boldsymbol{r}}(\cos\phi + \cos(3\phi)) + \hat{\boldsymbol{\phi}}(\sin\phi - \sin(3\phi))] \tag{5.37}$$

where $\alpha = \sqrt{2}$ for the $(-1,+1)$ disclination set, and $\alpha = 3/\sqrt{2}$ for the particle-defect pair. Using Eq. (5.32), at $r \gg 1$,

$$\boldsymbol{f}_1^{\parallel} = (\tilde{\epsilon} - \tilde{\mu}) \frac{\cos^2 t}{1+\Omega^2} \frac{\alpha}{2r^2} (\hat{\boldsymbol{r}} \cos\phi + \hat{\boldsymbol{\phi}} \sin\phi), \tag{5.38}$$

$$\boldsymbol{f}_3^{\parallel} = (\tilde{\epsilon} - \tilde{\mu}) \frac{\cos^2 t}{1+\Omega^2} \frac{\alpha}{2r^2} (\hat{\boldsymbol{r}} \cos(3\phi) - \hat{\boldsymbol{\phi}} \sin(3\phi)), \tag{5.39}$$

Define $\xi = r/R$. Then the "outer solutions" $\psi_1^{(o)}$, $p_1^{(o)}$, $\psi_3^{(o)}$ and $p_3^{(o)}$, satisfying the no-slip condition at $r = R$ are,

$$\begin{aligned}\psi_1^{(o)}(\xi,\phi,t) = Q^{(o)}(t)R\left[\left(a_1\xi^3 + b_1\xi - (4a_1+2b_1)\xi\log\xi - (a_1+b_1)\xi^{-1}\right)\cos\phi\right.\\ \left.+\left(c_1\xi^3 + d_1\xi - (4c_1+2d_1)\xi\log\xi - (c_1+d_1)\xi^{-1}\right)\sin\phi\right],\end{aligned} \tag{5.40}$$

$$p_1^{(o)}(\xi,\phi,t) = -\frac{Q^{(o)}(t)}{R}\left[\left(8c_1(\xi^2+1) + 4d_1 + \frac{1}{2}\right)\frac{\cos\phi}{\xi} - 4(2a_1(\xi^2+1)+b_1)\frac{\sin\phi}{\xi}\right], \tag{5.41}$$

$$\begin{aligned}\psi_3^{(o)}(\xi,\phi,t) = Q^{(o)}(t)R\left[(a_3\xi^5 + b_3\xi^3 - (4a_3+3b_3)\xi^{-1} + (3c_3+2d_3)\xi^{-3})\cos(3\phi)\right.\\ +(c_3\xi^5 + d_3\xi^3 - (4c_3+3d_3)\xi^{-1} + (3c_3+2d_3)\xi^{-3})\sin(3\phi)\\ \left.-\frac{\xi}{64}(\xi^2-1)^2\sin(3\phi)\right],\end{aligned} \tag{5.42}$$

$$\begin{aligned}p_3^{(o)}(\xi,\phi,t) = \frac{Q^{(o)}(t)}{R}\left[8\left(\left(\frac{1}{16} - 2c_3\right)\xi^6 + 4c_3 + 3d_3\right)\frac{\cos(3\phi)}{\xi^3}\right.\\ \left.+8((4-2\xi^6)a_3 + 3b_3)\frac{\sin(3\phi)}{\xi^3} + \frac{\cos(3\phi)}{4\xi}\right],\end{aligned} \tag{5.43}$$

with

$$Q^{(o)}(t) = (\tilde{\epsilon} - \tilde{\mu})\,\frac{\alpha\cos^2 t}{1+\Omega^2}. \tag{5.44}$$

The coefficients a_n, b_n, c_n, d_n would be determined by matching the outer solution to an inner solution which we do not compute. The qualitative difference between the two cases can be understood without the detailed inner solution. The last term in $\psi_3^{(o)}$ and the last term in $p_3^{(o)}$ cannot be cancelled by any combination of the other terms, due to their spatial structure. Thus these two terms will be present in the far-field solutions, while all other terms depend on the behavior of the inner solution. In particular,

unilke $\psi_3^{(o)}$ it is possible for $\psi_1^{(o)}$ to be zero, as every term is proportional to a linear combination of a_1, b_1, c_1, d_1. Therefore we find that while any system with a dipolar far-field director will have a stream function term proportional to $e^{3i\phi}$, the presence of a term proportional to $e^{i\phi}$ depends on the detailed form of the inner solution.

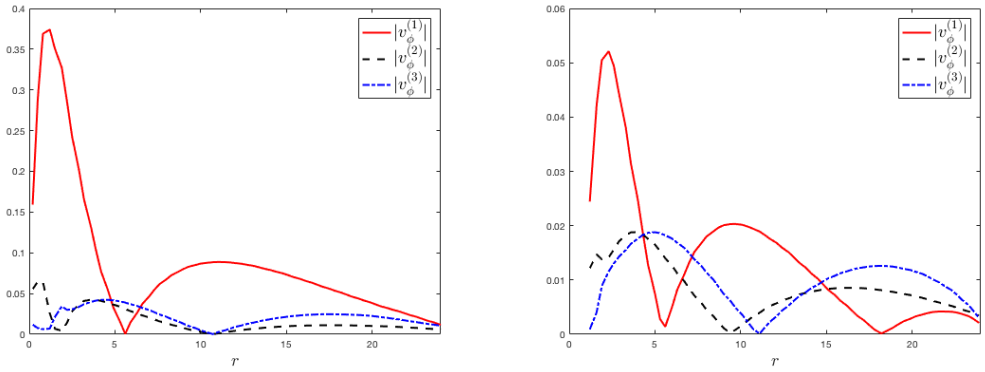

(a) (-1,+1) Disclination Set (b) Particle-Defect Pair

Figure 5.14: First three Fourier components of numerical angular velocity for a system with a (-1,+1) disclination set, (a), and a particle-defect pair, (b), averaged over a period of the field, plotted as a function of r.

It should also be noted that additional homogeneous terms $\psi_n^{(o)}$, $p_n^{(o)}$ of other harmonics $e^{in\phi}$ may be present in the full outer solutions to ψ and p. The existence of such terms depends on the nature of the inner solution only, as the far-field body force, Eq. (5.37), contains $e^{i\phi}$ and $e^{3i\phi}$ terms only. We do not write these terms explicitly for notational simplicity, but a complete investigation of the inner solution flow field would be necessary to determine if additional harmonics exist in the outer solution.

Figure 5.14 plots the magnitude of the Fourier components $|v_\phi^{(1)}|, |v_\phi^{(2)}|, |v_\phi^{(3)}|$ of the angular velocity for both director configurations as a function of r, where $\sum_n v_\phi^{(n)} e^{in\phi} = \boldsymbol{v}\cdot\hat{\boldsymbol{\phi}}$. As expected, both systems show a nonzero $|v_\phi^{(3)}|$ term at large r, but $|v_\phi^{(1)}|$ is smaller than $|v_\phi^{(3)}|$ at $r \gtrsim 20$ for the particle defect pair, while for the (-1,+1) disclination set, $|v_\phi^{(1)}|$ is larger than $|v_\phi^{(3)}|$. These results are consistent with the six vortices seen far from the particle in Fig. 5.13b, and the two vortices seen in Fig. 5.13a. Furthermore, these results show that the details of the inner solution lead to a non-negligible $|v_\phi^{(2)}|$ term even in the far-field, despite the fact that there is no $e^{2i\phi}$ term in the far-field body

force.

To summarize, while the disclination pair and the particle-defect pair are topologically equivalent and share the same far-field director orientation, the differences in their structure at $r \sim 1$ lead to very different far-field velocity behaviors. This is contrasted with the far-field charge densities of the two systems, where at $r \gg 1$ the two charge densities agree up to a constant of order unity. Thus while the system topology is enough to determine the charge behavior at long distances, the velocity depends strongly on the specifics of the director field at short distances. The difference between the charge density and velocity dependency on the inner behavior is due to differences in their far-field governing equations: At $r \gg 1$, the equation governing charge density contains no spatial derivatives, while the presence of the Laplacian term in Eq. (5.31) leads to homogeneous velocity terms that depend on the inner solution.

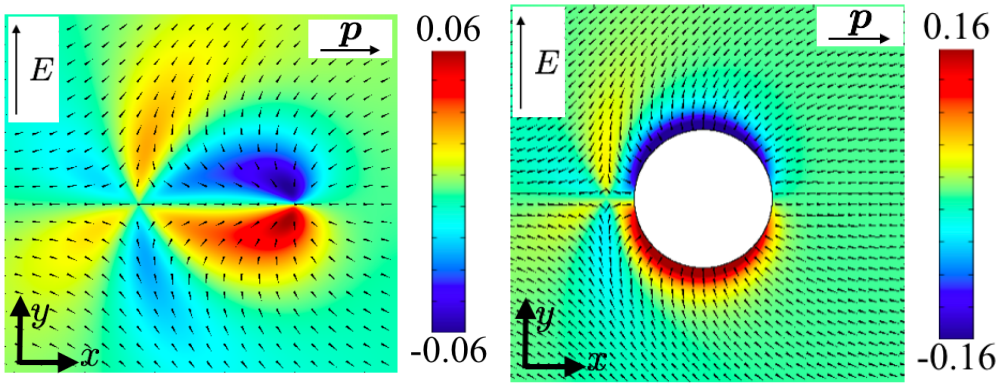

Figure 5.15: Numerical charge density at $t = 2\pi$ for a (-1,+1) disclination set, (a), and a particle-defect pair, (b), with applied field perpendicular to the elastic dipole $\boldsymbol{p}$.

Electric Field Perpendicular to Elastic Dipole

We consider next the case in which the applied field is *perpendicular* to the elastic dipole $\boldsymbol{p}$. As with the parallel field, we compare the particle-defect charge density to the that of a $(-1, +1)$ disclination pair in Fig. 5.15. We see a large accumulation of charge near the particle surface in Fig. 5.16b due to both LCEK and ICEK effects. We also see six charge lobes around the (-1) defect in both studies due to the topology of the defect

pair.

We again attempt to find an analytical solution valid away from particle boundaries and defect cores. Following a procedure similar to Chapter 4, the charge density in this region for the $(-1,+1)$ disclination system is,

$$\rho_{\perp}^{(d)}(\boldsymbol{r},t) = (\tilde{\epsilon}-\tilde{\mu})\,\frac{\cos(t-\delta)}{\sqrt{1+\Omega^2}}\left[\frac{\sin(\phi-2\phi_{-1})}{r}-\frac{\sin(2\phi-3\phi_{-1})}{r_{-1}}\right]. \tag{5.45}$$

while for the particle-defect system, the charge density is,

$$\begin{aligned}\rho_{\perp}^{(p)}(\boldsymbol{r},t) = (\tilde{\epsilon}-\tilde{\mu})\,\frac{\cos(t-\delta)}{\sqrt{1+\Omega^2}}\Bigg[&\frac{2\sin(3\phi-2\phi_{-1}-2\tilde{\phi}_{-1})}{r}\\ &-\frac{\sin(4\phi-3\phi_{-1}-2\tilde{\phi}_{-1})}{r_{-1}}\\ &-\frac{\sin(4\phi-2\phi_{-1}-3\tilde{\phi}_{-1})}{\tilde{r}_{-1}}\Bigg].\end{aligned} \tag{5.46}$$

The coordinates $r, \phi, r_{-1}, \phi_{-1}\tilde{r}_{-1}, \tilde{\phi}_{-1}$ are the same as the previous section. As was the case for the charge density with a parallel field, at $r \gg 1$, Eqs. (5.45) and (5.46) reduce to,

$$\rho_{\perp}(r\gg 1,\phi,t) \approx -\,(\tilde{\epsilon}-\tilde{\mu})\,\frac{\cos(t-\delta)}{\sqrt{1+\Omega^2}}\,\frac{\alpha\sin(2\phi)}{r^2}, \tag{5.47}$$

where $\alpha = \sqrt{2}$ for the $(-1,+1)$ defect system and $\alpha = 3/\sqrt{2}$ for the particle-defect system. Therefore we find that while the charge densities under a transverse field are different than under a parallel field, the overall conclusions are the same: near the particle surface, the particle polarization and the director distortions contribute to charge accumulation, but the far-field charge behavior differs from a $(-1,+1)$ disclination set by only a factor of 3/2.

Velocity Field

The velocity fields for both the (-1,+1) set and the particle-defect pair subject to a transverse field are plotted in Fig. 5.16. Unlike for the parallel field studies, where the qualitative features of the two velocity fields were very different, the flow structures in Fig. 5.16 are quite similar. Specifically, in both plots we see four vortices; two large

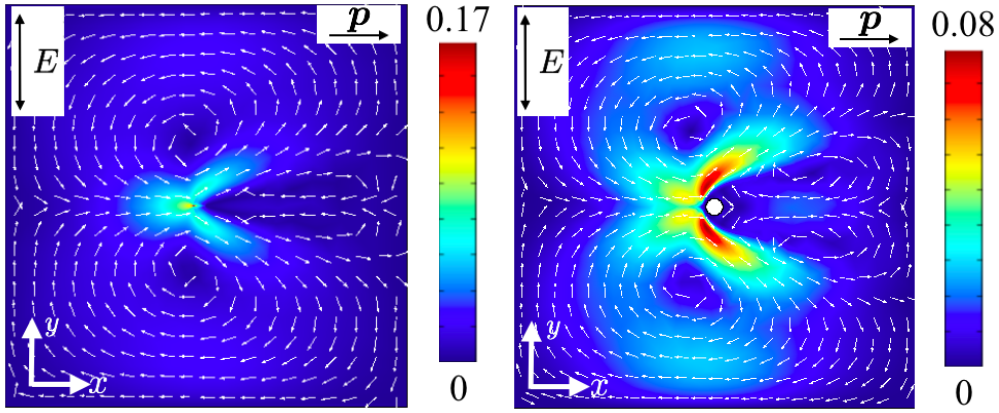

(a) (b)

Figure 5.16: Numerical velocity field for a (-1,+1) disclination system,(a), and a system containing a particle-defect pair, (b).

vortices extending across a large extent of the domain, and two thin vortices on the right side of the cell.

We again analytically investigate the "outer solution" for the velocity field in each system. Using Eq. (5.47), the electrostatic body force at $r \gg 1$ is,

$$\rho_\perp \boldsymbol{E}_\perp \approx -(\tilde{\epsilon}-\tilde{\mu})\frac{\cos^2 t}{1+\Omega^2}\frac{\alpha}{2r^2}[\hat{\boldsymbol{r}}(\cos\phi+\cos(3\phi))-\hat{\boldsymbol{\phi}}(\sin\phi-\sin(3\phi))] \tag{5.48}$$

where $\alpha=\sqrt{2}$ for the $(-1,+1)$ disclination set, and $\alpha=3/\sqrt{2}$ for the particle-defect pair. Using Eq. (5.32), we may write the Fourier components of Eq. (5.48) as,

$$\boldsymbol{f}_1^\perp = -(\tilde{\epsilon}-\tilde{\mu})\frac{\cos^2 t}{1+\Omega^2}\frac{\alpha}{2r}(\hat{\boldsymbol{r}}\cos\phi+\hat{\boldsymbol{\phi}}\sin\phi), \tag{5.49}$$

$$\boldsymbol{f}_3^\perp = (\tilde{\epsilon}-\tilde{\mu})\frac{\cos^2 t}{1+\Omega^2}\frac{\alpha}{2r}(\hat{\boldsymbol{r}}\cos(3\phi)-\hat{\boldsymbol{\phi}}\sin(3\phi)). \tag{5.50}$$

Remarkably, by comparing Eqs. (5.49)-(5.50) to Eqs. (5.38)-(5.39), one finds $\boldsymbol{f}_1^\perp=-\boldsymbol{f}_1^\parallel$, $\boldsymbol{f}_3^\perp=\boldsymbol{f}_3^\parallel$. Thus under a transverse applied field, the far-field particular solutions for pressure and velocity at $e^{i\phi}$ will be opposite those under a parallel applied field, and the solutions for either applied field will match at $e^{3i\phi}$.

We again approximate the viscous stress as Newtonian and write the momentum balance equation at the n^{th} harmonic as,

$$-\nabla p_n + \nabla^2 \boldsymbol{v}_n + \boldsymbol{f}_n^{\perp} = 0, \;\; \nabla \cdot \boldsymbol{v}_n = 0 \tag{5.51}$$

The outer solutions $\psi_1^{(o)}$, $p_1^{(o)}$, $\psi_3^{(o)}$ and $p_3^{(o)}$ for a circular domain of radius R with no-slip boundary conditions at $r = R$, are,

$$\begin{aligned}\psi_1^{(o)}(\xi,\phi,t) = Q^{(o)}(t)R\big[&\left(a_1\xi^3 + b_1\xi - (4a_1+2b_1)\xi\log\xi - (a_1+b_1)\xi^{-1}\right)\cos\phi \\ &+ \left(c_1\xi^3 + d_1\xi - (4c_1+2d_1)\xi\log\xi - (c_1+d_1)\xi^{-1}\right)\sin\phi\big],\end{aligned} \tag{5.52}$$

$$p_1^{(o)}(\xi,\phi,t) = -\frac{Q^{(o)}(t)}{R}\left[\left(8c_1(\xi^2+1) + 4d_1 - \frac{1}{2}\right)\frac{\cos\phi}{\xi} - 4(2a_1(\xi^2+1)+b_1)\frac{\sin\phi}{\xi}\right], \tag{5.53}$$

$$\begin{aligned}\psi_3^{(o)}(\xi,\phi,t) = Q^{(o)}(t)R\big[&(a_3\xi^5 + b_3\xi^3 - (4a_3+3b_3)\xi^{-1} + (3c_3+2d_3)\xi^{-3})\cos(3\phi) \\ &+ (c_3\xi^5 + d_3\xi^3 - (4c_3+3d_3)\xi^{-1} + (3c_3+2d_3)\xi^{-3})\sin(3\phi) \\ &- \frac{\xi}{64}(\xi^2-1)^2\sin(3\phi)\Big],\end{aligned} \tag{5.54}$$

$$\begin{aligned}p_3^{(o)}(\xi,\phi,t) = \frac{Q^{(o)}(t)}{R}\Bigg[&8\left(\left(\frac{1}{16} - 2c_3\right)\xi^6 + 4c_3 + 3d_3\right)\frac{\cos(3\phi)}{\xi^3} \\ &+8((4-2\xi^6)a_3 + 3b_3)\frac{\sin(3\phi)}{\xi^3} + \frac{\cos(3\phi)}{4\xi}\Bigg],\end{aligned} \tag{5.55}$$

with

$$Q^{(o)}(t) = (\tilde{\epsilon} - \tilde{\mu})\,\frac{\alpha\cos^2 t}{1+\Omega^2}. \tag{5.56}$$

Again $\xi = r/R$ and a_n, b_n, c_n, d_n are constants which depend on the inner solution. Apart from the first term in $p_1^{(o)}$, the outer solutions under a transverse applied field have the same form as the outer solutions under a parallel applied field.

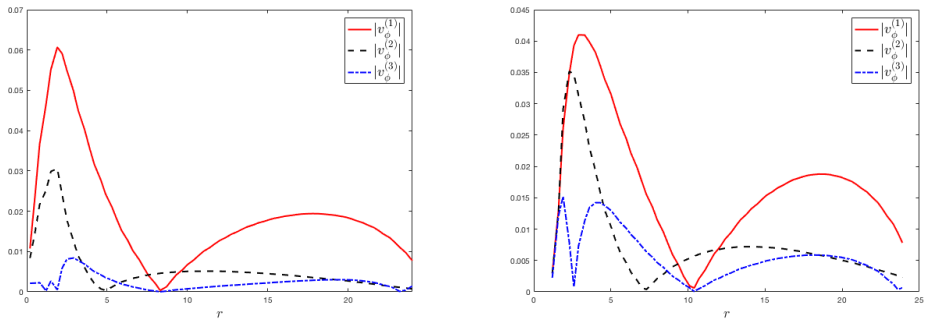

(a) $(-1,+1)$ Disclination (b)

Figure 5.17: First three Fourier velocity components for (a) a $(-1,+1)$ disclination set and (b) a particle-defect pair under an applied field perpendicular to the elastic dipole $\boldsymbol{p}$. Unlike the case of the applied field parallel $\boldsymbol{p}$, in this case the behavior at $r \sim 1$ leads to a nonzero far-field $|v_\phi^{(2)}|$ term.

Figure 5.17 plots first three Fourier components for angular velocity corresponding to the $(-1,+1)$ set and the particle defect pair. Despite the fact that the body force at $r \gg 1$ contains only $e^{i\phi}$ and $e^{3i\phi}$ terms, the details of the inner solution for both patterns leads to a nonzero $e^{2i\phi}$ velocity component in the far-field. Unlike the for the applied field parallel to the elastic dipole $\boldsymbol{p}$ depicted in Fig. (5.14), in which $|v_\phi^{(2)}|$ is always smaller than $|v_\phi^{(1)}|$ or $|v_\phi^{(3)}|$, Fig. (5.17) shows that the applied field perpendicular to $\boldsymbol{p}$ generates a velocity field in which $|v_\phi^{(2)}|$ dominates around $r \sim 10$ – corresponding with approximately the center of the two vortices on the right side of Figs. 5.16a and 5.16b. At larger distances, the two other vortices in Figs. 5.16a and 5.16b dominate, giving leading to $e^{i\phi}$ behavior, as shown in Fig. 5.17.

The difference in far-field behavior among the four cases above highlights the role of the electrokinetic behavior at $r \sim 1$ on the far-field velocity. The electrostatic force on the fluid at $r \gg 1$ allows for potentially matching velocity fields regardless of whether the system contains a $(-1,+1)$ disclination or a particle-defect pair, or whether the system is subject to a field parallel or perpendicular to the elastic dipole. However the details of the charge density and velocity at $r \sim 1$ lead to numerical flow fields that are qualitatively distinct. Under a parallel field, a disclination set produces two vortices, while a particle-defect pair produces six vortices. Under a transverse field, the disclination set and the particle-defect pair produce a qualitatively similar flow field

with four distinct vortices. We conclude that topology alone does not determine the electrokinetic behavior of a suspended particle. Rather, the behavior depends strongly on the details of the system near disclination cores and particle boundaries.

5.4.2 Effect of dimensionality and system size on LCEK velocity profile

In Sec. 5.4.1 we found that the qualitative features of the electrokinetic flow around a particle-defect pair are sensitive to the details of the specific configuration, even though the various configurations are topologically identical. In this section we consider how the dimensionality of typical particle-defect experiments affects the long distance behavior of the system.

Typical LCEK experiments consist of a particle with diameter $2a^* \sim 5 - 50\ \mu m$ placed in a cell of thickness $h^* \sim 50 - 100\ \mu m$ and lateral size $L^* \sim 10\ mm$ [5,44,79]. In these experiments, in which $h^* \ll L^*$, there is no evidence of three dimensional flows. Futhermore, except in the immediate vicinity of the particle, there is no evidence either of three dimensionality in the director field. The expectation therefore is that the long distance behavior of the charge and velocity fields are approximately two-dimensional. However, a circular particle in two dimensions corresponds to a cylinder in a thin film rather than a sphere. Furthermore, the leading order behavior of a dipolar field decays as $1/r$ in two dimensions and $1/r^2$ in three dimensions. Thus it is possible that some elements of the behavior of the experiments in thin films are not captured by either a two-dimensional model or a three-dimensional model. Rather, confinement effects in the third dimension may have to be resolved to provide even a qualitative understanding of the flows and particle motion.

In typical electrokinetic nematic colloid experiments, suspended particles are free to move, and understanding the electrophoretic velocity is the key result for applications in particle manipulation. We generally find that the direction of the force of electrokinetic origin on a spatially fixed particle in our numerical solutions does agree with the observed direction of motion of free particles in a variety of experiments with similar parameter values [44, 79, 80]. Somewhat surprisingly, the observed electroosmotic flow around a fixed particle, presented in Ref. [5], is qualitatively different than the

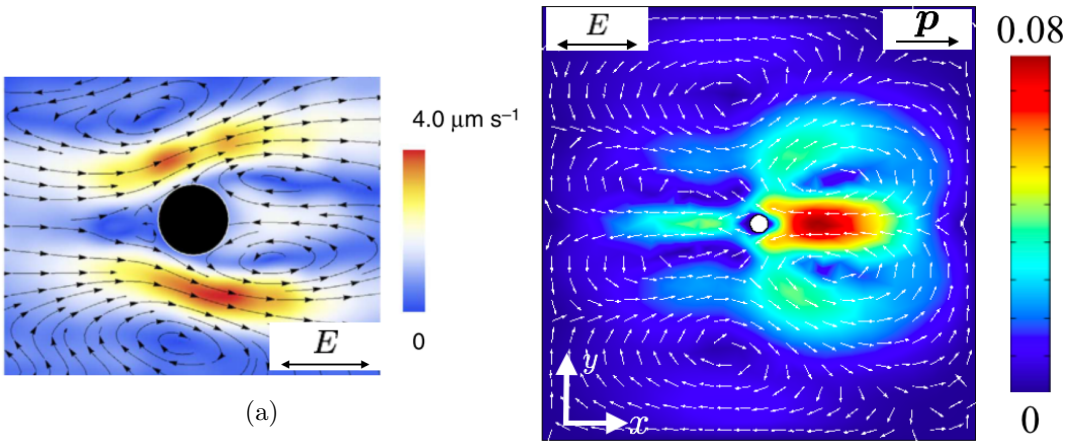

Figure 5.18: (a) Average experimental electroosmotic flow around a particle-defect pair, reproduced from Ref. [5]. The hedgehog defect is located on the left side of the particle in the figure, and the applied field is parallel to $\boldsymbol{p}$. (b) Numerical flow past a particle-defect pair in two dimensions, averaged over a period of the field, with applied field parallel to $\boldsymbol{p}$.

two-dimensional numerical velocity field, as shown in Fig. 5.18. Thus, while the two-dimensional assumption appears to produces the correct direction of particle motion, it does not appropriately characterize even the large scale of the flow structure.

We analyze two cases in order to ascertain the effects of dimensionality on the structure of the flow field. First, we compare our two-dimensional numerical results to fully three-dimensional axisymmetric numerical results described in Ref. [30]. Next, we perform a two-dimensional numerical particle-defect study similar to the one described above, except that instead of using the two-dimensional equilibrium solution for the director field, we assume that the director field is a two-dimensional slice of the fully three-dimensional variational solution from Sec 5.3.1. With this formulation, the far-field behavior of the director field is three-dimensional, yet the charge density and velocity fields are two-dimensional.

Particle-Defect Pair in $d = 3$. Axisymmetric configuration and DC field

Numerical investigations in three dimensions are limited by the large number of degrees of freedom required to adequately resolve the defect core, even when solving on an

Parameter	Value	Comment
E_0	40 mV/μm	Applied field amplitude
$\bar{D}$	5×10^{-11} m^2/s	Average diffusivity
a^*	1 μm	Particle radius
$\epsilon_\perp$	10	Dielectric permittivity perpendicular to $\hat{\boldsymbol{n}}$
$\Delta\mu/\mu_\perp$	1	Relative mobility anisotropy
$\Delta\epsilon/\epsilon_\perp$	0	Relative dielectric anisotropy

Table 5.2: Physical constants used in numerical simulations comparing an axisymmetric model using $\boldsymbol{Q}$ and a two-dimensional model using $\boldsymbol{n}$.

axisymmetric domain. To simplify the problem, our axisymmetric numerical study [30] uses a much smaller system size, $L = 10$, and a DC field with Dirichlet boundary conditions at the electrodes and Neumann boundary conditions $\nu_i \epsilon_{ij} \partial_j \Phi = 0$ on the remaining domain boundaries. The study also constrains the ionic concentrations using Dirichlet boundary conditions $c_1 = c_2 = 1/2$ at the electrodes. Furthermore, the three-dimensional study describes nematic order with the $\boldsymbol{Q}$-tensor rather than the director $\hat{\boldsymbol{n}}$.[1] In order to compare the two-dimensional model to the axisymmetric model, we solve the governing equations, Eqs. (2.49)-(2.53) , with the same domain size and boundary conditions, as well as with the same physical parameters, listed in Table 5.2.

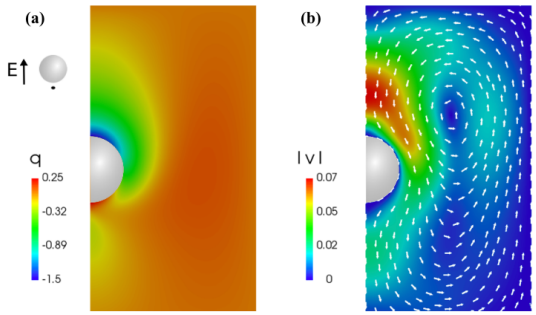

Figure 5.19: Numerical charge density and velocity for an axisymmetric particle-hedgehog configuration, with DC applied field along the elastic dipole $\boldsymbol{p}$. Note that unlike previous figures, $\boldsymbol{p}$ points vertically upward.

Despite these adjustments, a detailed comparison of the two studies is limited by

[1] The choice of $\boldsymbol{Q}$ rather than $\hat{\boldsymbol{n}}$ was made in this study order to also investigate Saturn ring configurations, which involve challenging singularities to model using $\hat{\boldsymbol{n}}$, as discussed in Sec. 5.3.2.

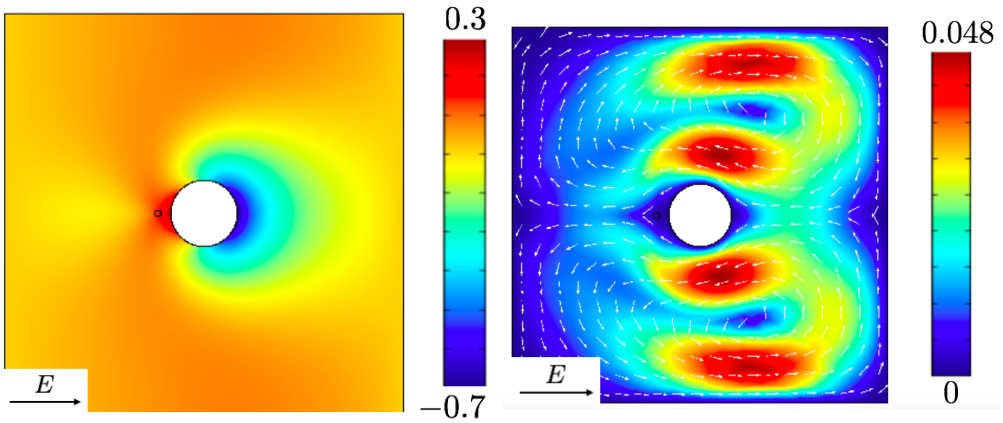

(a) (b)

Figure 5.20: (a) Charge density for system with same parameters as Fig. 5.19, except using $\hat{\boldsymbol{n}}$ in two-dimensions. The defect position is denoted by the small circle to the left of the particle. (b) Corresponding fluid velocity.

the difference in order parameter used. However, we see significant agreement in both charge density and velocity fields between the two studies, as shown in Figs. 5.19 and 5.20. The agreement in both qualitative structure and in magnitude suggests minimal difference between $\boldsymbol{Q}$-tensor electrokinetics in an axisymmetric geometry and $\hat{\boldsymbol{n}}$-vector electrokinetics in two dimensions.

However, the angular structure of the velocity field depicted in Fig. 5.20b is very different than the velocity field in the numerical study depicted in Fig. 5.18b, with two vortices in the former and six in the latter. To investigate whether this difference is due to the use of a DC field in Fig. 5.20b and an AC field in Fig. 5.18b, we have also computed the electrokinetic velocity with the same system size and with the same parameters listed in Table 5.2, except instead of Dirichlet boundary conditions for ionic concentrations and a DC applied field, we use zero-flux boundary conditions for concentrations and an AC applied field with characteristic frequency $\omega = 10\pi/s$. We find that unlike the two-vortices found with a DC field, Fig. 5.21a, the velocity field has six vortices when using an AC field, Fig. 5.21b. Unlike in Fig. 5.18b, the six vortices in Fig. 5.21b are not uniformly distributed across the cell – instead we see four vortices on the left side of the particle and two vortices on the right. We suspect the qualitative difference between Fig. 5.21b and 5.18b is due to the difference in system

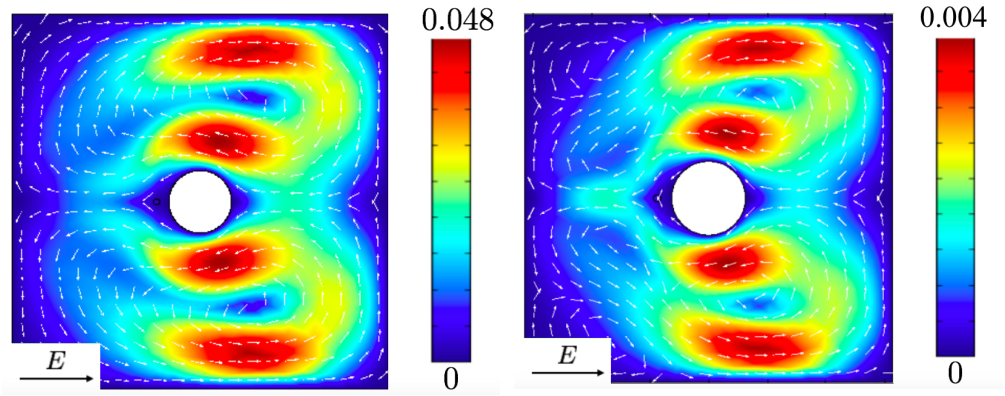

(a) DC field (b) AC field

Figure 5.21: (a) Fluid velocity obtained on a two-dimensional domain using director field $\hat{\boldsymbol{n}}$, with parameters matching Fig. 5.19 (b) Time-average velocity using the same parameters but with an AC field

size. Thus we find that the nature of the applied field, the boundary conditions for ionic concentrations, and the cell size contribute to the details of the flow field.

While we find good agreement between the axisymmetric $\boldsymbol{Q}$-tensor model and the two-dimensional $\hat{\boldsymbol{n}}$-vector model at small system size and with a DC field, we still find that the flow structure depicted in Fig. 5.20b does not agree with the experimental results depicted in Fig. 5.18a. Figure 5.18a shows four distinct vortices near the particle, while Fig. 5.20b only has two. Furthermore, in Fig. 5.18a the flow on the left side of the particle is toward the right, and flow on the right side of the particle is toward the left, while in Fig. 5.20b, the flow near the particle is always toward the left, with returning flows along the boundary walls. Detailed experimental observations of the fluid flow near the particle surface have not been done, so it is not clear whether the experimental flow at short length scales would be similar to Fig. 5.20b. Still, it is clear that the small cell axisymmetric system with a DC field does not exhibit the flow characteristics of a large thin film system under an applied AC field.

Two-dimensional flow and three-dimensional variation configuration of the director

Having found no qualitative agreement between experimental flows and a confined, axissymmetric model, we turn to our second method for investigating the effect of dimensionality on electrokinetic flow. In order to investigate the effect of the difference in far-field behavior of two-dimensional and three-dimensional director fields on electrokinetic flow, we compute the two-dimensional LCEK velocity of a system with a particle-defect pair using the same parameters as the large cell system of Sec. 5.4.1 but with a different director field. Instead of using the two-dimensional analytic solution for $\hat{\boldsymbol{n}}$, we use a two-dimensional slice of the three-dimensional variational solution discussed in Sec. 5.3.1,

$$\boldsymbol{\mathcal{E}}(\boldsymbol{r}) = \hat{\boldsymbol{x}} + \frac{q\boldsymbol{r}}{r^3} + \frac{3x\boldsymbol{r} - r^2\hat{\boldsymbol{x}}}{r^5},\ \hat{\boldsymbol{n}} = \frac{\boldsymbol{\mathcal{E}}}{|\boldsymbol{\mathcal{E}}|}, \tag{5.57}$$

with $q \approx 3.078$. Unlike the two-dimensional analytic solution, Eq. (5.10), this solution agrees with the three-dimensional multipole expansion, Eq. (5.3). Specifically, the leading order behavior of Eq. (5.57) decays as $1/r^2$, while the leading order far-field behavior of the two-dimensional equilibrium solution, Eq. (5.10) decays only as $1/r$. Since charge density scales with gradients of the director field, $\rho \sim \nabla\hat{\boldsymbol{n}}$, and the viscous force scales with the elastic force, $\nabla^2\boldsymbol{v} \sim \rho\boldsymbol{E}$, we expect $\nabla^2 v \sim \nabla\hat{\boldsymbol{n}}$. Therefore, the $1/r^2$ leading order far-field behavior of the ansatz implies $\boldsymbol{v} \sim \mathcal{O}(r^{-1})$ at $r \gg 1$, while the $1/r$ leading order behavior of the two-dimensional solution implies $\boldsymbol{v} \sim \mathcal{O}(\log r)$. Thus we see that the radial dependency of the velocity field depends strongly on whether at $r \gg 1$ the decay of the director field is two-dimensional or three-dimensional. Experimental investigations of the radial dependency of the electroosmotic velocity field around a suspended particle have not been performed, so it remains to be seen whether the far-field behavior of the director is two- or three-dimensional. By using the ansatz director field given by Eq. (5.57) while solving for other variables on a two-dimensional domain, this study models the behavior of the director field of a particle in a thin cell as three-dimensional, and the charge and velocity fields as two-dimensional.

The LCEK velocity field computed using the variational solution for the director, Eq. (5.57), is shown in Fig. 5.22a. Unlike both the axisymmetric confined-cell study, Fig. 5.19b, and the fully two-dimensional study, Fig. 5.18b, we find qualitative agreement

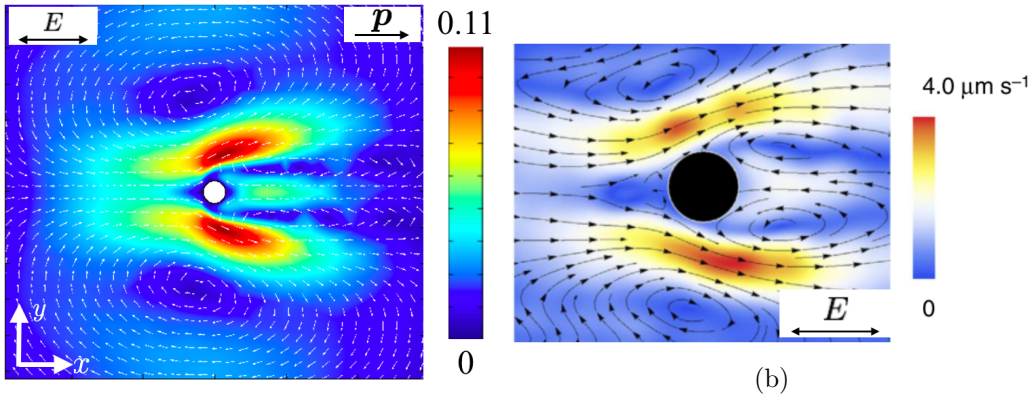

(a) (b)

Figure 5.22: (a) Time-averaged numerical velocity field obtained using a two-dimensional slice of the three-dimensional director ansatz given in Eq. (5.57). (b) Experimental electroosmotic flow past a particle-defect pair.

between the numerical velocity field of Fig. 5.22a and the experimental velocity field, Fig. 5.22b. Specifically, in both figures the velocity flow near the left of the particle flows to the right, while the velocity near the right of the particle flows to the left. Far from the particle, we see two vortices which dominate the flow behavior. This is in contrast with the velocity field in Fig. 5.18b obtained using the two-dimensional equilibrium solution, in which we see flow near the particle always to the left, and six vortices far from the particle.

We can begin to understand the the origins of the different flow behavior when using the ansatz director solution by considering the far-field behavior of the variational solution. For $r \gg 1$, the director field is approximately,

$$\hat{\boldsymbol{n}} \approx \hat{\boldsymbol{x}} + \frac{qy}{r^3}\hat{\boldsymbol{y}} = \hat{\boldsymbol{x}} + \frac{q\sin\theta}{r^2}\hat{\boldsymbol{y}} \tag{5.58}$$

Using Eqs. (5.26) and (5.58), the charge density for $r \gg 1$ to first order in Δ is approximately

$$\rho_{ans}(r,\phi,t) \approx (\tilde{\epsilon} - \tilde{\mu})\,\frac{\cos(t-\delta)}{\sqrt{1+\Omega^2}}\,\frac{q[-1+3\cos(2\phi)]}{r^3} \tag{5.59}$$

Comparing Eq. (5.59) with the far-field charge density generated by the two-dimensional

equilibrium director field, Eq. (5.30), we see that in addition to a more rapid radial decay, Eq. (5.59) contains an additional term ρ'_{ans} that is radially symmetric.

$$\rho'_{ans}(r,\phi,t) = -\left(\tilde{\epsilon}-\tilde{\mu}\right)\frac{\cos(t-\delta)}{\sqrt{1+\Omega^2}}\frac{q}{r^3}. \tag{5.60}$$

At first order in Δ, the body force $\rho'_{ans}\boldsymbol{E}$ due to this extra term written in polar coordinates is,

$$\rho'_{ans}\boldsymbol{E} = -\left(\tilde{\epsilon}-\tilde{\mu}\right)\frac{\cos(t-\delta)}{\sqrt{1+\Omega^2}}\frac{q}{r^3}(\hat{\boldsymbol{r}}\cos\phi - \hat{\boldsymbol{\phi}}\sin\phi) \tag{5.61}$$

Thus the presence of this additional radial term leads to an additional term in the body force with dipolar symmetry. While one must determine the charge and flow behavior near the particle in order to fully compute the velocity field, the presence of an additional dipolar term in the body force is consistent with the numerical and experimental observation of two vortices dominating the flow behavior at $r \gg 1$.

To summarize, we find that the experimental electroosmotic flow of a particle in a thin nematic film is best accounted for by a two-dimensional velocity field obtained from an effective three dimensional director field. While the two-dimensional and axisymmetric velocity fields agree in a confined cell, the flow structure does not match the experimental flow in a thin film. Despite these differences, we find the direction of the electrokinetic force on the particle, Eq. 5.21, is in the same direction in all systems studied.

5.4.3 Flow control through tuning of mobility and dielectric anisotropies

The far-field charge density solution for a particle-defect pair, Eq. (5.59), predicts that the charge density (and therefore the nematic velocity) is proportional to the difference in mobility and dielectric anisotropies. This suggests that the direction of electrophoretic motion of a free (unfixed) particle can be reversed by manipulating this difference. Dielectric anisotropy can by manipulated by using nematic mixtures with broadly varying dielectric anisotropy of the constituents, and by changes in the dielectric anisotropy with temperature. Flow reversals have been observed in isotropic electrolytes, but the mechanism is not yet understood [60]. In this section, we compare

numerical studies of LCEK flow past a particle with corresponding experiments at a variety of dielectric anisotropy values in order to verify this key element of the LCEK mechanism. We demonstrate that both the force on a fixed particle and the velocity of a free particle are proportional to the anisotropy difference, and can reverse sign as a function of composition and temperature. This result is confirmed experimentally.

Since the imposed two-dimensional slice of the three-dimensional ansatz, Eq. (5.57), produced a flow field that most resembled experimental flows, as discussed in the previous section, we will use it again in this section. The resulting far-field charge density, Eq. (5.59) predicts a body force which behaves at $r \gg 1$ as,

$$\rho \boldsymbol{E} \approx (\tilde{\epsilon} - \tilde{\mu}) \frac{\cos(t-\delta)\cos t}{\sqrt{1+\Omega^2}} \frac{q\hat{\boldsymbol{x}}[-1+3\cos(2\phi)]}{r^3} \tag{5.62}$$

Since this force is symmetric about the x axis, we expect the velocity to be along the x axis. This is consistent with the symmetry of the problem, as symmetry in $\hat{\boldsymbol{n}}$ is broken along $\hat{\boldsymbol{x}}$ only, due to the presence of the defect. Furthermore, since Eq. (5.62) is balanced by the divergence of the stress tensor, we anticipate the stress tensor, and therefore the electrokinetic force on the particle, to be proportional to $(\tilde{\epsilon}-\tilde{\sigma})\cos(t-\delta)\cos t/\sqrt{1+\Omega^2}$. Assuming the electrokinetic force is always balanced by a viscous drag, Eq. 5.62 predicts the time-averaged velocity of a spherical particle to be $\boldsymbol{u} = u\hat{\boldsymbol{x}}$, where

$$u = (\tilde{\epsilon} - \tilde{\sigma}) \frac{\beta}{1+\Omega^2}, \tag{5.63}$$

where $\tilde{\sigma} = \tilde{\mu}$ is the conductivity anisotropy, and β is a numerical parameter that should depend on the details of director configuration, finite surface anchoring, and anisotropy of viscoelastic parameters of the nematic; its exact theoretical value is not known. As predicted by Eq. (5.63), one can reverse the direction of fluid velocity $\boldsymbol{v}$ with respect to the structural dipole $\boldsymbol{p}$ by altering the sign of $(\tilde{\epsilon} - \tilde{\sigma})$. When $(\tilde{\epsilon} - \tilde{\sigma}) > 0$, the electrophoretic velocity is parallel to the elastic dipole, and when $(\tilde{\epsilon} - \tilde{\sigma}) < 0$, the two vectors are antiparallel.

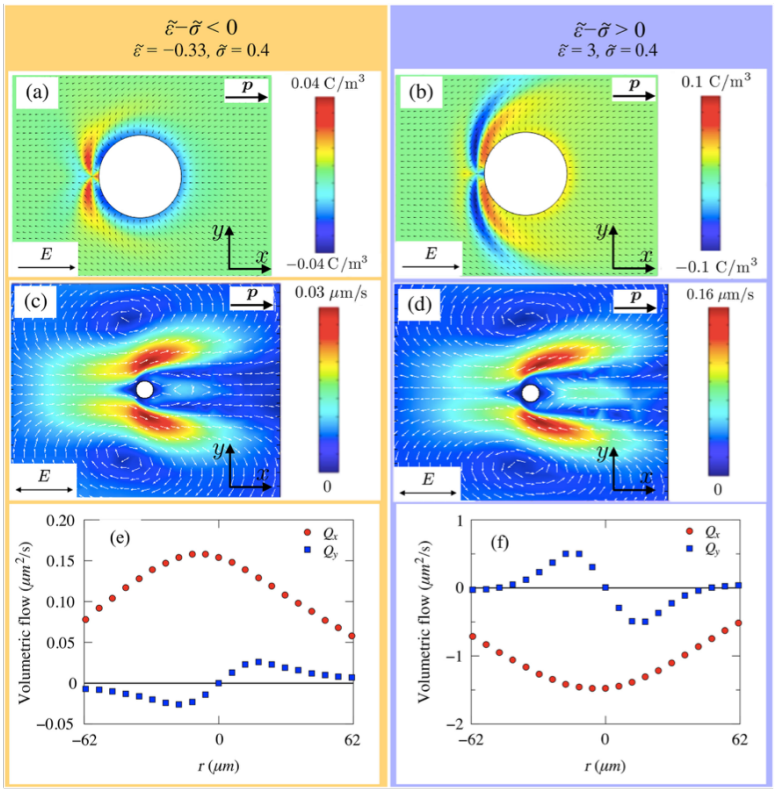

Figure 5.23: Numerical solutions for LCEK flows around fixed particle in two dimensions for various dielectric anisotropies, with applied field parallel to the dipole. (a)-(b) Charge density plotted in color, with arrows representing the director field. (c)-(d) Corresponding flow velocity map, showing flow reversal as $(\tilde{\epsilon}-\tilde{\sigma})$ changes sign. (e)-(f) Volumetric flows along the x-axis (Q_x) and along the y-axis (Q_y) pumped around the particle by the electric field.

Correlation of velocity reversals and material properties: numerical results

We consider a 2D geometry and neglect particle polarization and assume Er $\ll 1$. In order to best compare flow structure with experiments, we use as input the variational solution for the nematic field around a sphere with homeotropic anchoring, Eq. (5.57). We then solve for the charge distribution and velocity fields under a uniform and oscillatory AC electric field. The circular particle, a disc of unit radius, is considered as immobilized, with a fixed location. Physical parameters were chosen to match the experimental study, and are listed in Table 5.3.

Parameter	Value	Comment
ω	50π rad/s	Applied field frequency
E_0	19.75 mV/μm	Applied field amplitude
$\epsilon_\perp$	14	Perpendicular dielectric permittivity
$\Delta\mu/\mu_\perp$	0.4	Relative mobility anisotropy
a^*	4.8 μm	Particle radius

Table 5.3: Physical constants used in numerical calculations in Sec. 5.4.3, with all others listed in Table 2.1

Figure 5.23 shows the instantaneous charge distribution when $(\tilde{\epsilon} - \tilde{\sigma})$ is negative (Fig. 5.23a) and positive (Fig. 5.23b), and the corresponding flow fields (averaged over a period of the field), in Fig. 5.23c and 5.23d, respectively. Despite differences in the details, the resulting average flow fields for negative and positive $(\tilde{\epsilon} - \tilde{\sigma})$ are very similar, except that the flows are completely reversed, as clear from the comparison of Fig. 5.23c and 5.23d in which the arrows indicate the velocity fields. The electro-osmotic flows around the particle with hedgehog defect (Fig. 5.6) acquire dipolar symmetry due to left-right asymmetry of the dipolar director configuration around the colloid, Figure 5.6. The asymmetry in flows causes pumping of nematic electrolyte along the x-axis, either parallel or antiparallel to the structural dipole $\boldsymbol{p}$, depending on the sign of $(\tilde{\epsilon} - \tilde{\sigma})$ [3,5]. In order to determine the net pumping direction near the particle, we compute the volumetric flows along the x-axis, $Q_x = \int_{-y_0}^{y_0} v_x dy$ and along the y-axis, $Q_y = \int_{-x_0}^{x_0} v_y dx$, where $x_0 = y_0 = 4$. Under the action of the electric field, the nematic is pumped from one side of the colloid to another; there is no pumping in the orthogonal y direction, Fig. 5.23e and Fig. 5.23f. An alternative view of this pumping effect can be obtained by computing the viscous force along the x-axis on the immobile particle by integrating the normal component of the stress, Eq. (5.21). The dependency of this average force on $(\tilde{\epsilon} - \tilde{\sigma})$, Fig. 5.24, shows a reversal of the force direction with the change of the sign of $(\tilde{\epsilon} - \tilde{\sigma})$. When $(\tilde{\epsilon} - \tilde{\sigma}) < 0$, the nematic fluid around the immobilized disc is pumped along $\boldsymbol{p}$, Fig. 5.23e, and the viscous force on the particle is opposite $\boldsymbol{p}$, Fig. 5.24. The direction v of electrophoretic propulsion of a free particle would be in the direction of the viscous force when fixed, and is opposite the polarity of the electro-osmotic pumping. In the experiment, the free particles in the medium with $(\tilde{\epsilon} - \tilde{\sigma}) < 0$ are indeed moving

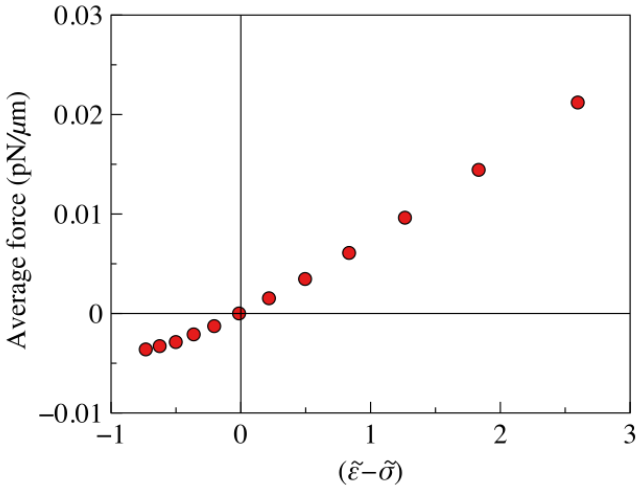

Figure 5.24: Average viscous force acting along the -direction on a fixed particle by the LCEK flow, calculated for a variety of values of $(\tilde{\epsilon} - \tilde{\sigma})$ by integrating the normal component of the viscous stress over the particle perimeter. Note that since the stress tensor is a force per unit area, the integration over the perimeter yields a force per unit length. The results show that the force changes sign with $(\tilde{\epsilon} - \tilde{\sigma})$.

towards the negative direction of the x-axis, $v < 0$, with the hedgehog leading the way, Figs. 5.27b, and 5.28. In other words, the electrophoretic velocity $\boldsymbol{v}$ is antiparallel to the dipole $\boldsymbol{p}$. For the case $(\tilde{\epsilon} - \tilde{\sigma}) > 0$, polarity of electroosmotic pumping, Fig. 5.23f, and viscous force, Fig. 5.24 are reversed. This also implies that the direction of electrophoretic motion with respect to the structural dipole should be reversed.

We have also computed the electrokinetic flow past a sphere for a variety of anisotropies when the applied field is perpendicular to $\boldsymbol{p}$. Figure 5.25 shows the charge density and velocity for two values of $(\tilde{\epsilon} - \tilde{\sigma})$, showing that the charge and velocity change sign with $(\tilde{\epsilon} - \tilde{\sigma})$.

Figure 5.26 shows the numerically-computed force on the particle, which changes sign with $(\tilde{\epsilon} - \tilde{\sigma})$. Thus if the particle were not fixed, the motion of the particle can be reversed by changing $(\tilde{\epsilon} - \tilde{\sigma})$. Note that the force on the fixed particle (and correspondingly the velocity of a free particle) for a transverse field is in the opposite direction as for a parallel field with the same value of $(\tilde{\epsilon} - \tilde{\sigma})$.

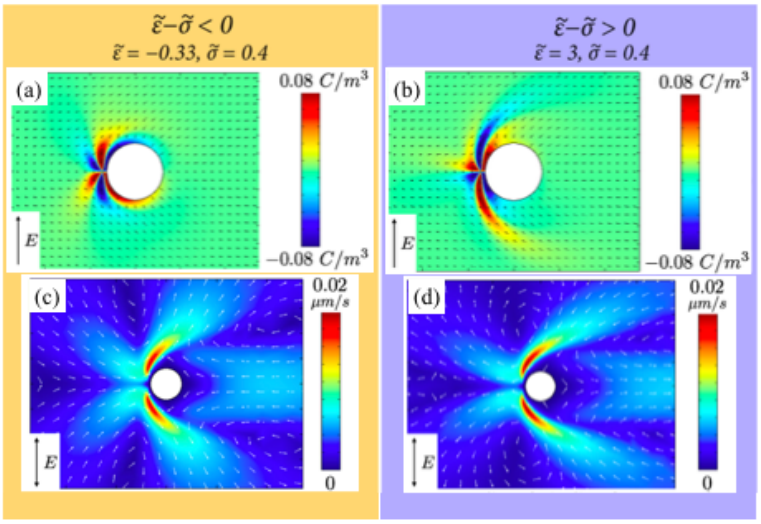

Figure 5.25: Numerical solutions for LCEK flows around fixed particle with field perpendicular to elastic dipole $\boldsymbol{p}$. (a)-(b) Charge density for transverse field, with $(\tilde{\epsilon}-\tilde{\sigma})<0$ and $(\tilde{\epsilon}-\tilde{\sigma})>0$, respectively. (c)-(d) Corresponding flow velocity, showing flow reversal as $(\tilde{\epsilon}-\tilde{\sigma})$ changes sign.

Correlation of velocity reversals and material properties: experimental results

Flow reversal experiments were performed with binary mixtures of room-temperature nematics pentylcyanobiphenyl (5CB) and HNG715600-100 (referred to as HNG in what follows). 5CB exhibits $\tilde{\epsilon}=1.9$ [81] and HNG exhibits $\tilde{\epsilon}=-0.7$ [82] at room temperature. Concentration variation of mixtures changes $(\tilde{\epsilon}-\tilde{\sigma})$ strongly, both in absolute value and in sign. Dry soda-lime-silica spheres of diameter $2a^*=(9.6\pm1)\mu$m were used as electrophoretic particles. The spheres were treated to impart perpendicular orientation of $\hat{\boldsymbol{n}}$. The nematic layers of thickness $h^*=60\mu$m were confined between two glass plates with planar alignment $\hat{\boldsymbol{n}}_0$. The AC electric field of frequency $f^*=25$Hz was applied parallel to $\hat{\boldsymbol{n}}_0$ using two aluminium strips separated by a distance $L^*=4$mm. The amplitude of the field acting on the particles in the center of the cells is $E_0=19.75\text{mV}/\mu\text{m}$, which is 79% of the applied field (the reduction is caused by the difference of dielectric permittivities of glass plates and the nematic [5] and was determined by numerical simulations).

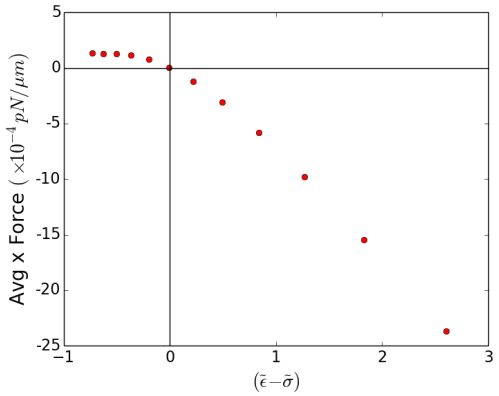

Figure 5.26: Numerical force on particle as a function of $(\tilde{\epsilon} - \tilde{\sigma})$, showing the force changes sign with $(\tilde{\epsilon} - \tilde{\sigma})$.

Experiments were conducted such that $\tilde{\epsilon}$ varied broadly from mixture to mixture while the anisotropy of conductivity remained constant, $\tilde{\sigma} = 0.4$. To achieve these conditions, the experiments were performed at the temperature $T - T_{NI} = -5°C$ for each mixture, where T_{NI} is the temperature of the isotropic-nematic transition of that mixture, Figure 5.27a. At high weight concentrations of 5CB, $c > 0.54$, the spheres move with the sphere leading the way, $u > 0$, Figure 5.27b. For $c < 0.54$, the polarity is reversed, $u < 0$, i.e., the sphere follows the hedgehog, Figure 5.27b. Equation (5.63) was fit to experimental data as shown in Fig. 5.27b, with $\beta = 110 \pm 20$.

Analysis of the data in Fig. 5.27 suggests that the polarity of electrophoresis can be reversed by simply changing the temperature of the nematic mixture with concentrations close to $c = 0.52$. Figure 3 shows that this is indeed the case, as the electrophoretic velocity changes from negative to positive as the temperature decreased, with $t_v \approx -7°C$ being the point of reversal. Equation (5.63) shows good agreement with experimental velocity, with $\beta = 120 \pm 20$.

Equation (5.63) has been deduced assuming $|\tilde{\epsilon} - \tilde{\sigma}| \ll 1$, while the numerical and experimental studies consider a much large range of values for $(\tilde{\epsilon} - \tilde{\sigma})$, so we anticipate higher order terms in $\tilde{\epsilon}$ and $\tilde{\sigma}$ to contribute to the particle velocity. Additionally, thus far we have not explicitly considered the exact details of the director field and charge density near the particle surface. It is possible that the director may be distorted by surface polarization and flexoelectric mechanisms [83] and by viscous flow effects [84]. In

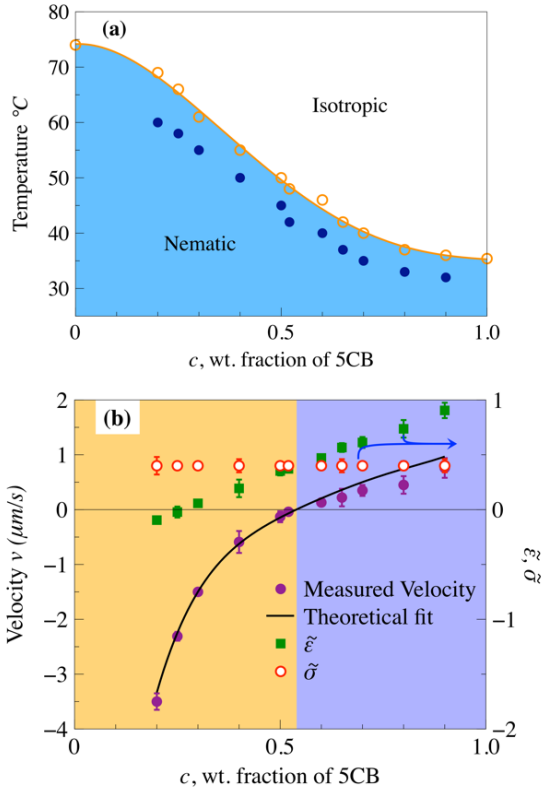

Figure 5.27: (a) Phase diagram of 5CB-HNC mixtures. Open circles show T_{NI} and the filled circles show the temperatures $t = T - T_{NI} = -5°C$ at which the material parameters and electrophoretic velocities were measured. (b) Concentration dependence of electrophoretic velocity v, dielectric $\tilde{\epsilon}$, and conductivity $\tilde{\sigma}$ anisotropies; solid line is the fit of $v(c)$ by Eq. (5.63) with $\beta = 110 \pm 20$.

the one elastic constant approximation, the field-induced realigning torques that rotate the director from the sphere-imposed direction by a small angle $\delta\theta$ can be estimated as $e'E_0\delta\theta$ for the flexoelectric-surface polarization effect [83]; where $e' = e_1 + e_3 \pm P$ where e_1 and e_3 are the flexoelectric coefficients, P is the surface polarization; e' can be as high as $\sim 10^{-10}$ C/m [83]. For the cited electric fields, $e'E_0 \sim 2 \times 10^{-6}$ J/m^2. This value is not negligibly small when compared to the expected polar anchoring strength $(10^{-6} - 10^{-4})$ J/m^2 [85–87] that is responsible for the appearance of the hedgehog next to the sphere of radius $a^* \approx 5\mu$m. The Ericksen number for this system is Er $= 0.084$, which while small, does not imply that viscous torques are completely negligible. Thus

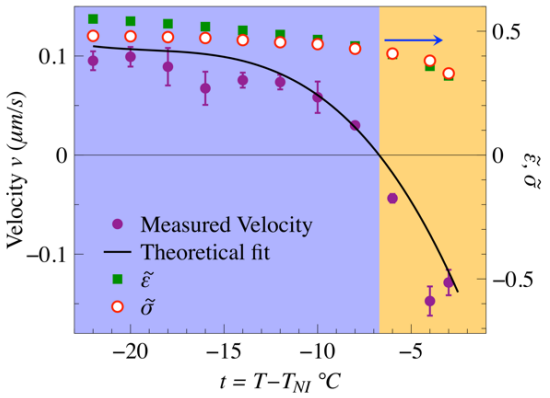

Figure 5.28: Temperature-triggered reversal of electrophoretic velocity v, plotted together with the temperature dependencies $\tilde{\epsilon}$ and σ fora binary mixture $c = 0.52$; the solid line is the fit of $v(t)$ by Eq. (5.63) with $\beta = 120 \pm 20$

both the field [83] and flow [84] might modify the director and influence β in Eq. (5.63). We discuss the effect of non-negligible viscous torques in particular in Sec. 5.4.5.

In conclusion, nematic electrolytes allow one to control both the magnitude and the polarity of electrokinetic flows by simply tuning the temperature or composition to change the value of $(\tilde{\epsilon} - \tilde{\sigma})$. We determined the numerical coefficient in Eq. (5.63) that connects the electrophoretic velocity to the material parameters as $\beta = 110 - 120$. Analysis of the experimental and numerical data also suggests that the next level of detailed description of LCEK in which β is derived as a function of higher orders in $\tilde{\epsilon}$, $\tilde{\sigma}$, flexoelectric and surface polarization effects, etc., should account for the dynamic nature of the director deformations in the applied electric field and their modification by the flows.

5.4.4 Effect of splay and bend on particle-defect flows

Having analyzed the mechanisms responsible for particle mobility, we now consider the effects neglected in our simplifying assumptions of Sec. 5.4.1. While in Sec. 5.4.2 we found that the experimental systems were best represented by considering a two-dimensional slice of the three-dimensional director field, this configuration requires the use of a known field, and thus does not allow for the investigation of the effects of non-equal elastic constants, backflows, or the presence of multiple particles. Thus, for the

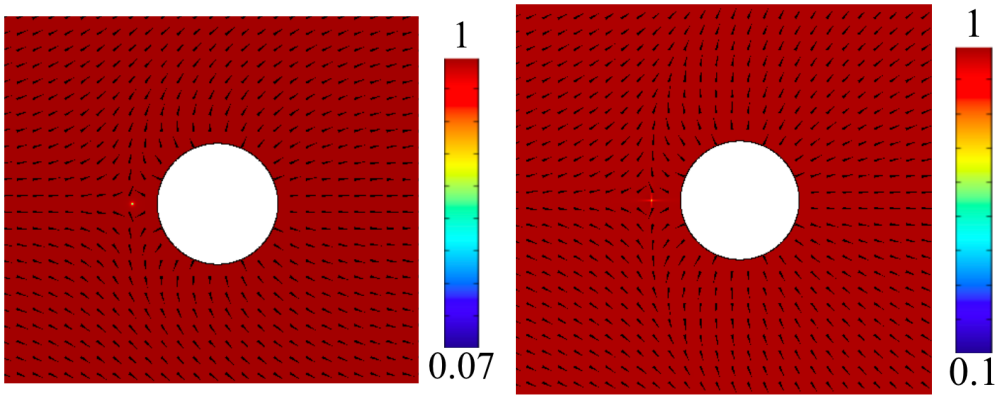

(a) (b)

Figure 5.29: (a) Equilibrium director field near the particle for $K_1/K_3 = 1$,with magnitude plotted in color. (b) Equilibrium director field near the particle for $K_1/K_3 = 0.1$ Note that the position of the defect is farther from the particle and the amount of bend near the particle is reduced.

remainder of this chapter, we return to the system of Sec. 5.4.1, in which the director field satisfies its governing equations in two dimensions, Eq. (2.53). As noted in Sec. 5.4.2, the electrokinetic force on the suspended particle for this system is consistent with particle motion in electrophoresis experiments, so we will consider this quantity the key result for experimental comparison.

We begin by considering the effect of $K_1 \neq K_3$ on the eletrokinetic flows and forces on a suspended particle with homeotropic anchoring. Recall that in two dimensions, the Oseen-Frank elastic free energy is,

$$f = \frac{K_1}{2}(\nabla \cdot \hat{\boldsymbol{n}})^2 + \frac{K_3}{2}(\hat{\boldsymbol{n}} \times \nabla \times \hat{\boldsymbol{n}})^2. \tag{5.64}$$

The first term in Eq. (5.64) is associated with splay distortions, while the second term is associated with bend. Thus at low K_1/K_3, the system will prefer splay distortions over bend distortion.

To understand the effect of K_1/K_3 on director orientation and electrokinetic flow, consider again a $(+1, -1)$ pair. Note that as the defect separation r_d increases, the amount of splay near the $(+1)$ defect increases, while the bend decreases. Thus as

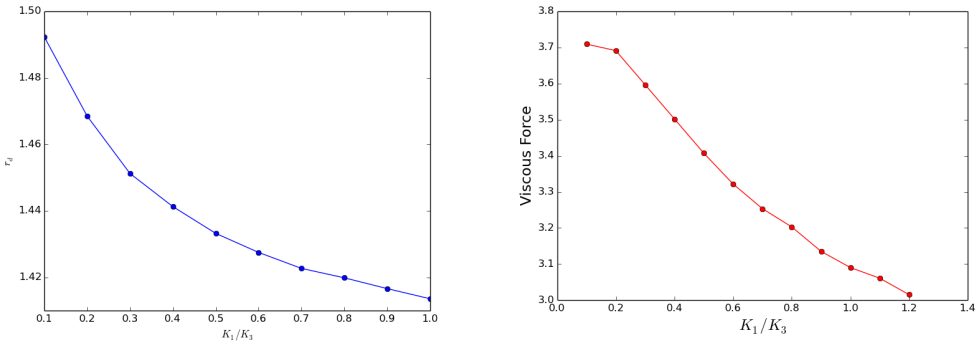

(a) (b)

Figure 5.30: (a) Defect position r_d as a function of K_1/K_3. (b) Viscous force acting on suspended particle as a function of K_1/K_3, averaged over a period of the field.

K_1/K_3 decreases, splay is preferred over bend; thus we anticipate r_d increases. Furthermore, since r_d is the characteristic length of a $(+1, -1)$ pair, and velocity scales with the characteristic length, we anticipate that flow velocity and particle forces will increase as K_1/K_3 decreases. Figure 5.29 plots the solutions to the regularized director $\boldsymbol{n}$ for $K_1/K_3 = 1$ and $K_1/K_3 = 0.1$ in two dimensions. We see that as expected from the $(+1, -1)$ analogy, the defect position r_d is larger and there is more splay for $K_1/K_3 = 0.1$. Figure 5.30a plots r_d as a function of K_1/K_3, showing a decrease in r_d as K_1/K_3 increases. Figure 5.30b shows the viscous force on the particle, averaged over a period of the field. The viscous force increases as K_1/K_3 decreases, consistent with our prediction that fluid velocity grows with r_d.

5.4.5 Particle-hedgehog flows with the inclusion of backflow effects

We examine next the effects of viscous torques on director orientation, which we have neglected thus far in Sec. 5.4.1. This consideration adds significant complexity to the problem, as the director field is now coupled to the other variables and is no longer solved independently. Specifically, recall from Sec. 5.3.2, the director field (with the regularization technique) satisfies,

$$\boldsymbol{h^0} - \mathrm{Er}(\boldsymbol{h'} + \tilde{\epsilon}(\boldsymbol{n} \cdot \boldsymbol{E})\boldsymbol{E}) = 0 \tag{5.65}$$

with $h' = \gamma_1 N_i + \gamma_2 A_{ij} n_j$, and in the one-constant approximation,

$$h_i^0 = \frac{\partial}{\partial x_j}\frac{\partial f}{\partial(\partial_j n_i)} - \frac{\partial f}{\partial n_i} = \nabla^2 n_i - \frac{1}{\delta^2}(\hat{\boldsymbol{n}}^2 - 1)n_i. \tag{5.66}$$

We obtain the numerical solution in two steps: first, we find the solution to $\hat{\boldsymbol{n}}$ which minimizes the regularized elastic free energy. We use this solution as an initial condition for $\hat{\boldsymbol{n}}$, and we simultaneously solve Eqs. (4.1)-(4.5), with a slight modification to Eq. (4.4). Recall from Chapter 2 the viscous stress tensor for nematics is,

$$\tilde{T}_{ij} = \alpha_1 n_i n_j n_k n_l A_{kl} + \alpha_2 N_i n_j + \alpha_3 n_i N_j + \alpha_4 A_{ij} + \alpha_5 n_j A_{ik} n_k + \alpha_6 n_i A_{jk} n_k \tag{5.67}$$

with $A_{ij} = (1/2)(\partial_j v_i + \partial_i v_j)$ and $N_i = (\Omega/W)\dot{n}_i - \Omega_{ij} n_j$. Since $\boldsymbol{N}$ contains time derivatives of $\boldsymbol{n}$, the equations for both momentum balance and director dynamics, Eqs. (4.4) and (4.5), depend on $\dot{\boldsymbol{n}}$, which makes the problem much more difficult to solve numerically. Since we have seen no significant differences between solutions with the full viscous stress tensor and the analytic analysis using the Newtonian stress tensor, (Secs. 3.2, 5.4.1), we simplify the numerical problem by replacing the Leslie viscous stress, Eq. (5.67), with the Newtonian stress tensor. Equation (2.52) then becomes,

$$-\nabla p + \frac{1}{\mathrm{Er}}\nabla \cdot \boldsymbol{T}^e + \nabla^2 \boldsymbol{v} + \rho \boldsymbol{E} = 0. \tag{5.68}$$

While we have assumed the nematic satisfies the momentum conservation equations of a Newtonian fluid, we still have nonzero rotational viscosities γ_1, γ_2 in the definition of $\boldsymbol{h}'$, for if $\gamma_1 = \gamma_2 = 0$, there is no viscous torque on the director.

Since the director is regularized in the numerical solution, there are no singularities in its field, even though there are defects present. However, since the defect core size is small ($\delta = 0.01$), we anticipate the divergence of the elastic stress, $\nabla \cdot \boldsymbol{T}^e$, is very large at the defect core for the following reason: Since the elastic stress is defined as,

$$T_{ij}^e = -\frac{\partial f}{\partial(\partial_j n_k)}\frac{\partial n_k}{\partial x_i}, \tag{5.69}$$

and $f \sim (\nabla \boldsymbol{n})^2$, the divergence of the elastic stress scales as $\nabla \cdot \boldsymbol{T}^e \sim (\nabla \boldsymbol{n})^2$. Near defect cores $\nabla \boldsymbol{n}$ scales as r^{-1}, as discussed in Sec. 5.3.2; thus we anticipate near defect

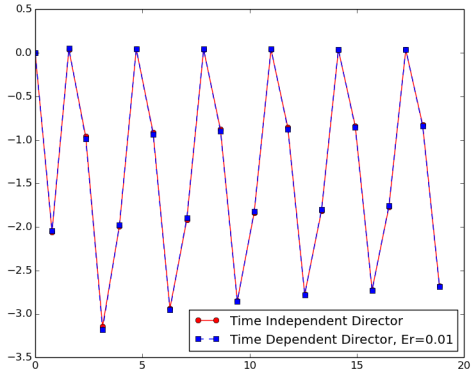

Figure 5.31: Viscous force on particle as a function of time computed in the numerical scheme with a time-independent director (Er = 0) and with a time-dependent director with Er = 0.01.

cores $\nabla \cdot \boldsymbol{T}^e \sim r^{-3} \sim \delta^{-3} \sim 10^6$, which is very large and makes Eq. (5.68) difficult to solve numerically.

We resolve this numerical challenge by using the definition $h_i^0 = \partial_j \pi_{ij} - \partial f / \partial n_i$, where $\pi_{ij} = \partial f / \partial(\partial_j n_i)$, to write Eq. (5.69) as,

$$-\partial_j T^e_{ij} = \partial_i n_k \left(h_k^0 + \frac{\partial f}{\partial n_k} \right) + \pi_{kj} \partial_j (\partial_i n_k) = h_k^0 \partial_i n_k + \frac{\partial f}{\partial n_k} \partial_i n_k + \pi_{kj} \partial_j (\partial_i n_k) \quad (5.70)$$

Using Eq. (5.65), note that $h_k^0 \partial_i n_k = \mathrm{Er}\,(h_k' \partial_i n_k - \tilde{\epsilon}(\hat{\boldsymbol{n}} \cdot \boldsymbol{E}) E_k \partial_i n_k)$.Using this and the definition of π_{ij}, we can write

$$\begin{aligned} -\partial_j T^e_{ij} &= \frac{\partial f}{\partial n_k} \partial_i n_k + \pi_{kj} \partial_j (\partial_i n_k) + \mathrm{Er}\left(h_k' \partial_i n_k - \tilde{\epsilon}(\hat{\boldsymbol{n}} \cdot \boldsymbol{E}) E_k \partial_i n_k \right) \\ &= \frac{\partial f}{\partial n_k} \partial_i n_k + \frac{\partial f}{\partial(\partial_j n_k)} \partial_j (\partial_i n_k) + \mathrm{Er}\left(h_k' \partial_i n_k - \tilde{\epsilon}(\hat{\boldsymbol{n}} \cdot \boldsymbol{E}) E_k \partial_i n_k \right) \end{aligned}$$

And then noting $\partial_j(\partial_i n_k) = \partial_i(\partial_j n_k)$ and using the chain rule, we find

$$-\partial_j T^e_{ij} = \partial_i f + \mathrm{Er}\left(h_k' \partial_i n_k - \tilde{\epsilon}(\hat{\boldsymbol{n}} \cdot \boldsymbol{E}) E_k \partial_i n_k \right). \quad (5.71)$$

The first term on the right hand side of Eq. (5.71) decays as r^{-3} near the defect core, since $f \sim (\nabla \boldsymbol{n})^2$. The remaining terms are all linear in $\nabla \boldsymbol{n}$, thus they decay as

r^{-1}. Thus the leading divergence in Eq. (5.71) is in ∇f only. Furthermore, we define $\tilde{p} = p + f/\mathrm{Er}$ and write Eq. (5.68) as,

$$-\nabla\tilde{p} - \left(h'_k \partial_i n_k - \tilde{\epsilon}(\hat{\boldsymbol{n}} \cdot \boldsymbol{E}) E_k \partial_i n_k\right) + \nabla^2 \boldsymbol{v} + \rho \boldsymbol{E} = 0. \tag{5.72}$$

We find that while $\nabla \cdot \boldsymbol{T}^e$ can be very large, scaling as r^{-3} near defect cores, its leading order divergence contributes only to a divergence in the pressure. The remaining terms in $\nabla \cdot \boldsymbol{T}^e$ scale as r^{-1}, as does the charge density around a single disclination, since $\rho \sim \nabla \boldsymbol{n}$. Thus all terms in Eq. (5.72) have the same scale near disclination cores, reducing the numerical difficulties in computing the fluid velocity.

We have first verified that the viscous force on the particle, the key result for experimental comparison, is appropriately captured for $\mathrm{Er} \ll 1$ by the time-independent director method used in Sec. 5.4.1. Figure 5.31 compares the viscous force on the particle as a function of time computed using the time-independent imposed director scheme and with a time-dependent director field with $\mathrm{Er} = 0.01$. We see good agreement between the two studies, verifying that at low Ericksen number the assumption of a fixed director field is valid.

Next we examine the difference in electrokinetic flow between $\mathrm{Er} = 0$ and $\mathrm{Er} = 1$. Figure 5.32 plots the difference in director and velocity solutions between $\mathrm{Er} = 1$ and $\mathrm{Er} = 0$. Figures 5.32a and 5.32b show that the difference in director is less than 0.1, and the difference is largest near the defect core. The velocity differences in Figs. 5.32c and 5.32d are normalized by the maximum velocity value for $\mathrm{Er} = 0$, and we see less than a 5% change in velocity magnitude due to backflow effects. The difference in charge density is not plotted; we find the difference is on the order of 10^{-4} or smaller.

To determine the origins of the small backflow effect, we consider the governing equations as a perturbation expansion in mobility anisotropy $\tilde{\mu}$ as before, except we now we assume $\mathrm{Er} = 1$ and explicitly expand the director $\boldsymbol{n}$ in powers of $\tilde{\mu}$ as well. For the purposes of this section, we assume $\Delta\epsilon = 0$ (as is the case in the numerical study above), allowing us to neglect the effect of dielectric torques.

At zero-th order in $\tilde{\mu}$, as seen in Chapter 3, the system behaves as an isotropic electrolyte, and is solved with $\rho^{(0)} = 0, C^{(0)} = 1$, $\boldsymbol{E}^{(0)} = \hat{\boldsymbol{x}} \cos t$, $\boldsymbol{v}_0 = 0$ and $\boldsymbol{n}^{(0)}$ in elastic equilibrium.

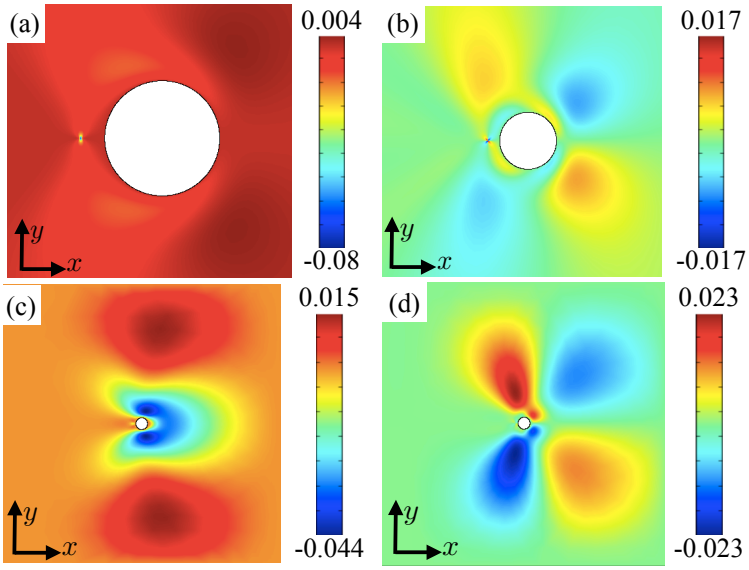

Figure 5.32: Time-averaged differences between solution with Er = 1 and Er = 0 for (a) n_x, (b) n_y, (c) v_x, and (d) v_y. The velocity differences (c)-(d) are normalized by the maximum value of the velocity when Er = 0.

At first order in $\tilde{\mu}$, the concentration and charge density equations become,

$$\Omega \frac{\partial C^{(1)}}{\partial t} = \gamma \nabla^2 C^{(1)} - Y^2 \cos(t) \frac{\partial \rho^{(1)}}{\partial x} \tag{5.73}$$

$$\Omega \frac{\partial \rho^{(1)}}{\partial t} = \gamma \nabla^2 \rho^{(1)} - \rho^{(1)} - \tilde{\mu} \frac{\partial}{\partial x_i} (n_i^{(0)} n_j^{(0)} E_j^{(0)}) - E_j^{(0)} \frac{\partial C^{(1)}}{\partial x_j}. \tag{5.74}$$

Since the driving term in Eq. (5.74) depends explicitly on $\tilde{\mu}$, at first order it is a function of only the zero order field $\boldsymbol{n}^{(0)}$. Thus to first order in $\tilde{\mu}$, the charge density and concentration equations do not depend on director reorientation.

By writing the divergence of the elastic stress as $\partial_j T^e_{ij} = -\partial_i f - h'_k \partial_i n_k$ as discussed above (with $\Delta\epsilon = 0$ and Er = 1), and defining $\tilde{p} = p + f$, the momentum equation, Eq. (4.4) at first order in $\tilde{\mu}$ is,

$$-\frac{\partial \tilde{p}^{(1)}}{\partial x_i} - h_k'^{(1)} \frac{\partial n_k^{(0)}}{\partial x_i} + \frac{\partial}{\partial x_j} \tilde{T}_{ij}^{(1)} + \rho^{(1)} E_i^{(0)} = 0. \tag{5.75}$$

There are only three terms in Eq. (5.75) which depend on $\boldsymbol{n}^{(0)}$. The first is $(\frac{\gamma_1\Omega}{W})\partial_t n_k^{(1)}\partial_i n_k^{(0)}$, which appears implicitly in the second term on the left hand side of Eq. (5.75). The second and third terms appear in the divergence of the viscous stress, and are $(\frac{\alpha_2\Omega}{W})\partial_j(n_j^{(0)}\partial_t n_i^{(1)})$ and $(\frac{\alpha_3\Omega}{W})\partial_j(n_i^{(0)}\partial_t n_j^{(1)})$ (note that these two terms are neglected in the numerical solution, as discussed above – we include them in our analysis here to highlight their negligible contribution and further justify this choice). In all three of these terms, the first-order correction to $\boldsymbol{n}$ appears as a time derivative. Since the system is driven by an oscillating field, we anticipate that after transient terms decay to zero, averaging over a period of the field yields $\langle\partial_t\boldsymbol{n}\rangle = 0$. Thus the effect of director torques on average velocity are negligible at $\mathcal{O}(\tilde{\mu})$.

Finally at first order in $\tilde{\mu}$ Eq. (5.65) becomes,

$$\nabla^2 n_i^{(1)} + \frac{1}{\delta^2}n_i^{(1)}([n_j^{(0)}]^2 - 1) + \frac{2}{\delta^2}n_i^{(0)}n_j^{(0)}n_j^{(1)} - \gamma_1 N_i^{(1)} - \gamma_2 A_{ij}^{(1)}n_i^{(0)} = 0 \qquad (5.76)$$

Unlike charge and velocity fields, it is unclear upon first examination of Eq. (5.76) why the variations in $\boldsymbol{n}$ shown in Fig. 5.32 are so small. For instance, if one assumes that far from defect cores, the first term on the left hand side of Eq. (5.76) is balanced by the last term on the left hand side of Eq.(5.76), i.e. $\nabla^2 n_i^{(1)} \sim \gamma_2 A_{ij}^{(1)} n_j^{(0)}$, then we estimate the scale of the corrections to the director field to be $\boldsymbol{n}^{(1)} \sim \gamma_2 \boldsymbol{v}^{(1)}$. From our numerical velocity results, we estimate $|\boldsymbol{v}^{(0)}| \sim 0.08$. Therefore this analysis predicts $\boldsymbol{n}^{(1)} \sim 0.1$, which is approximately one order of magnitude larger than what is experimentally observed (except near the defect core).

To summarize, we find the inclusion of director reorientation due to viscous torques does not significantly change the charge, velocity, or director fields, even at $\mathrm{Er} = 1$. We show that corrections to the charge density and velocity due to director reorientation do not appear at order $\mathcal{O}(\tilde{\mu})$. Further investigation is needed to determine why corrections to $\boldsymbol{n}$ at $\mathrm{Er} = 1$ are very small.

5.5 Two-particle flows

We now turn to investigating the LCEK interactions between two suspended particles. Studies of elastic interactions between multiple colloidal particles have been performed

experimentally [72, 75], analytically [77, 78, 88, 89], and numerically [90–93], but there are no studies addressing the effect of electrokinetics in inter particle interactions.

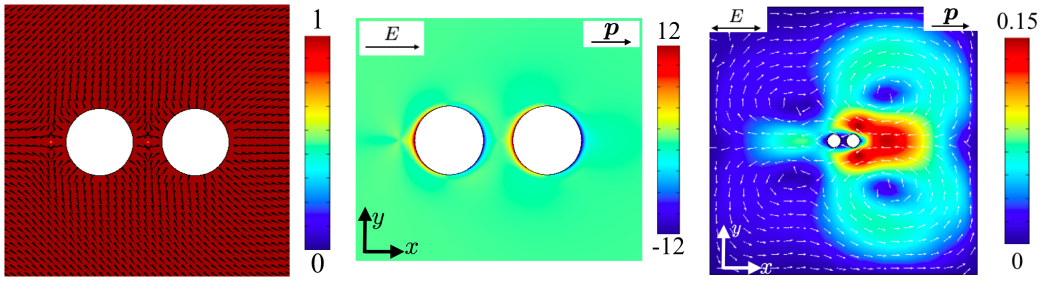

(a) (b) (c)

Figure 5.33: Numerical LCEK results for two-particles with homeotropic anchoring, separated by $s = 0.426$. (a) Director field at $t = 2\pi$, with magnitude plotted in color. (b) Charge density at $t = 2\pi$, with electric field pointing to the right. (c) Velocity field averaged over a period of the applied field.

5.5.1 Homeotropic anchoring

We first consider the electrokinetics of two circular particles with homeotropic anchoring, each with a companion hedgehog defect, and we compute the forces on the suspended particles. Recall the nematic stress tensor can be written as $T_{ij} = -p\delta_{ij} + \mathrm{Er}^{-1}T^e_{ij} + \tilde{T}_{ij}$, where T^e_{ij} and $\tilde{T}_{ij}$ are the elastic and viscous stress tensors, respectively. The total force $\boldsymbol{F}$ on a particle is computed by integrating the normal component of the stress over the particle surface, as given in Eq. (5.21). For the following investigations, it is useful to separate $\boldsymbol{F}$ into a component $\boldsymbol{F}^e$ originating from elastic distortions, and a component $\boldsymbol{F}^v$ originating from viscous stresses. As noted in Sec. 5.4.5, the divergence of the elastic stress $\boldsymbol{T}^e$ leads to a contribution $-f/\mathrm{Er}$ in the pressure, where f is the elastic free energy. Thus we may write the pressure as $p = \tilde{p} - f/\mathrm{Er}$, where $\tilde{p}$ is the pressure contribution due to viscous flow and $-f/\mathrm{Er}$ is the contribution due to elastic distortions. Grouping the elastic contributions together, the force $\boldsymbol{F}^e$ on the particle due to elastic distortions is,

$$F^e_i = \frac{1}{\mathrm{Er}} \oint (f\delta_{ij} + T^e_{ij})\nu_j dS, \tag{5.77}$$

where $\boldsymbol{\nu}$ is the unit normal to the particle. The force $\boldsymbol{F}^v$ on the particle due to viscous flow is the integral of the remaining terms,

$$F_i^v = \oint (-\tilde{p}\delta_{ij} + \tilde{T}_{ij})\nu_j dS. \tag{5.78}$$

Parameter	**Value**	**Comment**
E_0	50 mV/μm	Applied field amplitude
$\epsilon_\perp$	6	Perpendicular dielectric permittivity
$\Delta\mu/\mu_\perp$	0.4	Relative mobility anisotropy
$\Delta\epsilon/\epsilon_\perp$	0	Relative dielectric anisotropy

Table 5.4: Physical constants used in numerical calculations in Sec. 5.5, with remaining parameters listed in Table 2.1

In elastic equilibrium, particle-defect pairs form chains, with defects between adjacent particles [72, 74, 93]. Since electrokinetic forces on a single particle are along the elastic dipole $\boldsymbol{p}$, we expect that when subject to an electric field, and thus a nonzero viscous force, particles in a chain will remain collinear, though the inter-particle separation may change, and the chain pair will be subjected to a net force along $\pm\boldsymbol{p}$. There are a number of numerical challenges to solving the full system of LCEK equations with moving particles; instead we investigate specifically the electrokinetic effect on the average separation of two collinear particles by finding the separation length at which the time-averaged difference in viscous force balances the difference in elastic force.

We solve Eqs. (4.1)-(4.5) on a domain of size $L = 30$, with no-slip boundary conditions for velocity, zero-flux boundary conditions for ion concentration, and AC field of frequency $\omega = 2\pi$ rad/s applied in the horizontal, x-direction by Dirichlet boundary conditions $\Phi(-L/2, y, t) = -L\cos t$, $\Phi(L/2, y, t) = 0$, and Neumann boundary conditions $\epsilon_{yi}\partial_i\Phi = 0$ at $y = \pm L/2$. For this section, lengths are scaled by particle diameter $\ell^* = 2a^* = 25\ \mu m$, rather than particle radius. The remaining physical constants used are listed in Table 5.4. As in Sec. 5.4.5, our results for two-particle systems with homeotropic anchoring includes the effects of backflows.

Figure 5.33 plots the numerically obtained director field, instantaneous charge density, and time-averaged velocity field for two particles at separation $s = 0.426$. Far from the two particles, we anticipate the director to have a dipolar structure, leading to six

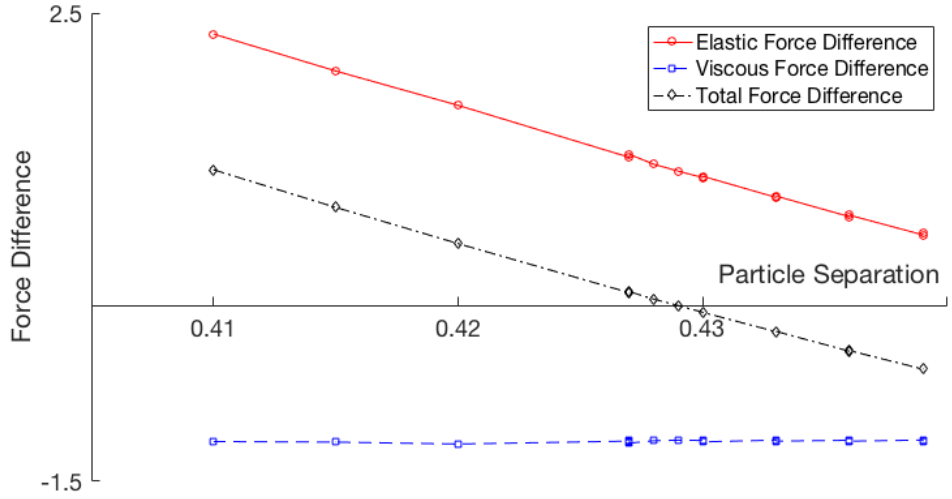

Figure 5.34: Numerical difference in viscous and elastic force between two particle with homeotropic anchoring at Er = 2, averaged over a period of the field and plotted as a function of particle separation. For the range of parameters plotted the viscous force is always attractive, while the elastic force is more repulsive at closer distances. The total force difference is also plotted, and we see the equilibrium position occurs at $s \approx 0.429$.

vortices as seen in Sec. 5.4.1. The behavior of the fluid between the two particles is less clear, but it appears that when the electric field points to the right, as in Fig. 5.33b, the left particle screens positive charges moving right, and the right particle screens negative charges moving left, leading to smaller charge accumulation between the particles.

Figure 5.34 plots the difference average elastic and viscous force between two particles as a function of particle separation at Er = 2. We see that for the range of parameters plotted, the viscous force is attractive and nearly independent of separation s, while the elastic difference is more repulsive as s decreases. We find the total average force difference is zero at $s \approx 0.429$. Thus while the total force on the two particles is not zero (the dipolar nature of the director field causes their center of mass to translate), the relative separation of the two particles is smaller than in the absence of the electrostatic field.

In order to compute the average separation of the two particles as a function of Ericksen number, we solved the electrokinetic system for a variety of particle separations

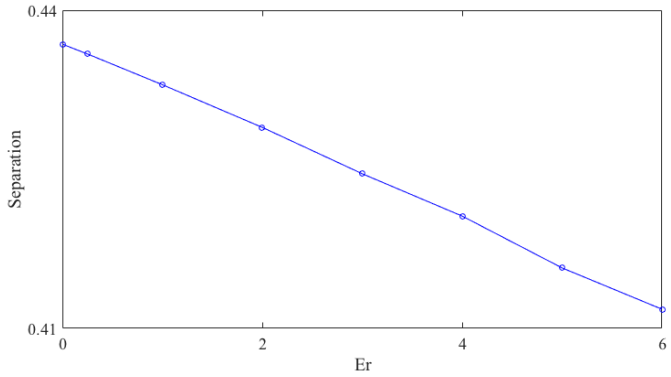

Figure 5.35: Particle separation as a function of Ericksen number. The decrease in separation as Er increases implies the viscous LCEK force is attractive.

s; at each s we find the value of Er at which the difference in viscous force between the two particles balances the difference in elastic force. Figure 5.35 plots the separation distance at which the average viscous force difference balances the elastic force difference, as a function of Ericksen number. We see that the separation decreases as the Ericksen number increases, consistent with an attractive viscous force. Therefore, we would expect a chain of particles suspended in a nematic would cluster more closely together when subject to an applied field. It is important to note that Fig. 5.35 plots only the average particle separation. Since the electric field is oscillating, the viscous force and therefore the interparticle separation will also oscillate. We have not considered the effects of particle oscillations, which will likely contribute to the electrokinetics of the system, particularly when the amplitude of the particle oscillations is on the order of the particle separations. Our results suggest that without the effects of particle oscillations, even at Ericksen number as high as 6, the decrease in interparticle separation is less than 6%.

5.5.2 Tangential anchoring

Spherical particles with tangential anchoring also form chains in elastic equilibrium, but the chains are oriented at an angle of $\sim 30^\circ$ from the far-field director orientation $\hat{\boldsymbol{n}}_0$ [75]. We model this behavior using circular particles with director angle $\theta = \tan^{-1}(-\nu_x/\nu_y)$ on the particle boundary, where $\boldsymbol{\nu}$ is the unit normal to the boundary. This boundary

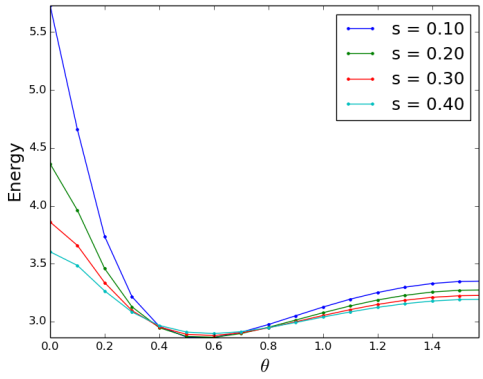

Figure 5.36: Elastic energy for system of two circles at various surface-to-surface separations s and angles θ (rad).

condition leads to two defects at opposite ends of each particle which are one-dimensional analogues of boojums on a sphere, as discussed in Sec. 5.3. A numerical advantage of this system is the lack of singularities in the bulk. The finite element method that we use can handle singularities on boundaries, so that the challenges described in Sec. 5.3.2 are not present, and no regularization of the director field is needed.

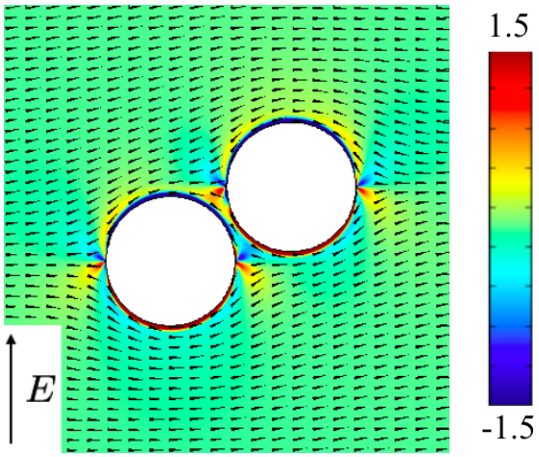

Figure 5.37: Instantaneous charge density in color for system of two circular particles fixed at the position minimizing elastic free energy, subject to an electric field pointing vertically upward

We first confirm the elastic equilibrium position for two circular particles by minimizing the elastic free energy at a variety of separations and angles, Fig. 5.36. We find elastic equilibrium at $\theta \approx 31.5°$, consistent with the experimental results in Ref. [75]. We also find the energy is minimized when the separation between the particle surfaces is approximately $s \approx 0.2$.

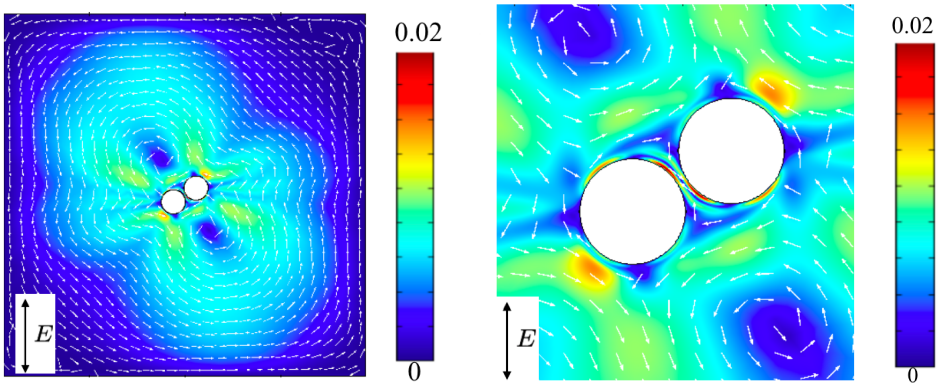

(a) (b)

Figure 5.38: (a) Time-averaged electrokinetic velocity for system of two circular particles with tangential anchoring and imposed field perpendicular to $\hat{\boldsymbol{n}}_0$. (b) Magnification of same result to show boundary layer near particle surfaces.

Figure 5.37 plots the instantaneous charge density for two circular particles fixed at the elastic equilibrium position and orientation, with director field perpendicular to $\hat{\boldsymbol{n}}_0$, while the corresponding average velocity is plotted in Fig. 5.38. For this study, we assume $\mathrm{Er} \ll 1$ and do not consider the effects of backflows. Unlike in the previous two-particle studies with homeotropic anchoring, we find the velocity forms a boundary layer near the particle surfaces; the origins of this boundary flow are not yet understood. Since the system has no dipole moment, we do not expect any systematic flow, and indeed we find no net force on the two-particle system. However, we do find two particles experience a repulsive viscous force and positive torque about their center of mass, suggesting that if free to move the particle separation would increase, as would their orientation angle relative to $\hat{\boldsymbol{n}}_0$. Further investigation is needed to determine the size of this effect and the mechanisms responsible for it.

5.5.3 Assymetrical particles

We have also considered LCEK of assymetrical particles, analogous to those studied in Ref. [94]. We consider two pear-shaped particles in two dimensions, with tangential surface anchoring and applied field perpendicular to far-field director orientation $\hat{\boldsymbol{n}}_0$. As with the circular particles with tangential anchoring above, in elastic equilibrium the pear-shaped particles will align at an angle ϕ_0 from $\hat{\boldsymbol{n}}_0$.

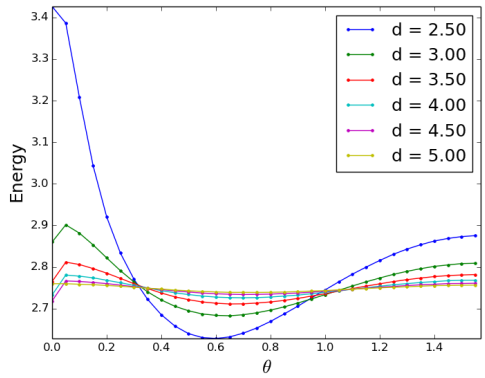

Figure 5.39: Elastic energy as a function of alignment angle of two anisometric particles relative to $\hat{\boldsymbol{n}}_0$.

Figure 5.39 plots the elastic free energy as a function of θ_0 for a variety of particle separations. Since the particles have assymmetrical boundaries, we write the particle separation as a function of d, the distance between the centers of the two particles, rather than the surface-to-surface distance s used in the previous section. We find the energy is minimized at $\theta_0 \approx 33.2°$ and at separation $d = 2.2$.

While boojums on the surface of three-dimensional particles have finite energy, one must take care in computing the energy of a two-dimensional system with point defects or defects on surfaces. Consider a point defect of charge m. The director angle in polar coordinates $\theta(r, \phi) = m\phi$, implying the free energy density is $f \sim m^2/r^2$. Therefore the total energy of a point defect is diverges logarithmically. Instead we introduce a core size ϵ_c and write the total energy as $F \sim \log(R/\epsilon_c) + F_{core}$ where F_{core} is an ansatz for the core energy [78].

To investigate the behavior of the defects at the surface of the pear-shaped particles, we compute the free energy density as a function of radial distance from a surface defect

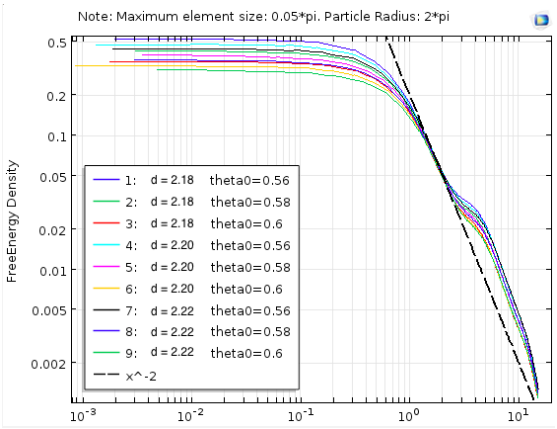

Figure 5.40: Log-log plot of elastic free energy density as a function of radial distance near the core of a defect at the surface of a pear-shaped particle. For $r \lesssim 1$ and at distances much greater than the mesh size, we see the energy density decays as r^{-2}, as expected for a point defect.

for a variety of particle separations and orientations, Fig. 5.40. We find that for $r \lesssim 1$ the free energy density decays as $\sim r^{-2}$, as anticipated for a two-dimensional point defect. The radial behavior changes as we approach the size of the numerical mesh. Thus we exclude a small core region of size $\delta_c = 0.01$ when computing free energy for both circular and pear-shaped particles.

The instantaneous charge density for the system fixed at elastic equilibrium is shown in Fig. 5.41, with velocity plotted in Fig. 5.42 The overall flow structure across the cell is qualitatively similar to the system of circular particles with tangential anchoring. Unlike the case of circular particles, the particle shape breaks left-right symmetry, leading to a net viscous force to the right at an angle approximately 11° below the x axis. Additionally, the relative viscous force on each particle is repulsive, and the two-particle system experiences a positive torque about its center of mass. Like the circular particles, the fluid velocity forms a boundary layer near the particle surface, Fig. 5.42b. The origins of this boundary layer are not known, and further investigation is required to understand the mechanisms and scale for the viscous forces and torques on the system. Additionally, our investigation was conducted assuming the dipole moment of each particle was aligned with $\hat{\boldsymbol{n}}_0$, based on the theoretical work of Ref. [74]. It is possible that the orientation of each individual particle, orientation of the two-particle system,

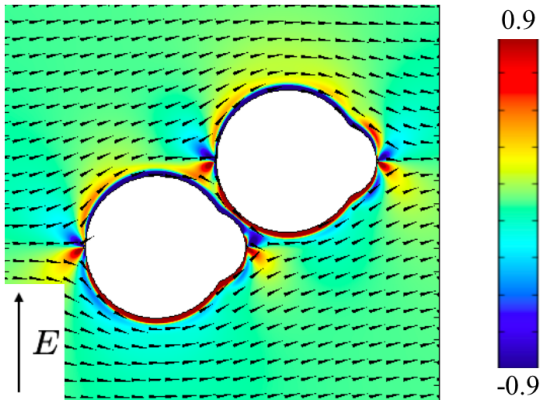

Figure 5.41: Instantaneous charge density for system of two anisometric particles fixed at elastic equilibrium. Note the electric field is oriented upward in the figure.

and inter-particle separation are all modified by LCEK flows.

To summarize, distortions and topological defects formed due to the presence of suspended particles drive LCEK fluid flow and particle motion in nematic colloids. Director distortions induce charge separation due to mobility and permittivity anisotropies, which drive fluid flow, as predicted from the electrokinetics of disclinations discussed in Chapter 4. LCEK velocities show a linear dependence on the difference in mobility and permittivity anisotropy, which can be manipulated to reverse motion of suspended particles via control of nematic composition and temperature. Particle-hedgehog pairs with homeotropic anchoring experience an attractive electrokinetic force, while the viscous force on circular and anisometric particles with tangential anchoring is repulsive. The off-axis alignment of particles with tangential anchoring leads to an additional torque due to LCEK flow, which has the potential to create more complex effects than in nematic colloids with homeotropic anchoring.

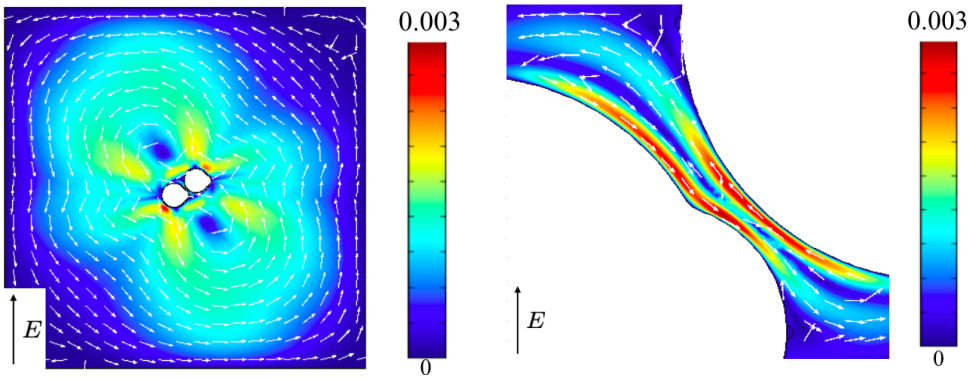

(a) (b)

Figure 5.42: (a) Time-averaged electrokinetic velocity for system of two anisometric particles with tangential anchoring and imposed field perpendicular to $\hat{\boldsymbol{n}}_0$. (b) Magnification of same result to show boundary layer near particle surfaces.

Chapter 6

Active-Like Flows in LCEK Systems

6.1 Introduction

In this chapter we investigate the ways in which the results that we have obtained for LCEK can be used to model a few elements of the behavior of active systems in a nematic matrix. Active systems are composed of particles which can self-propel along a particular direction. Examples include living systems such as bacterial colonies or schools of fish, and non-living particle collections such as rods on a vibrating membrane or catalytic motors in aqueous hydrogen peroxide [95, 96]. Experimental studies of quasi-2D active systems such as microtubules and kinesin motors in Ref. [97] find that active forces generically lead to the nucleation of numerous pairs of topological defects, and the combination of active stress and elastic stress drive fluid flow. Another type of active system is the so called living liquid crystal (LLC), composed of a mixture of active bacteria and a passive liquid crystal matrix in its nematic phase [66]. Experimental and numerical investigations of LLCs show a number of qualitatively interesting phenomena, including bacterial segregation induced by topological defects: higher bacterial concentration at $(+1/2)$ defects, and lower concentration at $(-1/2)$ defects [98]. These results suggest that nematic liquid crystalline matrices can be used to control the motion of active matter, a subject of considerable interest. Such tailor made flows can be orchestrated by photo-patterning techniques similar to those described in Chapter 2.

In addition, the effect of fixed isolated disclinations on active flows has been investigated experimentally, showing the unexpected result that bacterial macroscopic flows do not always align with the nematic director $\hat{\boldsymbol{n}}$, despite the local propensity of active particles to move parallel to the director [6].

This chapter proposes a possible mapping between the governing equations of certain LCEK systems and those of living liquid crystals. When two mutually orthogonal AC fields are applied to an LCEK system, we show that the time-averaged electrokinetic body force has the same the form as the postulated driving stress in an active system. We begin this chapter by considering a prototypical configuration in which the electrokinetic flow due to a rotating applied field would lead to a corresponding flow in an LLC. We then generalize these results and discuss the origins of the active stress, and how the resulting terms compare to electrokinetic stresses. Next we discuss the equations governing bacterial concentrations in LLC systems and the range of parameters in which they agree with the equations governing the motion of the ionic species in LCEK. We conclude with a discussion of the challenges and limitations in comparing these two distinct physical systems.

6.2 Electrokinetic and active flows due to a spiral director vortex

We begin with a prototypical example of a simple LLC system which produces systematic flow: bacteria in a nematic matrix with fixed spiral director field. This system has been considered experimentally in Ref. [6], in which a director field with director angle $\theta(r,\phi) = \phi - \pi/4$ is imposed through the same photo-patterning method discussed in Chapter 2. Experiments on the living system show that the bacterial ensemble rotates around the defect center, with an azimuth velocity profile that depends on the radial coordinate as $\boldsymbol{v}(r,\phi) \propto r \log r \; \hat{\boldsymbol{\phi}}$ (Fig. 6.1a [6]). In this section we extend the results of Chapter 3 to determine the electrokinetic velocity for the same imposed pattern; first with applied field $\boldsymbol{E} = \hat{\boldsymbol{x}} \cos t$ as before, and then with $\boldsymbol{E} = \hat{\boldsymbol{x}} \cos t + \hat{\boldsymbol{y}} \sin t$. We will compare these results to the velocity profile of the active system.

Consider a thin film of a nematic fluid with an imposed (+1) disclination director pattern, shifted by a phase $\pi/4$, $\theta(r,\phi) = \phi - \pi/4$. Following the same procedure as

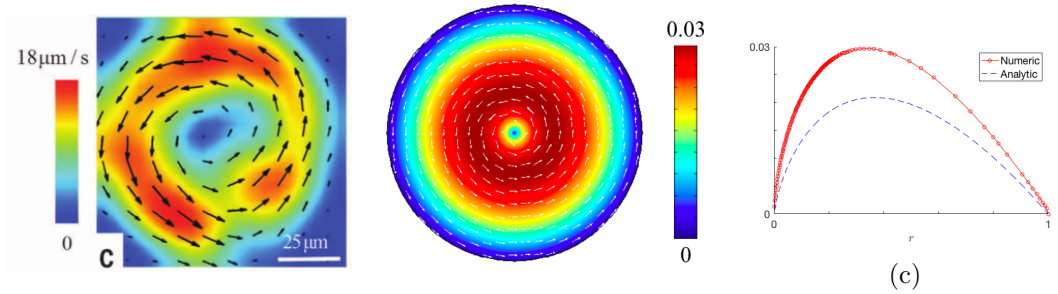

(a) (b) (c)

Figure 6.1: (a) Experimental average velocity field of LLC with imposed director angle $\theta = \phi - \pi/4$, reproduced from Ref. [6]. (b) Time-average numerical LCEK velocity generated by a rotating imposed field of constant magnitude and fixed director angle $\theta = \phi - \pi/4$. (c) Angular component of numerical velocity plotted as a function of r alongside the analytical solution given by Eq. (6.20). Both solutions exhibit $r \log r$ behavior.

deriving Eq. 3.30 in Chapter 3, under an applied field $\boldsymbol{E} = \cos(t)\hat{\boldsymbol{x}}$, the charge density for $r \gg 1$ to first order in Δ is,

$$\rho(\xi, \phi, t) = \left(\frac{\Delta\mu}{\bar{\mu}} - \frac{\Delta\epsilon}{\bar{\epsilon}}\right) \frac{\sin\phi}{2\sqrt{\gamma}(1+\Omega^2)^{\frac{1}{4}}} [e^{i(t-\delta/2)} f(\xi) + e^{-i(t-\delta/2)} f^*(\xi)], \tag{6.1}$$

where $\tan\delta = \Omega$, $\xi = r/\sqrt{\gamma/(1+i\Omega)}$, and,

$$f(\xi) = K_1(\xi) - \frac{1}{\xi}, \tag{6.2}$$

where $K_1(\xi)$ is a modified Bessel function. At $\xi \gg 1$, Eq. (6.1) becomes,

$$\rho(r, \phi, t) = -\left(\frac{\Delta\mu}{\bar{\mu}} - \frac{\Delta\epsilon}{\bar{\epsilon}}\right) \frac{\cos(t-\delta)}{\sqrt{1+\Omega^2}} \frac{\sin\phi}{r}. \tag{6.3}$$

Using Eq. (6.3), the electrostatic body force at first order in Δ at $\xi \gg 1$ is,

$$\rho\boldsymbol{E} = -\left(\frac{\Delta\mu}{\bar{\mu}} - \frac{\Delta\epsilon}{\bar{\epsilon}}\right) \frac{\cos(t-\delta)\cos t}{\sqrt{1+\Omega^2}} \frac{\sin\phi}{r} \hat{\boldsymbol{x}}, \tag{6.4}$$

and we recall the momentum balance equation in elastic equilibrium,

$$-\nabla p + \nabla \cdot \tilde{\boldsymbol{T}} + \rho \boldsymbol{E} = 0, \tag{6.5}$$

where $\tilde{\boldsymbol{T}}$ is the nematic stress tensor.

Equation (6.4) has one term proportional to $\sin(2t)$ which will average to zero over time, and a term proportional to $\cos^2 t$, which will have a nonzero temporal average. We will consider just the systematic part of Eq. (6.4), and write $\langle \rho \boldsymbol{E} \rangle = f_0 \boldsymbol{f}(r, \phi)$, where $\boldsymbol{f}(r, \phi) = \hat{\boldsymbol{x}} \sin \phi / r$ is just the spatial term in $\langle \rho \boldsymbol{E} \rangle$, and,

$$f_0 = -\left(\frac{\Delta \mu}{\bar{\mu}} - \frac{\Delta \epsilon}{\bar{\epsilon}} \right) \frac{1/2}{1 + \Omega^2}. \tag{6.6}$$

Writing $\boldsymbol{f}$ in polar coordinates, one obtains the resulting average body force on the fluid,

$$\boldsymbol{f} = \frac{\cos(2\phi)}{2r} \hat{\boldsymbol{\phi}} - \frac{1}{2r} \hat{\boldsymbol{\phi}} + \frac{\sin(2\phi)}{2r} \hat{\boldsymbol{r}}. \tag{6.7}$$

The first term in Eq. (6.7) may be written as ∇g, where,

$$g(\phi) = \frac{\sin(2\phi)}{4}, \tag{6.8}$$

and therefore the first term in Eq. (6.7) can be included in a redefintion of the pressure in this incompressible fluid. The second term in Eq. (6.7) also has zero curl, which would suggest that it too can be included in the pressure. However, this term may be rewritten as,

$$-\frac{1}{2r} \hat{\boldsymbol{\phi}} = \nabla \left(-\frac{\phi}{2} \right) \tag{6.9}$$

Thus if this term were included in the pressure, we would find that the pressure is not single valued, $p(\phi) \neq p(\phi + 2\pi)$, which is unphysical. Therefore the body force given by the second term in Eq. (6.7) even though irrotational must be balanced by a viscous force instead. Specifically, if we assume the viscous stress to be Newtonian, $\tilde{T}_{ij} = \partial_j v_i$, we can write $\boldsymbol{v}(r, \phi) = f_0(\boldsymbol{v}_1(r\phi) + \boldsymbol{v}_2(r, \phi))$ and $p(r, \phi) = f_0(p_1(r, \phi) + p_2(r, \phi) + g(\phi))$, with

$$-\nabla p_1 + \nabla^2 \boldsymbol{v}_1 - \frac{1}{2r} \hat{\boldsymbol{\phi}} = 0, \tag{6.10}$$

$$-\nabla p_2 + \nabla^2 \boldsymbol{v}_2 + \frac{\sin(2\phi)}{2r}\hat{\boldsymbol{r}} = 0. \tag{6.11}$$

Suppose we solve this system on a disc of unit radius with no-slip boundary conditions at $r = 1$. Equation (6.10) is solved with p_1 uniform and $\boldsymbol{v}_1$ defined as,

$$\boldsymbol{v}_1 = \frac{1}{4} r \log r \hat{\boldsymbol{\phi}}. \tag{6.12}$$

Meanwhile, Eq. (6.11) may be solved by defining the stream function ψ_2 such that $\nabla \times (-\psi_2 \hat{\boldsymbol{z}}) = \boldsymbol{v}_2$. Then taking the curl of Eq. (6.10), we find the following equation for ψ_2,

$$\nabla^4 \psi_2 = \frac{\cos(2\phi)}{r^2} \tag{6.13}$$

We recognize this as the solution for the stream function equation for a (+1) disclination with no phase, as discussed in Chapter 3, except with $\phi \to \phi - \pi/2$. The solution to Eq. (6.13) satisfying the stated boundary conditions is,

$$\psi_2 = -\frac{r^2}{16}\cos(2\phi)\left(\frac{1}{2}(1 - r^2) + \log r\right) \tag{6.14}$$

Therfore, the full stream function ψ satisfying $\nabla \times (-\psi \hat{\boldsymbol{z}}) = f_0(\boldsymbol{v}_1 + \boldsymbol{v}_2)$ is,

$$\psi(r, \phi) = -\frac{f_0}{16} r^2 (1 - 2\log r) - \frac{f_0 r^2}{16}\cos(2\phi)\left(\frac{1}{2}(1 - r^2) + \log r\right). \tag{6.15}$$

Thus the systematic (nonzero average) flow is a combination of a circulating flow and a quadrupolar flow.

Suppose instead that the applied field were $\boldsymbol{E} = \hat{\boldsymbol{y}} \sin t$. Since the system is radially symmetric, this change amounts only to a rotation and phase shift of the solution just given. Thus the charge density at $\xi \gg 1$ is,

$$\rho(r, \phi, t) = \left(\frac{\Delta\mu}{\bar{\mu}} - \frac{\Delta\epsilon}{\bar{\epsilon}}\right)\frac{\sin(t - \delta)}{\sqrt{1 + \Omega^2}}\frac{\cos\phi}{r}, \tag{6.16}$$

while the systematic part of the stream function is,

$$\psi(r, \phi) = -\frac{f_0}{16} r^2 (1 - 2\log r) + \frac{f_0 r^2}{16}\cos(2\phi)\left(\frac{1}{2}(1 - r^2) + \log r\right). \tag{6.17}$$

Since at first order in Δ the equation governing charge density is linear in both ρ and $\boldsymbol{E}$, the total charge density for a rotating field of constant magnitude, $\boldsymbol{E} = \hat{\boldsymbol{x}}\cos t + \hat{\boldsymbol{y}}\sin t$, is just the a linear combination of the two charge densities found above. Thus at $\xi \gg 1$, the charge density for this field is

$$\rho(r,\phi,t) = -\left(\frac{\Delta\mu}{\bar{\mu}} - \frac{\Delta\epsilon}{\bar{\epsilon}}\right)\frac{1}{\sqrt{1+\Omega^2}}\left(\frac{\cos(t-\delta)\sin\phi}{r} - \frac{\sin(t-\delta)\cos\phi}{r}\right), \tag{6.18}$$

Thus the systematic part of the electrostatic body force is $\langle\rho\boldsymbol{E}\rangle = f_0\boldsymbol{f}(r,\phi)$, where f_0 is again defined by Eq. (6.6) and,

$$\boldsymbol{f}(r,\phi) = -\frac{\hat{\boldsymbol{\phi}}}{r} + \frac{\Omega\hat{\boldsymbol{r}}}{r}. \tag{6.19}$$

The first term in Eq. (6.19) is twice the second term in Eq. (6.7). The remaining terms in Eq. (6.7) are cancelled by their corresponding terms due to the induced field along y. The second term in Eq. (6.19) originates from the systematic part of the cross terms $\cos(t-\delta)\sin t$ and $\sin(t-\delta)\cos t$. However, this term may be written as $\nabla(\Omega\log r)$, so it can be included in the pressure. The stream function corresponding to Eq. (6.19) is,

$$\psi = -\frac{f_0}{8}r^2(1-2\log r). \tag{6.20}$$

While the force on the fluid due to the rotating field $\boldsymbol{E} = \hat{\boldsymbol{x}}\cos t + \hat{\boldsymbol{y}}\sin t$ is not simply the sum of the forces due to $\hat{\boldsymbol{x}}\cos t$ and $\hat{\boldsymbol{y}}\sin t$, the additional cross terms in Eq. (6.19) only contribute to a change in pressure; thus the stream function Eq. (6.20) is the sum of Eqs. (6.15) and (6.17).

Equation (6.20) corresponds to a velocity field $\boldsymbol{v} = (f_0/2)r\log r\hat{\boldsymbol{\phi}}$. Thus to first order in Δ and far from defect cores, the velocity field of a nematic with fixed spiral pattern subject to a uniform rotating field has the same form as the observed velocity field of an LLC under a fixed spiral director configuration.

To further confirm Eq. (6.20) we have numerically computed the LCEK velocity for a spiral director pattern and under a rotating electrostatic field as described above. The parameters used are listed in Table 6.1. Figure 6.1b plots the numerical velocity field, averaged over a period of the applied field. Figure 6.1c plots the average angular component of both the analytical and numerical velocity field. While the numerical

Parameter	Value	Comment
ω	10π rad/s	Applied field frequency
ℓ^*	600 μm	Radius of nematic cell
E_0	40 mV/μm	Applied field amplitude
$\bar{\epsilon}$	6	Average dielectric permittivity
$\Delta\mu/\bar{\mu}$	0.34	Relative mobility anisotropy
$\Delta\epsilon/\bar{\epsilon}$	0	Relative dielectric anisotropy

Table 6.1: Physical constants used in numerical LCEK calculations in this chapter. The remaining parameters are the same as those listed in Table 2.1

and analytical solutions differ by a factor of approximately 1.4, they both exhibit $r \log r$ behavior. It is unclear why the difference in magnitude between the numerical an analytical results is so large, though we note that Eq. (6.20) was derived assuming small anisotropy, while the numerical value used, $\Delta\mu/\bar{\mu} = 0.34$ is not vanishingly small. Additionally, Eq. (6.20) neglects charge effects near the defect cores, which may not be negligible, as discussed in Chapter 5. However, the agreement in order of magnitude and in the $r \log r$ behavior of the numerical solution and Eq. (6.20) suggests that for this fixed nematic configuration, the electroosmotic flow generated by a rotating field mimics the flow generated by swimming bacteria in a nematic matrix with fixed director orientation.

6.3 General comparison of driving terms in active nematics and electrokinetic systems

Of course, the connection between both systems is not superficial. We explore in this section the equations governing fluid flow in both systems. The momentum equations for both systems may be written as,

$$-\nabla p + \nabla \cdot \boldsymbol{T}^r + \nabla \cdot \boldsymbol{T}^d + \boldsymbol{f} = 0 \tag{6.21}$$

where p is the pressure and $\boldsymbol{T}^r, \boldsymbol{T}^d$ are the reactive and dissipative parts of the stress, respectively. There are some differences in $\boldsymbol{T}^r, \boldsymbol{T}^d$ between LCEK and active systems due to their different physical nature. However, this discussion is beyond the scope of

this thesis. We focus here on the driving body force $\boldsymbol{f}$ which ultimately generates flows in both cases. In LCEK systems, it is the electrostatic force density $\rho\boldsymbol{E}$. In active nematics, it is the force on the fluid driven by active particles. We first explore the origins and form of $\boldsymbol{f}$ for active particles; then we examine the conditions in which the force $\rho\boldsymbol{E}$ in electrokinetic systems can be mapped onto the body force $\boldsymbol{f}$ in active systems.

6.3.1 Active Stress

Consider a collection of self-propelling particles in an ambient fluid. Let $\boldsymbol{a}^\alpha$ be the primary axis of particle α located at $\boldsymbol{r}^\alpha$ with length $|\boldsymbol{a}^\alpha|$. Following a procedure similar to Ref. [99], particle α exerts a force $\boldsymbol{f}^\alpha \propto \pm\boldsymbol{a}^\alpha$ on its surrounding fluid. By Newton's third law, the net force on the particle-fluid system is zero. Therefore, assume there is a pair of forces on the particle-fluid system $\pm\boldsymbol{f}^\alpha$ at $\boldsymbol{r}^\alpha \pm \frac{1}{2}\boldsymbol{a}^\alpha$. Summing over all particles, the force density $\tilde{\boldsymbol{f}}(\boldsymbol{r})$ is,

$$\tilde{\boldsymbol{f}}(\boldsymbol{r}) \propto \sum_\alpha \boldsymbol{a}^\alpha[\delta(\boldsymbol{r}-\boldsymbol{r}^\alpha-\frac{1}{2}\boldsymbol{a}^\alpha)-\delta(\boldsymbol{r}-\boldsymbol{r}^\alpha+\frac{1}{2}\boldsymbol{a}^\alpha)] \tag{6.22}$$

Assume particle lengths $|\boldsymbol{a}^\alpha|$ are much smaller than the system size L. Then to first order in $\boldsymbol{a}^\alpha$, Eq. 6.22 is,

$$\tilde{\boldsymbol{f}}(\boldsymbol{r}) \propto \frac{\partial}{\partial x_j}\left[\sum_\alpha a_i^\alpha a_j^\alpha \delta(\boldsymbol{r}-\boldsymbol{r}^\alpha)\right]. \tag{6.23}$$

We coarse grain Eq. (6.23) and write the coarse-grained active force density $\boldsymbol{f}(\boldsymbol{r}) = \langle\tilde{\boldsymbol{f}}(\boldsymbol{r})\rangle$ as the divergence of an active stress, $f_i = \partial_j\sigma_{ij}^A$, with

$$\sigma_{ij}^A = -\Lambda c(\boldsymbol{r}) n_i n_j \tag{6.24}$$

where $c(\boldsymbol{r})$ is the concentration of active particles and, as with passive nematics, the director field $\hat{\boldsymbol{n}}(\boldsymbol{r})$ is the coarse-grained average of active particle orientations, with $\hat{\boldsymbol{n}}^2 = 1$. The parameter Λ is the force dipole moment associated with the active particles, and is positive for "pusher"type particles and negative for "puller"types [14].

6.3.2 Active-like forces in LCEK

Given the form of the body force in active systems, we consider next the electrokinetic force generated by an electric field oscillating in the $\hat{\boldsymbol{x}}$ and $\hat{\boldsymbol{y}}$ directions, and a fixed director field. We begin by discussing the general case in which $\hat{\boldsymbol{n}}(\boldsymbol{r})$ is arbitrary and the applied field comprises two orthogonal components which differ in amplitude and phase. We then consider the special case of a rotating field of constant magnitude, and a director pattern that is fixed and has one single disclination in Sec. 6.2.

For the remainder of the chapter we use the scalings of Chapter 4, with $\epsilon_\perp, \mu_\perp$ as the characteristic permittivity and mobility for scaling rather than $\bar{\epsilon}, \bar{\mu}$ This choice allows us to more easily compare the governing equations for active and LCEK systems.

Consider a nematic thin film with the director orientation fixed by the boundaries, and assume that mass diffusion is small ($\gamma \ll 1$) with an overall ioninc concentration that is large ($Y^2 \ll 1$). Suppose an electric field is imposed, with two orthogonal components of different frequency and phase, $\boldsymbol{E} = \hat{\boldsymbol{x}}\cos t + A\hat{\boldsymbol{y}}\cos(\beta t + \gamma)$. This is a rotating field of constant magnitude when $A = 1$, $\beta = 1$, and $\gamma = \pi/2$. Far from defect cores, the equation for the charge density ρ can be written as,

$$\Omega\frac{\partial \rho}{\partial t} + \rho = (\tilde{\epsilon} - \tilde{\mu})\,\nabla\cdot(\boldsymbol{n}(\boldsymbol{n}\cdot\boldsymbol{E})), \tag{6.25}$$

where $\tilde{\epsilon} = \Delta\epsilon/\epsilon_\perp$ and $\tilde{\mu} = \Delta\mu/\mu_\perp$. As discussed in Chapter 4, the solution to Eq. (6.25) to first order in Δ is,

$$\rho(\boldsymbol{r}, t) = (\tilde{\epsilon} - \tilde{\mu})\,\frac{\cos(t-\delta)}{\sqrt{1+\Omega^2}}\nabla\cdot(\boldsymbol{n}n_x) + (\tilde{\epsilon} - \tilde{\mu})\,\frac{\cos(\beta t + \gamma - \delta_2)}{\sqrt{1+(\beta\Omega)^2}}A\nabla\cdot(\boldsymbol{n}n_y), \tag{6.26}$$

with $\tan\delta = \Omega$ and $\tan\delta_2 = \beta\Omega$. To first order in $(\tilde{\epsilon} - \tilde{\mu})$, the body force on the nematic fluid is $\boldsymbol{f} = \rho\boldsymbol{E} = \rho(\boldsymbol{r}, t)(\hat{\boldsymbol{x}}\cos t + A\hat{\boldsymbol{y}}\cos(\beta t + \gamma))$, or,

$$\begin{aligned}\boldsymbol{f} = (\tilde{\epsilon} - \tilde{\mu})\Bigg[&\frac{\cos t\cos(t-\delta)}{\sqrt{1+\Omega^2}}\nabla\cdot(\boldsymbol{n}n_x\hat{\boldsymbol{x}}) + \frac{A^2\cos(\beta t+\gamma)\cos(\beta t+\gamma-\delta_2)}{\sqrt{1+(\beta\Omega)^2}}\nabla\cdot(\boldsymbol{n}n_y\hat{\boldsymbol{y}})\\ &+\frac{A\cos(\beta t+\gamma)\cos(t-\delta)}{\sqrt{1+\Omega^2}}\nabla\cdot(\boldsymbol{n}n_x\hat{\boldsymbol{y}}) + \frac{A\cos t\cos(\beta t+\gamma-\delta_2)}{\sqrt{1+(\beta\Omega)^2}}\nabla\cdot(\boldsymbol{n}n_y\hat{\boldsymbol{x}})\Bigg]\end{aligned} \tag{6.27}$$

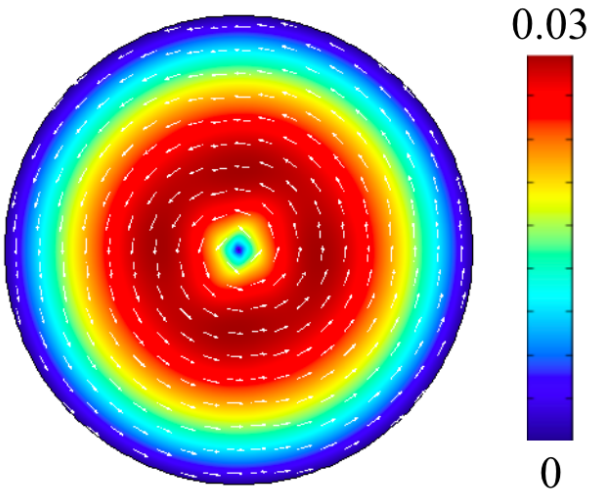

Figure 6.2: Average LCEK velocity for imposed director field $\theta = \phi - \pi/4$ and applied field given by Eq. (6.32) with $\beta = 2$.

We define a time-averaged force, $\langle \boldsymbol{f} \rangle = (1/T) \int_0^T \boldsymbol{f} dt$. Note that

$$\lim_{T\to\infty} \frac{1}{T} \int_0^T \cos(t-\delta)\cos(\beta t + \gamma) dt = \begin{cases} \frac{1}{2}\cos(\delta+\gamma), & |\beta| = 1 \\ 0, & \text{otherwise} \end{cases} \tag{6.28}$$

$$\lim_{T\to\infty} \frac{1}{T} \int_0^T \cos t \cos(\beta t + \gamma - \delta_2) dt = \begin{cases} \frac{1}{2}\cos(\delta-\gamma), & |\beta| = 1 \\ 0, & \text{otherwise} \end{cases} \tag{6.29}$$

Assume first $|\beta| \neq 1$. Then the last two terms of Eq. (6.27) average to zero, and the average force is,

$$\langle \boldsymbol{f} \rangle = (\tilde{\epsilon} - \tilde{\mu}) \left[\frac{\nabla \cdot (\boldsymbol{n} n_x \hat{\boldsymbol{x}})}{2(1+\Omega^2)} + \frac{A^2 \nabla \cdot (\boldsymbol{n} n_y \hat{\boldsymbol{y}})}{2(1+(\beta\Omega)^2)} \right] \tag{6.30}$$

Let $A = \sqrt{(1+(\beta\Omega)^2)/(1+\Omega^2)}$. Then Eq. (6.30) becomes,

$$\langle \boldsymbol{f} \rangle = (\tilde{\epsilon} - \tilde{\mu}) \frac{\nabla \cdot (\boldsymbol{n}\boldsymbol{n})}{2(1+\Omega^2)}. \tag{6.31}$$

Equation (6.31) has the same form as in active nematics, $f_i \propto \partial_j n_i n_j$. Thus for

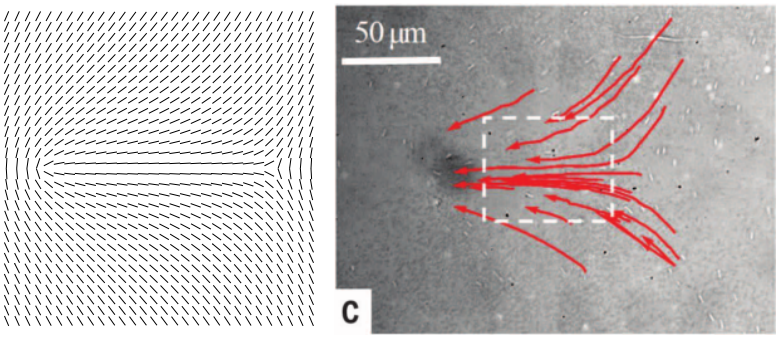

(a) (b)

Figure 6.3: (a) Director pattern for a $(+1/2, -1/2)$ disclination set. (b) Experimental trajectories of bacteria in an LLC with fixed $(1/2, -1/2)$ disclination pattern. Bacterial motion is away from the (-1/2) defect and toward the (+1/2) defect [6].

arbitrary $\Omega = \omega\tau_\rho$, the body force in the electrokinetic system equals that of the active system when the applied field has the form,

$$\boldsymbol{E} = \hat{\boldsymbol{x}} \cos t + \hat{\boldsymbol{y}} \sqrt{\frac{1 + (\beta\Omega)^2}{1 + \Omega^2}} \cos(\beta t + \gamma) \tag{6.32}$$

Figure 6.2 plots the numerically computed average velocity for the electrokinetic model when the director is given by the spiral pattern of Sec. 6.2 and the applied electric field is given by Eq. (6.32) with $\beta = 2$. This velocity field is nearly identical to the velocity field depicted in Fig. 6.1b. Note that the velocity field is not parallel to the local nematic as noted in the experiments. Whereas this is surprising in the context of a living liquid crystal in which bacteria are known to move parallel to the local director, it is not for an electrokinetic system. In the latter case, motion is due to the local body force that originates from charge separation, and does not in general follow director lines. Instead, charge accumulates in regions in which the director is normal to the imposed electric field.

We have also examined another configuration of interest that comprises a pair of fixed disclinations with topological charges $(+1/2, -1/2)$ (Fig. 6.3a). This configuration has been argued to allow steering of propelled particle motion, and therefore potentially useful in guiding and controling the motion of active particles by a nematic matrix. Experimental LLC studies find bacterial motion away from the $(-1/2)$ defect and toward

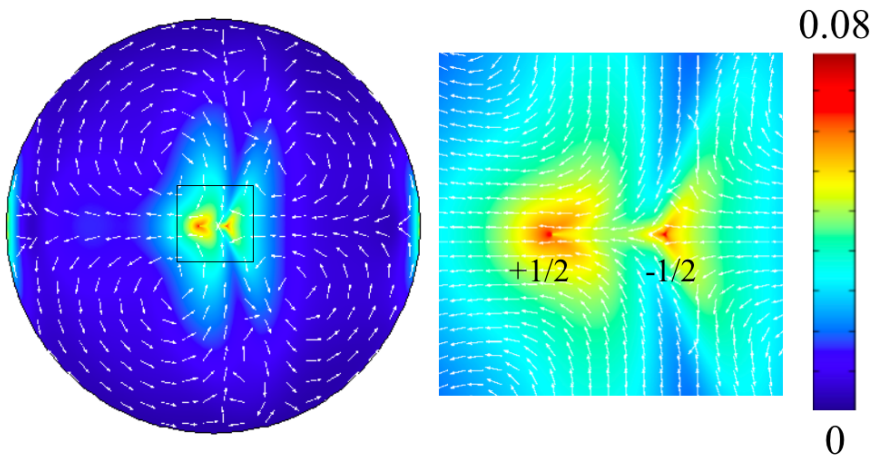

Figure 6.4: Average numerical LCEK velocity for $(+1/2, -1/2)$ disclination set, with magnification of the boxed region shown on the right. Velocity flows from the $(-1/2)$ defect toward the $(+1/2)$ defect.

the $(+1/2)$ defect, as shown in Fig. 6.3b. The average numerical LCEK velocity field obtained for the electrokinetic analog is shown in Fig. 6.4, which also has fluid flow directed toward the $(+1/2)$ defect.

Having shown that LCEK systems can produce active-like forces for $\beta \neq 1$, we next examine the case of a purely rotating field, $\beta = 1$ and $A = 1$. Then in the limit $T \to \infty$ the average force is,

$$\langle \boldsymbol{f} \rangle = (\tilde{\epsilon} - \tilde{\mu}) \frac{[\nabla \cdot (\boldsymbol{nn}) + (\cos\gamma + \Omega \sin\gamma)\nabla \cdot (\boldsymbol{n} n_x \hat{\boldsymbol{y}}) + (\cos\gamma - \Omega \sin\gamma)\nabla \cdot (\boldsymbol{n} n_y \hat{\boldsymbol{x}})]}{2(1+\Omega^2)}. \tag{6.33}$$

In order for the force Eq. (6.33) to generate flows of the type present in an active system, we must be able to write the second and third terms as the sum of a term proportional to $\nabla \cdot (\boldsymbol{nn})$ and a term that only contributes to a change in pressure, i.e.

$$(\cos\gamma + \Omega \sin\gamma)\nabla \cdot (\boldsymbol{n} n_x \hat{\boldsymbol{y}}) + (\cos\gamma - \Omega \sin\gamma)\nabla \cdot (\boldsymbol{n} n_y \hat{\boldsymbol{x}}) \propto \nabla(\boldsymbol{nn}) + \nabla h, \tag{6.34}$$

where h is continuous and differentiable away from disclination cores. Thus in general, such an applied field will not generate active-like forces for arbitrary $\hat{\boldsymbol{n}}(\boldsymbol{r})$, but only for those patterns for which the above condition holds.

Consider now the case of $\gamma = -\pi/2$, so $\boldsymbol{E} = \hat{\boldsymbol{x}}\cos t + \hat{\boldsymbol{y}}\sin t$ is a rotating field of constant magnitude. Equation (6.33) becomes,

$$\langle \boldsymbol{f} \rangle = (\tilde{\epsilon} - \tilde{\mu}) \frac{\nabla \cdot (\boldsymbol{n}\boldsymbol{n}) + \Omega \nabla \cdot (\boldsymbol{n}[n_y \hat{\boldsymbol{x}} - n_x \hat{\boldsymbol{y}}])}{2(1+\Omega^2)}. \tag{6.35}$$

Equation (6.35) is active-like for arbitrary $\hat{\boldsymbol{n}}(\boldsymbol{r})$ but only in the limit $\Omega \to 0$. Otherwise, a rotating field does not in general produce active-like forces.

Finally, suppose the director field consists of a single disclination of charge m located at the origin. In polar coordinates (r, ϕ), the director angle is $\theta(r, \phi) = m\phi + \alpha$, where α is an arbitrary phase shift. Equation (6.35) becomes,

$$\langle \boldsymbol{f} \rangle = (\tilde{\epsilon} - \tilde{\mu}) \frac{m(\hat{\boldsymbol{r}} \cos[2(m-1)\phi + 2\alpha - \delta] + \hat{\boldsymbol{\phi}} \sin[2(m-1)\phi + 2\alpha - \delta])}{2r\sqrt{1+\Omega^2}}. \tag{6.36}$$

For arbitrary $\Omega = \tan\delta$, Eq. (6.36) is the same as the active stress for $m = 1$ only. For $m = 1$, Eq. (6.36) is,

$$\langle \boldsymbol{f} \rangle = (\tilde{\epsilon} - \tilde{\mu}) \frac{\hat{\boldsymbol{\phi}} \sin(2\alpha - \delta)}{2r\sqrt{1+\Omega^2}} + \nabla \left[(\tilde{\epsilon} - \tilde{\mu}) \frac{\log r \cos(2\alpha - \delta)}{2\sqrt{1+\Omega^2}} \right]. \tag{6.37}$$

Thus only the first term in Eq. (6.37) contributes to the velocity in the incompressible case. If we assume the nematic obeys the Navier-Stokes equations (one viscosity) with the body force of Eq. (6.37), then momentum balance can be written as,

$$-\nabla p' + \nabla^2 \boldsymbol{v} + (\tilde{\epsilon} - \tilde{\mu}) \frac{\hat{\boldsymbol{\phi}} \sin(2\alpha - \delta)}{2r\sqrt{1+\Omega^2}} = 0, \quad \nabla \cdot \boldsymbol{v} = 0, \tag{6.38}$$

where

$$p' = p - (\tilde{\epsilon} - \tilde{\mu}) \frac{\log r \cos(2\alpha - \delta)}{2\sqrt{1+\Omega^2}}.$$

The solution to Eq. (6.38) in a disc of radius 1 with no-slip boundary conditions is constant p' and

$$\boldsymbol{v} = -(\tilde{\epsilon} - \tilde{\mu}) \frac{\hat{\boldsymbol{\phi}} \sin(2\alpha - \delta) r \log r}{4\sqrt{1+\Omega^2}}, \tag{6.39}$$

which agrees with the solution found in Sec. 6.2 when $\alpha = -\pi/4$. Note that the flow reverses as $2\alpha - \delta$ changes sign. Thus, unlike in active systems, the flow can be reversed

in the LCEK system by changing the driving frequency, with the velocity vanishing at $\Omega = \tan(2\alpha)$.

To summarize, we find that the average driving force in LCEK systems agrees with the driving force in active systems when the applied field consists of two orthogonal components of different frequencies and magnitudes satisfying Eq. (6.32). For a rotating field of constant magnitude, the LCEK force agrees with the active force for arbitrary director field only in the limit $\Omega \to 0$. However, for the specific case a single (+1) disclination with arbitrary phase, a rotating field does produce active-like forces for arbitrary Ω.

6.4 Correspondence between bacterial and ionic concentrations

Having shown a connection between stresses in LCEK flows and stresses in active systems, we next examine the relationship between mass transport of ionic species in LCEK and transport of bacteria in an LLC. We find agreement in the equations of motion within a narrow range of parameters, and show that the techniques and results from Chapter 3 can be used to determine characteristics of equilibrium bacterial concentrations around isolated disclinations.

Systems of bacterial colonies immersed in liquid crystals have been studied analytically and numerically in Ref. [98]. In that study, the concentration of bacteria c_a is separated into two species, c_a^+, c_a^-, where c_a^+ denotes bacteria moving in one direction along $\hat{\boldsymbol{n}}$ whereas c_a^- denotes bacteria moving in the opposite direction. Note that since the system is invariant under $\hat{\boldsymbol{n}} \to -\hat{\boldsymbol{n}}$, it must also be invariant under $(c_a^+, c_a^-) \to (c_a^-, c_a^+)$. With this definition, and in dimensional units, the concentrations have been argued to satisfy [98],

$$\frac{\partial c_a^{\pm *}}{\partial t^*} + \nabla^* \cdot (\pm V_0 \hat{\boldsymbol{n}} c_a^{\pm *} + \boldsymbol{v}_a^* c^{\pm *}) = \mp \frac{1}{\tau}(c^{+*} - c^{-*}) + D_a \nabla^{*2} c^{\pm *}, \tag{6.40}$$

where V_0 is the intrinsic bacterial velocity, $\boldsymbol{v}_a^*$ is the velocity of the nematic, and D_a is the bacterial diffusivity. The parameter τ is a bacterial reversal time, i.e. a bacterium in c_a^+ travels along $\hat{\boldsymbol{n}}$ for a time τ before reversing direction and thus joining c_a^-.

We anticipate a similarity between the evolution of bacterial concentrations $c_a^{\pm}$ and the average behavior of ionic concentrations c_k in LCEK for the following reasons: Recall from Chapter 2 that the electrostatic drift velocity $\boldsymbol{v}^*_{drift}$ for positive ions has two components,

$$\boldsymbol{v}^*_{drift}(\boldsymbol{r}^*, t^*) = \mu_{\perp}\boldsymbol{E}^*(\boldsymbol{r}^*, t^*) + \Delta\mu\hat{\boldsymbol{n}}(\boldsymbol{r}^*)[\hat{\boldsymbol{n}}(\boldsymbol{r}^*) \cdot \boldsymbol{E}^*(\boldsymbol{r}^*, t^*)]. \tag{6.41}$$

For simplicity, suppose $\boldsymbol{E}^*$ is a uniform rotating field of constant magnitude. For a specific position $\boldsymbol{r}^*$, by averaging over values of $\boldsymbol{E}^*$ for which $\hat{\boldsymbol{n}} \cdot \boldsymbol{E}^* > 0$, we find $\langle E^* \rangle = (2E_0/\pi)\hat{\boldsymbol{n}}$ and $\langle(\hat{\boldsymbol{n}} \cdot \boldsymbol{E}^*)\rangle = 2E_0/\pi$. Thus $\langle \boldsymbol{v}^*_{drift} \rangle = (2\mu_{\parallel}E_0/\pi)\hat{\boldsymbol{n}}$. Similarly, by averaging over values of $\boldsymbol{E}^*$ for which $\hat{\boldsymbol{n}} \cdot \boldsymbol{E}^* < 0$, we find $\langle \boldsymbol{v}^*_{drift} \rangle = -(2\mu_{\parallel}E_0/\pi)\hat{\boldsymbol{n}}$. Thus the average motion of a positive ion in a rotating field matches the motion of a bacteria in the c_a^+ population ($\boldsymbol{v} \sim \hat{\boldsymbol{n}}$) when $\hat{\boldsymbol{n}} \cdot \boldsymbol{E}^* > 0$ and a bacteria in the c_a^- population ($\boldsymbol{v} \sim -\hat{\boldsymbol{n}}$) when $\hat{\boldsymbol{n}} \cdot \boldsymbol{E}^* < 0$. By a nearly identical argument, we find the opposite correspondence for negative ions. Thus we anticipate c_a^+ to be represented by the average concentration of ions with charge sign matching the sign of $(\hat{\boldsymbol{n}} \cdot \boldsymbol{E}^*)$, and c_a^- represented by the average concentration of ions with charge sign matching the sign of $-(\hat{\boldsymbol{n}} \cdot \boldsymbol{E}^*)$.

Furthermore, we may define $c_a(\boldsymbol{r}, t) = c_a^+(\boldsymbol{r}, t) + c_a^-(\boldsymbol{r}, t)$ and $w_a(\boldsymbol{r}, t) = c_a^+(\boldsymbol{r}, t) - c_a^-(\boldsymbol{r}, t)$, where $c_a(\boldsymbol{r}, t)$ represents the total bacterial concentration at $(\boldsymbol{r}, t)$, while $w_a(\boldsymbol{r}, t)$ represents the difference in bacterial concentration. By the argument above and the definitions of c_a, and w_a, we anticipate c_a to be represented by the average total ionic concentration $\langle C \rangle$, while w_a is represented by the average value of ρ when $\hat{\boldsymbol{n}} \cdot \boldsymbol{E} > 0$ and by the average of $-\rho$ when $\hat{\boldsymbol{n}} \cdot \boldsymbol{E} < 0$.

Using the definitions of c_a and w_a, Eqs. (6.40) become,

$$\frac{\partial c_a^*}{\partial t^*} + \nabla^* \cdot (V_0\hat{\boldsymbol{n}}w_a^* + \boldsymbol{v}_a^* c_a^*) = D_a \nabla^{*2} c_a^*, \tag{6.42}$$

$$\frac{\partial w_a^*}{\partial t^*} + \nabla^* \cdot (V_0\hat{\boldsymbol{n}}c_a^* + \boldsymbol{v}_a^* w_a^*) = -\frac{2}{\tau}w_a^* + D_c \nabla^{*2} w_a^*, \tag{6.43}$$

and additionally, recall the nematic velocity satisfies,

$$-\nabla^* p^* + \nabla^* \cdot \boldsymbol{T}^* - \Lambda \nabla^* \cdot (c_a^* \hat{\boldsymbol{n}} \hat{\boldsymbol{n}}) = 0 \tag{6.44}$$

In order to best compare Eqs. (6.42) - (6.44) with the electrokinetic equations for ionic concentration and velocity, we scale lengths by system size ℓ^*, time by ℓ^*/V_0, $\boldsymbol{v}_a^*$ by V_0 c_a^* by its average c_a^*, w_a^* by $\tau V_0 c_a^*/\ell^*$. Then Eqs. (6.42) - (6.44) in dimensionless form are,

$$\Omega_A \frac{\partial c_a}{\partial t} + \nabla \cdot (\Omega_a^2 \hat{\boldsymbol{n}} w_a + \Omega_a \boldsymbol{v} c_a) = \gamma_a \nabla^2 c_a, \tag{6.45}$$

$$\Omega_a \frac{\partial w_a}{\partial t} + \nabla \cdot (\hat{\boldsymbol{n}} c_a + \Omega_a \boldsymbol{v} w_a) = -w_a + \gamma_a \nabla^2 w_a, \tag{6.46}$$

$$-\nabla p + \nabla \cdot \boldsymbol{T} - \kappa \nabla \cdot (c_a \hat{\boldsymbol{n}} \hat{\boldsymbol{n}}) = 0, \tag{6.47}$$

where $\Omega_a = \tau V_0/(2\ell^*)$, $\gamma_a = D_a \tau/\ell^{*2}$, and $\kappa = \Lambda c_{0a}^* \ell^*/(\eta V_0)$, where η is the average viscosity.

To further compare Eqs. (6.45)-(6.47) in a similar limit as the electrokinetic system of Chapter 2, assume $\Omega_a \ll 1$ [1] . The leading order behavior for c_a, w_a then satisfies,

$$\nabla^2 c_a \approx 0 \implies c_a \approx 1, \tag{6.48}$$

$$\nabla \cdot \hat{\boldsymbol{n}} \approx -w_a + \gamma_a \nabla^2 w_a. \tag{6.49}$$

Recall from Chapter 4 that to first order in Δ and assuming $Y^2/\gamma \ll 1$, the charge density satisfies,

$$\Omega \frac{\partial \rho}{\partial t} = \gamma \nabla^2 \rho - \rho - (\tilde{\epsilon} - \tilde{\mu}) \nabla \cdot (\hat{\boldsymbol{n}} (\hat{\boldsymbol{n}} \cdot \boldsymbol{E})), \tag{6.50}$$

where $\boldsymbol{E}$ is the (uniform) applied field. In particular, at low driving frequency, $\Omega \to 0$, Eq. (6.50) is,

$$0 = \gamma \nabla^2 \rho - \rho - (\tilde{\epsilon} - \tilde{\mu}) \nabla \cdot (\hat{\boldsymbol{n}} (\hat{\boldsymbol{n}} \cdot \boldsymbol{E})). \tag{6.51}$$

[1] Typical bacterial velocities are $V_0 \sim 10\ \mu\text{m}/s$ [6, 98], and reversal times $\tau \sim 50 - 100\ s$ [98]. If lengths are scaled by cell size $\ell^* \sim 10\ mm$, then these values imply $\Omega_a \sim 0.05 - 0.1$. While Ω_a is not vanishingly small for these values, it suggests that the assumption $\Omega_a \ll 1$ is not entirely unrealistic.

Note the homogeneous part of Eq. (6.49) agrees with Eq. (6.51).

Suppose $\boldsymbol{E}$ is a rotating field of constant magnitude: $\boldsymbol{E} = \hat{\boldsymbol{x}}\cos t + \hat{\boldsymbol{y}}\sin t$. We have already shown in Sec. 6.3.2 that in the limit $\Omega \to 0$, this field produces active-like forces in the momentum equation. Define $\tilde{w}$ such that,

$$\tilde{w}(\boldsymbol{r},t) = \begin{cases} \rho(\boldsymbol{r},t); & (\boldsymbol{n}\cdot\boldsymbol{E}) \geq 0 \\ -\rho(\boldsymbol{r},t); & (\boldsymbol{n}\cdot\boldsymbol{E}) < 0 \end{cases} \tag{6.52}$$

With this definition, Eq. (6.51) can be written as,

$$\gamma\nabla^2\tilde{w} - \tilde{w} = (\tilde{\epsilon} - \tilde{\mu})\,\nabla\cdot(\hat{\boldsymbol{n}}|\hat{\boldsymbol{n}}\cdot\boldsymbol{E}|). \tag{6.53}$$

By taking the average of Eq. (6.53) over a period of the field, one finds,

$$\gamma\nabla^2\langle\tilde{w}\rangle - \langle\tilde{w}\rangle = (\tilde{\epsilon} - \tilde{\mu})\,\nabla\cdot(\hat{\boldsymbol{n}}\langle|\hat{\boldsymbol{n}}\cdot\boldsymbol{E}|\rangle). \tag{6.54}$$

Note that $\langle|\hat{\boldsymbol{n}}\cdot\boldsymbol{E}|\rangle = \langle|\cos(t-\theta(\boldsymbol{r}))|\rangle = 2/\pi$. Thus Eq. (6.54) becomes,

$$\gamma\nabla^2\langle\tilde{w}\rangle - \langle\tilde{w}\rangle = \frac{2}{\pi}\,(\tilde{\epsilon} - \tilde{\mu})\,\nabla\cdot\hat{\boldsymbol{n}}. \tag{6.55}$$

Note that Eq. (6.55) agrees with Eq. (6.49) if $w_a = (\pi/(2\,(\tilde{\epsilon}-\tilde{\mu})))\langle\tilde{w}\rangle$. Thus we find a direct connection between w_a in active systems and charge density in LCEK systems; specifically the behavior of w_a for $\Omega_a \ll 1$ is proportional to the average of the quantity $\tilde{w}$ in an electrokinetic system under a rotating electric field. This is consistent with the physical argument given at the beginning of this section, w_a behaves as the average of ρ when $\hat{\boldsymbol{n}}\cdot\boldsymbol{E} > 0$ and as the average of $-\rho$ when $\hat{\boldsymbol{n}}\cdot\boldsymbol{E} < 0$.

We can use this connection and the results of Chapter 3 to compute w_a when $\hat{\boldsymbol{n}} = (\cos(\theta(\boldsymbol{r})), \sin(\theta(\boldsymbol{r})))$ is an anchored disclination of charge m with arbitrary phase α, i.e. $\theta(r,\phi) = m\phi + \alpha$. With this director, Eq. (6.49) becomes,

$$\frac{m\cos[(m-1)\phi+\alpha]}{r} = \gamma_a\nabla^2 w_a - w_a. \tag{6.56}$$

Equation (6.56) is exactly the spatial equation for charge density of a single disclination, Eq. (3.13), but with $\Omega \to 0$, $\left(\frac{\Delta\mu}{\bar{\mu}} - \frac{\Delta\epsilon}{\bar{\epsilon}}\right) \to 1$, and $\cos[(2m-1)\phi] \to \cos[(m-1)\phi+\alpha]$.

From Chapter 3, the solution to Eq. (6.56) is,

$$w_a(\xi,\phi) = \frac{m\cos[(m-1)\phi+\alpha]}{\sqrt{\gamma_a}} f_m(\xi), \tag{6.57}$$

where $\xi = r/\sqrt{\gamma_a}$, and $f_m(\xi)$ solves,

$$f_m''(\xi) + \frac{1}{\xi} f_m'(\xi) - \left(\frac{(m-1)^2}{\xi^2} + 1\right) f_m(\xi) = \frac{1}{\xi}, \tag{6.58}$$

As shown in Chapter 4, the solutions to Eq. (6.58) at $m = 1, m = 2$ are,

$$f_1(\xi) = \frac{\pi}{2}(L_0(\xi) - I_0(\xi)), \tag{6.59}$$

$$f_2(\xi) = K_1(\xi) - \frac{1}{\xi}, \tag{6.60}$$

Where $I_\nu(\xi), K_\nu(\xi)$ are modified Bessel functions, and $L_0(\xi)$ is the modified Struve function of order zero. For all other values of m, $f_m(\xi)$ can be found by variation of parameters,

$$f(\xi) = I_{|m-1|}(\xi)\int^{\xi} K_{|m-1|}(\xi')d\xi' - K_{|m-1|}(\xi)\int^{\xi} I_{|m-1|}(\xi')d\xi'. \tag{6.61}$$

Thus the similarities between the two systems in this limit allow us to use the solutions to the electrokinetic charge density to determine the solutions to w_a, which we show for the specific case of the patterned disclination.

It should be noted that while Sec. 6.3.2 shows that average LCEK forces map into active forces when $\boldsymbol{E} = \hat{\boldsymbol{x}}\cos t + \hat{\boldsymbol{y}} A\cos(\beta t + \gamma)$, with $A = \sqrt{(1+(\beta\Omega)^2)/(1+\Omega^2)}$, we do not find a mapping of ionic concentrations to active concentrations with this field, even in the limit $\Omega_a \ll 1$ discussed above. This is because for this field, the quantity $\langle|\hat{\boldsymbol{n}}\cdot\boldsymbol{E}|\rangle$ is a function of $\boldsymbol{r}$, while for a rotating field of constant magnitude, $\langle|\hat{\boldsymbol{n}}\cdot\boldsymbol{E}|\rangle$ is uniform. Therefore, while the LCEK system reproduces active forces with this two-frequency applied field, its average concentrations do not necessarily reproduce bacterial concentrations. However, for a rotating field of constant magnitude and in the limit $\Omega \ll 1$, our analysis shows that the time-averaged electrokinetic system agrees

with the LLC system in both concentration imbalance between particles swimming in opposite directions and driving body force.

6.5 Discussion

While the results above show a interesting connection between LCEK living liquid crystals, the connection has been derived under the assumption of fixed director orientation and uniform total ionic concentration. Below we discuss the significance of relaxing these assumptions.

While the experiments of Ref. [6] use photo-patterning to impose a specific director field within the thin film, the assumption of a fixed director is in general not realistic. For typical experiments, the Ericksen number is not small; reported as high as $\mathrm{Er} = 125$ in Ref. [100]. Thus viscous torques on director orientation will be at least as large as elastic torques, and the velocity field should distort the director orientation. Furthermore, the typical bacterial length in LLCs is $a^* \sim 5$ μm and cannot be necessarily well approximated as point-particles as ionic species are. A non-negligible size implies that a bacterium will produce director distortions of their own (the liquid crystal molecule tends to orient parallel to the surface of the active particle, or planar anchoring). Thus unlike ions in LCEK, whose presence and motion do not directly distort the nematic, the size and motion of bacteria in typical systems will significantly distort director orientation, with a behavior closer to that of suspended particles with planar anchoring. Therefore, one would need to investigate electrokinetic systems in the limit of finite Ericksen number to determine if the connection between LCEK and LLC is still valid.

The electrokinetic forces and velocities above were computed assuming $Y^2/\gamma \ll 1$, which implies uniform total ionic concentration to first order in Δ. Without this assumption, the equations for ρ and C to first order in Δ are,

$$\Omega \frac{\partial C^{(1)}}{\partial t} = \gamma \nabla^2 C^{(1)} - Y^2 \boldsymbol{E}^{(0)} \cdot \nabla \rho^{(1)} \tag{6.62}$$

$$\Omega \frac{\partial \rho^{(1)}}{\partial t} + \frac{\partial}{\partial x_i}(C^{(1)} \left(\tilde{\epsilon} - \tilde{\mu}\right) n_i (\hat{\boldsymbol{n}} \cdot \boldsymbol{E}^{(0)})) = \gamma \nabla^2 \rho^{(1)} - \rho^{(1)} - \boldsymbol{E}^{(0)} \cdot \nabla C^{(1)}, \tag{6.63}$$

as discussed in Chapter 3. The presence of active-like forces discussed in Sec. 6.3.2

assumes the the first and third terms on the right hand side of Eq. (6.63) are negligibly small. While the first term is negligibly small for $r \gg 1/\sqrt{\gamma}$, as discussed in Chapter 4, the second term is not negligibly small when $C^{(1)}$ is not uniform. Thus for conditions in which $C^{(1)}$ is not uniform ($Y^2/\gamma \gtrsim 1$), the average electrostatic body force $\langle \rho \boldsymbol{E} \rangle$ may not behave as an active force. While some active nematic systems have been investigated assuming uniform concentration of active particles [95,101], in general spatial variations concentration need not be small [6, 98]. More analysis is needed to determine if the similarities between the two systems persist when total concentration is not uniform.

In summary, we find that under certain conditions, the behavior of active nematics corresponds to the average behavior LCEK systems under time dependent electric fields. Specifically, we find that in the limit of low driving frequency, $\Omega \ll 1$, small anisotropy, $|\tilde{\mu}|, |\tilde{\epsilon}| \ll 1$, and uniform total ionic concentration, the average ionic charge density and electrostatic forces of LCEK systems do map onto bacterial concentration differences and active forces in LLC systems. Under an applied field with two orthogonal components at arbitrary unequal frequencies, the average body force in LCEK systems corresponds to the driving force in active nematics, though the evolution of ionic concentrations under such a field does not correspond with the evolution of bacterial concentrations. Further work is needed to determine whether the similarities between the two systems persist across a broader range of parameters.

The mapping just discussed is nevertheless useful in using some of the singularity solutions already known for LCEK systems to interpret singularity driven flows in LLC. However, clearly, the same flows could have been directly derived from the equations governing the motion of living liquid crystals [98]. The correspondence just discussed may also prove useful in that the experiments involving ionic systems are free of some of the complication inherent in handling active matter, including controling the activity during the experiments. In this respect, LCEK flows under rotating electric field may prove useful in studying synthetic configurations involving designer flows, later to be verified directly on the living liquid crystal.

Chapter 7

Conclusions and Future Work

7.1 Conclusions

Liquid crystal electrokinetic (LCEK) phenomena provide a new method for fluid and particle manipulation by an AC electric field. Because the symmetry breaking occurs in the suspending fluid itself rather than due to properties of the suspended material, LCEK allows for systematic transport of material of any phase (solid, liquid, gaseous) and with arbitrary (even neutral) charge.

This thesis has studied how molecular anisotropy in the nematic matrix (both anisotropic permittivity of the nematic solvent, $\Delta\epsilon$, and anisotropy in the mobility of ionic impurities, $\Delta\mu$), lead to spatial charge separation under an applied electrostatic field, and to streaming flows. Because the charge density is proportional to the electric field, $\rho \sim E$, the electrostatic body force is proportional to the square of the field, $\rho E \sim E^2$, which implies systematic flow even under an AC field.

Specifically, we have found that to first order in mobility and dielectric anisotropy, and assuming small variations in total concentration, the charge density satisfies,

$$\Omega \frac{\partial \rho}{\partial t} = \gamma \nabla^2 \rho - \rho + \left(\frac{\Delta\epsilon}{\epsilon_\perp} - \frac{\Delta\mu}{\mu_\perp} \right) \nabla \cdot (\hat{\boldsymbol{n}}(\hat{\boldsymbol{n}} \cdot \boldsymbol{E})), \tag{7.1}$$

where $\Omega = \omega\tau_\rho$ is the applied field frequency relative to the charging time $\tau_\rho = \epsilon_\perp \epsilon_0/(\mu_\perp e c_0)$, and $\gamma = \lambda_D^{*2}/\ell^{*2}$ is the square of the Debye length relative to a characteristic system length ℓ^*. The model, and many of the numerical calculations have

been conducted in parallel with experiments in prototypical nematic director configurations to validate both the model, the algorithm and the code. We have generally found good agreement with experiments in the large scale features of the flows (except for the case of a single, immersed particle), and between analytic predictions and the code for the case of singular director configurations.

We have also examined how the topology of the director configuration has a significant impact on charge density and induced velocity fields. Specifically, we find that the angular distribution of the charge density and velocity generated by a single disclination is a function of its topological charge. We find that whereas the far-field charge density can be determined for relatively complex systems through a multipole expansion of the director field and the topology of the defects, the far-field velocity depends strongly on the inner solution behavior, and it is more difficult to obtain.

In addition, we find that when the applied field has two oscillatory components that are mutually perpendicular, the electrokinetic system maps into an active set of particles suspended in a nematic matrix. We have studied the correspondence between the equations governing bacterial concentrations in active systems and ionic concentrations in LCEK systems with a rotating electric field, as well as the associated stresses, and have shown that LCEK results for charge density and flows can be used to determine bacterial concentrations within some range of physical parameters.

7.2 Future Work

Investigations of the electrophoresis of suspended particles in thin films present a number of modeling challenges regarding the dimensionality of the system. Since the nematic is contained in a thin film, one expects the behavior far from the particle to be quasi two-dimensional. However, the features of a spherical particle are inherently three-dimensional, and considering the dependency of the velocity field on the inner solution behavior discussed in Chapter 5, the difference between the electrokinetic flow around a circular particle in two dimensions and a spherical particle in a three-dimensional thin film may not be insignificant. While an axisymmetric model captures the dimensionality of the sphere, the cell geometry is no longer a thin film. Thus a fully three-dimensional model is necessary to capture all of the features of this experimental geometry. This

study is a precursor of a more comprehensive study of inter-particle interations of electrokinetic origin. Experiments show clustering of particles, as well as swarming, but there is no indication yet about the details of the interparticle forces.

Throughout the numerical work in this thesis we have represented the nematic by a polar vector. It is well known that this representation does not allow half integer singularities. This limitation has been useful in stabilizing a hyperbolic hedgehog in two dimensions for a range of particle sizes in which a disclination ring is known to be stable experimentally. To what extent the flows computed would depend on the aspect ratios between defect cores and particle radius, and particle radius to cell thickness, cannot be determined with our representation. This is certainly a factor that contributes to the discrepancy between our results in three dimensions, their two dimensional couterparts, and the experiments. A three dimensional numerical solution in the tensor order parameter representation appears not to be feasible at present for realistic experimental sizes.

In addition to our two-dimensional assumption, we have only considered systems in which the variations in total concentration C are small. Relaxing this assumption leads to an additional term $\boldsymbol{E} \cdot \nabla C$ in Eq. (7.1). It is not clear how this term will affect the charge behavior when it is of the same order as the last term on the right hand side of Eq. (7.1). While the presence of variations in C couples ρ with C, the system of equations is still linear, suggesting that a solution is possible.

Additionally, the focus of this thesis is on systems with small mobility and dielectric anisotropies. The relative mobility anisotropy in experimental systems is $\Delta\mu/\mu_\perp \approx 0.3$, while the dielectric anisotropy can be as high as $\Delta\epsilon/\epsilon_\perp \approx 0.5$; neither of which are vanishingly small [5, 44]. Thus it would be useful to investigate higher order anisotropy effects. In Chapter 3, we derive an alternative solution for the charge density due to a $(+1)$ disclination without the assumption of small anisotropy, and find the charge density depends radially on the anisotropy, decaying as $r\sqrt{\mu_\perp/\mu_\parallel}^{-2}$. This solution was possible because of the radial symmetry of the $(+1)$ defect; it is not clear whether a similar method could be derived for other topological defects. Furthermore, at higher dielectric anisotropy, the effects body force due to polarization and the dielectric torque on the nematic cannot be neglected. While the results of Ref. [30] investigate anisotropies as high as $\mathcal{O}(1)$, the difference in geometry between this study and the analysis in this

thesis make it difficult to evaluate the effect of higher anisotropy on isolated disclinations and particles in large thin cells. For larger anisitropies, flexoelectric effects cannot be neglected, adding another layer of complexity.

The systems studied are confined to zero or small Ericksen number. Together with the absence of flexoelectric phenomena, and the small thickness of the experimental cells, it is reasonable to assume that the director in the thin film is constant, and equal to that imposed at the boundaries in photo patterned cells. Indeed, there is no experimental indications of deviations due to flows or other phenomena. However, some of the experiments involve Ericksen numbers of order one, and hence one would expect director deviations of viscous origin. This subject remains virtually unexplored.

Finally, in Chapter 6 we predict that electrokinetic systems with electric fields with two oscillating components will produce flows similar to those of active nematics. This hypothesis has not been tested experimentally. It would be useful to determine if the higher order behaviors neglected in this analysis are indeed negligible in experimental studies, and if the behaviors of the two systems do agree. Furthermore, our comparison assumes uniform total concentration of active particles, which is generally not true. It remains an open question whether a mapping between the two systems exists without this assumption.

In summary, our work demonstrates that LCEK produces unique behaviors due to mobility and permittivity anisotropy, and our results suggest that further investigation provides an opportunity to better understand the effects of system geometry, variations in concentration, and high anisotropy on nematic flow. Additionally, we find a promising connection between LCEK and active nematics, but experimental verification of the connection is needed.

References

[1] A Ramos, A Gonzalez, A Castellanos, N G Green, and H Morgan. Pumping of liquids with ac voltages applied to asymmetric pairs of microelectrodes. *Physical Review E*, 67(056302):1–11, 2003.

[2] Sumit Gangwal, Olivier J Cayre, Martin Z Bazant, and Orlin D Velev. Induced-Charge Electrophoresis of Metallodielectric Particles. 058302(February):1–4, 2008.

[3] Chenhui Peng, Yubing Guo, Christopher Conklin, Jorge Viñals, Sergij V. Shiyanovskii, Qi-Huo Wei, and Oleg D. Lavrentovich. Liquid crystals with patterned molecular orientation as an electrolytic active medium. *Phys. Rev. E*, 92:052502, Nov 2015.

[4] T. C. Lubensky, David Pettey, and Nathan Currier. Topological defects and interactions in nematic emulsions. *Physical Review E*, 57(1):610–625, jan 1998.

[5] I. Lazo, C.H. Peng, J. Xiang, S.V. Shiyanovskii, and O.D. Lavrentovich. Liquid crystal-enabled electro-osmosis through spatial charge separation in distorted regions as a novel mechanism of electrokinetics. *Nature Comm.*, 5:5033, 2014.

[6] Chenhui Peng, Taras Turiv, Yubing Guo, Q.-H. Wei, and Oleg D. Lavrentovich. Command of active matter by topological defects and patterns. *Science*, 354(6314):882–885, 2016, 1611.06286.

[7] Vincent Studer, Anne Pépin, Yong Chen, and Armand Ajdari. An integrated AC electrokinetic pump in a microfluidic loop for fast and tunable flow control. *The Analyst*, 129:944–949, 2004.

[8] Cunlu Zhao and Chun Yang. Advances in electrokinetics and their applications in micro / nano fluidics. *Microfluid Nanofluid*, 13:179–203, 2012.

[9] Barett Comiskey, J. D. Albert, Hidekazu Yoshizawa, and Joseph Jacobson. An electrophretic ink for all-printed reflective electronic displays. *Nature*, 394(July):253–255, 1998.

[10] Susanne Klein. Electrophoretic liquid crystal displays : how far are we ? *Liquid Crystals Reviews*, 1(1):52–64, 2013.

[11] T.M. Squires and M.Z. Bazant. Induced-charge electro-osmosis. *J. Fluid Mech.*, 509:217–252, 6 2004.

[12] Chia-yen Lee, Chin-lung Chang, Yao-nan Wang, and Lung-ming Fu. Microfluidic Mixing : A Review. *Int. J. Mol. Sci.*, 12:3263–3287, 2011.

[13] Christopher Conklin and Jorge Viñals. Electrokinetic flows in liquid crystal thin films with fixed anchoring. *Soft Matter*, 13:725–739, 2017.

[14] Sriram Ramaswamy. The mechanics and statistics of active matter. *Annual Review of Condensed Matter Physics*, 1(1):323–345, 2010, 1004.1933.

[15] P.G. de Gennes and J. Prost. *The Physics of Liquid Crystals*. Clarendon, Oxford, 1993.

[16] Patricia Bauman and Daniel Phillips. Regularity and the behavior of eigenvalues for minimizers of a constrained q-tensor energy for liquid crystals. *Calculus of Variations and Partial Differential Equations*, 55(4):81, Jun 2016.

[17] P. M. Chaikin and T. C. Lubensky. *Principles of Condensed Matter Physics*. Cambridge University Press, Cambridge, 1995.

[18] Fong Liu and Gene F. Mazenko. Growth kinetics of systems with continuous symmetry. *Physical Review B*, 45(13):6989–7001, 1992.

[19] M. Kleman and O.D. Lavrentovich. *Soft Matter Physics: An Introduction*. Springer, New York, 2003.

[20] Gareth P. Alexander, Bryan Gin Ge Chen, Elisabetta A. Matsumoto, and Randall D. Kamien. Colloquium: Disclination loops, point defects, and all that in nematic liquid crystals. *Reviews of Modern Physics*, 84(2):497–514, 2012, 1107.1169.

[21] M. Kleman and O. D. Lavrentovich. Topological point defects in nematic liquid crystals. *Philosophical Magazine*, 86(25-26):4117–4137, sep 2006.

[22] Paul J. Ackerman, Jao van de Lagemaat, and Ivan I. Smalyukh. Self-assembly and electrostriction of arrays and chains of hopfion particles in chiral liquid crystals. *Nature Communications*, 6:6012, 2015.

[23] F. M. Leslie and J. L. Ericksen. Some Constitutive Equations for Liquid Crystals. *Liquid Crystals*, pages 265–283, 1967.

[24] Dieter Forster, Tom C. Lubensky, Paul C. Martin, Jack Swift, and P. S. Pershan. Hydrodynamics of liquid crystals. *Phys. Rev. Lett.*, 26:1016–1019, Apr 1971.

[25] P. C. Martin, O. Parodi, and P. S. Pershan. Unified hydrodynamic theory for crystals, liquid crystals, and normal fluids. *Phys. Rev. A*, 6:2401–2420, Dec 1972.

[26] Peter D Olmsted and Paul Goldbart. Theory of the nonequilibrium phase transition for nematic liquid crystals under shear flow. *Physical Review A*, 41(8):4578–4582, 1990.

[27] Anthony N. Beris and Brian J. Edwards. *Thermodynamics of Flowing Systems*. Oxford University Press, 1994.

[28] H. Stark and T. C. Lubensky. Poisson-bracket approach to the dynamics of nematic liquid crystals. *Physical Review E*, 67(6):061709, 2003.

[29] C. Neyts and F. Beunis. *Ion transport in liquid crystals*, pages 357–382. Wiley-VCH, Germany, 2014.

[30] Oleh M. Tovkach, Christopher Conklin, M. Carme Calderer, Dmitry Golovaty, Oleg D. Lavrentovich, Jorge Viñals, and Noel J. Walkington. Q-tensor model for electrokinetics in nematic liquid crystals. *Physical Review Fluids*, 2(053302):1–21, 2017, 1612.03446.

[31] S.R. de Groot and P. Mazur. *Non-equilibrium Thermodynamics*. Dover, New York, 1984.

[32] W. Helfrich. Conduction-induced alignment of nematic liquid crystals: Basic model and stability considerations. *J. Chem. Phys.*, 51:4092, 1969.

[33] M. E. Mullen, B. Lüthi, and M. J. Stephen. Sound velocity in a nematic liquid crystal. *Phys. Rev. Lett.*, 28:799–801, Mar 1972.

[34] I.W. Stewart. *The static and dynamic continuum theory of liquid crystals*. Taylor and Francis, New York, 2004.

[35] O.M. Tovkach, M.C. Calderer, D. Golovaty, O. Lavrentovich, and N.J. Walkington. *Phys. Rev. E*, 94:012702, 2016.

[36] Alexander Mielke. Variational approaches and methods for dissipative material models with multiple scales. In *Analysis and Computation of Microstructure in Finite Plasticity*, pages 125–155. Springer, 2015.

[37] André M. Sonnet and Epifanio G. Virga. *Dissipative ordered fluids: theories for liquid crystals*. Springer Science & Business Media, 2012.

[38] A. M. Sonnet, P. L. Maffettone, and E. G. Virga. Continuum theory for nematic liquid crystals with tensorial order. *Journal of Non-Newtonian Fluid Mechanics*, 119(1):51–59, 2004.

[39] André M. Sonnet and Epifanio G. Virga. Dynamics of dissipative ordered fluids. *Physical Review E*, 64(3):031705, 2001.

[40] Masao Doi. Onsager's variational principle in soft matter. *Journal of Physics: Condensed Matter*, 23(28):284118, 2011.

[41] J. Ericksen. Liquid crystals with variable degree of orientation. *Arch Rath. Mech. Anal.*, 113:97–120, 1991.

[42] N. Kuzuu and M. Doi. Constitutive equation for nematic liquid crystals under weak velocity gradient derived from a molecular kinetic equation. II. *J. Phys. Soc. Japan*, 53:1031–1040, 1984.

[43] M. Carme Calderer, Dmitry Golovaty, Oleg D. Lavrentovich, and Noel J. Walkington. Modeling of nematic electrolyte and nonlinear electroosmosis. *SIAM J. Appl. Math.*, 76:2260–2285, 2016.

[44] Sathyanarayana Paladugu, Christopher Conklin, Jorge Viñals, and Oleg D Lavrentovich. Nonlinear Electrophoresis of Colloids Controlled by Anisotropic Conductivity and Permittivity of Liquid-Crystalline Electrolyte. *Physical Review Applied*, 7(034033):1–8, 2017.

[45] P. Bauman and D. Phillips. Regularity and the behavior of eigenvalues for minimizers of a constrained q-tensor energy for liquid crystals. *arXiv:math.AP/1511.01039*, 2016, 1511.01039.

[46] Noel J. Walkington. Numerical approximation of nematic liquid crystal flows governed by the ericksen-leslie equations. *ESAIM: Mathematical Modelling and Numerical Analysis*, 45:523–540, 5 2011.

[47] Ricardo H. Nochetto, Shawn W. Walker, and Wujun Zhang. A finite element method for nematic liquid crystals with variable degree of orientation. *arXiv:math.NA/1601.00037*, 2016, 1601.00037.

[48] D. Svensek and S. Zumer. *Phys. Rev. E*, 66:021712, 2002.

[49] G. Toth, C. Denniston, and J.M. Yeomans. *Phys. Rev. Lett.*, 88:105504, 2002.

[50] Oleg Yaroshchuk and Yuriy Reznikov. Photoalignment of liquid crystals: basics and current trends. *J. Mater. Chem.*, 22(2):286–300, 2012.

[51] H. Stark. Physics of colloidal dispersions in nematic liquid crystals. *Phys. Rep.*, 351:387–474, 2001.

[52] Chenhui Peng, Taras Turiv, Yubing Guo, Sergij V. Shiyanovskii, Qi-Huo Wei, and Oleg D. Lavrentovich. Control of colloidal placement by modulated molecular orientation in nematic cells. *Science Advances*, 2(9):1–9, 2016.

[53] R. Ribotta and A. Joets. Oblique Roll Instability in an Electroconvective Anisotropic Fluid. *Physical Review Letters*, 56(5):1595–1598, 1986.

[54] Ingo Rehberg, Bernhard L. Winkler, Manuel de la Torre Juarez, Steffen Rasenat, and Wolfgang Schöpf. *Pattern formation in a liquid crystal*, pages 35–52. Springer Berlin Heidelberg, Berlin, Heidelberg, 1989.

[55] Dubois-Violette, E., de Gennes, P.G., and Parodi, O. Hydrodynamic instabilities of nematic liquid crystals under a. c. electric fields. *J. Phys. France*, 32(4):305–317, 1971.

[56] M. Kaiser, W. Pesch, and E. Bodenschatz. Mean flow effects in the electrohydrodynamic convection in nematic liquid crystals. *Physica D*, 59:320, 1992.

[57] Harald Pleiner and HR Brand. Hydrodynamics and electrohydrodynamics of liquid crystals. *Pattern Formation in Liquid Crystals*, pages 15–69, 1996.

[58] C. Conklin. *COMSOL code. Open Science Framework, DOI:10.17605/OSF.IO/UBQS9*, 2016.

[59] COMSOLAB. *COMSOL Multiphysics Reference Guide*, 2012.

[60] Martin Z. Bazant, Mustafa Sabri Kilic, Brian D. Storey, and Armand Ajdari. Towards an understanding of induced-charge electrokinetics at large applied voltages in concentrated solutions. *Advances in Colloid and Interface Science*, 152(12):48 – 88, 2009.

[61] *NIST Digital Library of Mathematical Functions.* http://dlmf.nist.gov/, Release 1.0.16 of 2017-09-18. F. W. J. Olver, A. B. Olde Daalhuis, D. W. Lozier, B. I. Schneider, R. F. Boisvert, C. W. Clark, B. R. Miller and B. V. Saunders, eds.

[62] George B. Arfken, Hans J. Weber, and Frank E. Harris. *Mathematical Methods for Physicists.* Elsevier, 2013.

[63] R. Di Leonardo, S. Keen, F. Ianni, J. Leach, M. J. Padgett, and G. Ruocco. Hydrodynamic interactions in two dimensions. *Physical Review E - Statistical, Nonlinear, and Soft Matter Physics*, 78(3):1–4, 2008, 0804.0850.

[64] I.S. Aranson. *Physics-Uspekhi*, 56:79, 2013.

[65] A. Zöttl and H. Stark. *Journal of Physics: Condensed Matter*, 28:253001, 2016.

[66] O.D. Lavrentovich. *Current Opinion in Colloid and Interface Science*, 21:97, 2016.

[67] J. Dobnikar, A. Snezhko, and A. Yethiraj. *Soft Matter*, 9:3693, 2013.

[68] A. Ramos. *Electrokinetics and Electrohydrodynamics in Microsystems*. Springer-Verlag, Wien, 2011.

[69] M.Z. Bazant and T.M. Squires. *Current Opinion in Colloid and Interface Science*, 15:203, 2010.

[70] Randall D Kamien. The geometry of soft materials : a primer. *Reviews of Modern Physics*, 74(October):953–971, 2002.

[71] Stan Alama, Lia Bronsard, and Xavier Lamy. Analytical description of the Saturn-ring defect in nematic colloids. *Phys. Rev. E*, 93(1):012705, 2016.

[72] P. Poulin, H. Stark, T.C. Lubensky, and D.A. Weitz. Novel colloidal interactions in anisotropic fluids. *Science*, 275:1770–1773, 1997.

[73] Yuedong Gu and Nicholas L. Abbott. Observation of Saturn-ring defects around solid microspheres in nematic liquid crystals. *Phys. Rev. Lett.*, 85(22):4719–4722, 2000.

[74] V. M. Pergamenshchik. Elastic multipoles in the field of the nematic director distortions. *European Physical Journal E*, 37(12):1–15, 2014.

[75] I. I. Smalyukh, O. D. Lavrentovich, A. N. Kuzmin, A. V. Kachynski, and P. N. Prasad. Elasticity-Mediated Self-Organization and Colloidal Interactions of Solid Spheres with Tangential Anchoring in a Nematic Liquid Crystal. *Physical Review Letters*, 95(15):157801, oct 2005, 0508331.

[76] Holger Stark. Saturn-ring defects around microspheres suspended in nematic liquid crystals: An analogy between confined geometries and magnetic fields. *Phys. Rev. E*, 66(3):032701, September 2002.

[77] M. Tasinkevych, N. M. Silvestre, P. Patrício, and M. M. Telo da Gama. Colloidal interactions in two-dimensional nematics. *The European Physical Journal E*, 9(4):341–7, nov 2002.

[78] David Pettey, T. C. Lubensky, and Darren R. Link. Topological inclusions in 2D smectic C films. *Liquid Crystals*, 25(5):579–587, 2010.

[79] O.D. Lavrentovich, I. Lazo, and O.P. Pishnyak. Nonlinear electrophoresis of dielectric and metal spheres in a nematic liquid crystal. *Nature*, 467:947–950, 2010.

[80] Israel Lazo and Oleg D. Lavrentovich. Liquid-crystal-enabled electrophoresis of spheres in a nematic medium with negative dielectric anisotropy. *Phil. Trans. R. Soc. London A: Mathematical, Physical and Engineering Sciences*, 371(1988), 2013, http://rsta.royalsocietypublishing.org/content/371/1988/20120255.full.pdf.

[81] J. Jadzyn and P. Kêdziora. *Molecular Crystals and Liquid Crystals*, 145:17, 1987.

[82] B.-X. Li, V. Borshch, S.V. Shiyanovskii, S.-B. Liu, and O.D. Lavrentovich. *Applied Physics Letters*, 104:201105, 2014.

[83] O.D. Lavrentovich, V.G. Nazarenko, V.V. Sergan, and G. Durand. *Phys. Rev. A*, 45:R6969, 1992.

[84] Junichi Fukuda, Holger Stark, Makoto Yoneya, and Hiroshi Yokoyama. Dynamics of a nematic liquid crystal around a spherical particle. *Journal of Physics: Condensed Matter*, 16(19):S1957–S1968, May 2004.

[85] Y.A. Natishin, R.D. Polak, S.V. Shiyanovskii, V.H. Bodnar, and O.D. Lavrentovich. *J. Appl. Phys*, 86:4199.

[86] L.M. Blinov. *Structure and Properties of Liquid Crystals*. Springer Netherlands, 2011.

[87] T. Rasing and I. Muševič. *Surfaces and Interfaces of Liquid Crystals*. Springer Berlin, Heidelberg, 2004.

[88] R. W. Ruhwandl and E. M. Terentjev. Long-range forces and aggregation of colloid particles in a nematic liquid crystal. *Physical Review E*, 55(3):2958–2961, mar 1997.

[89] V. M. Pergamenshchik and V. A. Uzunova. Dipolar colloids in nematostatics: Tensorial structure, symmetry, different types, and their interaction. *Physical Review E*, 83(2):021701, feb 2011.

[90] Francisco R. Hung, Orlando Guzmán, Brian T. Gettelfinger, Nicholas L. Abbott, and Juan J. de Pablo. Anisotropic nanoparticles immersed in a nematic liquid crystal: Defect structures and potentials of mean force. *Physical Review E*, 74(1):011711, jul 2006.

[91] K. Tojo, A. Furukawa, T. Araki, and A. Onuki. Defect structures in nematic liquid crystals around charged particles. *The European Physical Journal E*, 30(1):55–64, 2009.

[92] Takahiro Kishita, Noboru Kondo, Kenji Takahashi, Masatoshi Ichikawa, Jun-ichi Fukuda, and Yasuyuki Kimura. Interparticle force in nematic colloids: Comparison between experiment and theory. *Physical Review E*, 84(2):021704, aug 2011.

[93] Jun-ichi Fukuda, Holger Stark, Makoto Yoneya, and Hiroshi Yokoyama. Interaction between two spherical particles in a nematic liquid crystal. *Physical Review E*, 69(4):041706, apr 2004.

[94] S. Hernández-Navarro, P. Tierno, J.A. Farrera, J. Ignes-Mullol, and F. Sagués. Reconfigurable swarms of nematic colloids controlled by photoactivated surface patterns. *Angewandte Chemie-International Edition*, 53:10696–106700, 2014.

[95] M. C. Marchetti, J. F. Joanny, S. Ramaswamy, T. B. Liverpool, J. Prost, Madan Rao, and R. Aditi Simha. Hydrodynamics of soft active matter. *Reviews of Modern Physics*, 85(3):1143–1189, 2013, 1207.2929.

[96] Walter F. Paxton, Kevin C. Kistler, Christine C. Olmeda, Ayusman Sen, Sarah K. St. Angelo, Yanyan Cao, Thomas E. Mallouk, Paul E. Lammert, and Vincent H. Crespi. Catalytic nanomotors: autonomous movement of striped nanorods. *Journal of the American Chemical Society*, 126(41):13424–13431, 2004, http://dx.doi.org/10.1021/ja047697z. PMID: 15479099.

[97] Stephen J Decamp, Gabriel S Redner, Aparna Baskaran, Michael F Hagan, and Zvonimir Dogic. Orientational order of motile defects in active nematics. *Nature materials*, 14(August):1110–1115, 2015.

[98] Mikhail M Genkin, Andrey Sokolov, Oleg D Lavrentovich, and Igor S Aranson. Topological Defects in a Living Nematic Ensnare Swimming Bacteria. *Physical Review X*, 7(1):11029, 2017.

[99] R. Aditi Simha and Sriram Ramaswamy. Hydrodynamic Fluctuations and Instabilities in Ordered Suspensions of Self-Propelled Particles. *Physical Review Letters*, 89(5):058101, 2002.

[100] Sumesh P. Thampi, Ramin Golestanian, and Julia M. Yeomans. Velocity correlations in an active nematic. *Physical Review Letters*, 111(11):2–6, 2013, arXiv:1302.6732v1.

[101] Richard Green, John Toner, and Vincenzo Vitelli. The geometry of threshold-less active flow in nematic microfluidics. *arXiv preprint*, pages 1–17, 2016, 1602.00561.